STUDIES ON
GIANT MAGNETOSTRICTIVE ACTUATOR
FOR DISC BRAKE APPLICATION

Thesis

Submitted in partial fulfillment of the requirement for the degree of

DOCTOR OF PHILOSOPHY

by

RAGHAVENDRA JOSHI

DEPARTMENT OF MECHANICAL ENGINEERING

NATIONAL INSTITUTE OF TECHNOLOGY KARNATAKA,

SURATHKAL, MANGALORE – 575025

January-2016

D E C L A R A T ION

I hereby declare that the Research Thesis entitled "**STUDIES ON GIANT MAGNETOSTRICTIVE ACTUATOR FOR DISC BRAKE APPLICATION**" which is being submitted to the **National Institute of Technology Karnataka, Surathkal** in partial fulfillment of the requirements for the award of the degree of **Doctor of Philosophy** in **Department of Mechanical Engineering** *is a bonafide report of the research work carried out by me.* The material contained in this Research Synopsis has not been submitted to any University or Institution for the award of any degree.

Register Number:**100538ME10F04**

Name of the Research Scholar: **Raghavendra Joshi**

Signature of the Research Scholar:

Department of Mechanical Engineering

Place: NITK-Surathkal

Date: 13/ 01/2016

CERTIFICATE

This is to certify that the Research Thesis entitled "**STUDIES ON GIANT MAGNETOSTRICTIVE ACTUATOR FOR DISC BRAKE APPLICATION**" submitted by **Mr Raghavendra Joshi (Register Number: 100538ME10F04)** as the record of the research work carried out by him, *is accepted as the Research Thesis submission* in partial fulfillment of the requirements for the award of the degree of **Doctor of Philosophy.**

Dr. Ravikiran Kadoli

Research Guide & Professor

Department of Mechanical Engineering

National Institute of Technology Karnataka,

Surathkal-575025, India.

Dr. K. V. Gangadharan

HOD & Chairman-DRPC

Department of Mechanical Engineering

National Institute of Technology Karnataka,

Surathkal – 575025, India.

Date: 13/01/2016

In dedication to the loving memory of my Father, my Mother for making me be who I am, and my Wife and Son for supporting me all the way.

ACKNOWLEDGEMENT

ABSTRACT

The present study discusses the implementation of magnetostrictive actuation in disc brake system for braking action. In line with this, disc for a caliper unit is chosen and for a range of speeds, the axial braking force and braking torque required on each frictional pad is estimated. Based on the axial force required, an appropriate size of Terfenol-D rod is selected for the magnetostrictive actuator. A separate coil is used for biasing instead of permanent magnet in addition to excitation coil in the layout of a Terfenol-D actuator. The coaxial coils of Terfenol-D actuator are designed based on the required magnetic field strength. The number of coil turns obtained for coaxial coils with Ampere's law is verified from reluctance approach. The shape factor of coaxial coils were found to be, 0.1653 and 0.1154 for coil 1 and coil 2, respectively which are close to 0.179 for maximum magnetic field at the centre of coils. The magnetic flux densities of coaxial solenoids in free air are verified analytically, experimentally and numerically using MAXWELL 2D solver. The distribution of axial, radial magnetic flux density and flux distribution in the actuator assembly with different housing materials namely mild steel, cast iron and aluminium with and without Terfenol-D are discussed considering the effect of magnetic permeability of housing materials. It is observed that the magnetic flux distribution is stronger in an actuator with mild steel housing compared to cast iron and aluminium housing. Theoretically, the magnetic field strength on a Terfenol-D rod is arrived at by taking the inductance of driving coils. Energy based Jiles-Atherton model is used to calculate the magnetization of a Terfenol-D material. Non-constitutive model takes into account of parameters such as magnetization, applied prestress and Young's modulus to quantify the magnetostriction of a Terfenol-D material. The existing non-constitutive magnetostriction model does not consider strain at resonance condition. The strain or magnetostriction at resonance condition is accounted by the term called quality factor. The present study considers the influence of quality factor into the existing non-constitutive models. Two magnetostrictive models are proposed to consider the influence of quality factor. The first magnetostriction model proposed considers the quality factor on the magnetostriction due to applied prestress. The

second magnetostriction model considers the quality factor on the magnetostriction due to magnetization of Terfenol-D. Magnetostriction of a Terfenol-D material was estimated using the proposed magnetostriction model I and II. The output obtained from the proposed magnetostriction models are verified with experimental data as well as quadratic and non-linear magnetostriction models from the literature. Experiments were conducted on a Terfenol-D actuator for DC input under prestress conditions. Performance parameters such as displacement, repeatability, step response, and response time are measured. The results indicate a better performance of the actuator at each point of excitation when step input is biased to one of the coils instead of varying the step input equally to coaxial coils. Force exerted by a Terfenol-D actuator is compared for zero and other prestress conditions using magneto-mechanical coupling equations. Hydraulic amplification unit is designed assuming amplification ratio of 5 to boost the displacement obtained from the Terfenol-D actuator. Displacement and output energy capability of a Terfenol-D actuator as well as displacement amplified Terfenol-D actuator are evaluated using stiffness match principle. Based on stiffness ratio, theoretically the amplification ratio is evaluated and verified with the value assumed in the design of amplification unit. After amplification, the braking force and braking torque available at each annular pad are evaluated from the theoretical and experiment output of a Terfenol-D actuator under different preload conditions. Further, these results are verified with the results obtained based on disc specifications. It is summarized that the braking force and torque achieved at the annular pads of a caliper unit for an applied step input and preload are sufficient to decelerate or stop the disc till the rated speed of 800 rpm. Finally, attempts are made to verify the output at the end of a hydraulic amplification unit without brake fluid by coupling a Terfenol-D actuator assembly.

Key words: Terfenol-D, Disc brake, Coaxial coils, Maxwell 2D solver, Step input, Repeatability, Step response, Inductance of driving coils, Jiles-Atherton model, Quality factor, Hydraulic amplification unit, Stiffness match principle.

CONTENTS

LIST OF FIGURES

xiv

xv

xvii

xx

LIST OF TABLES

NOMENCLATURE

A_{coil}	Cross-sectional area of coil (mm^2)
A_i	Cross-sectional area of ith component (i =1, 2…9 in mm)
A_l	Cross-sectional area of a larger end of a piston (mm^2)
A_s	Cross-sectional area of a smaller end of a piston (mm^2)
A_T	Cross-sectional area of a Terfenol-D rod (m^2)
a	Shape parameter of anhysteretic curve
a_1 and a_2	Inner and outer radii of coil (mm)
$\mathbf{A}$	Magnetic vector potential
B	Magnetic flux density (Tesla)
b	Stiffness ratio
b_{opt}	Optimum stiffness ratio
c	Reversibility coefficient
C	Speed of the disc (rpm)
d_{2i}	Outer radii of ith coaxial coils (mm)
d_{2i-1}	Inner radii of ith coaxial coils (mm)
d_{33}	Magnetostrictive strain coefficient (N-m/A)
d and d^*	Piezomagnetic cross-coupling coefficients
E^B	Young's modulus at constant magnetic flux density (N/m^2)
E^H	Young's modulus at constant magnetic field (N/m^2)
E_T	Young's modulus of a Terfenol-D rod (N/m^2)
$E_e^{'}$	Output energy coefficient of a Terfenol-D actuator
$E_e^{''}$	Output energy coefficient of an amplified Terfenol-D actuator
E_{TA}	Output energy of a Terfenol-D actuator (N-mm)
E_{ref}	Reference output energy of a Terfenol-D actuator (N-mm)
F_B	Blocked force (N)

F_T	Force exerted by a Terfenol-D rod (N)
f	Arbitrary function of effective field
G_{coil}	Shape factor of coil
$H_{coil\ 1}$ and $H_{coil\ 2}$	Magnetic field produced by coil 1 and coil 2 (A/m)
H_{qi}	Magnetic field strength in a quality factor term
$H_{qi=1}$	Magnetic field in a quality factor term of magnetostriction model I
$H_{qi=2}$	Magnetic field in a quality factor term of magnetostriction model II
H_T	Magnetic field strength of Terfenol-D rod (A/m)
I_{coil}	Input current to coil (A)
I_{disc}	Mass moment of inertia of the disc (kg-m^2)
J_{coil}	Current density (A/m^2)
J_i	Current density of ith coaxial coils (A/m^2)
k_c	Magneto-mechanical coupling factor
K_{coil}	Coil compensation coefficient
k	Pinning constant
K_T	Stiffness of Terfenol-D rod (N/mm)
K_B	Stiffness of Belleville springs (N/mm)
K_e	Equivalent external stiffness (N/mm)
K_i	Internal stiffness of Terfenol-D (N/mm)
K_P	Stiffness of plunger (N/mm)
K_{PR}	Stiffness of piston rod (N/mm)
K_{WC}	Stiffness of wheel cylinder piston (N/mm)
$l_{Coil\ 1}$ and $l_{Coil\ 2}$	Length of coil 1 and coil 2 (mm)
l_i	Length of ith component (i =1, 2…9 in mm)
l_T	Length of the Terfenol-D rod (mm)

L_{coil}	Inductance of the coil (mH)
L_s	Self-inductance of coil (mH)
L_m	Mutual inductance of coil (mH)
M_s	Saturation magnetization (A/m)
M_{an}	Anhysteretic magnetization (A/m)
M_{tot}	Total magnetization (A/m)
M_{irr}	Irreversible magnetization (A/m)
M_{rev}	Reversible magnetization (A/m)
$N_{Coil\ 1}$ and $N_{Coil\ 2}$	Number of turns in coil 1 and coil 2
$P_{coil\ losses}$	Coil losses
P_f	Braking force (N)
Q_3	Quality factor (3-20)
R_{coil}	Resistance of the coil (Ω)
R_m	Mean radius of frictional pads (mm)
r_0 and r_i	Outer and inner radii of frictional pads (mm)
S	Output displacement coefficient of a Terfenol-D actuator
S'	Output displacement coefficient of an amplified Terfenol-D actuator
S'_{opt}	Optimum amplification ratio
T_T	Stress induced in a Terfenol-D rod (N/m^2)
T	Braking torque (N-m)
T_c	Curie temperature (^{o}C)
v	Volume of the disc (mm^3)
v_T	Volume of the Terfenol-D rod (mm^3)
v_{coil}	Volume of the coil (mm^3)
X	Displacement of actuator due to magnetostriction effect (μm)
z	Axial distance along the axis of coaxial coils (mm)

Z	Hydraulic gain of an amplifying cylinder
Z_{opt}	Optimum hydraulic gain

GREEK SYMBOLS

ϕ	Total magnetic flux (Wb/m^2)
μ_T	Relative permeability of a Terfenol-D rod
$\Re$	Total reluctance (AT/Wb)
χ	Fill factor
ρ	Electrical resistivity of the copper wire (Ω-m)
μ_0	Permeability of material in free space ($4\pi\times10^{-7}$ T-m /A)
μ^σ	Relative magnetic permeability at a constant stress
$L\ (x)$	Langevin function
λ	Magnetostriction (ppm)
λ_{max}	Maximum magnetostriction (ppm)
λ_s	Saturation magnetostriction (ppm)
σ	Applied prestress (MPa)
σ_s	Saturation prestress (MPa)
ω	Angular velocity of disc (rad/sec)
μ	Coefficient of friction between frictional pads and disc

ABBREVATIONS

TC	Terfenol-D and Coil
TCM	Terfenol-D, Coil and Permanent Magnet
TMC	Terfenol-D, Permanent Magnet and Coil
MTC	Permanent Magnet, Terfenol-D and Coil
TCC	Terfenol-D with coaxial coils
DOT	Department Of Transportation
SAE	Society of Automotive Engineers
$K.E.$	Kinetic energy of disc

CHAPTER 1

INTRODUCTION

1.1. OVERVIEW OF BRAKE SYSTEM

Recent years, the brake technology has undergone many improvisations as it is one of the vital system in an automobile. Brakes are also used in automatic transmissions, as a backstop (devices designed to present reversal of rotation), bucket conveyors, hoists, punch and forming presses, overhead cranes and aircraft. Brakes are required to possess the ability to generate high torque and absorb energy at extremely high rates for short periods of time. They must have the mechanism to keep the heat of absorption capability for extended periods of time (Newcomb and Spurr, 1967). The brakes must have good anti-fade characteristics so that their effectiveness should not decrease with constant usage especially while descending hills. These requirements demand that the cooling of the brakes should be very efficient (Nathi et al., 2012). The highly efficient brakes cause rapid wear of tyres, brake linings and are always at a risk of losing vehicle control when brakes are applied. The brake efficiency in general use varies from 50% to 80%, which enable the vehicle to stop within practical distance (Srinivasan, 2003). Stopping ability of any automobile can be increased by understanding the performance limits such as force, deflection, wear, temperature and tire traction (Phun, 1985). In general, there are two types of brake one is drum brake and the other is disc brake (Orthwein 2004, Newcomb and Spurr, 1967). Disc brakes wear longer, are less affected by water, are self-adjusting, self-cleaning, less prone to grabbing or pulling and stop better than any other system around (Nathi et al., 2012 and Rajput, 2007). In addition to these advantages, disc brakes present themselves with short response time and good performance provided the choice of disc brake in the present work. The difference between drum brakes and disc brakes is shown in Table 1-1. The conventional brakes in terms of various features have been compared qualitatively in Table 1-2.

Table 1-1. Difference between drum and disc brake (http://www. sime-strogmag.com).
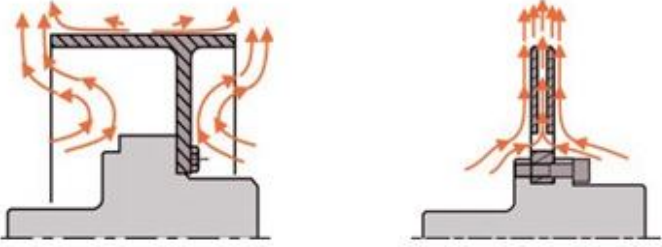
Table 1-2. Comparison of conventional brakes.

	Constru-ction	Mainte-nance	Initial Cost	Friction	Wear	Weight	Efficiency
Drum Brake	Complex	Difficult	Low	More	Medium	More	**85-90%**
Disc Brake	Simple	Simple	More	Less	More	Low	**90-95%**

1.2 BRAKE ACTUATION SYSTEMS

The actuation mechanism is part of the brake system which transmits force from the rider to the actual braking system. The actuation mechanisms used in practice are mechanically operated, hydraulic actuation, pneumatic actuation and electromagnetic actuation. Most of the brake systems used in automobiles, particularly the disc brake are of hydraulic type as they are less expensive and have low operating cost compared

to other alternatives. A qualitative comparison of the hydraulic actuation with other actuation systems is tabulated in Table 1-3.

Table 1-3. Comparison of conventional actuation systems in practice.

	Pneumatic Actuation	Hydraulic Actuation	Electric Actuation
Construction	Complicated	Simple	Simple
Maintenance	Simple	Difficult	Easier
Initial cost	Costly	Medium	Limited
Friction	Medium	More	Less
Wear	Very less	Low	Limited
Weight	Medium	More	Less
Efficiency	90-95%	85-95%	80-90%

1.2.1 Hydraulic actuation

In hydraulic actuation brake the fluid pressure is used for controlling a mechanism. A complete schematic hydraulic braking system contains master cylinder that operates several wheel cylinders is shown in Fig. 1.1.
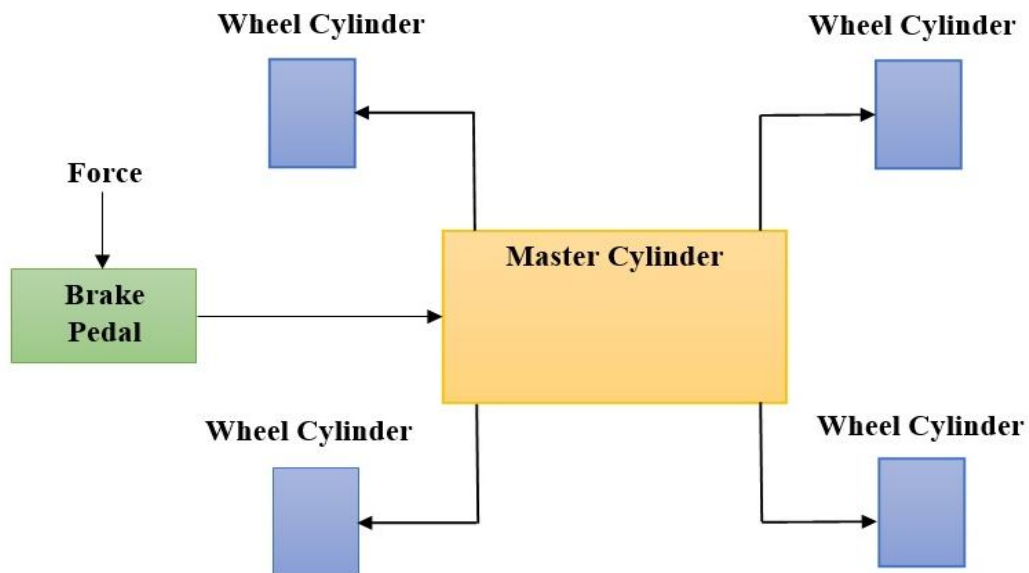
Fig. 1.1. Conventional hydraulic actuation system in brakes.

The master cylinder piston is brought in to operation by the brake pedal. It is like a pump in its simplest form that forces the brake fluid through pipes. Pressure in the pipe causes a small movement to operate either brake shoes or pads. The wheel

cylinders work like a pump only in overturn. Hydraulic brakes also use brake levers to push fluid from a reservoir through a hose to move pistons in a caliper thus forcing pad against a braking surface. Two types of brake fluid are used today: mineral oil and DOT (Department Of Transportation) fluid. Mineral oil is generally inert, while DOT has a higher boiling point. The three types of DOT fluids namely DOT 3, DOT 4 and DOT 5 having boiling points of 205 ^{0}C, 230 ^{0}C and 260 ^{0}C are recommended for use in hydraulically actuated drum and disc brake (Phun, 1985 and Siddiqui, 2011). Hydraulic actuation in braking systems has several advantages such as equal braking on all wheels, increased braking force, low wear rate and flexibility of brake linings. Apart, the disadvantages like leakage of braking fluid from brake linings, fluid pressure inside the tube and boiling of fluid fails the whole braking system.

1.3. REVIEW OF SMART MATERIAL BASED ACTUATORS

In manufacturing industries, smart materials have been widely used to achieve high precision actuation and controlled response. Over the past decades, with advances in material sciences and actuation technologies for high precision purposes, the demand for the design and control of high precision actuators of smart structures such as piezoelectric, electrostatic and magnetostrictive actuators has grown quite distinctly. One of the common characteristics of smart material is that they react mechanically to external stimuli.
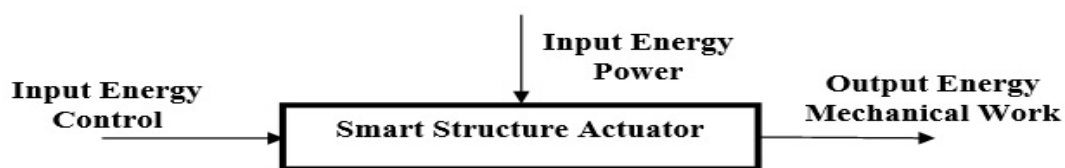
Fig. 1.2. Fundamental principle of a smart structure actuator.

Fig. 1.2 shows the fundamental principle of a typical actuator using smart material which will transform the various inputs of physical energy in the form of power energy or control energy into mechanical work i.e. the desired actuation displacement, velocity or acceleration. This property is ideal for actuators.

1.3.1 Limitations of conventional actuators over smart material actuators

An extensive research and exercise is still on to develop simple, more reliable, more powerful, easier to maintain and inexpensive actuators in engineering and other applications. Presently conventional actuators in use have certain limitations such as conversion of different types of energy (mechanical, hydraulic and electrical), large number of parts, high vulnerability of the hydraulic pipes and frequency bandwidth (Giurgiutiu, 2000). Due to these limitations, the use of smart materials offers direct conversion of electrical energy to high frequency linear motion.

Recently, solid-state induced-strain actuators are in the limelight and indicated a significant increase of usage in various applications due to their excellent features. Primarily developed revolutionary actuators for high frequency and low-displacement acoustic applications are now finding suitable in many areas of mechanical and aerospace design. Solid-state induced-strain devices have a very promising future in the application of linear actuation for vibration and aero elastic control (Giurgiutiu et al., 1995 and Giurgiutiu, 2000). The induced strain actuation using smart materials eliminates the requirement of hydraulic power systems (Giurgiutiu, 2000) and directly depends on the conversion of electrical to mechanical. The induced-strain actuators are compact, reliable and directly transform input electrical energy into output mechanical energy.

Separate hydraulic power unit furnished with large electric motor and hydraulic pump required for conventional actuator is the major drawback in aerospace and robotic applications. This drawback also initiated the automobile designers to promote "brake-by-wire" concept which is scheduled to enter the commercial market in the next few years (Hoseinnezhad and Bab-Hadiashar, 2009).

At present, electro-mechanical actuation that directly converts electrical energy into mechanical energy is increasingly preferred in several industrial applications. The most widely used high-power electro-mechanical actuators are electric motors. However, they can deliver only rotary motion and need to utilize gearboxes and rotary-to-linear conversion mechanisms to achieve linear motion. This route is cumbersome, leads to additional weight and has low frequency bandwidth. Direct conversion of electrical energy into linear force and motion is possible but its

practical implementation in the form of solenoids and electrodynamic shakers is marred by typically low force performance. The use of solenoids or electrodynamic shakers to perform the actuator duty cycle of hydraulic cylinders does not seem conceivable. Solid-state induced-strain actuators offer a viable alternative which can produce remarkably high force though their output displacement is relatively small (Giurgiutiu et al., 1995; Giurgiutiu et al., 1996a). The induced-strain actuators can achieve output strokes similar to conventional hydraulic actuators with well-architectured displacement amplification and with much wider bandwidth.

1.3.2 Advantages and limitations of piezoelectric actuation materials

Piezoelectric ceramics, e.g. PZT are essentially small-stroke large-force solid-state actuators with very good high-frequency performance. However PZT have certain limitations in many engineering applications and most obvious is requirement of mechanical amplification. Other limitations reported by Giurgiutiu (2000) are electrical breakdown, depoling, Curie temperature, non-linearity, and hysteresis.

- Electrical breakdown: The direction along which the dipoles align is known as poling direction. Material is subjected to a very high electric field that orients all the dipoles in the direction of the field during poling. When an electric field is switched off or breakdown, most of the dipoles do not return back to their original orientation. This results in pinning effect produced by the microscopic defects in the crystalline lattice. Therefore, in the absence of power supply or electric breakdown destroys the piezoelectric properties of the material.

- Depoling: When an electric field is applied opposite to the poling direction, it results in degradation of the piezoelectric properties or even polarization in the opposite direction due to depoling. The depoling field (coercive field) may be as low as half of the electrical breakdown field.

- Curie temperature: At temperatures close to Curie temperature, depoling is facilitated, aging and creep are accelerated and the maximum safe mechanical stress is decreased. For typical PZT materials, the Curie temperature is about 350°C. The operating temperature should generally be at least 50^{0}C lower than the Curie temperature.

6

- Non-linearity and Hysteresis: Real-life piezoceramics are non-linear and hysteretic. Hysteresis is due to internal sliding events in the polycrystalline piezoelectric material. Upon removal of the electric field, remanent mechanical strain is observed. Hysteresis of common piezoelectric may range from 1 to 10%. Under high frequency operation, hysteresis may generate excessive heat and loss of performance may occur if the Curie temperature is exceeded.

1.3.3 Advantages and limitations of magnetostrictive actuators

Magnetostrictive materials, like Terfenol-D, are essentially small-stroke large-force solid-state actuators that have wide frequency bandwidth. However, they also display certain limitations. The most obvious one is that, in actuation applications, some form of mechanical amplification is required. The main advantage of magnetostrictive actuation over electrostrictive actuation may be found in the fact that it is sometimes easier to create a high intensity magnetic field than a high intensity electric field. High electric fields require high voltages which raise important insulation and electric safety issues. According to Ampere's law, high magnetic fields could be realized with lower voltages using coils with a large number of turns per unit length through which high amperage current flows.

1.3.4 Comparison of piezoelectric and magnetostrictive actuator

Fig. 1.3 (a) shows the relationship between voltage and displacement for a PZT actuator. It was noticed that the stack can produce a maximum expansion of 120 µm. The maximum contraction of -20 µm has been achieved by reversing polarity up to 25-30 %. Total static displacement of the actuator is 150 µm. Therefore, the static free strain is 0.15 % for a PZT stack length of 100 mm. The actuator was electrically biased superimposing with alternating current for dynamic applications. The dynamic free strain is ± 75 %. A significant hysteresis has been observed in the induced strain PZT actuator. On the other hand, the Fig. 1.3 (b) shows the behaviour of displacement with respect to the applied input current for magnetostrictive materials. It was too biased for dynamic operation. The maximum expansion and contraction of the actuator was 70 µm. The total free displacement of 140 µm has been achieved with Terfenol-D actuator. The free strain of the induced strain actuator was 0.1 % for a

7

Terfenol-D length equal to 140 mm. The free strain of ± 0.5 % has been achieved during dynamic operation.

(a)   (b)
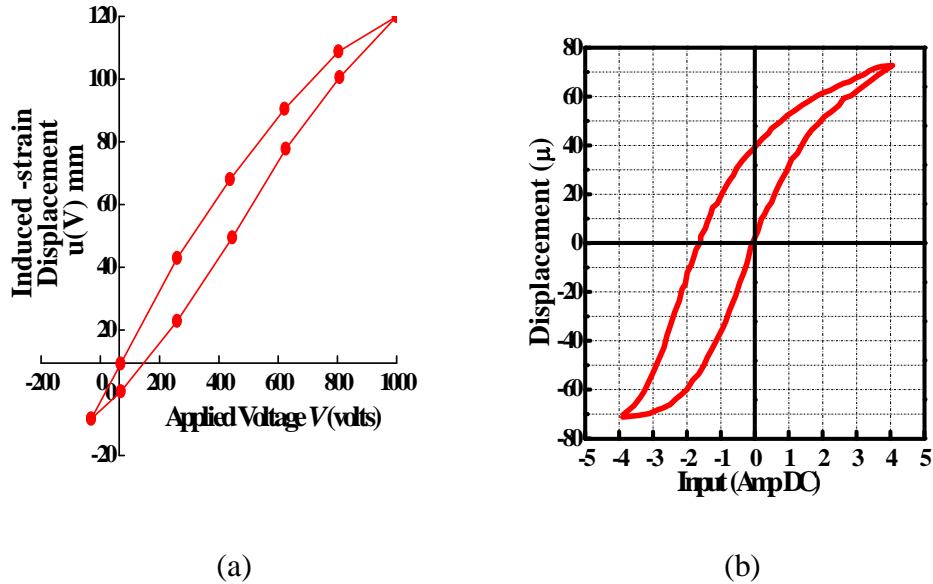
Fig. 1.3. The induced strain-displacement for (a) Piezoelectric actuator (b) magnetostrictive actuator (reproduced from Giurgiutiu, 2000).

To overcome the foregoing problems and with the development of new technology, the actuators made of magnetostrictive materials are being explored for use. The giant magnetostrictive actuator exhibits unique performances such as precision position resolution, several kilonewtons of force output, fast frequency response and high strain. These features made actuators to use in electromagnetic devices or MEMS such as precise positioning of machine tools (Michler et al., 1993; Kanizar et al., 2000), optical systems (Hua et al., 2011), micro pumps (Chuan-li et al., 2010) and active vibration applications (Geng and Haynes, 1994; Zhang et al., 2004).

1.3.5 History of magnetostrictive materials

In 1842 English physicist James Prescot Joule identified the very first magnetostrictive effect when he observed that a sample of nickel changed in length while being magnetized (Culshaw, 1996; Olabi and Grunwald, 2008a and Liu et al., 2012). Subsequently cobalt, iron and alloys of these materials were found to show a significant magnetostrictive effect with strains of about 50 ppm. In the 1960s, the rare-earth elements terbium (Tb) and dysprosium (Dy) were found to have between

8

100 and 10,000 times the magnetostrictive strains compared to nickel alloys. However these properties are valid at very low temperature. Since then researchers have looked for a material that would operate at a high temperature and still have a large magnetostrictive strain at a low magnetic field. It is found that the addition of iron to Tb and Dy to form the compounds $TbFe_2$ and $DyFe_2$ brought the magnetostrictive properties to room temperature (Kikuchi, 1968; Clark and Belson, 1972; Clarke, 1980; Clark, 1989; Duenas et al., 2002; Wu, 2004; Hristoforou and Ktena, 2007; Palit, 2012). These materials also required very large magnetic fields to generate large strains. By alloying the two compounds the magnetic field required to produce saturated strains was considerably reduced. The resulting alloy $Tb_{0.27}$ $Dy_{0.73}$ $Fe_{1.95}$ commercially known as Terfenol-D is at present the most widely used magnetostrictive material. Terfenol-D is capable of having strains as high as 2000-3000 ppm. In contrast, the value of magnetostriction (λ) is only 20 ppm for iron as reported by Kellogg (2000).Therefore the value of λ is the indicator of the level of magnetostriction. Since 1980 it has been a commercially available material for application in many areas.

1.3.6 Phenomenon of magnetostriction

Generally, magnetostriction is the change in shape of materials under the influence of an external magnetic field. The magnetostrictive effect was first described in the 19th century (1842) by an English physicist James Prescot Joule reported in Olabi and Grunwald (2008a). He observed that a sample of ferromagnetic material, i.e. iron changes its length in the presence of a magnetic field. This change in length is the result of the rotation of small magnetic domains. This rotation and re-orientation causes internal strains in the material structure. The strains in the structure lead to the stretching in the direction of magnetic material in the case of positive magnetostriction. The idealized behaviour of change in length versus applied magnetic field is shown in Fig. 1.4 (a). The physical background to the re-orientation of magnetic domains due to applied is portrayed in Fig.1.4 (b). Magnetic domains do not have common orientation pattern due to small applied magnetic field in between 0 to 1. A small amount of common orientation of domains indicates a permanent magnet bias. This resulting magnetostriction depends on homogeneity of the base

9

structure of the magnetostrictive material and the material formulation. Between the regions 1 to 2, perfectly there is a linear relationship between strain and magnetic field. It is easier to predict the behaviour of active material due to simple linear relationship between these two points. Therefore, the devices are designed to operate in the region in between 1 to 2. More particularly, this region is preferable in the design of magnetostrictive actuators. At high applied fields most of the magnetic domains align in the direction of magnetic field and the material behaves non-linear beyond the point 2. Saturation effect arises at point 3 that prevents further increase in the magnetostriction.
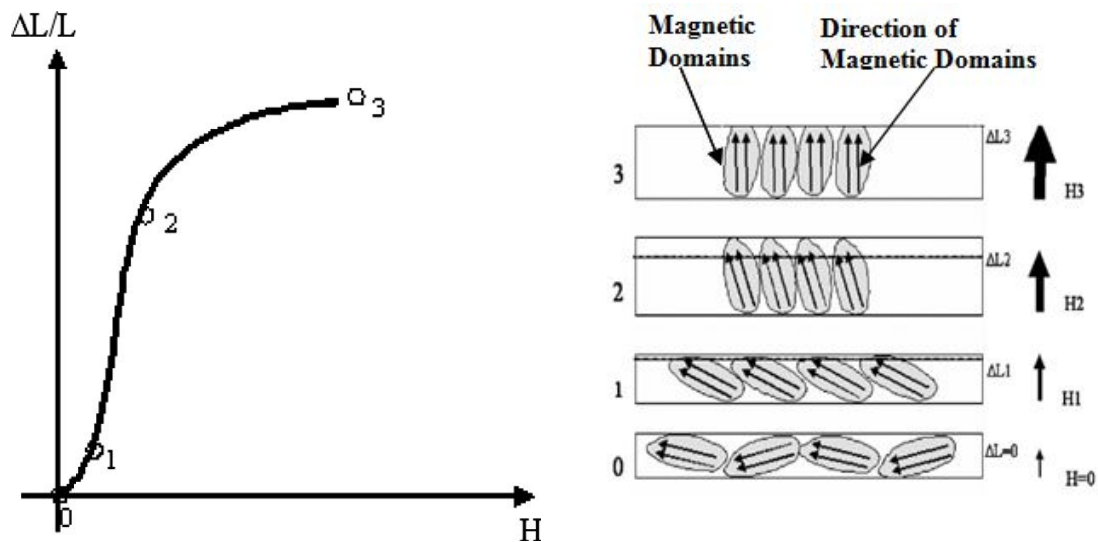
Fig.1.4. (a) Strain versus magnetic field and (b) Orientation of magnetic domains for applied magnetic field during magnetostriction phenomenon.
(Source of figure: Olabi and Grunwald, 2008a).

1.3.7 Terfenol-D and its properties

Terfenol-D is an alloy containing terbium (Tb) and dysprosium (Dy) with iron (Fe). Terbium (Tb) generates strains; dysprosium (Dy) minimizes the field strengths required to generate the strains; iron (Fe) allows the alloys exceptional transduction properties to be used at or above room temperature. The name Terfenol-D comes from its metallic elements: TER- terbium, FE -iron, NOL -Naval Ordinance Laboratory, where the material was first developed, and D-dysprosium (Engdahl, 2000). The Terfenol-D devices require low voltage level input and it can produce "giant" magnetostriction i.e. a strain greater than the most available commercial smart

10

materials (Claeyssen et al., 1997). Terfenol-D, the best known alloy with the typical composition is $Tb_{0.3}Dy_{0.7}Fe_{1.95}$. Few important properties of Terfenol-D are listed in Table 1-4 referred from Engdahl (2000).

Table 1-4. Properties of Terfenol-D.

Property	Symbol	Value	Property	Symbol	Value
Modulus at constant H	E^H	10-76 GPa	Thermal Conductivity	k	13.5 W/m^{0}k
Modulus at constant B	E^B	30-80 GPa	Specific heat	C	0.33 kJ/kg^0 K
Dynamic strain	d_{33}	15-20 N-m/A	Tensile strength	----	28-40 MPa
Relative permeability	μ_{33}^r	4-12	Compressive strength	----	304-880 MPa
Coupling coefficient	k_{33}	0.6-0.85	Coefficient of thermal	α	11x10^{-6}/^{0}K
Electrical resistivity	ρ	0.6×10^{-6} Ωm	Curie temperature	T_c	357^{0}C

1.4. APPLICATIONS OF GIANT MAGNETOSTRICTIVE MATERIAL

Magnetostrictive material exhibits high force at nearly instantaneous speed and actuators made of these materials occupy a small volume and require relatively low voltage input. Applications such as micro-positioners, fluid injectors, active damping systems, helicopter blade control systems as well as some hybrid applications in combination with piezoelectric effects have been introduced. The following brief discussion is an excerpts from Olabi and Grunwald (2008a) on applications using magnetostrictive material mainly Terfenol-D.

1.4.1. A standard Terfenol-D actuator

A standard Terfenol-D actuator developed by ETERMA Products Inc. gives displacements up to 250 mm, force up to 2200 N and operates at frequencies up to 2500 Hz. The operational temperature of this actuator is typically in the range from -20 ^{0}C up to +100 ^{0}C.

1.4.2. Linear motor (Worm motor) based on Terfenol-D

The linear motor is a rod of Terfenol-D surrounded by an electric coil which when energized causes the rod to elongate. The actuator is mounted between two clamps.

By operating the actuator and the clamps in an appropriate sequence, the rod of smart material moves forward or backward. A very accurate control of position to within a few microns over a total stroke length of 20 mm and a holding force capability up to 3000 N has been achieved by this arrangement.

1.4.3. Terfenol-D in sonar transducers

Good sonar transducers should produce high mechanical power at low frequencies as their magnetomechanical coefficients is as high as 0.8 and quality factor Q is low. A typical Tonpilz transducer can operate over a bandwidth of 200 Hz at the resonant frequency of 2000 Hz ($Q^m = 10$), a source level of 200 dB and other various designs of sonar transducers to convert the linear motion of Terfenol-D into appropriate controllable vibrations.

1.4.4. Terfenol-D wireless rotational motor

A prototype based on principle of operation "Inch worm" functionality developed to convert the elongation movement of a magnetostrictive material into a rotary motion to form a micro-stepping rotary motor gives an output of high torque and precise positional control in a power-off self -blocking arrangement. A prototype with dimensions of $260 \times 115 \times 108$ was capable of producing 12.2 N-m torque at rated power of 600 W and 0.5 rpm rotational speed (Olabi and Grunwald, 2008a).

1.4.5. Terfenol-D electro-hydraulic actuator

A linear motor actuator in combination with conventional technologies like hydraulic technology was used as the working principle in a simple pump for high pressure fluid flow. The system consists of a magnetostrictive pump, a hydraulic flow distribution sub system to convert hydraulic energy into mechanical energy and control electronics. A prototype of this arrangement achieved an operational pressure of 4.2 MPa and a fluid flow rate of more than 3 l/m.

1.4.6. Wireless linear micro-motor

The linear micro-motor is a self-moving silicon plate with small magnetostrictive films applied to its surface. The applied magnetic field produces a resonating flexing

shape which leads to the vibration of the plate and causes a motion of approximately 10-20 mm/s.

1.4.7. Magnetostrictive contactless torque sensors

In magnetostrictive contactless torque sensor, the torque was applied to the shaft and shear stress is generated along the length of the shaft. This will also produce tensile and compressive stresses in the direction of $\pm 45^0$ to the longitudinal shaft axis. When the shaft contains a magnetostrictive or has a collar containing a magnetostrictive material attached to it, the magnetic permeability measured along these directions will change. Changes in magnetic flux can be measured contact-less.

1.5. ORGANISATION OF DISSERTATION

This dissertation consists of six chapters, four appendices and a list of references. Chapters one and two are the introduction and literature review, chapter three is the design and magnetic field analysis of Terfenol-D actuator, chapter four is the responsive characteristics of a Terfenol-D actuator using magnetostrictive models, chapter five is the experimental setup and response characteristics of a Terfenol-D actuator under DC driving conditions, and chapter six is the analysis of performance characteristics of a magnetostrictive disc brake system. Summary for each chapter is presented below.

Chapter one discusses on the important feature of a brake, drum and disc brakes. A brief description of hydraulic actuation for brakes is presented. Following this, is the actuator based on smart materials is discussed with their merits and demerits. Magnetostrictive materials and their applications will be highlighted.

Chapter two presents the literature review related to magnetostriction technology under taken by various researchers. This chapter summarizes the past work on magnetostriction of giant magnetostrictive materials, magnetic circuit design, magnetic field analysis, design, experiments and applications of giant magnetostrictive actuators in the area of magnetostriction technology. The different aspects in the displacement amplification of a giant magnetostrictive actuator are also discussed. Objectives of the current study are listed at the end of this chapter.

Chapter 3 contains the electrical aspects for the design of coaxial coils based on the size of Terfenol-D rod. Combination of approaches among the analytical, numerical and experimental are used to study the magnetic field parameters generated from the coaxial coil, coaxial coil with Terfenol-D and in general the Terfenol-D actuator itself.

Chapter 4 deals with the formulation of magnetic field strength from the coaxial coils for step input, Jiles-Atherton hysteresis model for magnetization. A comparison of proposed magnetostriction models with existing models is elaborated.

Chapter five includes a detailed description of various components in the experimental setup for evaluating the performance characteristics of Terfenol-D actuator.

Chapter six discusses the implementation of magnetostrictive actuator for disc brake system. Design of hydraulic amplification unit is highlighted and the comparison of response curves for Terfenol-D actuator and actuator coupled with displacement amplification unit without brake fluid are discussed.

The conclusions of the dissertation and scope for future work have been presented in chapter seven.

The list of the cited references is provided after chapter seven. Four appendixes are provided. The four appendices contain variety of calculations, additional experimental results and photographs of different parts of the Terfenol-D actuated disc brake system.

CHAPTER 2

REVIEW OF LITERATURE

2.1. INTRODUCTION

The drawbacks of conventional actuation methods existing in practice can be conquered successfully by an alternative actuation using smart materials. The most promising smart material that offers possible actuation is magnetostrictive material. Actuators developed using magnetostrictive material namely Terfenol-D are reported to be compact, high force capability, fast response, work at lower power input and provide comparatively large displacement. This chapter provides a brief review on literature related to hysteresis of giant magnetostrictive materials, design of magnetic circuit, magnetic field analysis, design and experiments conducted with different type of input excitations, applications and displacement amplification principles to enhance the output of giant magnetostrictive actuators in the area of magnetostriction technology.

Rare earth-iron magnetostrictive alloy, mainly Terfenol-D features giant magneto-strains i.e. static strain of the order 1000-2000 ppm and dynamic strain of 3500 ppm. This permits to build various actuating devices such as actuators and motors at macro and micro level (Claeyssen et al., 1997). Measurement of magnetostriction is very important during the testing stage of magnetostrictive actuator. To this effect Ekreem et al. (2007) elaborated on direct measurement techniques like strain guage, dilatometry, capacitance, optical interferometry methods and indirect measurement techniques like ferromagnetic resonance, small-angle-magnetization rotation (SAMR) and strain modulated ferro-magnetic resonance (SMFMR) methods for measuring magnetostriction. Several new insights including the effective categorization of available actuator technologies based on stimuli generation and actuator configuration together with the practical presentations of performance data in terms of three principal figures of merit of force, stroke and frequency are discussed by Poole and Booker (2011). Three case studies on ball

valve, spot welder and flapping wing actuator have been outlined to demonstrate the actuator selection strategy based on industrial and research projects.

2.2. LITERATURE REVIEW ON MAGNETIC CIRCUIT DESIGN FOR TERFENOL-D ACTUATOR

Many researchers have worked on the design of magnetic circuit of Terfenol-D actuator by minimizing the magnetic resistance. The magnetic source and the energy conversion of Terfenol-D material can be effectively improved by analysis and optimization of the magnetic circuit. Especially, the resistance of the actuator housing is to be minimized apart coils, so that the magnetic flux produced by the coil will improve and it can take a path uniformly along length of Terfenol-D rod.

The popular book "Handbook on Giant Magnetostrictive Materials" by Engdahl (2000) is a ready reference for researchers on the procedure for optimization of electric, magnetic, thermal and mechanical issues related to magnetostrictive material. The magnetic energy of the magnetostrictive material (Terfenol-D) determines the magnetizing arrangement of the actuator. For the best functioning of magnetizing arrangement, reluctance flow path through the component ($\Re_{path}$) should be low and leakage reactance should be high. The reluctance is given by,

$$\Re_{path} = \frac{l_{path}}{\mu_r \mu_0 A_{path}} \tag{2.1}$$

Where μ_0 is the permeability of free space, μ_r is the relative permeability of a material, l_{path} and A_{path} are the equivalent geometrical length and equivalent cross-sectional area of actual path of the component.

The leakage inductance describes how much magnetic reactance is associated with magnetic flux leakage in solenoid. The leakage inductance is mathematically described in detail in Chapter 3.

Dehui et al. (2008) proposed an equivalent magnetic circuit equation to evaluate the electromagnetic performance of giant magnetostricitve actuator. The effect of magnetic circuit components, gap magnetic permeability and evenness of driving

magnetic field was analyzed based on equivalent magnetic circuit equation. According to principle of continuity of magnetic flux,

$$\phi = \phi_c = \phi_{air} + \phi_{gmm} \tag{2.2}$$

Where, ϕ_c is the magnetic flux through shell (casing), ϕ_{air} is the magnetic flux passing through air gap of actuator and ϕ_{gmm} is the magnetic flux through GMM rod. When the leakage flux exists, then from Ampere's loop theorem and Ohm's law for magnetic circuit, Eq. (2.2) becomes,

$$\phi = B.A = \left(\frac{NI}{k_{coil}} \right) \bigg/ \left(\Re_c + \frac{\Re_{GMM} \Re_{air}}{\Re_{GMM} + \Re_{air}} \right) \tag{2.3}$$

Where, $\Re_c$ is the magnetic resistance of shell, $\Re_{GMM}$ is the magnetic resistance of GMM rod, and $\Re_{air}$ is the magnetic resistance of air inside the coil.

According to the definition of magnetic resistance, Eq. (2.3) can be expressed as:

$$\phi = \left(\frac{NI}{k_{coil}} \right) \bigg/ \left(\frac{l_c}{\mu_0 \mu_c A_c} + \frac{l_{GMM} l_{air}}{\mu_0 \pi \left[\mu_{GMM} l_{air} \left(\frac{d_1 - d_{GMM}}{2} \right)^2 + l_{GMM} \mu_{air} \left(\frac{d_{GMM}}{2} \right)^2 \right]} \right) \tag{2.4}$$

Where l_c is the length of shell or casing, μ_c is the relative magnetic conductivity of shell, A_c is the surface area of magnetic circuit, μ_0 is the magnetic conductivity in vacuum, μ_{GMM} is the relative magnetic conductivity of giant magnetostricitve material, d_{GMM} is the diameter of giant magnetostricitve material rod and d_1 is the internal diameter of drive coil.

Driving coil structure was designed and its shape was optimized based on G-factor using electromagnetic field analysis function available in ANSYS. The distribution of magnetic intensity along the center line of the hollow coil is given by

$$H_x = 2\pi n_1 n_2 I \left(x + \frac{l}{2} \right) \ell n \left(\frac{r_2 + \left[r_2^2 + \left(x + \frac{l}{2} \right)^2 \right]^{\frac{1}{2}}}{r_1 + \left[r_1^2 + \left(x + \frac{l}{2} \right)^2 \right]^{\frac{1}{2}}} \right) + \left(\frac{l}{2} - x \right) \ell n \left(\frac{r_2 + \left[r_2^2 + \left(\frac{l}{2} - x \right)^2 \right]^{\frac{1}{2}}}{r_1 + \left[r_1^2 + \left(\frac{l}{2} - x \right)^2 \right]^{\frac{1}{2}}} \right)$$

$$\tag{2.5}$$

17

Where the number of turns per unit length of coil is n_1, n_2 is the number of turns on unit height of coil and H_x is the magnetic field intensity along the axis of coil.

The designed coil dimensions have been optimized using the criteria given by

$$\frac{k_{coil}Hl}{4} < A_{coil} < \frac{k_{coil}Hl}{2} \tag{2.6}$$

Where the compensation coefficient of drive coil is k_{coil}, A_{coil} is the area of coil and l is the length of the coil.

Meeker and Dozor (1989) presented a simple one dimensional magnetic model for the prediction of magnetic field inside the magnetostrictive drive rod. Using magnetic model, the magnetic field can be evaluated very quickly. The coil geometry was optimized with least dissipated power by considering the effect of permeable magnetostrictive materials on the magnetic field. The volume integral method was used to evaluate the magnetic field in the magnetostrictive material. The arrangement is composed of a coil and magnetized solid rod in free space. Therefore, the magnetization is the resultant of component of magnetic field intensity from the coil as well as from magnetized solid.

The magnetic field along the axis of a non-zero thickness coil is given by,

$$
\begin{aligned}
H_{coil}(z) = & \left(\frac{J\left(l_{coil}+2z\right)}{4}\right) \log\left[\frac{OD_{coil}+\sqrt{OD_{coil}^2+\left(l_{coil}+2z\right)^2}}{ID_{coil}+\sqrt{ID_{coil}^2+\left(l_{coil}+2z\right)^2}}\right] + \\
& \left(\frac{J\left(l_{coil}-2z\right)}{4}\right) \log\left[\frac{OD_{coil}+\sqrt{OD_{coil}^2+\left(l_{coil}-2z\right)^2}}{ID_{coil}+\sqrt{ID_{coil}^2+\left(l_{coil}-2z\right)^2}}\right]
\end{aligned}
\tag{2.7}
$$

Where $H_{coil}(z)$ is the magnetic field along the axis of a coil in A/m, J is the current density of coil in A/m², l_{coil} is the height of the coil, OD_{coil} is the outer diameter of coil, ID_{coil} is the inner diameter of coil and z is the axial distance along the axis of coil.

Magnetic field from a uniformly magnetized solid per unit of magnetization in free space can be expressed as,

18

$$h_{magnet(z)} = \frac{(l_{coil} - 2z)}{\sqrt{4a^2 + (l_{coil} - 2z)^2}} + \frac{(l_{coil} + 2z)}{\sqrt{4a^2 + (l_{coil} + 2z)^2}} \qquad (2.8)$$

Where the magnetic field from a magnetized solid per unit magnetization is $h_{magnet}(z)$ and a is the radius of the loop. Eq. (2.8) is the basis to determine the magnetic field when a Terfenol-D rod is present in the coil.

However, the magnetization of a Terfenol-D carried by the coil is evaluated. Once the magnetization is known, the magnetic field in the Terfenol-D rod can be determined by dividing the magnetization with magnetic susceptibility.

$$M = \frac{\chi}{1 + \chi}\left(H_{coil} + H_{magnet}\right) \qquad (2.9)$$

Where the magnetic field $\left(H_{coil}\right)$ from the coil can be computed using the Eq. (2.7) and magnetic field $\left(H_{magnet}\right)$ from the Terfenol-D rod can be calculated on multiplying magnetization with Eq. (2.8). Eq. (2.9) gives the magnetization of a Terfenol-D rod.

The magnetic field obtained was maximized by defining Terfenol-D time constant that quantifies the coil performance. Terfenol-D time constant is the ratio of magnetic field energy stored in the Terfenol-D rod to the power required to produce the field and mathematically given by,

$$\tau_T = \left(\frac{1}{2}\right)\mu H_{avg}^2 v_{terf} \Big/ \rho v_{coil} J^2 \qquad (2.10)$$

Where τ_T is the Terfenol time constant in sec, μ is the permeability of Terfenol-D material equal to $\mu_0 \mu_{r(T)}$, H_{avg} is the resultant of magnetic field intensity due to coil alone as well as coil with Terfenol-D, v_{terf} is the volume of Terfenol-D rod, ρ is the resistivity of the coil and J is the current density of the coil.

Coil geometry was optimized by choosing the three sizes of Terfenol-D rods. The diameters were 1.5, 2 and 2.5 mm, and their length and magnetic permeability equal to 15 mm and 8 respectively chosen for Terfenol-D in the work. The inner diameter of the coil was close to the diameter of Terfenol-D rod in each case. The outer diameter of coil was chosen to optimize Terfenol-D time constant. It was confirmed that the

optimal outer radius and coil quality decreased rapidly when the coil is thinner than optimal, but decreased rather slowly for a thicker than optimal coil.

2.3. LITERATURE REVIEW ON MAGNETIC FIELD ANALYSIS OF A TERFENOL-D ACTUATOR

The magnetic field analysis of Terfenol-D actuators to determine associated parameters like field strength, flux density and flux distribution are essential to improve the intensity and uniformity of the magnetic field on drive rod. An extensive workout has been undertaken by many researchers to improve the same using different packages like Maxwell solver, FEM and COMSOL multiphysics.

Lhermet et al., (1993) discussed the comparison of modeling and prototype results to generate a high bias field of 80 kA/m using Terfenol-D. FLUX2D and FLUX3D software for bias design and ATILA code for electromagnetic design was used.

1 : Head mass
2 : Magnetic circ
3 : Terfenol - D r
4 : Excitation and polarisation coil
5 : Prestress bolts

(a)

1 : Head mass
2 : Magnetic circuit
3 : Excitation coil
4 : Terfenol - D rod
5 : Permanent magnets
6 : Prestress bolts

(b)

1 : Head mass
2 : Excitation coil
3 : Terfenol - D rod
4 : Magnetic circuit with permanent magnets
5 : Prestress bolts

(c)
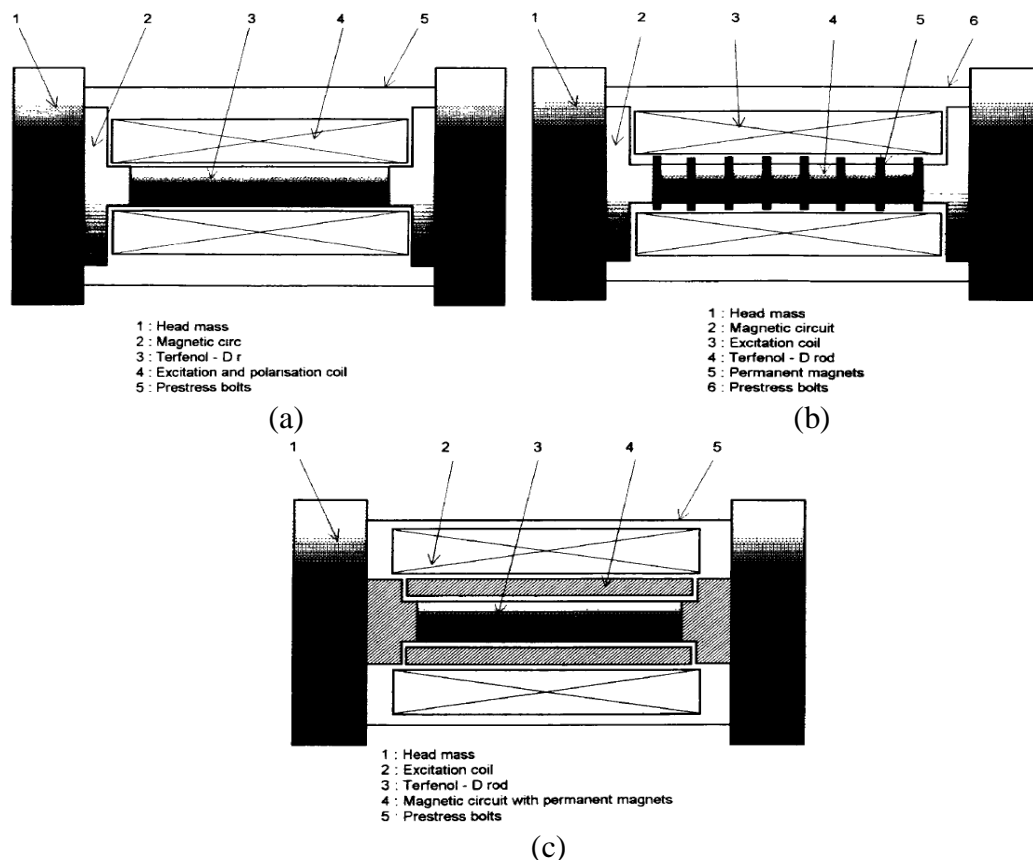
Fig. 2.1 Schematic of actuator configurations biased with (a) DC current in the coil (b) series of permanent magnets and (c) new magnet configuration (Source of figure: Lhermet et al., 1993).

A method for a bias design was proposed and implemented on three prototypes of magnetostrictive actuators. The first prototype in which biasing was done by DC current in the coil surrounding the rod, second prototype had a 100 kA/m bias done by a series of permanent magnets and third prototype equipped with new magnet configuration provided 90 kA/m and are shown in Fig. 2.1 (a), (b) and (c) respectively. It was concluded that the third prototype has good effective coupling factor, high strain capability, simple construction and good efficiency (no DC dissipated power) compared to first and second prototype.

Benbouzid et al. (1995) performed the extensive computer modeling to ensure homogeneous magnetic field along the magnetostrictive rod. Finite element method has been used to analyze different magnetic circuit configurations and to quantify leakage flux. Concept of open magnetic circuit i.e. the magnetic return path is surrounding air outside the coil has been demonstrated. It has been found that, when the end cap total surface is large compared to rod section, then small energy is stored in magnetic return path compared to energy stored in rod. It has been found that the suppression of pole pieces allows better degree of freedom for coil dimension.

Wang et al. (2006) proposed a multi-scale external concavity structure with a hollow column coil to improve the uniformity of magnetic field distribution on Terfenol-D material. Model of hollow column coil was built which analyzed the magnetic field distribution using finite element analysis.

Wang et al. (2011a) analyzed the radial distribution of internal magnetic field intensity and Wang et al. (2011b) analyzed the radial distribution rules of internal stress and strain on Terfenol-D to improve the performance of a high frequency driven actuator. A transient simulation on Terfenol-D rod conducted using finite element ANSYS software, at a frequency of 20000 Hz revealed that the restrain eddy current is one of the key parameter to improve the performance of the magnetostrictive material. Few possible ways to restrain eddy current are using composite slices and cutting slits, and the thickness of the slice must be smaller than the skin depth of the corresponding incentive frequency in addition to adding the

resistivity of magnetostrictive material in order to improve the performance of the magnetostrictive material. The shape of the Terfenol-D rod should be solid or hollow cross-section cylinder and radial opening seam can interdict eddy current which in turn improves the utilization of magnetostrictive material.

Han et al. (2008) carried out finite element analysis using Ansoft Maxwell V10 to establish the relation between the GMM actuator coils and the magnetic field intensity of GMM rod with both DC and AC input supply. 2D magnetostatic solver and 2D eddy current solver were used to analyze the DC and AC magnetic field. Experiments were conducted on an actuator to measure displacement under AC excitation and achieved an displacement of 61.5 µm at 3 A.

Li et al. (2007a) improved the uniformity of driving magnetic field in GMM rod by optimizing the structure parameters of the field circuit and adopting multi-section solenoid. Based on the analysis of FEM, a prototype of GMA with a Terfenol-D rod of size $\phi14\times38.5$ mm was fabricated and tested. Static and dynamic response characteristics were measured using CCD laser displacement sensor. Output displacement of 38.3 µm was achieved in 0.03 s under an optimum preload of 864 N at 14 A. The dynamic response of actuator was measured at 20 Hz. The temperature rise of GMM rod and coil were tested at different modes. It was concluded that the temperature rise was less than 2 ^{0}C and the highest rise was about 5 ^{0}C for 60 and 600 s in an actuator assembly.

Olabi and Grunwald (2008b) presented the results of magnetic field simulation with FEMM software package and experimental measurements of the magnetic circuit of magnetostrictive actuator. It was summarized that the difference in the simulated results and the measured flux density was estimated and the deviations were attributed to the housing materials and measurement tolerances.

Zhifeng et al. (2009) discussed the necessity of laminating the Terfenol-D rod to design a magnetostrictive actuator for dynamic applications. Lamination of Terfenol-D reduced the eddy current losses and decreased the stiffness of Terfenol-D rod. An analytical approach was described for the magnetic field distribution in the cross-

section of the Terfenol-D rod. Experiments were conducted to measure the mechanical efficiency of the giant magnetostrictive actuator.

Lu et al. (2010) carried out studies on giant magnetostrictive actuator integrated with double water-cooling cavums using finite element method that includes thermal and magnetic design aspects.

Chen et al. (2006) developed an axial symmetry model of giant magnetostrictive actuator to analyze magnetic field using finite element method. Elongation of giant magnetostrictive rod was calculated under different excited current with numerical integration. Giant magnetostrictive actuator was used with two coils namely biasing coil and excitation coil, and GMM rod of 8 mm and 50 mm in length. From the comparison of model and experimental results, it was concluded that the linear working domain of actuator was observed with an output displacement at exciting current range of 0 - 1.2 A and biasing current of 2.6 A.

2.4. LITERATURE REVIEW ON HYSTERESIS AND MAGNETOSTRICTION OF A GIANT MAGNETOSTRICTIVE MATERIALS

Magnetic properties are often conveniently expressed as magnetization curves or family of hysteresis loops in most of the ferromagnetic material applications. The effective use of magnetostrictive material is quite challenging due to strong hysteresis compared to other smart materials like piezoelectric and shape memory alloys. A material with a wide hysteresis loop has low permeability, high remanence, coercivity, reluctance and residual magnetism. Small hysteresis is required to develop sensor and actuator using smart material.

General form does not exist for modeling hysteresis curves of ferromagnetic materials. In general, the shape of the hysteresis was designated as sigmoid curve. Jiles-Atherton (1983, 1984, and 1986) presented a mathematical model of hysteresis mechanism for ferromagnets to generate similar sigmoid curve based on existing ideas of domain wall motion including bending, translation and rotation.

Calkins *et al*. (2000) discussed a quadratic model based on the geometry of moment rotations was used to quantify the magnetostriction generated by the transducer. On comparison with experimental results, the characterization of magnetostriction was adequate at moderate drive levels though there was degeneration at high drive levels due to unmodeled non-linearities and hysteresis.

Zheng and Liu (2005) proposed a constitutive model for Terfenol-D rods to predict accurately the curves of magnetostrictive strain versus applied magnetic field under various compressive prestress levels and different magnetic field regions. The proposed model had wider applicability and higher precision mainly in the region of the high field.

Zhou et al. (2007) used non-linear constitutive relations for the numerical simulation of active vibration control of Terfenol-D rod. Negative displacement and velocity control law was used to feedback the signals to the actuator aiming to suppress the vibration of the displacement at the free end of a Terfenol-D rod.

2.5. LITERATURE REVIEW ON DESIGN, EXPERIMENT AND APPLICATIONS OF TERFENOL-D ACTUATOR

The actuators using magnetostrictive material (Terfenol-D) were designed, fabricated and their performance investigated with respect to various applications by many researchers. Static and dynamic tests have been conducted to harness the material's special properties such as high strain, good magneto-mechanical coupling and high force capability in response to an external stimulus.

Sun et al. (2011) designed and analyzed the key parts of giant magnetostrictive actuator, flexure hinge and pre-stress disc spring. An ideal spring force-deformation curve of the pre-stressed spring was put forward to improve output efficiency of the giant magnetostrictive actuator.

Dhilsha et al. (1997) designed and fabricated a Tonpilz type single ended low frequency giant magnetostrictive transducer. It consists of two active elements; one head mass and a tail mass, two solenoids, a magnetic coupler and a stress rod. The

impulse method was used for measurement of underwater acoustic parameters like transmitting current response, transmitting voltage response and receiving sensitivity in the frequency range of 2 kHz to 6 kHz.

Aston et al. (1997) fabricated and evaluated the performance of a high non-resonant actuator using Terfenol-D. Two types of spring with different compliances were used to preload the actuator. Terfenol-D rod of diameter 20 mm and 250 mm long was chosen in the work. Separate field coils were designed for biasing instead of permanent magnet to produce 75 kA/m of magnetic field. Actuator performance was measured with load cell and displacement sensor.

Calkins et al. (1997) investigated experimentally the effects of pre-stress, magnetic bias and drive level on the performance of a Terfenol-D transducer under quasi-static conditions. Quasi-static strain versus applied field plots at high drive levels showed differences in trends with prestress.

Lei et al (2010) presented a magnetostrictive actuator based on the use of permanent magnet which will reduce the problem of non-linearity arising due to effect of temperature and the displacement of traditional GMA. The skin effect and eddy current were avoided by using the driving magnetic field produced by permanent magnet.

Park and Kim (2004) developed a magnetostrictive micro actuator capable of controlling displacement from millimeter to nanometer resolution. The dimension of Terfenol-D was 5 mm diameter and 10 mm long. The magnetostrictive micro actuator produced 25 N of force and 3 μm of displacement with 1.5 A of input current.

Kellogg and Flatau (1999 and 2004) investigated the blocked force characteristics of a Terfenol-D transducer. Effective blocked force was calculated using the following equation.

$$F_{Beff} = K_B \varepsilon_{max}^H L \left[1 - \frac{K_B}{K_B + K_S} \right] \tag{2.11}$$

Where, $K_B = \dfrac{AE^H_{Beff}}{L}$

A is the cross sectional area of Terfenol-D, L is the length of Terfenol-D and ε_{max} is the strain for constant magnetic field.

Grunwald and Olabi (2008) proposed a cost effective magnetostrictive actuator using Terfenol-D material. The actuator comprised a Terfenol-D rod of diameter 8 mm, length 80 mm and solenoid surrounded by a permanent magnet, its performance was optimized by applying prestress. An output strain of 1000 ppm and blocked force of over 4500 N was obtained at an applied input of 10 A.

Olabi and Grunwald (2008a) discussed the physical background for the re-orientation of magnetic domains in magnetostriction phenomenon. Terfenol-D production and their properties such as Young's modulus, magnetomechanical coupling factor, magnetostrictive coefficient, quality factor, permeability and blocked force characteristics were discussed. An overview on applications of magnetostrictive applications such as reaction mass actuator, standard Terfenol-D actuator, linear motor based on Terfenol-D (Worm motor), wireless rotational motor, wireless micro motor, electro-hydraulic actuator, sonar transducers, magnetostrictive thin film applications, magnetostrictive contactless torque sensors and many other applications were discussed.

Yamamoto et al. (2000) presented two kinds of novel applications of giant magnetostrictive materials; a compact fine positioners and a wire clamper. The micro-positioner has 20 μm motion range. A wire clamper was developed for a wire bonding task in semiconductor chip manufacturing process. The unique merit of giant magnetostrictive material wire clamper is that there is no fatigue fracture observed as far as cyclic test goes.

Zhang et al. (2009a) discussed the configuration and working principle of dual pressure common rail system (DPCRS). It can inject fuel to injector at two levels. One level is rail pressure and the other is intensified pressure. Pressure level switch and

injection rate were controlled using two solenoids. Magnetostrictive actuator with displacement amplifier was designed to enhance the performance of a DPCRS.

Ge and Deng (2009) designed a non-contact jet dispensing device based on giant magnetostrictive material used in the fields of packaging technology and fluid dispensing system. GMA provides the driving force for jet dispenser. Displacement amplifying mechanism with flexure hinges was designed to amplify the output displacement of giant magnetostrictive actuator.

Braghin et al. (2011) introduced a linear model for magnetostrictive actuators under certain assumptions. On comparison of the numerical and experimental results of two different actuators between the applied input and force for active vibration revealed that the model can predict the dynamic behaviour in the frequency range from 40 to 2000 Hz.

Bartlett et al. (2001) proposed the design, manufacture and testing of two transducers using Terfenol-D material. Terfenol-D rod was surrounded by AC drive coil and permanent magnet which is suitable for high power output and low frequency less than 1 kHz in anti-vibration application.

Li et al. (2008) presented studies on the performance characteristics of a giant magnetostrictive actuator (GMA) for fuel injector. Characteristics such as magneto-strain of giant magnetostrictive actuator for applied excitation current to the solenoid, prestress, and temperature rise for the continuous operation were reported. It was concluded that the cooling device or constant temperature control system is necessary for improving the performance of giant magnetostrictive actuator.

Yang et al. (2006) developed an inchworm linear motion mini actuator to position an object over a range of some millimeters with nanometer resolution. Tests conducted on an actuator showed that the designed prototype can perform linear movement in the fast-positioning mode with a velocity of 97.2 µm/sec at an applied input and frequency of 7 A and 10 Hz respectively and achieved a positioning resolution of 4 nm.

Yang et al. (2012) designed and implemented a giant magnetostrictive assembled actuator (GMAA) for stable nano-resolution positioning, large stroke, instant response and high load capacity required to drive segmented mirrors in very large astronomical telescopes (VLAT). They presented the integrated design of actuator with amplification mechanism, the control system and the test results from the prototype. Test results proved the capacity and positioning accuracy of the actuator in large strokes in addition to effectiveness of the control system and control method. Tests on GMAA verified that, it is able to perform a stroke of 2.2 mm with approximately 60 nm of displacement resolution at an applied external load of 600 N.

Yoshioka et al. (2013) developed a rotary-linear motion platform combined with linear motion mechanism driven by a giant magnetostrictive actuator to meet the requirements like machining and measuring three dimensional geometries in a spindle system. Performance evaluation results revealed that the developed platform provided linear positioning resolution of 10 nm at 0 rpm and of 1 μm at 4000 rpm as shown in Fig. 2.2.
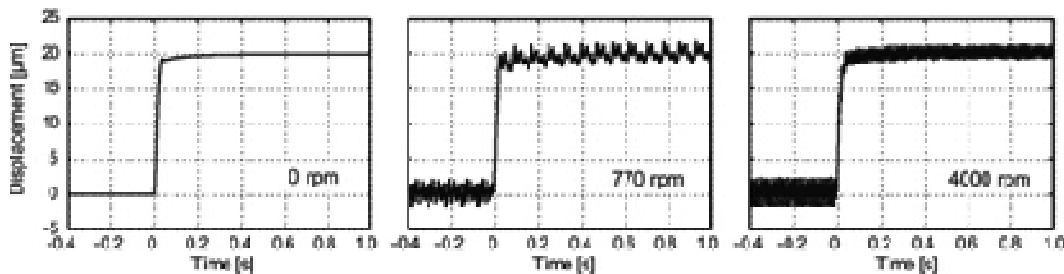
Fig. 2.2. Step response of the platform at three rotational speeds
(Source of figure: Yoshioka et al., 2013).

In addition, the different applications using magnetostrictive material implemented in real time applications by researchers have been summarized. Linear magnetostrictive actuator as a vibration control (Moon et al., 2007), integrated with the flexure-flapper assembly of the flapper-nozzle servo valve by replacing the conventional torque motor (Karunanidhi and Singaperumal, 2010), compact and power efficient high speed magnetostrictive mirror defector (Angara et al., 2009), control of micro-vibration (Nakamura et al., 2000) and DoD inkjet head (Yoo and Park, 2010) are few applications implemented in real time using Terfenol-D material.

2.6. LITERATURE REVIEW ON DISPLACEMENT AMPLIFICATION OF GIANT MAGNETOSTRICTIVE ACTUATOR

Some of the benefits such as reliability, autonomy and compactness make induced strain actuators (ISA) conceptually to use in many commercial applications in place of conventional hydraulic and electro-magnetic devices. Their energy requirements appear to be within the capabilities of commercially available induced strain devices. However, a significant challenge lies in the amplification of very small output displacement (order of 0.1 mm) obtained from the induced strain actuators. The displacement amplification of induced strain actuator using mechanical and hydraulic amplification concepts undertaken by many researchers are summarized below.

Giurgiutiu et al. (1995) studied the feasibility of indirect actuation for rotor blade active vibration control instead of direct actuation using ISA devices. It was proved that, an excessive effect of compressibility (displacement loss and dependent strain energy) occurs with direct actuation. They discussed the coupling of available stocks with optimally designed displacement amplifier based on force, stroke, energy and output power requirements to meet bench mark specifications. Closed form formula was developed to find optimal amplification gain for each required value of the closed loop amplification ratio. It was concluded that the indirect actuation through a displacement amplifier was found to be feasible, as it allows for matching of internal and external stiffness.

Giurgiutiu et al. (1996a) discussed the basic concepts and innovative ideas associated with the analysis, design and experimentation of induced strain actuators for rotor blade aeroelastic vibration control. Hydraulically amplified large displacement induced strain actuator was considered to actuate a trailing-edge servo-flap. The principle of high power induced strain actuation, and the energy and energy density of existing ISA were presented. A full scale proof of concept demonstrator and hydraulically amplified high displacement induced strain (HAHDIS) was designed. Static and dynamic tests proved that the full scale proof of concept demonstrator is good in the frequency range of 1 to 30 Hz.

Giurgiutiu et al. (1997) presented stiffness concepts for the effective utilization of induced strain principles in quasi-static actuation of structures and devices using smart materials. The displacement and output energy capability of conventional induced strain actuators was reviewed. Basic principles of displacement amplification were outlined. Influences of structural and amplification elasticity were discussed. An illustration of effective induced strain actuator with displacement was provided. With this, the LARIS actuator was designed based on warping-torsion coupling produced in excess of 6^0 displacements over the frequency range of 0-50 Hz.

Bushko et al. (1991) presented a design to apply the idea of a hybrid magnetostrictive /hydraulic system for large stroke actuation. The design concept utilized hydraulics to transform a small change of a linear dimension of the magnetostrictive rod into a useful stroke of almost range. The phenomenon of magnetostriction was used to generate a high pressure fluid flow which powers a conventional linear or rotational motion hydraulic actuator. The application of magnetostriction was used to develop a high performance hydraulic supply. This system comprises a magnetostrictive high pressure pump, hydraulic pressure delivery and distribution system, conventional linear or rotational hydraulic actuator, power and control electronics.

Wang et al. (2010) discussed a new clamping system to clamp the work piece which comprises of a giant magnetostrictive material as working medium and the displacement amplifier with area effect. The displacement was amplified by the displacement amplifier and the work piece was clamped through the displacement output device. On the other hand, the reset spring will place the piston rod of displacement output device move backward to release work piece. Two sets of displacement output devices were used, capable of exerting different clamping force in different directions and clamp the work piece in multi-direction.

Chaudhuri et al. (2009) developed a hybrid actuator using magnetostrictive material Terfenol-D as driving material and hydraulic oil as the working fluid. Terfenol-D driven hydraulic actuator is the initiation of flow due to the oscillation of a mechanical piston being driven by elongation/contraction of a smart material upon the

application of a periodic electrical signal. Typical hybrid pump uses the principle of frequency rectification to produce a net flow rate out of the pump. This can be achieved by passive uni-directional reed valves housed inside the pumping head as shown in Fig. 2.3 (a).
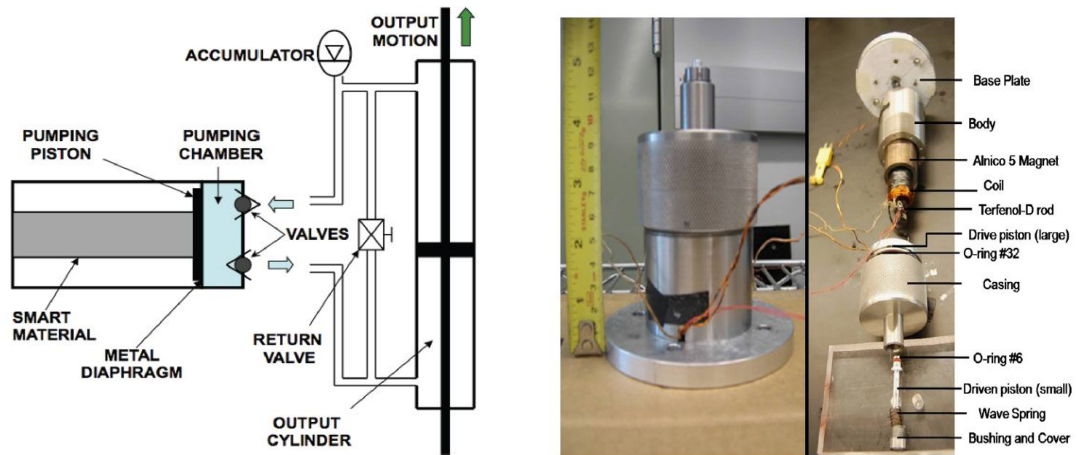
Fig. 2.3. (a) Schematic of a hybrid actuator test setup (Source of figure: Chaudhuri et al., 2009) and (b) Assembled and exploded view of the hydraulically amplified magnetostrictive actuator (Source of figure: Chakrabarti and Dapino, 2012).

It allows fluid flow either out of the pumping chamber or into the pumping chamber. The hybrid pumping device operates in four distinct stages namely compression, discharge, expansion and intake. Tests were conducted at no load and loading conditions to measure the performance for uni-directional motion of the output piston at different pumping frequencies. Simulation results obtained for no-load velocities of the actuator at different pumping frequencies were compared with experimental data for model validation.

Chakrabarti and Dapino (2012) described the dynamic performance of a hydraulically amplified magnetostrictive actuator using a coupled axi-symmetric finite element model for active power mount. Assembly of the hydraulically amplified actuator is shown in Fig. 2.3(b). Finite element model formulation was done for Terfenol-D based on the weak form representations of Maxwell's equations for electromagnetic and Navier's equation for mechanical systems coupled using a nonlinear magneto-mechanical constitutive law. Parametric studies were conducted using an actuator model. It reveals that the displacement of actuator improved up to 140 % by doubling

the thickness of the fluid chamber components and reducing seal friction to a fourth of its original value.

2.7. MOTIVATION

Now-a-days the conventional brake systems existing in automobiles are having hydraulic actuation. Conventional hydraulic brake uses oil pressure as a driving source. Construction and assembly of hydraulic brake system has become complex due to number of parts that constitutes hydraulic piping equipment and a regulating mechanism. Moreover, the recent tendency is to provide features like antilock braking system and traction control system in an automobile braking system. Therefore, the conventional hydraulic brake with an electric hydraulic control circuit is needed. Particularly, it is required for converting a predetermined electric signal into the mechanical operation of a hydraulic actuator in response to the locked or slipping condition of the wheel. Due to this reason, currently, the fine braking action in automobiles is difficult even under the application of servo effect featuring hydraulic mechanism.

This rendered the intelligent braking action proposed by Fargier (1991) using a rotary-linear conversion mechanism and Imoto et al. (1988) using a piezoelectric ceramic material as a driving source in an electrically driven brakes. However, using a rotary-linear conversion mechanism makes the apparatus bulky. Small displacement, less provision for wear and requirement of high voltage reduces the loading capacity using a piezoelectric ceramic material in an electrical driven brake. These major drawbacks gave scope to for an alternative actuation in automotive brake system.

The proper deployment of brakes using Terfenol-D material is expected to eliminate the need for complex and heavy mechanical or hydraulic parts. Also it enhances the efficiency and stability of brake control due to fast and accurate generation of brake torque. Moreover, the design and development of magnetostrictive disc brake system is quite challenging due to involvement of complete change in requirements from hydraulic to electro-hydraulic braking systems (Murata and Yamada, 1998). Recently, Pramod et al., 2010 discussed the mechanical and magnetic design issues in the design of magnetostrictive brake, Diftler and Hulse

32

(2010) of NASA proposed magnetostrictive brake as energy-efficient alternative to a magnetic fail-safe brake in a robot.

2.8. OBJECTIVE OF THE PRESENT STUDY

During the present study, the design of magnetic circuit of a Terfenol-D actuator contained with coaxial coils (TCC) is presented. An insight into the magnetic field parameters for coaxial coils in free air and Terfenol-D actuator assembly contained with different housing materials is analyzed. An experimental setup for measuring the displacement is fabricated and experimental data for step input under different preloads will be used for validating the proposed magnetostriction models of the present study. Amplification concepts are discussed to evaluate the output energy of a Terfenol-D actuator with amplification unit. An experimental test rig is designed, fabricated and attempts are made to implement magnetostrictive actuation in disc brake. From the foregoing review of literature, the objectives of the current study are as follows,

- To design a Terfenol-D actuator focusing on electromagnetic parameters, Belleville springs for prestress mechanism, and hydraulic displacement amplifying unit and their fabrication as per design specifications.
- To verify the coaxial coil geometry for the suitability of producing the desired magnetic field using analytical method.
- To analyze magnetic field quantities like magnetic field strength and magnetic flux density of a Terfenol-D actuator with different housing materials using Maxwell 2D solver.
- To evaluate magnetic field strength from the driving coils considering inductance, magnetization using Jiles-Atherton model, magnetostriction using quadratic model, non-constitutive model and proposed magnetostrictive model considering quality factor in to account.
- To study the actuator characteristics like displacement, blocked force, response time under preload for step input by conducting experiments on Terfenol-D actuator. Periodic step input and gradually changing step input

from zero to maximum value are other input conditions used. Theoretical actuator characteristics are compared with experimental results.

- To analyze displacement and output energy of a Terfenol-D actuator using stiffness match principle. Further examine the Terfenol-D actuator coupled with hydraulic amplification unit and caliper assembled disc for maximum output energy, output displacement, optimum gain, and optimum amplification ratio.

- To evaluate and compare the brake performance characteristics such as braking force and braking torque from the theoretical and experimental output of a Terfenol-D actuator.

- To test the performance of assembled prototype magnetostrictive actuator coupled with hydraulic amplification for step input under different preloads.

CHAPTER 3

DESIGN AND MAGNETIC FIELD ANALYSIS OF A TERFENOL-D ACTUATOR

3.1. INTRODUCTION

The main objective of actuator design is to obtain large output strain, thus making possible the effective the use of Terfenol-D material. In this chapter, the details of designing Terfenol-D actuator addressing different aspects related to electrical design are discussed. Primarily, the number of coil turns and wire size are two significant parameters involved in the design of Terfenol-D actuator. These two parameters are evaluated based on required amount of magnetic field strength. Shape factor determines whether the dimensions of coaxial coil are suitable to achieve the desired magnetic parameters such as magnetic field intensity, magnetic flux density and magnetic flux. Analytical, experimental and numerical approach with Maxwell 2D solver is discussed to evaluate the magnetic field strength of coaxial coils alone in free air. Numerical magnetic field strength of coaxial coils alone and as well coaxial coils carrying different sizes of Terfenol-D rod including the working sample used in the present work is examined. More particularly, the detailed overview involved in magnetic field analysis under direct current input for a Terfenol-D actuator with different housing materials having different magnetic permeabilities namely mild steel, cast iron and aluminium is discussed.

3.2. FACTORS AFFECTING THE PERFORMANCE OF A GIANT MAGNETOSTRICTIVE ACTUATOR

All material properties of Terfenol-D are highly variable under different operating conditions like prestressing, thermal conditions and exposure to magnetic field. The various factors affecting the performance of giant magnetostrictive actuator are as follows:

i.	Applied magnetic field (H)	vii.	Type of manufacturing process
ii.	Direction of magnetic field	viii.	Composition of the material
iii.	Surrounding temperature	ix.	Young's modulus of the material
iv.	Permeability of material	x.	Type of layout
v.	Magneto-mechanical coupling factor and magnetostrictive coefficient	xi.	Applied pre-stress
vi.	Quality factor	xii.	Magnetic bias

3.2.1 Applied magnetic field $\left(H \right)$

Strain of the magnetic material depends on applied magnetic field. It leads to stretching of the material in the direction of the magnetic field in case of positive magnetostriction. Applying a stronger field leads to stronger and more definite re-orientation of more and more domains in the direction of magnetic field (Callister and Balasubramaniam, 2007). When all the magnetic domains have become aligned with the magnetic field, the saturation point has been achieved.

3.2.2 Direction of magnetic field

The strain of the magnetic material will change by changing the direction of applied magnetic field. Generally, strain occurred by negative magnetic flux is equal to the strain achieved by positive magnetic flux, but the domain rotation is different. For all materials, there is a crystallographic direction in which magnetization is easiest i.e. in this direction the saturation magnetization can be achieved at the lowest magnetic field (Callister and Balasubramaniam, 2007). This is called direction of easy magnetization. On the other hand, a hard crystallographic direction is the direction for which saturation magnetization is most difficult.

3.2.3 Surrounding temperature

Temperature will also influence the magnetic characteristics of materials (Callister and Balasubramaniam, 2007). Temperature rise of solids results in an increase in the amplitude of thermal vibrations of atoms. The atomic magnetic moments are free to rotate at higher temperature. Hence, the rising of temperature results in increasing

thermal motion of atoms. The thermal motion leads to randomize the direction of any moments that may be aligned.

3.2.4 Permeability of the material

The permeability of most materials is close to the permeability of the free space. These materials are called paramagnetic or diamagnetic. In the case of ferromagnetic materials, the permeability is very large and it is common to express the permeability in terms of a new property, the relative permeability. The relative permeability therefore indicates the amplification of magnetic effects in a magnetic material which is expressed as the amplitude of the magnetic flux density in a magnetic material in response to a given magnetic field. The relative permeability of Terfenol-D is 4-10 which is very much less than magnetic iron which is equal to 1150 (Yensen, 1928). When the material has a very small response to an applied magnetic field as in case of aluminium as shown in Fig. 3.1, the behaviour is similar to that of free space and the relative permeability is almost equal to one.
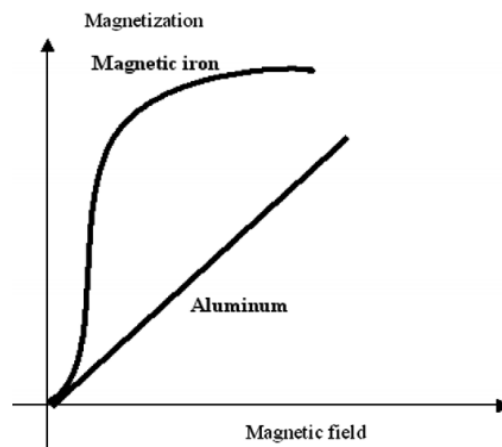
Fig. 3.1 Comparison of magnetization of magnetic iron and aluminium
(Source of figure: Olabi and Grunwald, 2008a).

3.2.5 Magneto-mechanical coupling factor and the magnetostrictive coefficient

One of the basic principles of actuator is the conversion of magnetic energy into mechanical energy. The efficiency of energy converting process is governed by the magneto-mechanical coupling factor. The value of this factor usually varies between 0.5 and 0.7 indicating that the efficiency varies between 50 % and 70 % (Claeyssen et al., 1997). The material properties of interest all relate to longitudinal axis as the

37

longitudinal elongation is of interest in the applications of standard actuator. This mode is called 33-mode and the magneto mechanical coupling factor is called k_{33}.

The magneto mechanical coupling factor is given by,

$$k_{33}^2 = \frac{d_{33}^2}{\mu_{33}^T} . E^H \tag{3.1}$$

Where d_{33} = Magnetostrictive strain coefficient

= Slope of the strain versus magnetic field

$= \dfrac{d\lambda}{dH}$ and μ_{33} = Permeability of Terfenol-D material at 33-mode
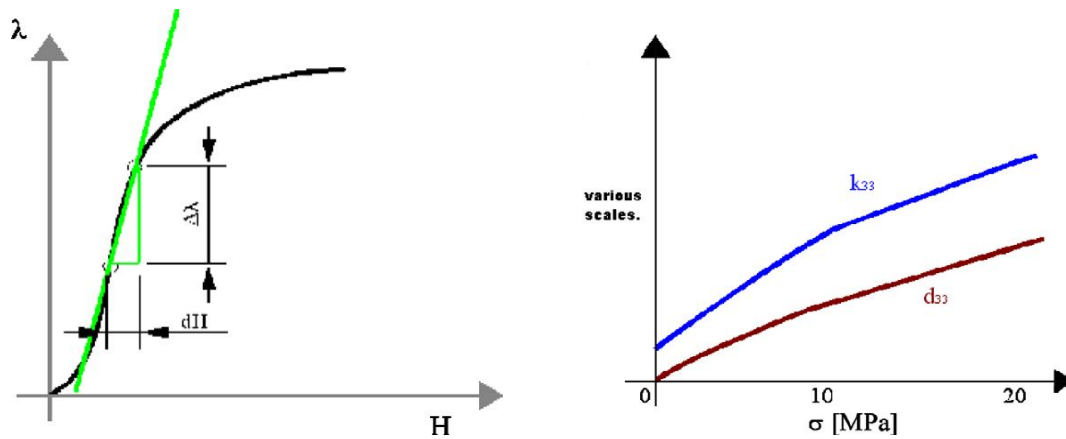
Fig. 3.2 (a) Strain versus magnetic field and (b) k_{33} and d_{33} versus applied stress
(Source of figure: Olabi and Grunwald, 2008a).

The variation of magnetostriction (λ) with respect to applied field is shown in Fig. 3.2 (a). There is a region in the graph where the slope is high and the relationship between the strain and the magnetic field is almost linear. This range is preferred for converting the magnetic into mechanical energy due to minimization of losses and almost the linear relationship. Neither the magnetomechanical coupling factor k_{33} nor the magnetostrictive coefficient d_{33} is constant throughout the operating conditions in real applications of magnetostrictive material. The impact of applied prestress on magnetomechanical coupling factor k_{33} and magnetostrictive coefficient d_{33} is shown in Fig. 3.2 (b) due to inconsistency in Terfenol-D material. It is recurrent for both coefficients to show maxima at a given value of pre-stress. Two coefficients d_{33} and

38

k_{33} are need to be as high as possible for effective and efficient operation (Olabi and Grunwald, 2008a). The coefficient d_{33} is also called as magnetostrictive strain coefficient and its value is in the range of 5-70 N-m/A. Both coefficients depend not only on the pre-stress as in Fig. 3.2 (b), but also on the applied magnetic field as illustrated in Fig. 3.2 (a).

3.2.6 Quality factor

More often, the long Terfenol-D rod is used in an actuator. It will be subjected to an excitation field parallel to the axis of the rod. Simple theory of the longitudinal mode can be applied to get a preliminary design before using numerical models. A pure longitudinal mode can be obtained on assuming (i) Radial stresses are equal to zero (ii) No shear effect and (iii) transverse excitation fields are negligible. To simplify the theory, consider an actuator with one end working either in the air (no load) or against a purely resistive load. Other end of the actuator is clamped. The vibration against resistive load produces a mechanical output power. Most of the devices can be analyzed as systems including compliance, an effective mass and a mechanical resistance due to internal mechanical losses. The Terfenol-D rod is activated by a longitudinal field produced by a coil driven by an excitation current. This results in conversion of strain into displacement of the free mass.

Under quasi-static condition and neglecting stiffness of prestress spring as shown in Fig. 3.2 (a) for a first approximation, the strain of Terfenol-D in an unloaded actuator is

$$\lambda_{33} = d_{33}.H_3 \tag{3.2}$$

The coefficient d_{33} is found to be almost constant for most frequencies and H_3 is the magnetic field strength in the longitudinal direction.

When the unloaded actuator is excited with constant field amplitude versus frequency, a sharp crest of vibration is obtained. The natural longitudinal vibration mode occurs. This mode is magnetically excited due to coupling. The strain at resonance is due to magnetic excitation and a factor is known as device mechanical factor Q_m.

$$\lambda_{33} = Q_m.d_{33}.H_3 \tag{3.3}$$

The mechanical quality factor defines the damping of the resonance. When the vibrating end is unloaded, the damping is only due to internal mechanical losses. When a load is applied, the resistive part of the load provides an additional damping which reduces the device mechanical quality factor (Q_m) to material quality factor (Q^H).

3.2.7 Type of manufacturing processes

Terfenol-D is a rare earth alloy, silver in colour, brittle at room temperature. It is not easy to produce raw materials as they are highly reactive and contain impurities. At least four different methods have been developed to produce Terfenol-D and are utilized on a near-production basis as reported by McMasters (1991) and Olabi and Grunwald (2008a). The methods are Free Stand Zone Melting (FSZM), Modified Bridgmann (MB), Sintered Powder Compact and Polymer Matrix Composites of Terfenol-D Powder Techniques. The most used methods are MB and FSZM. In FSZM-method, material in the melting zone is held in suspension by surface stress. This method is also called as Directional Solidification Method. In MB-method, the material is melted completely and crystals are grown starting with a seed crystal. Because side nucleation from mould walls tends to overwhelm the primary axial dendrite crystal growth, the minimum Terfenol-D rod diameter is approximately 10 mm. In both processes the material solidification is specifically controlled by reducing heat flow in a way which encourages a crystallographically aligned structure. The Sintered and Composite processes are used more for the production of Terfenol-D rods for high frequency (higher than 1 kHz) applications otherwise eddy currents would cause high losses.

3.2.8 Composition of the material

Terfenol-D is an alloy of Terbium, Dysprosium and ferrous material. It is in general represented as $Tb_x Dy_{1-x} Fe_y$ in which x = 0.2 to 0.3 and y = 1.9 to 1.95. The good composition of Terfenol-D can be achieved by choosing small values of x and y, but it is very difficult to manufacture the material with that composition since it will take much time for the bonds to form between the atoms (Chilambarasan et al., 2014).

Table 3.1 shows the strain in ppm for the different ratios of Terfenol-D at 13.5 MPa pre-stress (Engdahl, 2000).

Table 3-1. Strain (in ppm) for different ratios of Terfenol-D at 13.5 MPa pre-stress.

Applied Field (H)	500(Oe)	1000(Oe)	1500(Oe)	2000(Oe)
$Tb_{0.3}Dy_{0.7}Fe_{1.95}$	1084	1393	1544	1643
$Tb_{0.3}Dy_{0.7}Fe_{1.92}$	1118	1358	1536	1678
$Tb_{0.3}Dy_{0.7}Fe_{1.90}$	1054	1368	1552	1658

3.2.9 Young's modulus of the material

Young's modulus varies almost linearly with the magnetic field as shown in Fig 3.3. Young's modulus at constant value of magnetic flux density E^B can be expressed as follows (Olabi and Grunwald, 2008a):

$$E^B = \frac{E^H}{(1-k_{33})} \tag{3.4}$$

Where k_{33} = Magneto mechanical coupling factor, E^B = Young's modulus at constant magnetic flux density and E^H = Young's modulus at constant magnetic field.
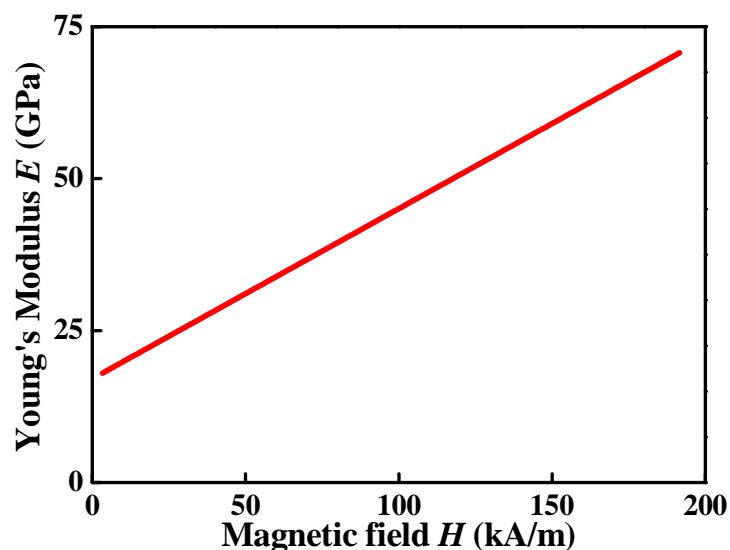
Fig. 3.3 Young's modulus versus magnetic field (ΔE Effect)
(Reproduced from Olabi and Grunwald, 2008a).

As the Eq. (3.4) suggests, theoretically there is a value of flux density at which Young's modulus becomes infinite. This condition arises whenever the coupling factor (k_{33}) becomes unity. When this property occurs in a sample of Terfenol-D, it is said to have reached ''a blocked state'', and no rotation of magnetic domains is possible. Blocked force is the force at which material is prevented from changing its dimensions in response to stress.

3.2.10 Type of layout used

Layout used to produce magnetic field also influences the strain of the Terfenol-D material. The four different layouts are TC (Terfenol-D, Coil) layout, TCM (Terfenol-D, Coil, Permanent Magnet) layout, TMC (Terfenol-D, Permanent Magnet, Coil) layout and MTC (Permanent Magnet, Terfenol-D, Coil) layout and its features as listed in Table 3.2.

Table 3-2. Comparison of standard layouts of actuator (Grunwald and Olabi, 2008).

T - Terfenol-D C - Coil M - Permanent Magnet	C T C	M C T C M	C M T M C	C T M T C
Magnetic bias with	DC coil	Permanent		
Magnetic bias level	Low	Medium	Medium, high	High
Terfenol-D shaped	Rod, bar	Rod	Rod	Hollow
Structure	Simple	Medium	Medium	Complex
Field in-homogeneity	Low	Low	Medium	High

Each layout is having its own advantages and disadvantages. The TC and TCM layouts are preferred as these are simple in construction and cost effective with high energy density. But in case of TC layout, eddy current losses are more. Electrical currents that are induced in a magnetic material by a magnetic field that varies in magnitude and direction with time are called eddy currents. Eddy current losses are different in different layouts and hence strain differs by changing the layout.

3.2.11 Applied pre-stress

The need for the prestress is twofold. First, because of the nature of magneto-elastic coupling, the material can achieve better performance when a prestress of compressive nature is applied. The magnetic domain orientation can be manipulated by changing the state of stress in the material. As shown in Fig 3.4, larger magnetostrictive strain can be obtained with same magnetic field when the prestress is increased (Engdahl, 2000 and Karunanidhi and Singaperumal, 2010). The material is quite strong in compression but it can sustain little tensile or shear load. Therefore, prestressing is required to evade tensile loading hazard.
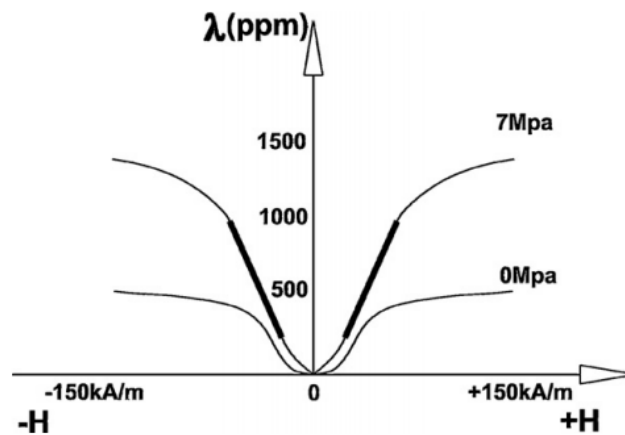
Fig. 3.4 Effect of prestress on magnetostriction
(Source of figure: Karunanidhi and Singaperumal, 2010).

3.2.12 Magnetic bias

The magnetostrictive transducer comprises of the magneto-elastic material and a surrounding coil. A current in the coil will produce a magnetic field in the magneto-elastic material. The magneto-elastic energy is then transformed to mechanical work. The strain of the magnetostrictive material is independent of the sign of the applied longitudinal magnetization field. An input current of alternating sign will therefore result in a strain with a doubled frequency compared to the input current frequency. This can be avoided by applying a bias magnetization, H_0 such that a more linear relation is established between the applied coil current and the strain as shown in Fig.3.5. The bias is created by using a permanent magnet and actuator is operated in the region where the slope of the curve is maximum as shown in Fig.3.5.

43
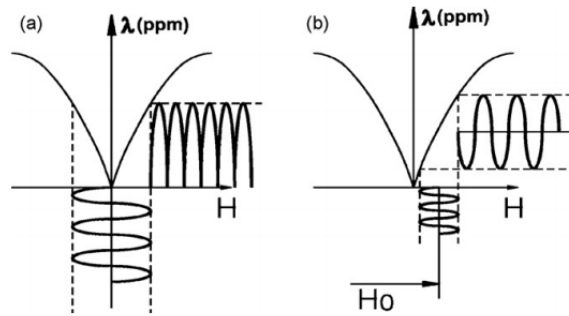
Fig.3.5 Magnetostriction (a) without and (b) with a bias magnetic field
(Source of figure: Engdahl, 2000 and Karunanidhi and Singaperumal, 2010).

It is summarized that the above list of influencing parameters are to be targeted in order to achieve the controlled output strain. A TCC (Terfenol-D and coaxial coils) layout type of configuration is chosen for actuator in the present work. Different magnetic permeabilities of materials for the actuator housing are selected and numerical evaluation of magnetic field strength from the coaxial coils of an actuator will be investigated. Effect of quality factor is considered in the numerical evaluation of magnetostriction of Terfenol-D material. Separate coil for biasing the magnetic field is used rather than permanent magnet in an actuator assembly. Disc springs are being used to apply the preload on Terfenol-D in an actuator. These parameters that affect the output of a Terfenol-D actuator are considered in the present work.

3.3 STRUCTURE AND LAYOUT OF A TERFENOL-D ACTUATOR

Many researchers have used TCM layout as it possess features like low field in-homogeneity and medium magnetic bias level (for example, Lhermet et al., 1993 and Lei et al., 2010). The magnetic biasing is achieved with permanent magnets in order to eliminate eddy current losses. In the present work, TCC layout i.e. Terfenol-D surrounded by two co-axial coils is used in the layout of a Terfenol-D actuator. One of the coils is used for the excitation of actuator. The other coil is used for producing bias magnetic field in place of permanent magnet.

3.3.1 Selection of coaxial coils for the Terfenol-D actuator

Bias magnetic field is required to establish the linear relationship between applied input and magnetostriction. This could be achieved to the best possible extent using permanent magnets. Engdahl (2002) indicates that the use of permanent magnets in a

44

Terfenol-D actuator for bias field is preferred when the ratio of length to the radius of Terfenol-D rod is less than or equal to 3.5. If the ratio exceeds 3.5, the amplitude and homogeneity of bias field decreases drastically. In addition, the magnetic field strength exhibited by the permanent magnet depends on material being used for the permanent magnet. It is to be magnetized as most of its properties vary significantly with temperature (Brauer, 2006). The desired magnetic flux varies due to accumulation of magnetic field in a permanent magnet i.e. residual magnetic field. It is too expensive and availability of required size is drawback when permanent magnets are preferred. Magnetic power of permanent magnets will reduce at temperatures above ambient temperature equal to 30^0 C. The magnetic field of permanent magnets decreases above 30^0 C and lies in the range of 0.12 % to 0.2 %. All types of permanent magnets will lose all their magnetic power at Curie temperature. The permanent magnets will be affected due to vibration and mechanical shock (Edward, 2004).These disadvantages can be minimized or reduced to certain extent by using a separate coil for generating bias magnetic field. Magnetic field can be adjusted over a wide range and strength levels can be varied using a separate coil. Required magnetic properties can be attained for an applied input current and the same can disappear as the input current is taken-off. The magnetic power developed from the coil is much more than producing with permanent magnet. The magnetic field and gradient of a coil depend on the number of turns and the coil current (Edwards, 2004). All these characteristics gave way to look for a coil to produce bias magnetic field rather than permanent magnet in the layout of an actuator. Eddy current losses are another problem that arises using a coil. However, the DC input is supplied to both coils (bias coil and excitation coil) to avoid eddy current loss that arise supplying AC input to the coils.

The arrangement of actuator consisting of a Terfenol-D surrounded by two coaxial coils namely coil 1 and coil 2 is shown in Fig. 3.6. The two coils are separated by a short distance and independently operated. The coil 1 is meant for biasing purpose so that the actuator could be operated in the linear region. The coil 1 is always supplied with direct current. Superimposed on this is the field produced by coil 2 which will be excited with either direct or alternating current. Numerically the magnetic flux density

is evaluated for the configurations such as single coil, coaxial coils and single coil with permanent magnet, without using coaxial coils directly in the layout of an actuator. The flux density could be achieved at the center of coils with greatest magnitude using coaxial coils (refer section I.1 in APPENDIX – I). The size of Terfenol-D rod is to be arrived at based on maximum axial braking force required to stop rotor or disc of a prototype magnetostrictive disc brake system (refer CHAPTER 6). Terfenol-D rod was made available from Defence Metallurgical Research Laboratory, Hyderabad, India.
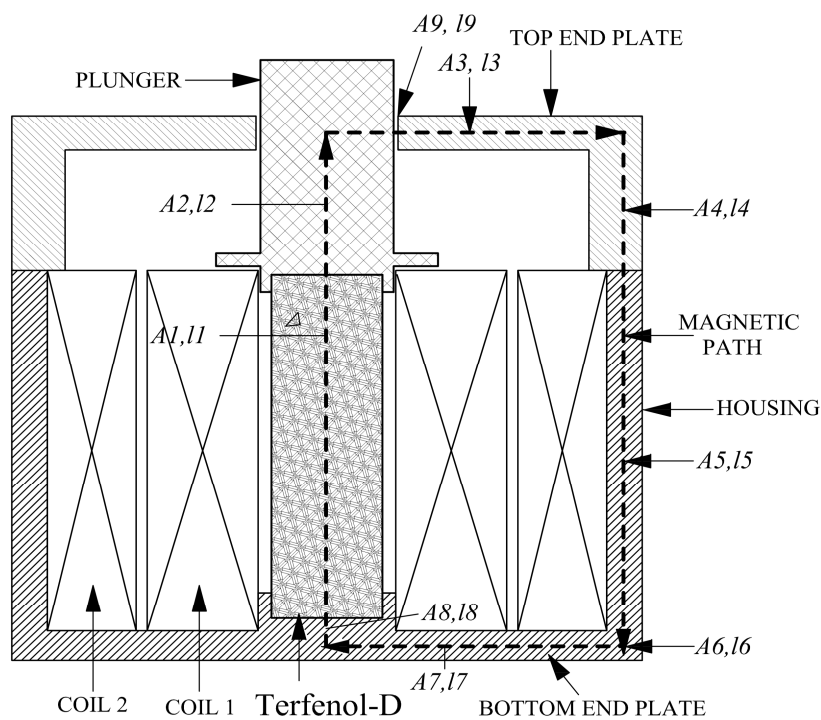
Fig. 3.6. Schematic layout and path of a magnetic flux in the coils of a Terfenol-D actuator.

It was available with diameter ranging from 25 to 30 mm and length between 80 to 120 mm. Terfenol-D rod of diameter 28 mm and length of 80 mm was chosen. With this, the length to radius ratio of Terfenol-D rod is 5.7. This ratio exceeds 3.5. Recollecting on the debate over the use of permanent magnet in a Terfenol-D actuator based on length to radius ratio of Terfenol-D rod, the present work proposes to use coaxial coils. Suitable material for bobbin is chosen as the material that must be conductive or permeable for the magnetic field lines. The material of the bobbin used in the present work is aluminium. This permits the flux lines to concentrates towards

46

and along the Terfenol-D rod so that maximum magnetostriction is obtained. The Terfenol-D rod is placed at the center of co-axial coils and altogether is enclosed in a separate housing. The housing material will be chosen from among mild steel, cast iron and aluminium after due magneto-static analysis. The main source of magnetic field is coil 1 and coil 2 and the magnetic field strength will depend on number of turns in each coil. Analytically the required number of turns for coils is calculated using Ampere's law. The first hand calculation for number of turns is verified using the reluctance approach. Prestressing of active material is required to predict the desired output from the Terfenol-D. The magnetic domains of an active material will be aligned parallel to easy magnetic axis during prestressing, so that the desired output can be attained. Disc springs are used to apply the prestress on Terfenol-D rod. Disc springs are mounted over the portion of plunger between coil upper part and top cover plate. Desired load on Terfenol-D can be applied by turning the top cover plate of actuator assembly. The applied load on Terfenol-D rod is monitored using force transducer.
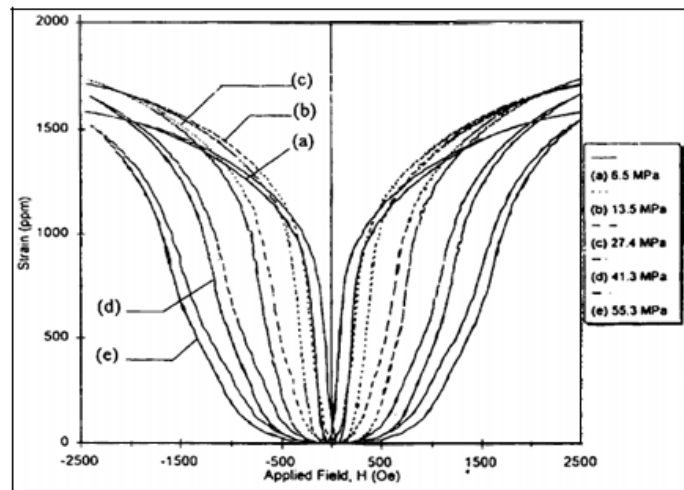
Fig. 3.7 Magnetostriction curves of a Terfenol-D for different pre-stresses
(Source of figure: Engdahl, 2000).

The magnetostriction versus magnetic field curve (Fig. 3.7) reported in Engdahl (2000) for an optimum pre-stress of 6.5 MPa was referred to herein to obtain the desired field from the Terfenol-D actuator. For a pre-stress of 6.5 MPa, the linear behaviour of Terfenol-D material was found at an applied field ranging from 48 kA/m

(603 Oe) to 52 kA/m (654 Oe), and the corresponding magnetostriction is 1000-1800 ppm. To generate a magnetic field strength of 50 kA/m, the contribution from bias coil (coil 1) is 28 kA/m and that from coil 2 is 22 kA/m. Assuming an input current ranging from 0 to 4 A, the maximum amperage of wire is chosen and is designated as 17 SWG (BS6722, 1986) with a diameter of 1.423 mm. Terfenol-D rod and hollow cross-sectioned coaxial coils in an actuator layout together forms a conductor carrying a current for which Ampere's law was used to find number of coil turns. According to Ampere's law, number of turns required for coil 1 and coil 2 are 560 and 440 for producing 28 and 22 kA/m using 4 A.

3.3.2 Verification of coil turns using reluctance approach

The path of a magnetic flux line distribution inside a Terfenol-D actuator assembly depends on the reluctance of surrounding materials such as top end plate, bottom end plate, plunger, Terfenol-D rod seat, housing, air gap between the plunger and top end plate. These materials should possess low reluctance. The main magnetic path through the magnetostrictive actuator is shown in Fig. 3.6. There are nine designated sections through which the magnetic flux passes. For each section, length of magnetic path (l) is identified and the magnetic field (H) is calculated. The length is fixed by the geometry of Terfenol-D actuator but the magnetic field (H) is calculated by the use of magnetic properties of the material.

According to Ampere's law the relationship between the current (*I*) and magnetic field intensity (*H*) can be expressed as,

$$\oint H.dl = NI \tag{3.5}$$

The magnetic flux passes through the nine designated sections in the magnetic path of a Terfenol-D actuator as designated in Fig. 3.6. Therefore from Eq. (3.5), the magneto-motive force is expressed as:

$$NI = H_1 l_1 + H_2 l_2 + H_3 l_3 + H_4 l_4 + H_5 l_5 + H_6 l_6 + H_7 l_7 + H_8 l_8 + H_9 l_9 \tag{3.6}$$

Where H = Magnetic field in a particular component, l = Length of corresponding magnetic path.

However, the total flux (ϕ) remains constant throughout the magnetic path in any magnetic circuit of a Terfenol-D actuator.

The total magnetic flux (ϕ) in the magnetic circuit of an actuator is given by:

$$\phi = \int B dA \qquad (3.7)$$

Where A is the cross sectional area of individual component along the magnetic path and B is the magnetic flux density of a magnetic circuit.

As the magnetic flux is constant throughout the path, the product of the magnetic flux density and cross sectional area will be constant for each material (Grunwald and Olabi, 2008).

$$\phi_T = \phi_{mildsteel} \qquad (3.8)$$

Further Eq. (3.8) can be written as:

$$B_T A_T = B_{mildsteel} A_{mildsteel} \qquad (3.9)$$

The magnetic flux density (B) depends on the properties of the medium and particularly on the relative permeability (μ_r) of materials used in the assembly of the Terfenol-D actuator. According to this, the magnetic flux density of Terfenol-D and mild steel materials can be expressed as:

$$B_T = \mu_0 \mu_{r(T)} H_T \text{ and}$$

$$B_{mildsteel} = \mu_0 \mu_{r(mildsteel)} H_{mildsteel} \qquad (3.10)$$

The reluctance $\mathfrak{R}$ in the magnetic circuit is analogous to resistance in electric circuit. Analytical expression for calculating the reluctance of circuit is given by,

$$\mathfrak{R} = \frac{N_{coil} I}{\phi} \qquad (3.11)$$

From Eq. (3.11) and Eq. (3.8) to Eq. (3.10) the number of turns required for coaxial coils is given by:

$$N_{coil} = \frac{\mathfrak{R} \mu_0 \mu_{r(T)} H_T A_T}{I} \qquad (3.12)$$

Where $\mathfrak{R}$ =Total reluctance of magnetic circuit.

It is equal to $\mathfrak{R}_1 + \mathfrak{R}_2 + \mathfrak{R}_3 + \mathfrak{R}_4 + \mathfrak{R}_5 + \mathfrak{R}_6 + \mathfrak{R}_7 + \mathfrak{R}_8 + \mathfrak{R}_9$, $\mathfrak{R}_1 =$ reluctance offered by Terfenol-D rod, $\mathfrak{R}_2 =$ reluctance offered by plunger, $\mathfrak{R}_3 =$ reluctance offered by top end plate, $\mathfrak{R}_4 =$ reluctance offered by top end plate edge, $\mathfrak{R}_5 =$ reluctance offered by housing thickness, $\mathfrak{R}_6 =$ reluctance offered by bottom end plate edge, $\mathfrak{R}_7 =$ reluctance offered by bottom end plate , $\mathfrak{R}_8 =$ reluctance offered by bottom support of Terfenol-D and $\mathfrak{R}_9 =$ reluctance offered by the air gap between the plunger and top cover plate. The reluctance of the disc springs used for prestressing is neglected. The individual reluctance of each component along the path can be calculated by:

$$\mathfrak{R}_i = \frac{l_i}{\mu_0 \mu_r A_i} \tag{3.13}$$

Table 3-3. Reluctances of individual components of actuator assembly.

Part No.	Name of the component	Material	Length (mm)	Diameter (mm)	Area ($\times 10^{-3}$ m^2)	Reluctance ($\mathfrak{R}$) of component AT/Wb
1	Terfenol-D rod	Tb$_{0.3}$Dy$_{0.70}$Fe$_{1.95}$	80	28	0.62	25.86×10^6
2	Plunger	Mild steel	35	30.2	0.7	9.7×10^3
3	Top end plate	Mild steel	8	-	10.5	151.6
4	Top end plate edge	Mild steel	35	-	4.1	1.7×10^3
5	Housing	Mild steel	83	-	3.4	4903
6	Bottom end plate	Mild steel	67	-	1.05	94.2
7	Bottom end plate edge	Mild steel	25	-	3.4	147.7
8	Terfenol-D rod seat	Mild steel	28	-	0.49	8.1×10^3
9	Air gap between the plunger and top cover plate	Air	7	-----	0.008	15.9×10^6
$\mathfrak{R}_{Total} = 2.8 \times 10^7$ AT/Wb						

Where $l_i =$ section length of the component, $A_i =$ cross sectional area of the component and $i = 1, 2, 3, 4, 5, 6, 7, 8$ and 9. Using Eq. (3.13) the reluctances of individual components in a Terfenol-D actuator assembly is calculated and tabulated

in Table 3-3. Further, using Eq. (3.12), the number of turns for Coil 1 will be 567 turns and 454 turns for coil 2 to produce 28 kA/m of biasing magnetic field and 22 kA/m of peak magnetic field respectively which are in close agreement to 560 and 440 that is obtained using Ampere's law.

3.3.3 Dimensions of coaxial coils for the Terfenol-D actuator

The various dimensions such as length, inner and outer diameter of each coil are assumed to accommodate the calculated number of turns. The inner diameter of coil 1 is assumed very close to diameter of Terfenol-D rod, inner diameter of coil 2 is very close to the outer diameter of coil 1 to minimize the air gap so that flux leakages will be minimum. Top and bottom cups are provided in the top and bottom cover plates to hold firmly the Terfenol-D rod. Therefore, a small amount of allowance is considered to fix the diameters of coil 1 and coil 2. Using Eq. (I.1 – I.4) of section I.2 in APPENDIX-I the dimensions of coil 1 and coil 2 are fixed and tabulated in Table 3-4.

Table 3-4. Dimension of coaxial coils.

S. No	Parameters	Value
1	Wire diameter	1.423 mm
2	Length of the coil	83 mm
3	Inner diameter of coil 1	33 mm
4	Number of turns per unit run for coil 1	58
5	Number of runs required for 560 turns of coil 1	10
6	Outer diameter of coil 1	73 mm
7	Inner diameter of coil 2	75 mm
8	Number of turns per unit run for coil 2	58
9	Number of runs required for 440 turns of coil 2	8
10	Outer diameter of coil 2	115 mm

3.4 OTHER ELECTRICAL ASPECTS IN THE DESIGN OF TERFENOL-D ACTUATOR

Electrical parameters such as geometry of the coil, flux leakage, Q_{coil} value of driving coil, magnetic coupling coefficient and inductance of the coil are considered in the design of Terfenol-D actuator other than the number of coil turns and wire diameter. The analytical expressions reported by Engdahl (2000) have been used to compute these electrical parameters in the present study.

3.4.1 Geometry of the coil and flux leakage

Electrical design of a Terfenol-D actuator explores the design of its coil for excitation at an applied input current. The function of drive coil is very vital for attaining highest total efficiency of the actuator. Part of the total available magnetic power P_{mag} will be used for magnetic transduction in an active material. The typical geometry of driving coil is shown in Fig. 3.8. Magnetic circuit is assumed as ideal i.e. no losses occur in the magnetic circuit to distinguish the performance of coils.

The coil function can be described by the following parameters:

Magnetic field in the center of the coil is given by (Engdahl, 2000),

$$H_{coil} = G_{coil} \sqrt{\left(\frac{P_{coil\, losses}\, \chi}{\rho a_1} \right)} \qquad (3.14)$$

Where H_{coil} = Magnetic field intensity at the center of coil, G_{coil} = Shape factor of the coil, $P_{coil\, losses}$ = Coil losses, χ = Fill factor $= \pi/4$ for circular coil wire, ρ = Electrical resistivity of the copper wire and a_1 = Inner radius of coil.
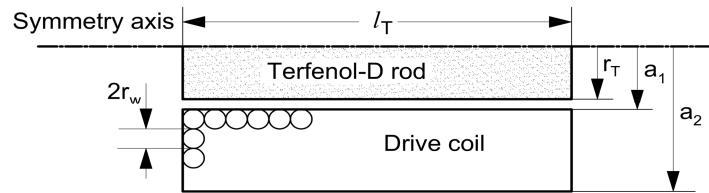
Fig. 3.8. Typical geometry of the drive coil.

Shape factor of coil is expressed as (Engdahl, 2000):

$$G(\alpha, \beta) = G_{coil} = \frac{1}{5} \left(\frac{2\pi\beta}{(\alpha^2 - 1)} \right)^{\frac{1}{2}} \ln \left(\frac{\alpha + (\alpha^2 + \beta^2)^{\frac{1}{2}}}{1 + (1 + \beta^2)^{\frac{1}{2}}} \right) \qquad (3.15)$$

Where $\alpha = a_2/a_1$, $\beta = l_T/2a_1$ and $\gamma = a_1/r_T$, a_1 and a_2 are the inner and outer radii of the coils, l_T is the length of the Terfenol-D rod and r_T is the radius of the Terfenol-D rod.

Coil resistance is given by

$$R_{coil} = \frac{N_{coil}^2 \rho \pi (\alpha + 1)}{\chi l_T (\alpha - 1)} \qquad (3.16)$$

52

The coil losses can be expressed as:

$$P_{coil\ losses} = \frac{N_{coil}^2 \rho \pi (\alpha + 1)}{\chi l_T (\alpha - 1)} I^2 \qquad (3.17)$$

On substituting the Eq. (3.17) in Eq. (3.14), magnetic field strength at the center of the coil can be expressed as:

$$H_{coil} = G_{coil} N_{coil} I \sqrt{\frac{\pi (\alpha + 1)}{l_T a_1 (\alpha - 1)}} \qquad (3.18)$$

Eq. (3.18) represents the "Best design" as it gives maximum magnetic field at the centre of coaxial coils with respect to least dissipated power in coaxial coils (Engdahl, 2000). The calculations of shape factor and flux leakage is carried out in APPENDIX I, Section I.3. i.

3.4.2 Q_{coil} value of the driving coils

Q_{coil} value of driving coil is the ratio of maximum stored magnetic energy in the Terfenol-D material to the dissipated energy in the coil resistance during one cycle. It is calculated using the shape factor (G_{coil}) of the coil. The maximum magnetic energy delivered by the coil to the Terfenol-D material can be expressed as:

$$E_{mag,max} = \frac{1}{2} \mu_{r(T)} H_{coil}^2 V_T \qquad (3.19)$$

Where $\mu_{r(T)}$ is the relative magnetic permeability equal to 5 and V_T is the volume of Terfenol-D rod.

Shape factor of coil can be expressed using Eq. (3.14) as:

$$H_{coil}^2 = G_{coil}^2 \left(\frac{P_{coil-losses} \chi}{\rho a_1} \right) \qquad (3.20)$$

The coil losses during one cycle are given by:

$$E_{coil\ losses} = P_{coil\ losses} \times \frac{2\pi}{\omega} = H_{coil}^2 \frac{2\pi \rho a_1}{\chi G_{coil}^2 \omega}$$

According to the definition, the Q_{coil} value of the coil is expressed as

$$Q_{coil} = \frac{E_{max.mag}}{E_{coillosses}} = \frac{1}{4} \mu_{r(T)} \frac{\chi G_{coil}^2 \omega r_T l_T}{\gamma \rho} \qquad (3.21)$$

Where $\gamma = a_1/r_{coil}$, ω is the frequency equal to $2\pi f$ rad/sec and the frequency is assumed as 1 Hz and ρ is the resistivity of the copper wire equal to 1.68×10^{-8} Ω-m (Gray, 1967). With this, the amount of maximum magnetic energy stored in the Terfenol-D material can be computed by considering the energy dissipation in the coil during each cycle. The associated calculation can be found in APPENDIX I, section I.3-ii.

3.4.3 Magnetic coupling coefficient of the coils

One of the key parameter of coil is the magnetic coupling coefficient which is the ratio of magnetic energy stored in a Terfenol-D rod to the total magnetic energy stored in an actuator. The coupling coefficient depends entirely on coil on assuming an ideal flux return path. According to the geometry shown in Fig. 3.8, the magnetic coupling coefficient can be expressed as (Engdahl, 2000):

$$k_c^2 = \frac{\dfrac{1}{2}\mu_{r(T)}H_T^2\pi r_T^2 l_T}{\dfrac{1}{2}\mu_{r(T)}H_T^2\pi r_T^2 l_T + \dfrac{1}{2}\mu_0 H^2\pi\left(a_1^2 - r_T^2\right)l_r + \dfrac{1}{2}\mu_0\int H^2\left(r_T\right)dV} \tag{3.22}$$

Where $1/2\mu_r H^2\pi r_T^2 l_T$ is the magnetic energy stored in a Terfenol-D rod, $1/2\mu_0 H^2\pi\left(a_1^2 - r_T^2\right)l_T$ magnetic energy stored between the rod and coil winding and $1/2\mu_0\int H^2\left(r_T\right)dV$ is the magnetic energy stored in the coil windings respectively.

Magnetic field strength and flux density fields in a coil varies linearly according to Ampere's law for an assumed ideal magnetic flux return path with no fringing fields at the ends of a Terfenol-D rod.

$$H\left(r_T\right) = H_{ex}\frac{a_2 - r_T}{a_2 - a_1} \tag{3.23}$$

Where H_{ex} = Magnetic field at the boundary of the Terfenol-D rod.

On substituting the magnetic field strength from Eq. (3.23) in Eq. (3.22) and simplifying, the analytical expression for the magnetic coupling coefficient is given by,

$$k_c^2 = \cfrac{1}{1 + \cfrac{\mu_0}{\mu_r}\left(\gamma^2 - 1\right) + \cfrac{\pi\mu_0}{6\mu_r}\gamma^2\left(\alpha - 1\right)\left(\alpha + 3\right)} \qquad (3.24)$$

Specific resistivity also known as specific electric resistance of a coil is an inherent property that quantifies how strongly the copper wire material opposes the flow of electric current. Copper wire that is wound round the aluminium bobbin is having low specific resistivity. Low resistivity indicates a material that readily allows movement of electric charge for an applied input, in turn yields fewer amounts of coil losses. The coil 1 and coil 2 are separated by a short distance due to which the high mutual inductance exists between them. The high mutual inductance may be the reason for the less coil losses. On other side, the two coils are much sensitive for an applied input current as they are separated by short distance. The reason is due to a high coupling factor as it is equal to 0.74. Therefore, the Eq. (3.24) shows that there is a good agreement between a high coupling factor and low specific resistive coil losses. The ratio of radii of coil i.e. α =1 in Eq. (3.24) gives the maximum value of $k_c^2 \approx 1$ which implies infinite coil losses. The associated calculation can be found in APPENDIX I, section I.3-iii.

3.4.4 Inductance of the coils

Another important parameter in the design of coil is the computation of $L_{coil\ leakages}$. Ideal flux return path with no fringing fields at the ends of a Terfenol-D is assumed. Ampere's law indicates a linear variation of the magnetic field $\left(H\right)$ in the coil is given by Eq. (3.23). Also, it is assumed that the average effective magnetic permeability of the magnetostrictive rod is $\mu_{r(T)}$. Based on the geometry of the coil shown in Fig. 3.8, magnetic energy stored in the coil winding is given by:

$$\frac{1}{2}\mu_0\int H^2\left(r_T\right)dV = \frac{1}{2}\mu_0 H_{ex}^2 \pi r_T^2 l_T \left(\gamma^2 - 1\right) \qquad (3.25)$$

Magnetic energy stored between the rod and coil winding is given by:

$$\frac{1}{2}\mu H_{ex}^2 2\pi l_{coil}\int_{r_1}^{r_2}\left(\frac{a_2 - r}{a_2 - a_1}\right)^2 dr = \frac{1}{2}\mu_{r(T)}H_T^2\pi r_T^2 l_T \qquad (3.26)$$

The expression for magnetic energy $E_{mag.coil}$ in the coil winding and between the coil and the magnetostrictive rod for a selected geometry of the coil can be expressed as:

$$E_{mag.coil} = \frac{1}{2}\mu_0 H_{ex}^2 \pi r_T^2 l_T \left(\gamma^2 - 1\right) + \frac{\pi}{12}\mu_0 H_{ex}^2 a_1^2 l_T \left(\alpha - 1\right)\left(\alpha + 3\right) \tag{3.27}$$

Assuming a homogeneous field inside the rod then $H_{ex} = H_{coil}$ which gives

$$H_{ex} = H_{coil} = G_{coil} N_{coil} I \sqrt{\frac{\pi(\alpha+1)}{l_T a_1(\alpha-1)}} \tag{3.28}$$

Substituting the Eq. (3.28) in Eq. (3.27) and on simplifying yields the coil leakage as,

$$L_{coil\ leakage} = \frac{2E_{mag.coil}}{I^2} = G_{coil}^2 N_{coil}^2 \pi^2 \mu_0 \left[r_T \frac{\left(\gamma^2 - 1\right)\left(\alpha+1\right)}{\gamma(\alpha-1)} + \frac{1}{6}a_1(\alpha+1)(\alpha+3) \right] \tag{3.29}$$

The factor $\gamma = a_1/r_{coil}$ is a small value. Taking the square of this term present in the parenthesis gives too small value. Hence, by neglecting first term in the parentheses, then Eq. (3.29) yields:

$$L_{coilleakage} = \mu_o \frac{\pi^2}{6} G_{coil}^2 N_{coil}^2 a_1 (\alpha+1)(\alpha+3) \tag{3.30}$$

Table 3-5. Details of parameters in electrical design.

S. No	Parameter	Coil 1	Coil 2
1	Shape factor $\left(G_{coil}\right)$	0.1635	0.1154
2	Coil compensation coefficient $\left(K_{coil}\right)$	0.981	1.233
3	Resistance of coil $\left(R_{coil}\right)$	0.698 Ω	1.334 Ω
4	Power losses in a coil $\left(P_{coil\ losses}\right)$	11.17	21.344
5	Magnetic field strength $\left(H_{coil}\right)$	28 kA/m	21 kA/m
6	Flux leakage of coil	4.4 %	18 %
7	Q_{coil} value of coil	3750	1191
8	Magnetic coupling coefficient $\left(k_c\right)$	0.52	0.22
9	Inductance of coil $\left(L_{coil}\right)$	3.878 mH	2.1824 mH

From the Eq. (3.30) it is clear that the number of coil turns largely influences the coil leakage inductance. Table 3-5 lists the different electrical design parameters for each coil. Detailed calculation of electrical design parameters are discussed in section I.3 of APPENDIX I. From Table 3-5, the shape factor $\left(G_{coil}\right)$ for coil 1 and coil 2 is 0.1635

and 0.1154 respectively. The expected shape factor is 0.179 (Engdahl, 2000). Coil 1 is very close to the desired value whereas the coil 2 has shape factor less than the desired. It indicates that the coaxial coils will produce magnetic fields with least dissipated resistive power. The compensation coefficient $\left(K_{coil}\right)$ does not provide a measure of efficiency of magnetizing coils, however this coefficient signifies the impact of magnetic leakage flux. Due to flux leakage of coil 1 and coil 2 which are found to be 4.4 % and 18 % the magnetic field strength produced by the coils are 27 kA/m and 21 kA/m respectively which are close to 28 kA/m and 22 kA/m that obtained from Ampere's law. The magnetic energy stored in the Terfenol-D rod to the total magnetic energy stored in the actuator i.e. total magnetic coupling coefficient of the coils is the sum of coupling coefficients obtained for the coil 1 and coil 2 equal to 0.74. The reason is that the coils are placed coaxially and is well within in the range of 0.5 to 0.75 (Olabi and Grunwald, 2008a). Inductance of the coil 1 and coil 2 is very low and equal to 3.878 and 2.1824 mH respectively. However, one has to choose an ideal return path with high inductance value which will control the supplied input current. Subsequently more magnetic energy is stored for transformation of magnetic energy into mechanical energy in active material from the coaxial coils.

3.5 VERIFICATION OF COAXIAL COIL DIMENSIONS

Dimensions of the coaxial coils are verified for suitability in an actuator and as well to produce required magnetic field strength. The magnetic circuit of an actuator consists of coaxial coils, bulk rod of Terfenol-D, and housing with other accessories like top and bottom end cover plate possessing magnetic resistance. The objective is to verify the magnetic flux by minimizing the total magnetic resistance of the magnetic circuit of a Terfenol-D actuator as shown in Fig. 3.6. The total magnetic resistance of the magnetic circuit should be as low as possible, particularly the magnetic resistance of housing in the process of verification. Magnetic field produced from the coaxial coils should follow a right path. It means the flux lines should reach the end face of the active material to achieve the desired path. Housing, top and bottom end plates should be manufactured with soft magnetic materials that have high magnetic conductivity. The magnetic circuit should be closed and thickness of air gap in a magnetic circuit

should be reduced as much as possible. All these aspects are considered in the process of verification to achieve maximum magnetic field from coaxial coils.

In the present work, the magneto motive force produced by the coaxial coils should act effectively on Terfenol-D rod. Hence the driving coils are to be designed as hollow in cross-section. The electric-magnetic turnover ratio is to be improved as much as possible and energy consumed by coils must be very small so that heat generated by the coaxial coils will be minimized in order to meet the requirement of magnetic field strength produced by the coils. Electric-magnetic turnover ratio depends on coil geometry. Therefore the geometry of the coaxial coils is to be verified and it is established considering four parameters; namely inside and outside radii of coils, length and shape of the coils.

Considering the coil losses, the magnetic field distribution at the center of hollow coil is given by Eq. (3.18). This analytical expression represents the "Best design" as it gives maximum magnetic field at the centre of coaxial coils with respect to dissipate power in coaxial coils. With G_{coil} (shape factor) and known values of α and β, the maximum magnetic field using Eq. (3.18) at the center of each coil is given by

$$H_{coil1} = 12.98 N_{coil1} I_{coil1} \tag{3.31}$$

$$H_{coil2} = 8.14 N_{coil2} I_{coil2} \tag{3.32}$$

The Eq. (3.31) and Eq. (3.32) are compared with the ideal magnetic circuit. According to which, the magnetic field from the coil is

$$H_{coil} = \frac{N_{coil} I_{coil}}{0.083} = 12.05 N_{coil} I_{coil} \tag{3.33}$$

On comparing Eq. (3.31) and Eq. (3.32) with Eq. (3.33), the flux leakage in the design of coil 1 and coil 2 are 4.4 % and 18 % respectively. The two coils are coaxially placed and separated by a short distance. Therefore, the average flux leakage from the coaxial coils is around 11 % during the magnetic transduction. The percentage of flux leakage is almost in close agreement with the value reported by Engdahl, 2000 and is equal to 10 %. Based on this, it is evident that the Eq. (3.18) gives most efficient design with respect to dissipated resistive power in the coil. The reason is that the magnetic field is considered along the axis of coaxial coils. This efficient design gives the best possible strength of magnetic field at the center. At its center, the magnetic

field is maximum as it varies along its length, gradually reducing towards its ends (Angara, 2000 and Wang et al., 2006). Therefore the length of the coils should be slightly larger than the length of the Terfenol-D rod. The length of coaxial coils was assumed as 83 mm. With the length and inside radii of the coils fixed, the objective will be to examine the suitability of outer radii of coils.

Leakage of magnetic flux in a magnetic circuit can be accounted in the Ampere's theorem by means of compensation coefficient of the drive coil K_{coil} (Engdahl, 2000; Dehui et al., 2008) as follows,

$$N_{coil}I = K_{coil}H_{coil}l_T \qquad (3.34)$$

On comparing Eq. (3.31) and Eq. (3.32) with Eq. (3.34), the coil compensation coefficient for each coil is computed and listed in Table 3-6. Further, it is used in the verification criteria that verify the outer radii of coaxial coils.

According to the definition for current density of the coil:

$$J = \frac{N_{coil}I}{A_{coil}} = \frac{K_{coil}H_{coil}l_T}{A_{coil}} \qquad (3.35)$$

Where A_{coil} = area of coil and l_T = length of Terfenol-D rod. In practical application, the current density of coil under the different work system are as follows: for long duration of operation J has a range of 2×10^{-6} to 4×10^{-6} A/m^2; when actuator has to undergo intermittent operation J has a range of 5×10^{-6} to 12×10^{-6} A/m^2; and finally for short duration of operation the current density J is 13×10^{-6} to 30×10^{-6} A/m^2. In the present work the current density for long term operation was assumed, then requirement on the area of the coil A_{coil} is

$$\frac{K_{coil}\,H_{coil}\,l_T}{4\times10^{-6}} \le A_{coil} \le \frac{K_{coil}\,H_{coil}\,l_T}{2\times10^{-6}} \qquad (3.36)$$

Eq. (3.36) is the verification criterion for outer radii of coaxial coils based on surface area of coil. The surface area of coil 1 and coil 2 meets the constraints of the criteria given by Eq. (3.36) with respect to current density based on long term operation. This implies the high electro-magnetic conversion efficiency from coil 1 and coil 2. The high electro-magnetic conversion efficiency indicates the least power is consumed by the coaxial coils to generate the required amount of magnetic field strength. The

detailed calculation of the parameters listed in Table 3-6 is available in section I.4 of APPENDIX I.

Table 3-6. Details of coils.

Parameters	Coil 1	Coil 2
G -Factor $\,$ - $G_{coil}\left(\alpha,\beta\right)$	0.1635	0.1154
Magnetic field intensity $\left(H_{coil}\right)$	28 kA/m	21 kA/m
Coil compensation $\left(K_{coil}\right)$	0.981	1.233
Area of coil $\left(A_{coil}\right)$	7.47×10^{-4} m^2	5.81×10^{-4} m^2
Current density $\left(J\right)$	1350 kA/m^2	1060 kA/m^2
Inner and outer radii $\left(a_1 \text{ and } a_2\right)$	16.5 mm and 36.5 mm	37.5 mm and 57.5 mm
Length of coil $\left(l_{coil}\right)$	83 mm	83 mm

Another verification criterion is based on shape factor of each coil. The shape factor $\left(G_{coil}\right)$ for coil 1 is 0.1635 with $\alpha=2.2121$, $\beta=2.5151$ and for coil 2 is 0.1154 with $\alpha=1.5333$, $\beta=1.1067$. The shape factor obtained for each coil is well within the range from 0.1 to 0.179 as reported by Engdahl, 2002 for most of the coil geometries. It is concluded that the coaxial coils designed with these arrived dimensions can produce the magnetic field at their center with least dissipated power as they met the constraints of Eq. (3.36) and as well with acceptable shape factor.

3.6 ANALYTICAL MAGNETIC FLUX DENSITY OF COAXIAL COILS IN FREE AIR

The axial magnetic flux density distribution can be calculated using the analytical expression (Wang et al., 2006) along the axis of the coil. According to Biot-Savart law,

$$
\left.
\begin{aligned}
B_\rho &= \frac{\mu_0 J}{2\pi}\int_0^\pi d\theta \int_{a_1}^{a_2} d\rho' \int_{z_1}^{z_2} \frac{-\rho' z'\cos\theta}{r^3}\,dz' \\
B_\theta &= 0 \\
B_z &= \frac{\mu_0 J}{2\pi}\int_0^\pi d\theta \int_{a_1}^{a_2} d\rho' \int_{z_1}^{z_2} \frac{\rho'\left(\rho'-\rho\cos\theta\right)}{r^3}\,dz'
\end{aligned}
\right\}
\tag{3.37}
$$

Where $r = \left(\rho'^2 + \rho^2 - 2\rho'\rho\cos\theta + z'^2\right)^{\frac{1}{2}}$, $\theta = \phi' - \phi$, z_1 is the coordinate of coil bottom, z_2 is the coordinates of coil top, ρ', ϕ' *and z'* are cylindrical coordinates and μ_0 is the permeability of free space. Evaluating the integrals given in Eq. (3.37) yields an expression for magnetic flux density is a function of the *z*-axis (detailed derivation is available in section I.5 of APPENDIX I),

$$B_z = \frac{\mu_0 J}{2}\left[(z+b)\ \ln\frac{a_2 + \sqrt{a_2^2 + (z+b)^2}}{a_1 + \sqrt{a_1^2 + (z+b)^2}} + (b-z)\ \ln\frac{a_2 + \sqrt{a_2^2 + (b-z)^2}}{a_1 + \sqrt{a_1^2 + (b-z)^2}}\right] \qquad (3.38)$$

The schematic diagram of the coaxial coils is shown in Fig. 3.9. The present work involves two coils separated by short distance. Hence the magnetic flux density will be the sum that is produced from coil 1 and coil 2, accordingly Eq. (3.38) can be generalized as follows:

$$B_z = \sum_{i=1}^{2}\frac{\mu_0 J_i}{2}\left[(b-z)\ln\frac{a_{2i} + \sqrt{a_{2i}^2 + (b-z)^2}}{a_{2i-1} + \sqrt{a_{2i-1}^2 + (b-z)^2}} + (b+z)\ln\frac{a_{2i} + \sqrt{a_{2i-1}^2 + (b+z)^2}}{a_{2i} + \sqrt{a_{2i-1}^2 + (b+z)^2}}\right]$$

$$(3.39)$$
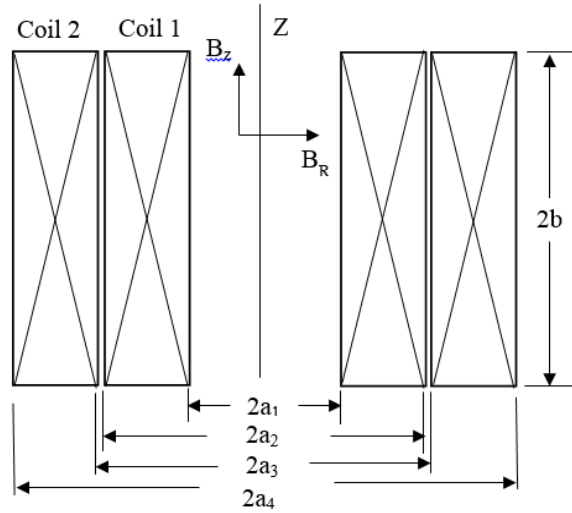
Fig. 3.9. Schematic of coaxial coils in free air.

Where μ_0 is the permeability of material in free space ($4\pi\times10^{-7}$ T-m /A), J_i is the current density of coaxial coils in A/m^2, $2\,b$ is the height of the coaxial coils, a_{2i} is the outer radii of coaxial coils, a_{2i-1} is the inner radii of coaxial coils and z is the axial

distance along the axis of coaxial coils. The cross-section and other parameters of a coaxial coils are $a_1 = 16.5$ mm, $a_2 = 36.5$ mm, $a_3 = 37.5$ mm, $a_4 = 57.5$ mm, $b = 41.5$ mm, as shown in Fig. 3.9. The axial magnetic flux density distribution has been calculated using the Eq. (3.39) along the length of the Terfenol-D rod in steps of 10 mm on either side of mid-plane. The input to the coil 1 and 2 was 4 A and the corresponding current densities are $J_1 = 1350$ kA/m^2 and $J_2 = 1060$ kA/m^2.

3.7 FUNDAMENTAL EQUATION OF FINITE ELEMENT ANALYSIS FOR LINEAR MAGNETOSTATIC FIELD

The most common methods such as reluctance method, finite difference method and finite element method are used to solve magnetic field parameters like magnetic flux density (B), magnetic field intensity (H) and magnetic flux (ϕ). Reluctance method is an approximation method. Finite element method is one approach for analyzing the magnetic field and it provides more insight into the problem when the domain is two dimensional.

3.7.1 Energy functional and its minimization

Under static magnetic fields, the energy input due to magnetic field should be equal to the magnetic energy stored in the material provided there is no power loss (Brauer, 2006).

$$W_{in} = W_{stored} \tag{3.40}$$

The energy input due to magnetic field is a function of current density $\mathbf{J}$ and is equal to $\frac{1}{2}\int \mathbf{J}.\mathbf{A}dv$. Where $\mathbf{A}$ is the magnetic vector potential and the differential volume of the material is dv. The magnetic energy stored in a ferromagnetic material is a function of B and equal to $\int \frac{B^2}{2\mu} dv$. Therefore Eq. (3.40) can be written as

$$\frac{1}{2}\int \mathbf{J}.\mathbf{A}dv = \int \frac{B^2}{2\mu} dv \tag{3.41}$$

The magnetic vector potential $\mathbf{A}$ is related to the magnetic flux density as follows

$$\mathbf{B} = \nabla \times \mathbf{A} \tag{3.42}$$

The energy functional is the difference between stored energy and input energy for linear magnetic fields.

$$F = W_{stored} - W_{input} \qquad (3.43)$$

$$F = \left[\int \frac{B^2}{2\mu} dv - \frac{1}{2} \int \mathbf{J}.\mathbf{A} dv \right] \qquad (3.44)$$

The law of energy conversation requires the functional F to be zero. In finite element method, the functional F is minimized to obtain the magnetic vector potential $\mathbf{A}$ and magnetic flux density B, i.e.

$$\frac{\partial F}{\partial \mathbf{A}} = 0 \text{ i.e. } \frac{\partial}{\partial \mathbf{A}} \left(\int \frac{B^2}{2\mu} dv - \frac{1}{2} \int \mathbf{J} dv \right) = 0 \qquad (3.45)$$

Eq. (3.45) is the basis for finite element analysis of linear magneto-static (DC magnetic) fields.

3.7.2 Discretization of volume using three node linear triangular element

Triangular finite elements are chosen to discretize the domain. Figure 3.10 shows the triangular finite element with three nodes in the $x-y$ plane and magnetic flux density B is assumed to lie in the same plane since $\mathbf{J}$ lies only in the z - direction, the unknown magnetic vector potential $\mathbf{A}$ lies only in the z - direction.
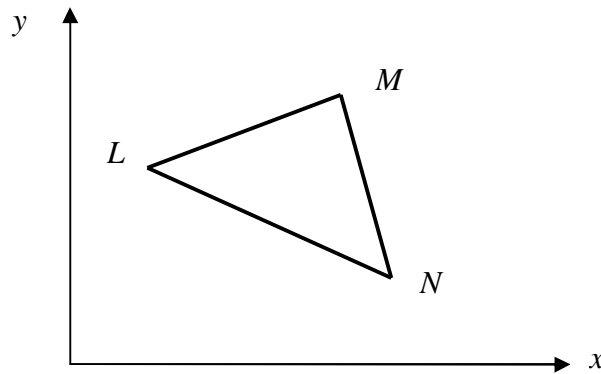
Fig. 3.10. Triangular finite element in *x-y* plane.

The magnetic vector potential is assumed to vary linearly and is expressed as

$$\mathbf{A}(x, y) = \sum_{k=L,M,N} \left[A_k \left(a_k + b_k x + c_k y \right) \right] \qquad (3.46)$$

Where A_k is the nodal magnetic vector potential and $(a_k + b_k x + c_k y)$ are the shape functions corresponding to nodes L, M, and N.

The coefficients a_k, b_k, and c_k are found from the following relation

$$\begin{pmatrix} a_L & a_M & a_N \\ b_L & b_M & b_N \\ c_L & c_M & c_N \end{pmatrix} = \begin{pmatrix} 1 & x_L & y_L \\ 1 & x_M & y_M \\ 1 & x_N & y_N \end{pmatrix}^{-1}$$
(3.47)

Substituting the curl of magnetic vector potential for the magnetic flux density given by Eq. (3.42) into the minimization of the functional given by Eq. (3.45) yields

$$\frac{\partial}{\partial \mathbf{A}_k} \left[\frac{1}{2\mu} \int \left\{ \left(\frac{\partial \mathbf{A}_y}{\partial x} \right)^2 + \left(\frac{\partial \mathbf{A}_x}{\partial y} \right)^2 \right\} dxdy - \frac{1}{2} \int \mathbf{J}.\mathbf{A} \; dxdy \right] = 0$$
(3.48)

3.7.3 Matrix equation

In the final phase, unknown vector potentials at the three nodes of a triangle will be evaluated by integrating over its volume. On minimizing Eq. (3.48) yields the finite element equation as:

$$\mathbf{K} \, \mathbf{A} = \mathbf{J}$$
(3.49)

Where, the unknown nodal vector potential is $\mathbf{A} = \begin{bmatrix} A_L \\ A_M \\ A_N \end{bmatrix}$, the stiffness matrix is

$$\mathbf{K} = \left(\frac{S}{\mu} \right) \begin{pmatrix} (b_L b_L + c_L c_L) & (b_L b_M + c_L c_M) & (b_L b_N + c_L c_N) \\ (b_M b_L + c_M c_L) & (b_M b_M + c_M c_M) & (b_M b_N + c_M c_N) \\ (b_N b_L + c_N c_L) & (b_N b_M + c_N c_M) & (b_N b_N + c_N c_N) \end{pmatrix}$$, the known nodal current

density vector is

$$\mathbf{J} = \left(\frac{S}{3} \right) \begin{bmatrix} J_L \\ J_M \\ J_N \end{bmatrix}$$ and $S = $ Area of triangular finite element.

Eq. (3.49) is a matrix representation of three equations with three unknowns, in which the domain is discretized using triangular finite elements. Similarly if n number of

elements is used for discretization, then the Eq. (3.49) is assembled for n number of triangular elements and will result in n equations with n number of unknown nodal vector potential. Further the required magnetic field strength can be extracted using magnetic vector potentials. Curl of a magnetic vector potential is known as magnetic flux density and symbolic representation is given by $B = \nabla \times A$. The magnetic field strength can be evaluated using the expression given by $B = \mu H$. The magneto-static equation given by Eq. (3.45) is solved numerically using Maxwell 2D solver. Maxwell 2D is an interactive software package for analyzing electric and magnetic fields in structures with uniform cross-sections or full rotational symmetry.

3.7.4 Axi-symmetric model of coaxial coils in free air and coils with housing of an actuator built in a Maxwell 2D solver

The axi-symmetric models of coaxial coils namely coil 1 and coil 2 alone in free air as well as with different housing materials have been built in a Maxwell 2D environment. Material for coil 1 and coil 2 is copper and for housing, mild steel, cast iron and aluminium have been assigned from the material library.

(a)   (b)
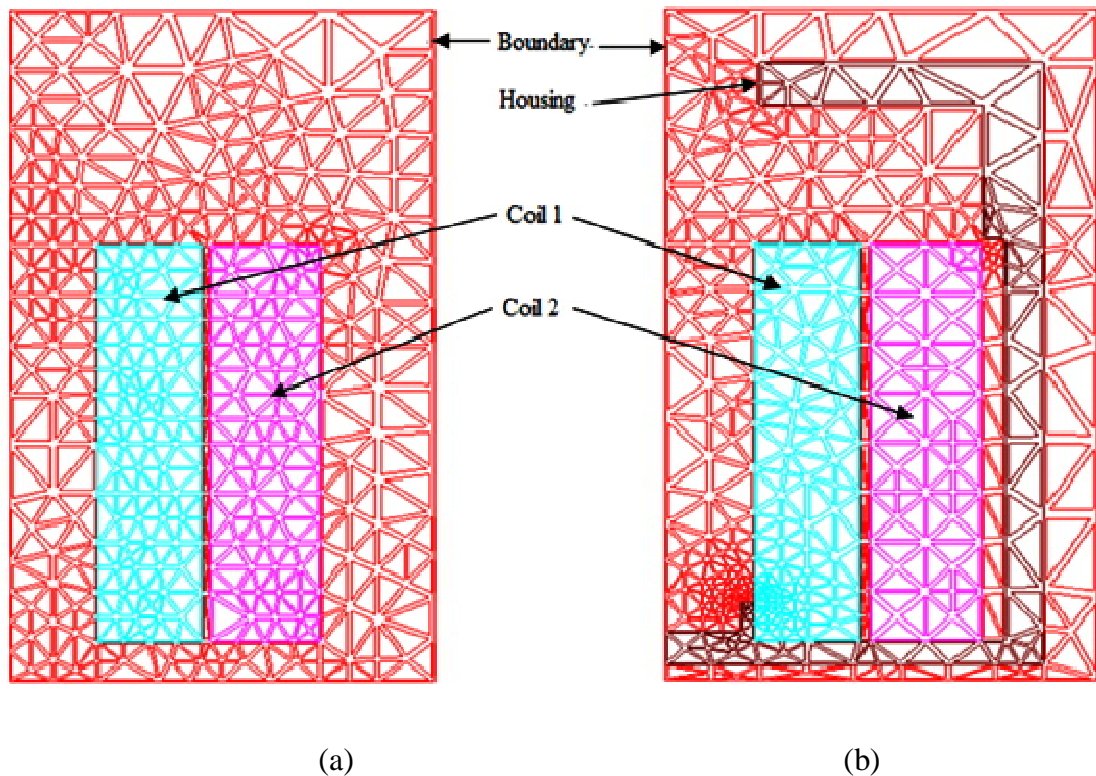
Fig. 3.11. Discretization of axi-symmetric models of (a) coaxial coils in free air and (b) coaxial coils in mild steel housing using triangular finite elements.

65

The input to the coils is the current density. Balloon is boundary for the region surrounding the coaxial coils. Balloon means the region beyond which there is no leakage of flux. The model of coaxial coils in free air and coils contains mild steel housing material is discretized with triangular finite elements using Maxwell 2D solver is shown in Fig. 3.11 (a) and (b). The axi-symmetric model of coaxial coil and as well coaxial coils with different housing materials in free air are solved independently. In convergence test, the energy error will be minimized as much as possible with respect to the target error. Here, the built-up axi-symmetric model is discretized using finite element triangles during each pass. Energy error will be calculated in each pass. Software takes care of discretizing the model in each and every pass. The mesh refinement has been carried out within the solver such that number of passes chosen was 10 with 1 % refinement. With this, number of triangular elements used was 667 and 518, energy error was 0.952 % and 9.81 %, for a converged solution of coaxial coils in free air and coaxial coils contained with mild steel housing respectively.

3.7.5 Axi-symmetric model of Terfenol-D actuator assembly built in a Maxwell 2D solver

The axi-symmetric model of Terfenol-D actuator assembly with and without Terfenol-D rod has been built in the environment of Maxwell 2D solver. The materials for coaxial coils are copper, for housing, top cover plate and end mass known as plunger are mild steel, cast iron, aluminium materials, and for Terfenol-D rod the B-H values are assigned. The boundary conditions are same as discussed in section 3.74. All these objects have been included in the solution during the phase of setup executive parameters. The model of actuator assembly contained mild steel housing with and without Terfenol-D rod are discretized with triangular finite elements using Maxwell 2D solver are shown in Fig. 3.12 (a) and (b). The adaptive mesh analysis type is selected to solve these models. The mesh refinement has been carried out within the solver such that number of passes chosen was 10 with 1 % refinement. With this, number of triangular elements used was 1595 and 2318, energy error was 0.669 % and 0.888 % for a converged solution of Terfenol-D actuator assembly in the absence and as well in the presence of Terfenol-D rod.

(a)   (b)
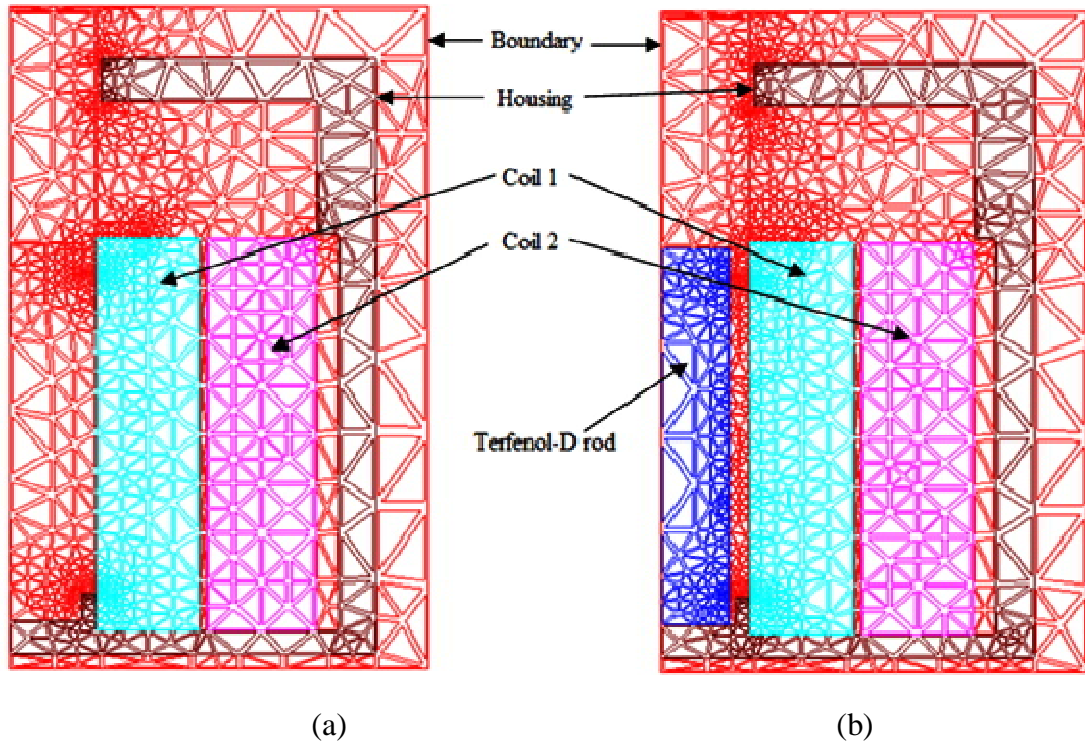
Fig. 3.12. Discretization of axi-symmetric models of an actuator (a) without and (b) with Terfenol-D rod in a mild steel housing using triangular finite elements.

3.8 MAGNETIC FORCE PRODUCED BY THE TERFENOL-D ROD BASED ON FLUX

Magnetic force exerted by a Terfenol-D actuator is one of the important parameter to be analyzed in addition to the other field associated parameters such as magnetic flux density, magnetic field intensity and flux distribution. The magnetic vector potential and magnetic flux density are calculated using the Maxwell 2D solver will be used for calculating the magnetic force exerted by Terfenol-D rod. One of the basic methods to find the magnetic force is the method of virtual work (Engdahl, 2000). Magnetic force is proportional to the square of flux density. This force tends to reduce the reluctance of the magnetic circuit of a Terfenol-D actuator. Therefore, the magnetic force is also known as reluctance force. The magnetic force exerted by a Terfenol-D rod is computed using the expression (Peng et al., 2008).

$$F_T = \frac{A_T B^2}{\mu_0} \tag{3.50}$$

Where A_T is a cross-sectional area of Terfenol-D rod equal to 6.1575×10^{-4} m^2, μ_0 is permittivity of free space equal to $4\pi \times 10^{-7}$ Henry/meter and B is a magnetic flux density produced by a magneto-elastic effect in Terfenol-D rod.

3.9 RESULTS AND DISCUSSION

The comparative analysis of analytical, numerical and experimental magnetic flux density of coaxial coils in a free air and coaxial coils with different housing materials are discussed. Analytical magnetic flux density of coaxial coils in free air is calculated using Eq. (3.39). Numerical magnetic field strength of coaxial coils in free air and as well with Terfenol-D is evaluated using Maxwell 2D solver. Magnetic flux density is measured using Lake-shore Guassmeter and the details of measurement along with setup can be referred in section I.6 from the APPENDIX I. Numerical magnetic flux density in an actuator contained with different housing materials in the absence and in presence of Terfenol-D is evaluated and compared. Further, the comparison of numerical magnetic flux distribution in an actuator contained with different housing materials in the presence of Terfenol-D is discussed.

3.9.1. Numerical magnetic flux density of co-axial coils in free air

The axial magnetic flux density for coaxially placed coils in free air has been extracted by creating points B_1, B_2 to B_9 along the axial direction of coils as shown in Fig. (3.13). The input to the coil 1 and coil 2 are current density equal to 1350 kA/m^2 and 1060 kA/m^2 respectively for a corresponding step input of 4 A. The contour of magnetic flux density and its variation in two dimension plane is illustrated in Fig. 3.13(a). The reason around the center of coaxial coil has a large flux density distribution and reduces towards either ends of the inner coil. The distribution of axial magnetic flux density is plotted along the length of coaxial coils for a step input of 4 A as shown in Fig. 3.13 (b). It is observed that the distribution is symmetric about the center of coils. Maximum magnetic flux density has been observed at the center and gradually decreases on either side from the center of coaxial coils. The magnetic flux lines do not penetrate in the air, due to which the magnetic flux density concentrates at the center of coaxial coils. This will also result in gradual reduction of flux density on either side as we move from the center of coaxial coils.
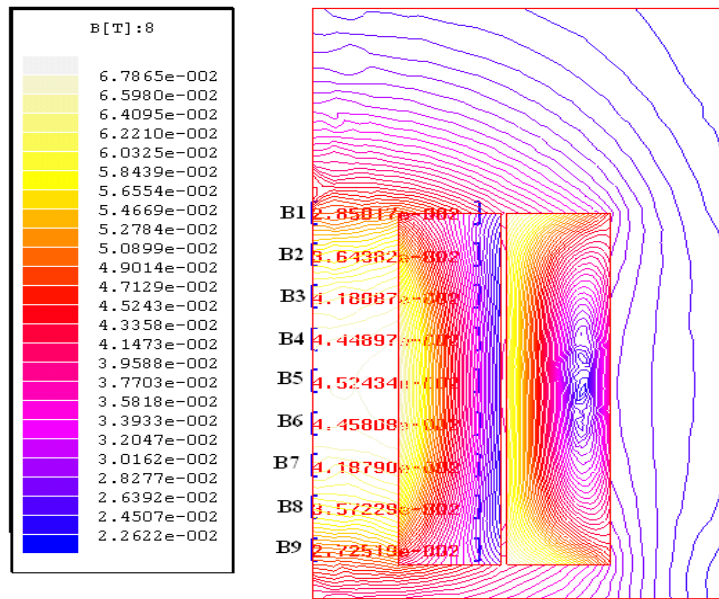
(a)
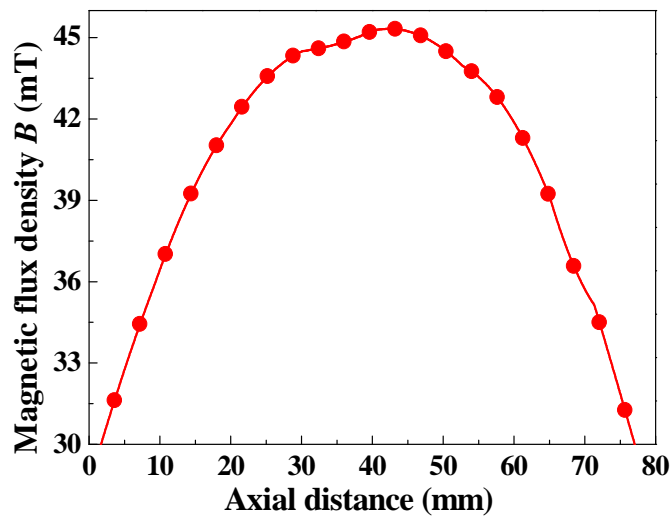
(b)

Fig. 3.13. (a) Schematic of axi-symmetric model of coaxial coils in free air showing selected points along the axial direction in a Maxwell 2D solver and (b) Numerical magnetic flux density distribution along the axis of coaxial coils in free air.

The magnetic flux density along the radial direction at each specified point B_{10}, B_{11}, B_{12} and B_{13} has been extracted from the numerical solution. The DC input was varied from 0 to 4 A with a step of 0.25 A. It has been observed that the magnitudes of magnetic flux density along the radial direction is gradually decreasing with

69

increasing distance from the center of coaxial coils as shown in Fig. 3.14 (a). This is because the magneto motive force generated by the coaxial coils goes on decreasing as the distance increases from center. Magnetic flux density is decreasing as the distance from the Terfenol-D rod increases as it is evident from Fig. 3.14 (a) for points B_{12} and B_{13}.
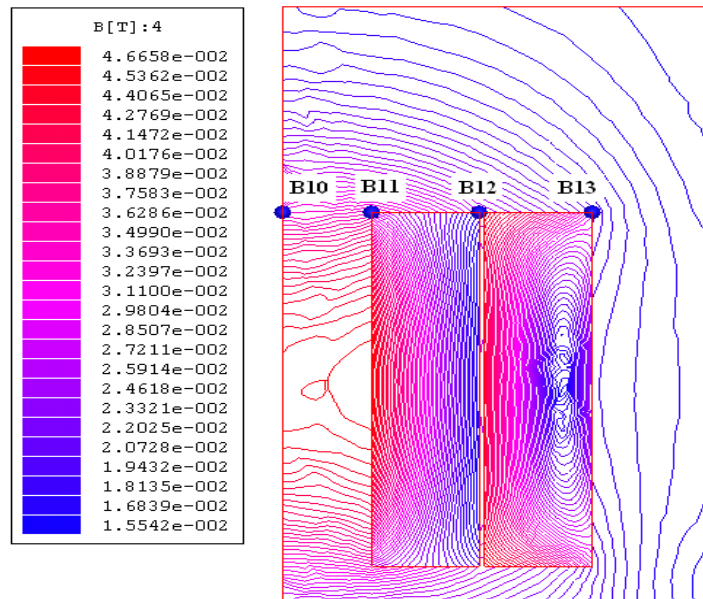
(a)
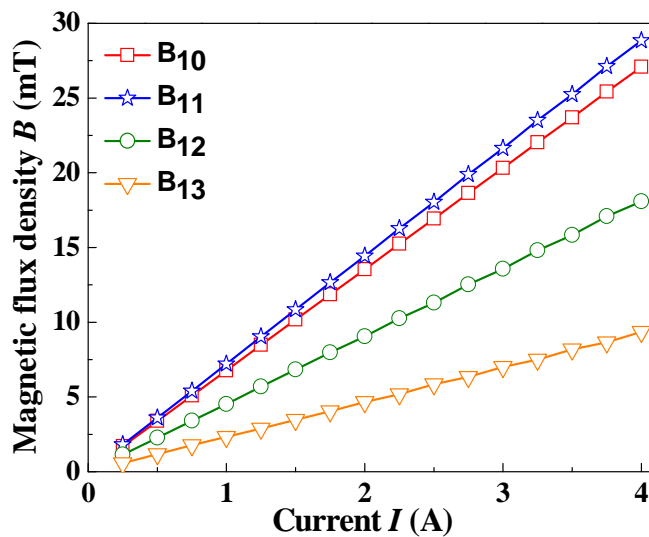
(b)

Fig. 3.14. (a) Schematic of axi-symmetric model of coaxial coils in free air showing selected points along the radial direction in a Maxwell 2D solver and (b) Numerical radial flux density distribution at radial points against the applied step input.

Fig. 3.14 (b) shows the magnetic flux density evaluated at radial points against the applied input current. The input current was varied from 0 to 4 A in an increment of 0.25 A. The magnetic flux density increases as the input current is increased at each point and shows the linear behaviour. The reason is that the applied input current is directly proportional to the induced magnetic flux density produced from the coils. The magnetic flux density obtained for B_{10} and B_{11} do not differ much for the applied input current. B_{10} is on the centre line of the coils and on a plane containing the top face of the coil. B_{11} is close to B_{10} as a result the flux density do not differ considerably for applied current. B_{12} and B_{13} are further from the center of coaxial coil and the flux densities at these locations are much less. The flux lines will not penetrate towards B_{12} and B_{13} due to lower permeability. The reason is that these two points are located at which permeability is equal to permeability of free space. Another observation is that the magnetic flux density is more at point B_{11} compared at point B_{10} for an applied input. The reason is that the magnetic flux density is decreasing due to presence of air in between the points B_{10} and B_{11}.

3.9.2. Comparison of numerical magnetic field intensity of co-axial coils with and without Terfenol-D in free air

Magnetic flux intensity of coaxial coils in the presence and absence of different diameters of a Terfenol-D in free air is evaluated using Maxwell 2D solver. The numerical exercise is taken up primarily to understand how the magnetic field intensity changes along the axis of coaxial coils due to the presence of Terfenol-D rod. Three sizes of Terfenol-D rod with 80 mm length and diameters of 12.5, 13 and 13.5 mm are chosen. The size of Terfenol-D rod of 13 mm is based on the maximum braking force required (refer CHAPTER 6). The inner diameter of coil 1 is close to the diameter of drive rod in each case and inner diameter of coil 2 is close to outer diameter of coil 1 has been assumed. The outer diameter of coil 2 is fixed as 115 mm. With these dimensions, the axi-symmetric model of coaxial coils in the absence and presence of Terfenol-D has been analyzed using Maxwell 2D solver. The dimensions for each coil along with the average magnetic field produced by them are listed in Table 3-7. From the Table 3-7, it is observed that the magnetic field strength produced by the coils at the center reduces from 45.3 kA/m to 42.9 kA/m in the presence of

Terfenol-D rod. Further, it increases to 44.5 kA/m at the center in the presence of Terfenol-D rod. Therefore, the optimum value of magnetic field is 42.9 kA/m produced by the Terfenol-D rod of size equal to 13 mm.

Table 3-7 Geometric data for numerical exercise on evaluation of magnetic field intensity.

S. No.	Diameter of Terfenol-D rod (mm)	Coil 1		Coil 2		Magnetic field (kA/m)	
		ID (mm)	OD (mm)	ID (mm)	OD (mm)	Without Terfenol-D	With Terfenol-D
1	12.5	14	73	75	115	52.6	45.3
2	13	14.5	73	75	115	50.4	42.9
3	13.5	15	73	75	115	50.2	44.5

With this, the comparison of magnetic field strength distribution along the coaxial coils and coils carrying Terfenol-D is plotted to draw conclusion. Fig. 3.15, 3.16 and 3.17 shows the comparison of magnetic field with the coaxial coils in free air and coaxial coils with Terfenol-D assembly for a step input of 4 A respectively. The input to the coaxial coils is a current density. The current density for coil 1 is equal to 2200 kA/m^2 and that for coil 2 is 1975 kA/m^2.
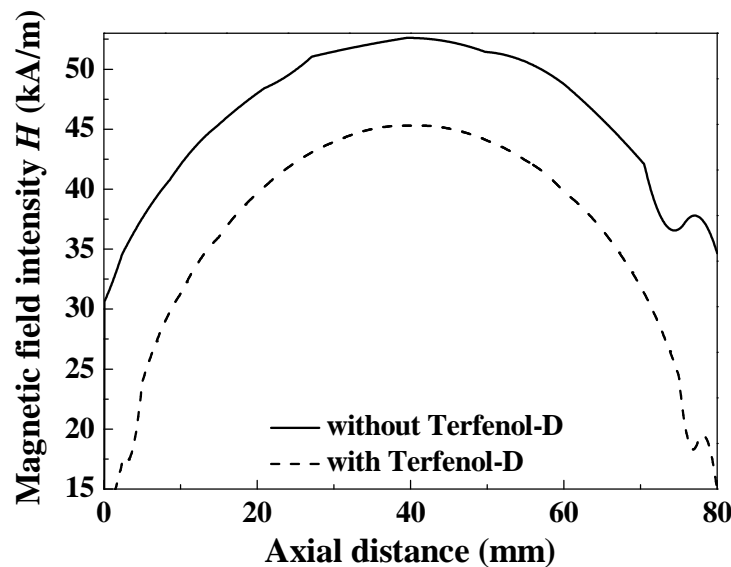
Fig. 3.15. Magnetic field intensity along the axial direction of coaxial coils carrying 12.5 mm Terfenol-D rod.

72

In each case, it has been observed that the field intensity with Terfenol-D is slightly less than the field intensity without the Terfenol-D rod. The field intensity with Terfenol-D rod decreases by 16 %, 17 % and 13 % for 12.5 mm, 13 mm and 13.5 mm compared to field intensity at the center of coaxial coils alone. The magnetic field intensity at the end of the coaxial coils in the absence of the Terfenol-D rod is approximately 1/2 of the value achieved at the center of coils in each case. Similarly, for each case in the presence of Terfenol-D rod, the magnetic field intensity at the end of the rod falls approximately 1/3 of the value obtained at the center of coils.
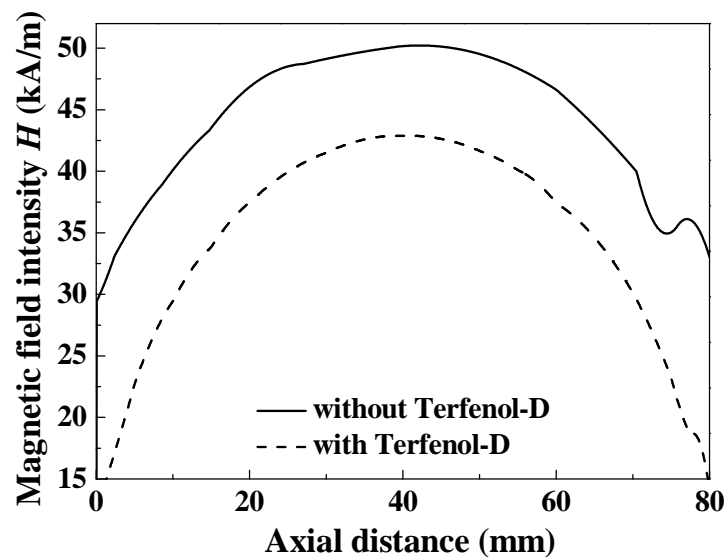
Fig. 3.16. Magnetic field intensity along the axial direction of coaxial coils carrying 13 mm Terfenol-D rod.

Saturated internal kink mode has been observed in the axial magnetic field strength distribution of coaxial coils in free air. This mode often causes rotation flattening in the core material of coil. Also, it humiliates or loss of magnitude in field strength and stored magnetic energy in the coil (Chakrabarti, 2011). Magnetic field strength distribution in the absence of Terfenol-D is more in all the cases. This is due to the sufficient energy available to setup the magnetic flux in the hollow cross-section coaxial coils that have air gap. The magnetic field distribution in the assembly of coaxial coils and Terfenol-D is less in all the three cases. The reason may be due to energy required to produce magnetic flux in the presence of Terfenol-D is very much small that decreased the magnetic field strength.
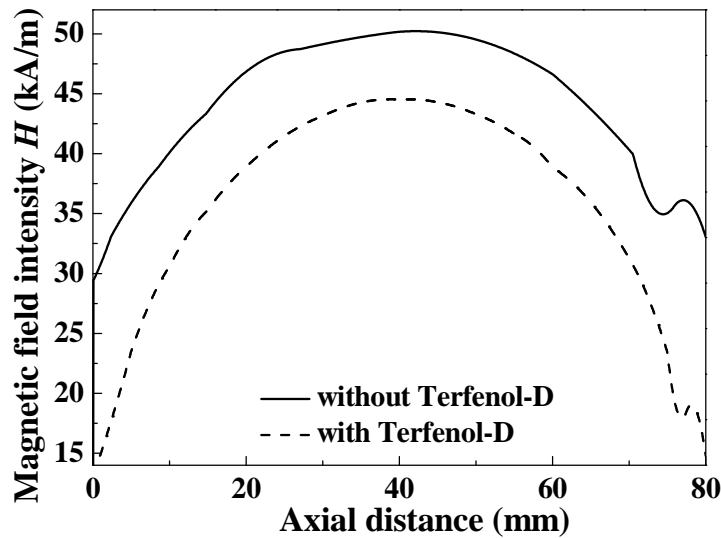
Fig. 3.17. Magnetic field intensity along the axial direction of coaxial coils carrying 13.5 mm Terfenol-D rod.

With this it is concluded that the suitable size of Terfenol-D having dimensions equal to 13 mm diameter and 80 mm length is preferable to be carried by the coaxial coils. There was a major constraint in fixing the required size of Terfenol-D as per the requirement. Therefore, the size of Terfenol-D having diameter 28 mm and 80 mm length is chosen in the present work. Based on size of drive rod, the coils dimensions such as length, inner and outer radii are assumed. The length of coaxial coils based on Fabry factor and current density for long term operation should have been two times the inner diameter of coils i.e. 66 mm. However, the length of Terfenol-D rod is 80 mm and length of each coil is fixed as 83 mm. The length of the coil is 3 mm more compared to the Terfenol-D rod in order to obtain uniform magnetization along the Terfenol-D rod.

Fig. 3.18 shows the comparison of magnetic field intensity of coaxial coils alone in free air as well as coils with Terfenol-D rod along the axial direction at 4 A input for a Terfenol-D rod of diameter 28 mm. The input to the coaxial coils is a current density i.e. for coil 1 and coil 2 is equal to 1350 kA/m^2 and 1060 kA/m^2. It has been observed that the field intensity with Terfenol-D is slightly less than the field intensity without the Terfenol-D rod. Kinks were observed in the magnetic field strength distribution of a coaxial coils carrying Terfenol-D. Due to small negative anisotropy constant (60

74

kJ/m3) of Terfenol-D material results energy minima along the eight <111> directions. Without the preferential alignment of moments along the <111> axes, it would be much more difficult to arrange the reorientation of magnetic moments along the directions perpendicular to the applied field (Chakrabarti, 2011).
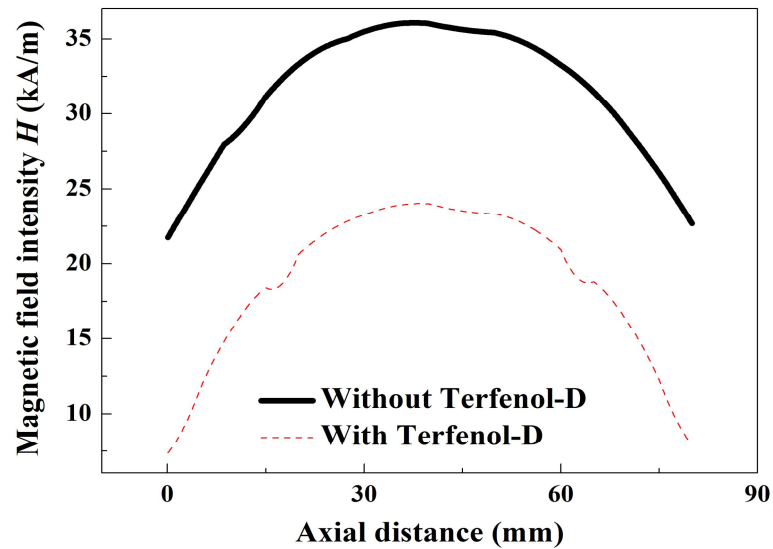
Fig. 3.18. Magnetic field intensity along the axial direction of coaxial coils carrying 28 mm Terfenol-D rod.

When no compressive stress is applied, all the <111> orientations have equal energy and jumps occur at very low input currents. Domains should stick on to a particular set of orientations until additional input current is applied to overcome the magnetoelastic energy. This domain attachment may be the reason to cause kinks in the distribution of axial magnetic flux density (Chakrabarti, 2011). Maximum magnetic field intensity of coaxial coils alone in free air is 36 kA/m and reduced to 24 kA/m at 4 A DC input for a coaxial coils with Terfenol-D rod assembly at the center along the axial direction. The field intensity with Terfenol-D rod is reduced by 50 % for 28 mm compared to field intensity at the center of coaxial coils alone. The magnetic field intensity at the end of the coaxial coils in the absence of the Terfenol-D rod is approximately 1/2 of the value achieved at the center of coils. Similarly, in the presence of Terfenol-D rod, the magnetic field intensity at the end of the rod falls approximately 1/3 of the value obtained at the center of coils. Axi-symmetric models

with their discretization and tables of converged solution for the all the three sizes of Terfenol-D rod are illustrated in APPENDIX-I of section I.7.

3.9.3. Comparison of analytical, numerical and experimental axial magnetic flux density distribution of coaxial coils in free air

Fig. 3.19 shows the comparison of experimental, analytical and numerical values of magnetic flux density distribution in coaxial coils in free air for an applied step input. It has been observed that the analytical and numerical axial flux density values are in close agreement with each other and are symmetric about the center line of coaxial coils. But, the experimental flux density was skewed about the center line of coaxial coils compared to numerical and analytical results. The reason is that the coaxial center is located arbitrarily and also the probe may be not moved along the axial direction of coaxial coils due which the experimental flux density may be skewed compared to the analytical and numerical results. However, this may be eliminated by taking proper care and proper calibration of the instrument. Mean sum of squares of error between analytical and experimental results is 1.08 and 1.09 between the numerical and experimental results over all test points.
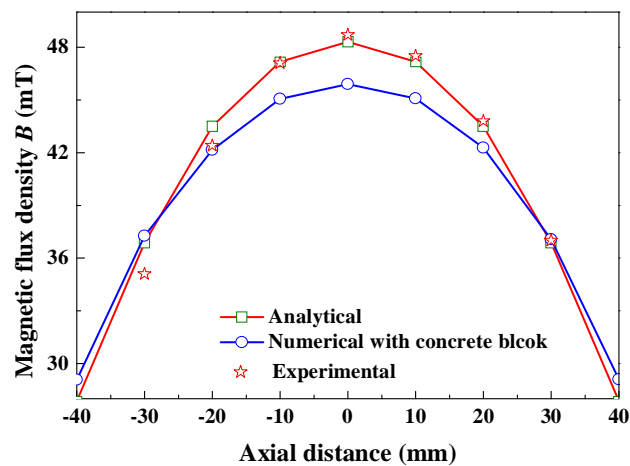
Fig. 3.19. Comparison of axial magnetic flux density of coaxial coils in free air.

Fig. 3.20 shows the comparison of the experimental flux density measured in the absence and presence of Terfenol-D within the coaxial coils in free air. Magnetic flux density is measured at a point contained by the intersection of the axis of the coaxial coil and the plane having its normal as the axis of the coil. This point is just above the

top face of coaxial coil approximately 2 to 5 mm. DC input is supplied between 0 to 4 A in an increment of 0.25 A. It is observed that the magnetic flux density increases as the applied input increases to the coils in free air. The magnetic flux density increasing linearly in the absence of Terfenol-D rod shows non-linear behaviour in the presence of Terfenol-D rod. This may be due to the presence of air gap between coils and Terfenol-D which results in disturbance for the continuous and uniform flow of magnetic flux from the coils and Terfenol-D. Magnitude of the flux density is large when the Terfenol-D rod is placed within the coil. It is also observed that the magnetic flux distribution is stronger by 167 % when the coaxial coils are contained with Terfenol-D.
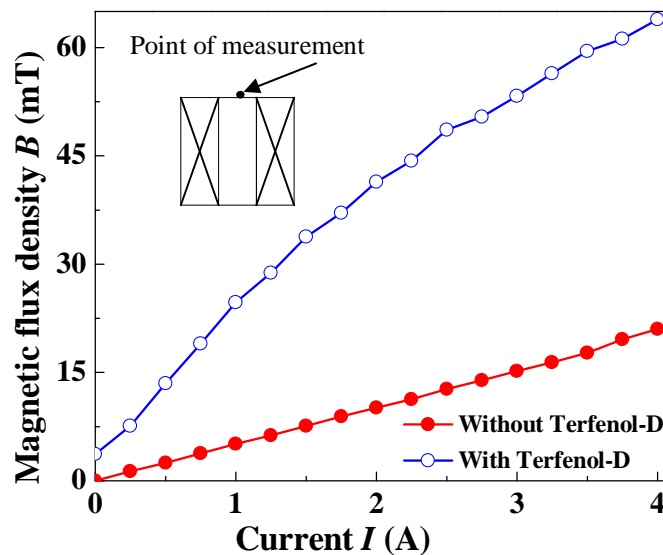
Fig. 3.20. Comparison of experimental magnetic flux density in coaxial coils with and without Terfenol-D.

3.9.4. Comparison of numerical and experimental axial magnetic flux density distribution of coaxial coils with different housing materials

Fig. 3.21 shows the comparison of experimental and numerical axial magnetic flux density distribution along the length of coaxial coils placed in different housing materials. It is observed that the axial flux density values are in close agreement with each other and small deviations are observed due to varying experimental conditions. The magnitude of axial magnetic flux density has been observed 32.3 mT in mild

steel housing with coils compared to cast iron and aluminium housing with 31.1 mT and 26.9 mT respectively. Mean sum of squares of error are 1.8, 3.6 and 0.4 between the numerical and experimental magnetic flux density of a coaxial coils contained with mild steel, cast iron and aluminium housing respectively.
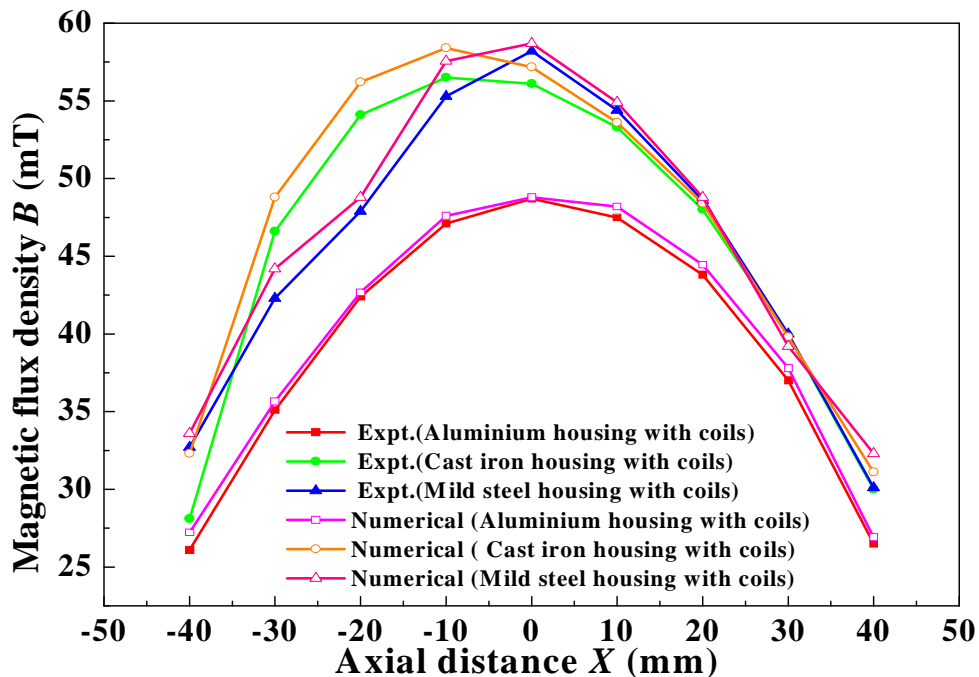
Fig. 3.21. Axial magnetic flux density of coaxial coils in free air contained with different housing materials.

3.9.5. Numerical axial and radial magnetic flux density distribution in a Terfenol-D actuator

Fig. 3.22 (a), (b) and Fig. 3.23 (a), (b) shows the comparison of axial and radial magnetic flux density distribution with and without Terfenol-D in an actuator with mild steel and cast iron housing. The current density input to the coil 1 and coil 2 are 1350 and 1060 kA/m^2 for 4 A respectively. It is observed that the magnetic flux density increases from either ends and remains uniform inside within the coil with Terfenol-D rod and without Terfenol-D. The radial magnetic flux distribution has discontinuities due to the presence of various materials. The radial magnetic flux density is uniform in air and in presence of Terfenol-D over the radial length of 20 mm and 16 mm respectively as observed in all housing materials. Beyond this, in the absence of Terfenol-D rod, the radial flux density decreases linearly due to the

78

presence of coil. When the Terfenol-D rod is present in the actuator, the radial flux density immediately falls sharply and decreases linearly due to presence of coils, bobbin material and wall of the housing as shown in Fig. 3.22, 3.23 and 3.24 (a) and (b).

(a)   (b)
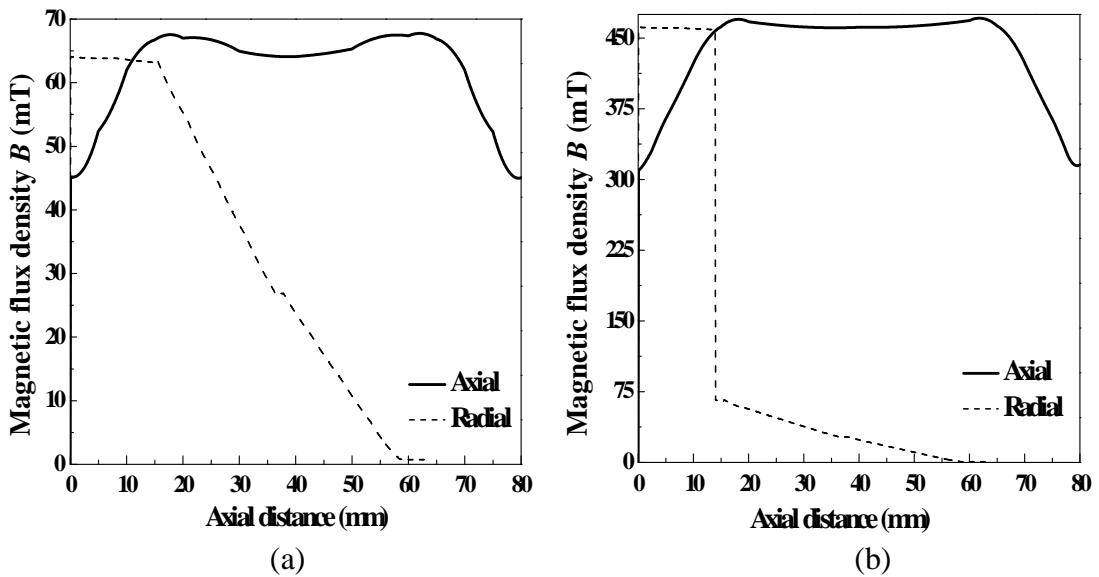
Fig. 3.22. Axial and radial magnetic flux density distribution in an actuator assembly in a mild steel housing (a) without Terfenol-D (b) with Terfenol-D.

(a)   (b)
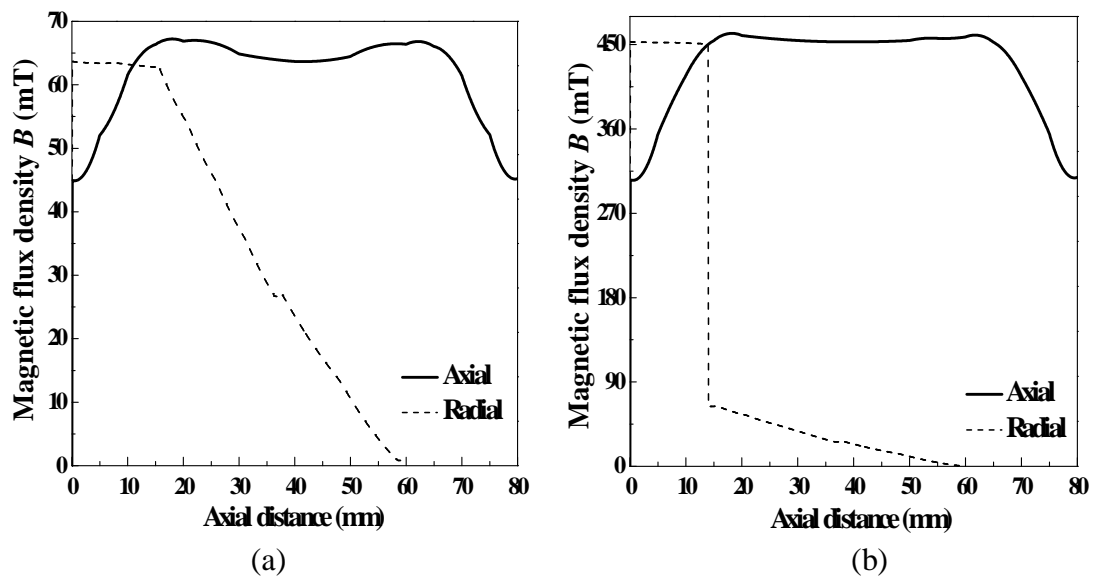
Fig. 3.23. Axial and radial magnetic flux density distribution in an actuator assembly in cast iron housing (a) without Terfenol-D (b) with Terfenol-D.
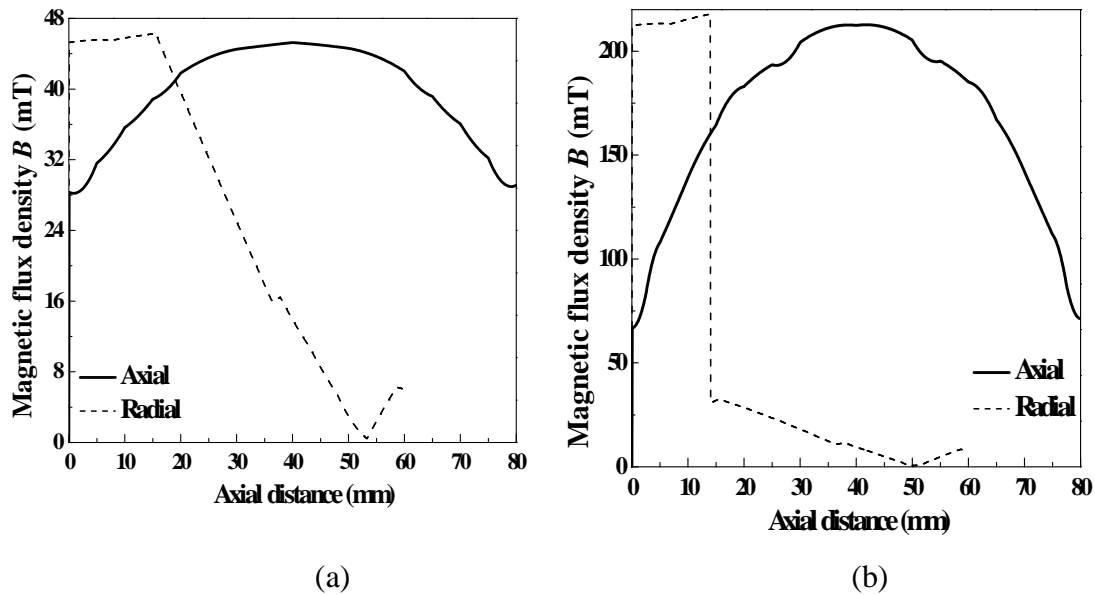
Fig. 3.24. Axial and radial magnetic flux density distribution in an actuator assembly
in aluminium housing (a) without Terfenol-D (b) with Terfenol-D.

Fig. 3.24 (a) and (b) shows the comparison of axial and radial magnetic flux density distribution with and without Terfenol-D in an actuator with aluminium housing. It is observed that the magnitude of axial magnetic flux density is more at the center of coils with and without Terfenol-D. The radial distribution of magnetic flux density is almost same compared to both mild steel and cast iron housing. The profile of axial magnetic flux density distribution is uniformly distributed along the axial direction. This may be because of relative permeability of aluminium material which is almost equal to relative permeability of free space. The distribution of flux density is uniform along the axial direction. However, the magnitude of flux density is more at both ends of a Terfenol-D. The magnetic flux lines penetrate more in to the plunger and seater, due to which the magnetic flux density is more at the ends compared to in between them. This may be the reason for having two bumps at the ends of a Terfenol-D rod (Ekreem, 2009). Magnetic permeability of these parts are higher compared to Terfenol-D rod, due to which magnetic flux density observed is little bit smaller in the portion of the length exposed directly to magnetic field. The maximum magnetic flux density is observed at the center and gradually decreasing on its either side, when actuator contained aluminium housing. The reason is that the magnetic flux by-pass both ends of a Terfenol-D covered with plunger and seater that are made up of

80

aluminium. This may be due to lower permeability of aluminium (equal to permeability of free space) compared to Terfenol-D. Other reason may due to flux leakage in the coaxial coils. Uniform magnetic field distribution in an actuator contained with mild steel compared to cast iron and aluminium housing has been achieved. This may be due to two reasons. One of the reason is that the aspect ratio of Terfenol-D rod chosen in an actuator. Aspect ratio of Terfenol-D used in the present work is more than the desired value and it is equal to 2.86. Aspect ratio of the working specimen should be at least equal to 2 as reported by Dapino, 2000. Placing of Terfenol-D between plunger and seater not only provides mechanical load, but homogenize the magnetic flux entering the Terfenol-D. This may be the other reason due to which the uniformity is achieved in the distribution of magnetic field.

3.9.6. Comparison of numerical magnetic flux distribution in a Terfenol-D actuator contained with different housing materials

Fig. 3.25, 3.26 and 3.27 (a), (b) shows the distribution of flux in an assembly of actuator having mild steel, cast iron and aluminium housing with and without Terfenol-D rod. It is observed that the intensity of flux lines are more and magnitude of flux is also high in a mild steel housing compared to cast iron and aluminium housing. This is due to high relative permeability of mild steel $\left(\mu_r = 2000 \right)$ compared to cast iron $\left(\mu_r = 600 \right)$ and aluminium $\left(\mu_r = 1 \right)$. According to Lenz's law, the rate of flux transfer from the housing material will be effectively transferred whenever the relative permeability of housing material is more compared to Terfenol-D rod. It is observed that the intensity of flux lines are more and magnitude of flux is also high in an actuator having mild steel housing compared to other cast iron and aluminium housing with Terfenol-D rod. Maximum flux of 4.556×10^{-5} Wb/m^2 and 8.517×10^{-5} Wb/m^2 is observed in a mild steel housing without and with Terfenol-D rod respectively with an input supply of 4 A. Moreover the magnetic conductivity of the mild steel housing material is high compared to the Terfenol-D as it is equal to $\mu_T = 4$ to 12. The magnetic permeability of a Terfenol-D rod equal to 7 is used in the present study.
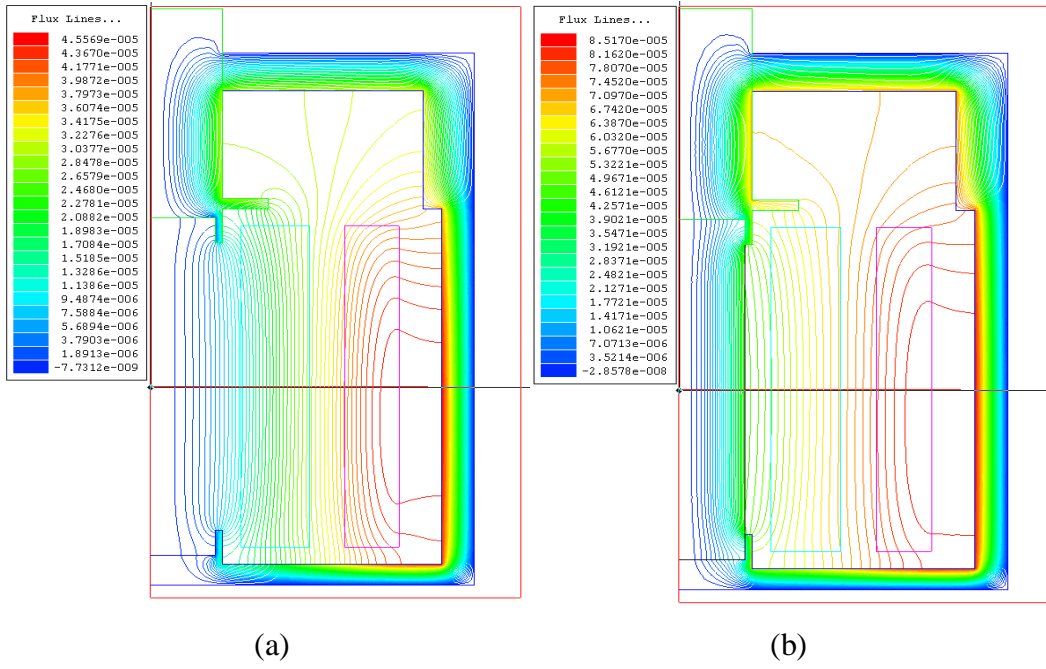
Fig. 3.25. Flux distribution in actuator assembly (a) without Terfenol-D and (b) with Terfenol-D rod in a mild steel housing.
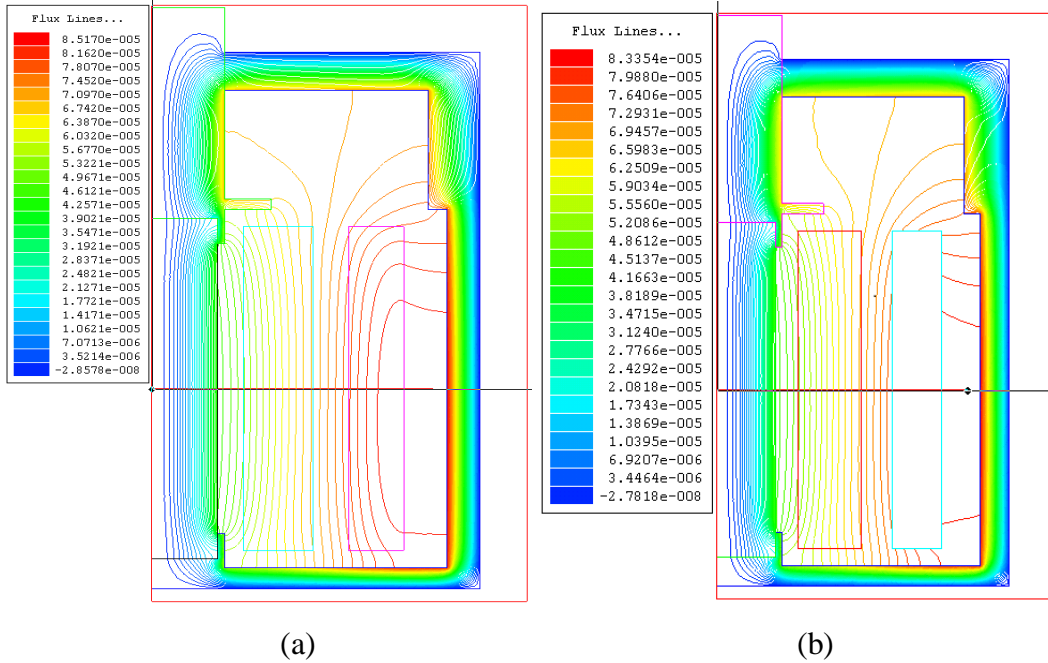
Fig. 3.26. Flux distribution in actuator assembly (a) without Terfenol-D and (b) with Terfenol-D rod in cast iron housing.

<div align="center">(a)   (b)</div>
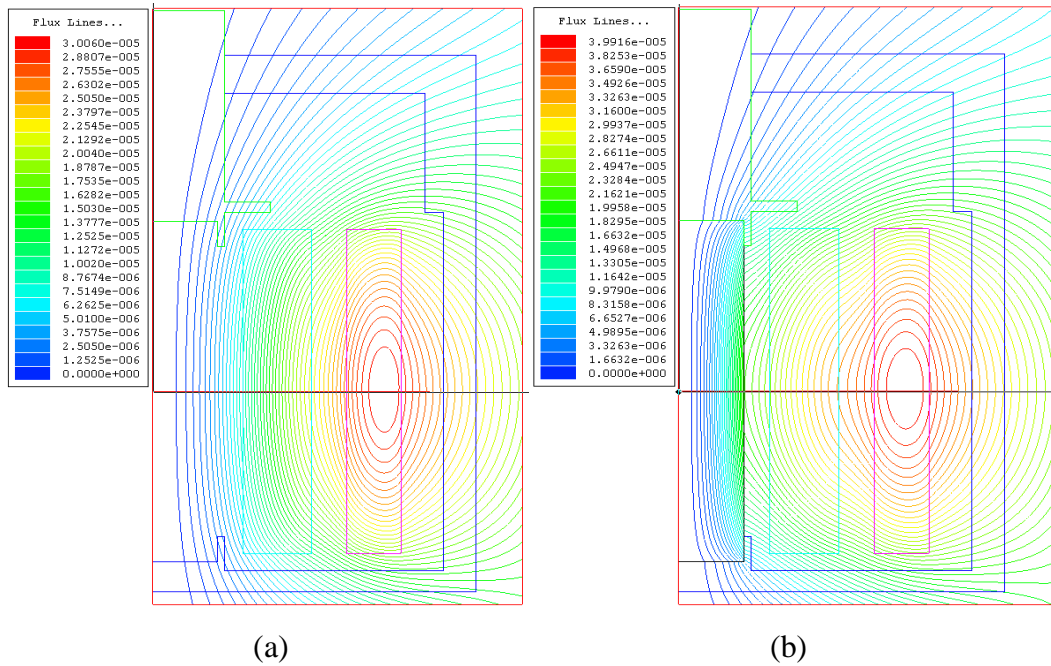
Fig. 3.27. Flux distribution in actuator assembly (a) without Terfenol-D and (b) with Terfenol-D rod in aluminium housing.

Table 3-8 shows the percentage of variation in flux for an actuator assembly with different housing materials. Magnetic flux is increased, when the actuator and their components are mild steel. The reason is that the flux will always by pass the air gap as it is easier to travel along the Terfenol-D whose permeability is higher than air (Ekreem, 2009). Similar kind of observation is found when the actuator contained with cast iron housing and allied components of it.

Table 3-8. Percentage of flux in an actuator assembly with different housing materials.

Housing material	Flux without Terfenol-D (T)	Flux with Terfenol-D (T)	Flux variation (%)	
			Increase	Decrease
Mild steel	4.5778×10^{-5}	1.1123×10^{-4}	58.8	-----
Cast iron	4.5059×10^{-5}	1.09×10^{-4}	58.6	-----
Aluminium	2.7312×10^{-5}	4.62×10^{-5}	-----	40.8

However, the magnetic flux is more and increases by 58.8 % in an actuator contained with mild steel housing compared to cast iron as it is equal to 58.6 %. This is due to higher magnetic permeability of mild steel $\left(\mu_r = 2000 \right)$ compared cast

iron $\left(\mu_r = 900\right)$. When actuator contained aluminium housing along with other associated components, the magnetic flux lines are passing away from the Terfenol-D. Magnetic flux lines are unable to penetrate through the Terfenol-D rod. This is due to the less magnetic permeability of aluminium $\left(\mu_r = 1\right)$ as compared to Terfenol-D as it lies between 2 to 10. It is summarized that the magnetic flux distribution in a Terfenol-D actuator assembly with mild steel housing becomes stronger by 2 % and 58 % compared to cast iron and aluminium housing.

3.9.7. Comparison of numerical and experimental force exerted by a Terfenol-D actuator contained with different housing materials

Magnetic force (reluctance force) exerted by a Terfenol-D rod is evaluated using Eq. (3.50) from the numerical and experimental results of magnetic flux density. Fig. 3.28 shows the comparison of numerical and experimental force exerted by a Terfenol-D actuator contained with different housing materials. It is observed that the exerted force is increasing linearly in an actuator assembly contained with all housing materials at an applied DC input on verifying both numerical and experimental results.
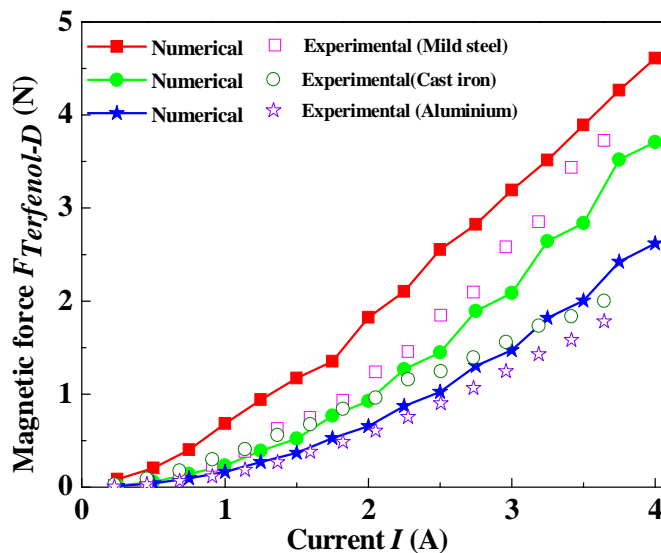
Fig. 3.28. Comparison of force produced by Terfenol-D contained with different housing materials.

Maximum force of 4.6 N with numerical and 3.7 N with experimental is achieved at an applied DC input of 4 A in an actuator assembly containing mild steel housing compared to other housing materials. Mean sum of squares of errors are 0.6, 0.58 and 0.2 between numerical and experimental magnetic force in an actuator assembly contained with mild steel, cast iron and aluminium housing respectively. The effective rate of flux distribution is more and uniform along the length of Terfenol-D rod due to higher permeability, when surrounded by mild steel housing compared to cast iron and aluminium housing.

3.10 SUMMARY

In this chapter, the magnetic circuit design and magnetic field analysis of a Terfenol-D actuator has been discussed. Suitable number of turns required for the coaxial coils has been computed using Ampere's law and the same was verified by adopting reluctance approach. The design of Terfenol-D actuator has been discussed elaborately by considering different electrical design parameters such as flux leakage, Q_{coil} value, magnetic coupling coefficient and inductance of each coil apart from magnetic design. Based on shape factor, the verification of coil geometry has been carried out using the analytical approach to achieve axial magnetic field at the center of coaxial coils with minimum power loss. Analytical, numerical and experimental approach for evaluating the magnetic field parameters such as magnetic field strength, magnetic flux density and magnetic flux was outlined.

Based on the exercises carried out in the design and magnetic field analysis of a Terfenol-D actuator and its associated components, the following observations have been made,

1. Number of turns obtained for coil 1 and coil 2 are 560 and 440 to produce 28 kA/m of biasing magnetic field and 22 kA/m of peak magnetic field respectively using Ampere's law which is in close agreement to 567 and 454 turns that are obtained using reluctance approach.

2. Based on shape factor, the verification process carried out for coaxial geometry in free air reveals that the coil 1 and coil 2 can produce a maximum magnetic field of 28 kA/m and 21 kA/m with least dissipated power.

3. From the axial distribution of coaxial coils alone, it is confirmed that the magnetic flux density was maximum at the center and gradually decreases on either side from the center of coaxial coils. Magnetic flux density along the radial direction gradually decreases when moving away from the center of coaxial coils.

4. From the axial distribution in a Terfenol-D actuator, it is observed that the magnetic flux density increases from either ends and remains uniform inside within the coil with Terfenol-D rod and without Terfenol-D. The radial magnetic flux density was uniform in air as well as in presence of Terfenol-D. It fell sharply and decreased linearly due to the presence of coils, bobbin material and wall of the housing.

5. From the magnetic flux distribution in an actuator assembly contained with different housing materials, it is confirmed that the flux distribution is stronger by 58.8% with mild steel, 58.6% with cast iron and weaker by 40.8 % with aluminium when the actuator is contained with Terfenol-D.

6. Comparison of analytical and numerical axial flux density values are in close agreement with each other and are symmetric about the center of coaxial coils. But, the experimental flux density was skewed about the center line of coaxial coils compared to numerical and analytical results due to reasons such as arbitrary selection of center and non-proper movement of probe along the axial direction. Comparison of numerical flux density for coaxial coils in the presence and absence of Terfenol-D rod reveals that the flux density distribution becomes stronger by 167 % when the coaxial coils are contained with Terfenol-D.

7. Maximum magnetic force of 4.6 N with numerical and 3.7 N with experimental has been achieved at an applied DC input of 4 A, in an actuator assembly containing mild steel housing.

8. It is summarized that the magnetic field distribution on Terfenol-D is influenced due to magnetic permeability of housing material. Therefore, a suitable housing material like mild steel is preferable for the effective magnetic field distribution and to improve the performance of actuator.

CHAPTER 4

DISPLACEMENT OUTPUT OF A TERFENOL-D ACTUATOR USING MAGNETOSTRICTION MODELS

4.1 INTRODUCTION

Analytical models for evaluating magnetostriction of a Terfenol-D actuator comprise three parts. In the first part, the required magnetic field strength is formulated by considering the induction of a coaxial coil. Secondly, the magnetization state of a Terfenol-D rod caused by magnetic field is determined using Jiles-Atherton magnetization model. Existing non-constitutive magnetostriction model is examined for suitability by considering the quality factor. The magnetostriction curves obtained using proposed models are compared with the existing magnetostriction models in this chapter.

4.2 MAGNETIC FIELD STRENGTH FROM THE DRIVING COILS OF A TERFENOL-D ACTUATOR

The magnetic flux density is related to the magnetic field intensity as:

$$B = \mu^{\sigma} H \tag{4.1}$$

Where B is a magnetic flux density on Terfenol-D rod in Tesla, μ^{σ} is the relative magnetic permeability at a constant stress and H is a magnetic field intensity on Terfenol-D rod for an applied input to a coil in kA/m. Further, the inductance of driving coils is considered for computing the distribution of magnetic field intensity on Terfenol-D rod. The concept of inductance originates from Faraday's law. According to this, it characterizes the relationship between the counter emf induced to the current supplied to the coil. Different factors like number of turns, core material, length and area of coils will dictate the inductance that affects the magnetic flux distribution over the length of Terfenol-D rod. The coaxial coils surrounding the Terfenol-D rod produce a magnetic field due to flow of current. The magnetic force

lines encircle in the form of concentric circles around the Terfenol-D rod. When the field strength increases or decreases, the magnetic force lines expands outwards from the center or contracts inwards toward the center of the Terfenol-D rod. This expansion and contraction of the magnetic field as current varies causes an emf of self-inductance which opposes any further changes in current. The coaxial coils powered with direct current input which is normally constant except when the power is turned on and off to start and stop the current flow. Hence the generation of emf of self-inductance or simply termed as inductance affects the coaxial coils during the supply or removal of direct current input. Therefore, the inductance of driving coils is considered in the formulation of magnetic field strength of a Terfenol-D actuator.

The magnetic flux density on Terfenol-D rod in terms of inductance can be expressed as:

$$B = L_{coil}. I / N_{coil} A_T \tag{4.2}$$

In general L_{coil} is the inductance of driving coil, I is the input to coil, N_{coil} is number of turns in a coil and A_T is cross-sectional area of the Terfenol-D rod.

Substituting the magnetic flux density of Eq. (4.2) into Eq. (4.1), the magnetic field strength is given by:

$$H = \frac{L_{coil}. I}{N_{coil} A_T \mu^{\sigma}} \tag{4.3}$$

When the actuator coil is excited with DC step input, the current rises exponentially (Brauer, 2006) and is given by,

$$I = I_{dc}[1 - e^{-t/\tau}] \tag{4.4}$$

On substituting Eq. (4.4) into Eq. (4.3), the magnetic field strength from the actuator coil for step DC input is given by,

$$H = \frac{L_{coil} I_{dc}\left[1 - e^{-\frac{t}{\tau}}\right]}{N_{coil} A_T \mu^{\sigma}} \tag{4.5}$$

Where steady state current to a coil is I_{dc}, t is time and $\tau = L_{coil}/R_{coil}$ has the units of time, L_{coil} and R_{coil} are the inductance and resistance of the coil.

However, when there are two coils either connected in series or separated by short distance with different magnitudes of current input, then the total inductance of each coil will differ. Inductance in such a case is due to the contribution of self-inductance (L_s) and mutual inductance (L_m). The induced emf in a coil due to current flowing in a same coil is self-inductance. Emf induced in a coil due to current flowing in nearby coil is known as mutual inductance. Therefore the total inductance (L_{coil}) of a coil is,

$$L_{coil} = L_s + L_m$$

The self-inductance of a coil (Engdahl, 2002) is given by:

$$L_s = \mu_0 \frac{\pi^2}{6} G_{coil}^2 N_{coil}^2 a_1 (\alpha + 1)(\alpha + 3) \tag{4.6}$$

Where G_{coil} depends on shape and cross-section of coil 1 or coil 2 equal to

$\frac{1}{5} \left[\frac{2\pi\beta}{\alpha^2 - 1} \right]^{1/2} \ell n \left[\frac{\alpha + \sqrt{\alpha^2 + \beta^2}}{1 + \sqrt{1 + \beta^2}} \right]$. Where $\alpha = \frac{a_2}{a_1}$ and $\beta = \frac{l_{coil}}{2a_1}$, a_1 and a_2 is the inner

and outer radii of coil, μ_o is permeability of a material in free space, N is number of turns of coil 1 or coil 2, a_1 is the inner radius of coil 1 or coil 2 and α is the ratio of outer radius to inner radius of coil 1 or coil 2.

Similarly the mutual inductance can be expressed as (Young et al., 2007):

$$L_m = \frac{\mu_o N_{coil1} N_{coil2} A_{coil}}{l_{coil}} \tag{4.7}$$

Where N_{coil1} and N_{coil2} are number of turns in coil 1 and coil 2, A_{coil} and l_{coil} are the cross-sectional area and length of coaxial coils.

Based on the selected layout for the actuator, the inductance of each coil is the resultant of Eq. (4.6) and (4.7). Therefore the total inductance of coil 1 (L_{coil1}) is equal to the sum of self-inductance of coil 1 and mutual inductance of coil 2 with respect to coil 1 as,

$$L_{coil1} = L_{s1} + L_m = \mu_0 \frac{\pi^2}{6} G_{coil1}^2 N_{coil1}^2 a_1 (\alpha + 1)(\alpha + 3) + \frac{\mu_o N_{coil1} N_{coil2} A_{coil1}}{l_{coil}} \tag{4.8}$$

Similarly the total inductance of coil 2 (L_{coil2}) is equal to the sum of self-inductance of coil 2 and mutual inductance of coil 1 with respect to coil 2 as,

$$L_{coil2} = L_{s2} + L_m = \mu_0 \frac{\pi^2}{6} G_{coil2}^2 N_{coil2}{}^2 a_1 (\alpha+1)(\alpha+3) + \frac{\mu_o N_{coil1} N_{coil2} A_{coil2}}{l_{coil}} \qquad (4.9)$$

Further the maximum magnetic field strength is equal to the sum of field strength distribution on Terfenol-D by coil 1 and coil 2 in terms of inductances as,

$$H = \frac{L_{coil1} \, I_{coil1} \left[1 - e^{-\frac{tR_{coil1}}{L_{coil1}}} \right]}{N_{coil1} A_T \, \mu^{\sigma}} + \frac{L_{coil2} \, I_{coil2} \left[1 - e^{-\frac{tR_{coil2}}{L_{coil2}}} \right]}{N_{coil2} \, A_T \, \mu^{\sigma}} \qquad (4.10)$$

4.3 MAGNETIZATION OF A TERFENOL-D ROD USING ENERGY BASED JILES - ATHERTON MODEL

Magneto-mechanical hysteresis curves of a Terfenol-D actuator for DC input under pre-stress conditions are analyzed using Jiles-Atherton (J-A) theory (Jiles and Atherton, 1984). It is a hysteretic model describing the relationship between external magnetic field intensity and magnetization. Based on assumption, primarily hysteresis originates from domain wall pinning. Subsequently, the release of domain walls from their pinning sites cause the magnetization to change in such way as to approach the anhysteretic state. The anhysteretic magnetization is figured through consideration of the thermodynamic properties of the magnetostrictive material.

The J-A model of hysteresis starts with anhysteretic magnetization in which coupling of field and inter domain magnetization are formulated using mean field theory. The magnetization in response to the magnetic field for a ferromagnetic material can be expressed as:

$$M = M_s f(H) \qquad (4.11)$$

Where H is an magnetic field given by Eq. (4.10), saturation magnetization of a Terfenol-D material is M_s and f is an arbitrary function of effective field. Impurity sites and non-magnetic inclusions are not considered in the model. This is true in case of ideal material in which impedance to the domain wall motion is in the form of pinning sites. In actual practice, the presence of pinning sites is unavoidable. Eq.

(4.11) describes only the anhysteretic curve or ideal magnetization curve in practice and can be expressed as:

$$M_{an}(H) = M_s f(H) \tag{4.12}$$

Where M_{an} is an anhysteretic magnetization. Jiles and Atherton used the Langevin function to suit the shape of anhysteretic curve to calculate anhysteretic magnetization. Eq. (4.12) can be modified as follows:

$$M_{an}(H) = M_s L\left(\frac{H}{a}\right) \tag{4.13}$$

Where the Langevin function $L(x) = \coth x - (1/x)$. With this Eq. (4.13) in terms of Langevin function can be expressed as:

$$M_{an}(H) = M_s\left(\coth\left(\frac{H}{a}\right) - \left(\frac{a}{H}\right)\right) \tag{4.14}$$

Where a is a shape parameter of anhysteretic curve. Pinning sites have the effect to decrease the initial permeability $(\partial M / \partial H)$ of a ferromagnetic material and increase its coercive force. By considering pinning sites into account the resulting magnetization referred as irreversible magnetization M_{irr} can be written as:

$$M_{irr} = M_{an} - \delta k\left(\frac{dM_{irr}}{dB}\right) \tag{4.15}$$

Where k is a pinning constant, δ is a parameter which takes on value +1 when H increases in the positive direction which means that $dH/dt > 0$ and it takes values −1 when H increases in negative direction i.e. $dH/dt < 0$. Solving and rearranging Eq. (4.15), the irreversible magnetization change in the material can be expressed as (Jiles and Atherton, 1984):

$$M_{irr} = M_s\left\{ L\left(\frac{H}{a}\right) - (k\delta)\left(L^1\left(\frac{H}{a}\right) - L^1\left(\frac{H_{max}}{a}\right)\right) + (k\delta)^2 L^2\left(\frac{H}{a}\right)\right\} \tag{4.16}$$

Depending on the order of the derivative that encompasses the series, the solution of M_{irr} will vary. Reversible magnetization of the material can be written in terms of irreversible magnetization and anhysteretic magnetization as:

$$M_{rev} = c\left(M_{an} - M_{irr}\right)$$

(4.17)

Where c is called reversible coefficient.

Further total magnetization is evaluated as the sum of reversible and irreversible magnetization. The total magnetization equals to

M_{tot} or $M = M_{rev} + M_{irr}$

(4.18)

4.4 EVALUATION OF MAGNETOSTRICTION USING MAGENTOSTRICTION MODELS

The magnetostriction $\lambda = dl_T/l_T$ specifies the relative change in the length of the material from the ordered domains. It means from unaligned state to aligned state i.e. random orientation of magnetic domains in to proposed direction along the easy axis. The magnetostriction does not quantify the effects of domain order or thermal effects. It provides a measure of the strains generated in a Terfenol-D material. An extensive work has been reported by many researchers to improve the magnetostrictive model by accounting various influencing parameters like magnetization, applied pre-stress and Young's modulus. Assuming the pre-stress is sufficiently large, the magnetostriction was characterized using quadratic model at a given magnetization level (Jiles, 1992; Calkins, 1997 and Calkins *et al.*, 2000) as:

$$\lambda = \frac{3}{2}\frac{\lambda_s}{M_s^2}M^2$$

(4.19)

Where saturation magnetostriction is λ_s and M_s is saturation magnetization.

Eq. (4.19) represents as a first approximation to the relationship between the magnetization and magnetostriction in isotropic materials. Quadratic magnetostriction model exhibits minimum hysteresis at low drive levels i.e. less than 300 Oe ($\approx$24kA/m). However, at high drive levels the model produces significant hysteresis and apart saturates from a quadratic to linear solution. It was concluded that the performance of quadratic model is much less accurate at high drive levels due to magnetic hysteresis caused by the prestress mechanism.

Defining Gibbs-free energy as a function of stress, magnetic field and temperature and applying Taylor's series on Gibbs-free energy, Carman and Mitrovic (1995) have

derived non-linear constitutive relations for dependent variables like strain, temperature and magnetic field. Yongping et al. (2003) and Wan et al., (2003) have developed hierarchical magnetostriction non-linear constitutive models using the Gibbs free energy based on domain activity. The simplest among them was the standard square model, obtained by series expansion of the Gibbs free energy. This non-linear constitutive model predicted magnetostriction very well for low and moderate magnetic fields. This was improved by adopting hyperbolic tangent function in the Gibbs free energy and was referred to as hyperbolic tangent constitutive relations. This model tries to predict magnetostriction reasonably well for high magnetic fields. Wan et al., (2003) adopted the magnetic domain behaviour mathematically by defining domain density switching function. The domain motion is due to magnetic field as well as applied prestress. Thus incorporating the domain switching density function in the Gibbs free energy, constitutive relations are derived that embodies the switching activity of the magnetic domains. The most notable work on the development of non-linear constitutive model for Terfenol-D rod in the recent times is from Zheng and Liu (2005). The constitutive model of Zheng and Liu can be applied to magnetostrictive material that exhibits positive and negative magnetostriction. Further, various parameters such as relaxation factor, initial and saturation Young's modulus, saturation magnetostriction and saturation magnetization which are the inputs for the model to be obtained from experiments. The model takes into account the variation of Young's modulus due to magnetic field and the applied load. Zheng and Liu have proved that the constitutive model developed provide good results for low, moderate and high magnetic fields. Zheng and Liu's model has been adopted by few researchers, Zhou et al., (2007) and Yong and Lin (2009), to study the performance of Terfenol-D rod for actuator application. This model can capture effectively the mechanical-magnetic coupling characteristics of magnetic, magnetostrictive and elastic properties of Terfenol-D rods. It includes the effect of the tensile or compressive pre-stress on the magnetostrictive strain and the effect of stress and the magnetic field on the Young's modulus which is known as ΔE effect. Studies indicated that the Young's modulus of the magnetostrictive material changes with the stress and the magnetic field non-linearly. However, the Young's modulus is treated

as constant in the proposed model. The analytical constitutive model for magnetostriction accounting the prestress as well as ΔE effect from Zheng and Liu is as follows:

$$\lambda = \frac{\sigma}{E_s} + \frac{\lambda_s}{2}\tanh\left(\frac{2\sigma}{\sigma_s}\right) + \left(1 - \frac{1}{2}\tanh\frac{2\sigma}{\sigma_s}\right)\lambda_s\left(\frac{M}{M_s}\right)^2 \qquad (4.20)$$

Where the applied prestress is σ, σ_s is saturation prestress and E^s is the Young's modulus at constant stress. In addition to these parameters, the quality factor is one of the key parameter influencing the output strain of a Terfenol-D actuator (Engdahl, 2000; Olabi and Grunwald, 2008a) and thus will be taken into account in the magnetostriction model. It is generally recommended to use Terfenol-D under pre-load to obtain high magnetostriction with same magnetic field. Strain is strongly dependent on the application of both magnetic field and pre-stress (Claeyssen et al., 1997), while Young's modulus of the material also changes with local stress in the rod (Zhou et al., 2007). Secondly, the Terfenol-D material can support little tensile or shear load. Thus to avoid a risk of tensile loading, a prestress is usually required (Engdahl, 2000; Karunanidhi and Singaperumal, 2010). Consider the operation of Terfenol-D rod to an applied step input. During the transient, the blocked force and the applied preload can vary. Apart, the rod is likely to undergo longitudinal oscillation. However, the Terfenol-D rod possesses a resonance frequency in the longitudinal direction. To observe this, the Terfenol-D rod must be free to vibrate by operating an actuator under no load conditions. These factors call upon to adopt the magnetostrictive strain coefficient (d_{33}) in the magnetostriction model. The strain at resonance is much higher than it is under quasi-static conditions (Claeyssen et al., 1997; Olabi and Grunwald, 2008a). The strain at resonance condition is given by:

$$\lambda_{33} = Q_3 d_{33} H_{qi} \qquad (4.21)$$

Here two forms of strain at resonance are considered in the magnetostriction model. The first form is strain at resonance due to applied prestress on Terfenol-D is added to the existing non-constitutive magnetostrictive model. The second form is strain at resonance due to magnetization of Terfenol-D is added to the existing non-

94

constitutive magnetostriction model. In Eq. (4.21), Q_3 is an amplification factor known as quality factor, $H_{q1}(i=1)$ is a magnetic field due to applied prestress on Terfenol-D, $H_{q2}(i=2)$ is a magnetic field due to DC input to the coils, and the coefficient d_{33} is called magnetostrictive strain coefficient and it is independent of the longitudinal frequency.

Assuming zero prestress and as well as linear relationship between λ and H_q, then quality factor will be unity in Eq. (4.21) for an applied magnetic field on Terfenol-D. Devices using Terfenol-D will be designed in the linear region. However, the behaviour of Terfenol-D material will be non-linear due to inherent property of magnetostrictive material. This brings the existence of non-linear relationship between strain and magnetic field. Due to non-linear relationship, the quality factor will exist in Eq. (4.21) whose value ranges from 3 to 20 (Engdahl, 2000; Olabi and Grunwald, 2008a). Considering quality factor, the magnetostriction is computed by combining Eq. (4.20) and Eq. (4.21) for a Terfenol-D material as follows:

$$\lambda = \frac{\sigma}{E_s} + \frac{\lambda_s}{2}\tanh\left(\frac{2\sigma}{\sigma_s}\right) + \left(1 - \frac{1}{2}\tanh\frac{2\sigma}{\sigma_s}\right)\lambda_s\left(\frac{M}{M_s}\right)^2 + Q_3 d_{33} H_{qi} \qquad (4.22)$$

Where Eq. (4.22) gives the magnetostriction of a Terfenol-D material under the influence of applied preload (σ), Young's modulus (E_s), magnetization (M) and quality factor. The magnetic field strength (H_{qi}) in Eq. (4.22) is considered to be expressed in two forms as reported in Sun and Zheng (2005), and Karunanidhi and Singaperumal, 2010. This leads to two forms of magnetostriction models named as magnetostriction model I and magnetostriction model II. The two forms models are described as follows:

4.4.1 Magnetostrictive model- I

The distribution of magnetic field strength $H_{qi}(i=1)$ on Terfenol-D due to applied prestress is given by Sun and Zheng, 2005 and as well Yong and Lin, 2009 is as follows,

$$H_{qi}(i=1) = \left\{ 4\sigma - \sigma_s \ln\left[\cosh\left(\frac{2\sigma}{\sigma_s}\right)\right] \right\} \frac{\lambda_s M}{2\mu_0 M_s^2} \tag{4.23}$$

Substituting $H_{qi}(i=1)$ given by Eq. (4.23) into Eq. (4.22) yields,

$$\lambda = \frac{\sigma}{E_s} + \frac{\lambda_s}{2}\tanh\left(\frac{2\sigma}{\sigma_s}\right) + \left(1 - \frac{1}{2}\tanh\frac{2\sigma}{\sigma_s}\right)\lambda_s\left(\frac{M}{M_s}\right)^2 + \frac{Q_3 d_{33}\lambda_s M}{2\mu_o M_s^2}\left\{4\sigma - \sigma_s\ln\left[\cosh\left(\frac{2\sigma}{\sigma_s}\right)\right]\right\}$$
$$\tag{4.24}$$

Eq. (4.24) gives the magnetostriction of a Terfenol-D rod under the influence of magnetization, applied prestress, young's modulus and quality factor. At zero prestress, the magnetostriction is a function of magnetization and Young's modulus of a Terfenol-D rod as the quality factor term included in the Eq. (4.24) vanishes. There is an existence of magnetostriction for any applied preload other than zero preload, due to the effect of quality factor.

4.4.2 Magnetostrictive model- II

Magnetic field strength $H_{qi}(i=2)$ on Terfenol-D as a function of magnetization reported in Karunanidhi and Singaperumal, 2010 is given by,

$$H_{qi}(i=2) = \frac{M}{(\mu_T - 1)} \tag{4.25}$$

Where magnetization is M and μ_T is relative permeability of a Terfenol-D material. Substituting $H_{qi}(i=2)$ in Eq. (4.22) and rearranging yields:

$$\lambda = \frac{\sigma}{E_s} + \frac{\lambda_s}{2}\tanh\left(\frac{2\sigma}{\sigma_s}\right) + \left(1 - \frac{1}{2}\tanh\frac{2\sigma}{\sigma_s}\right)\lambda_s\left(\frac{M}{M_s}\right)^2 + Q_3 d_{33}\frac{M}{(\mu_T - 1)} \tag{4.26}$$

Eq. (4.26) gives the magnetostriction of a Terfenol-D rod that depends on magnetization, applied prestress, Young's modulus and quality factor. This magnetostriction model can predict the magnetostriction at all applied preloads, whereas the magnetostriction model given by Eq. (4.24) evaluates the magnetostriction at all applied preload other than zero load. This is the difference between the two proposed models.

4.5 PARAMETER IDENTIFICATION FOR J-A MODEL

The magnetic and magnetostrictive parameters like pinning constant, anhysteretic parameter, reversibility coefficient, saturation magnetization and saturation magnetostriction are unknown for a magnetization and magnetostrictive model. These parameters are associated with the composition and production processes of Terfenol-D rod. In the present work, the saturation magnetization and saturation magnetostriction are made available by DMRL, Hyderabad. The other factors like pinning constant, anhysteretic parameter for a Terfenol-D material used in the present study are referred from Calkins et al., 2000. The parameters used in the J-A model are listed in Table 4-1.

Table 4-1. Parameters used in Jiles-Atherton model.

S. NO	Parameters	Value
1	Saturation magnetostriction (λ_s)	1350 ppm
2	Saturation magnetization (M_s)	675250 A/m
3	Pinning constant (k)	3283 A/m
4	Anhysteretic parameter (a)	7012 A/m
5	Reversibility co-efficient (c)	0.88
6	Applied pre-stress (σ)	0 ,0.812,1.624,2.436 3.248 MPa
9	Saturation pre-stress (σ_s)	200 MPa
10	Magnetostrictive strain coefficient (d_{33})	15×10^{-9}
11	Quality factor (Q_3)	3 – 20 (15 is assumed in the present study

4.6 TERFENOL-D RESPONSE FOR DC INPUT USING DIFFERENT MAGNETOSTRICTIVE MODELS

Magnetization and magnetostriction responses for a Terfenol-D actuator under DC input for different pre-stress conditons are evaluated using proposed magnetostriction models I and II. Magneto-mechanical characteistics like magnetic field, magnetization for both models, strain and displacement for model I and for model II were calculated as a function of time using Eq. (4.10), Eq. (4.18), Eq. (4.23) and Eq. (4.26) respectively.

Response curves shown in Fig. 4.1 and 4.2 is for a step input ranging from 1 A to 4 A under zero pre-stress conditions. They indicates the behaviour of different parameters

like magnetic field, magnetization, strain and displacement between point of excitation to steady state as a function of time. It is observed that these parameters increase with the increase in applied input. Displacement output is initially transient from the point of excitation until it reaches a steady state value. The maximum displacement obtained are 51.6 and 32 µm respectively for an DC input of 4 A from model I and model II as shown in Fig. 4.2 (a) and (b). The displacement achieved with the magentostriction model I is more than that achieved with magentostriction model II. Magnetostrictive model II takes into account the quality factor, whereas quality factor vanishes in magnetostriction model I at zero preload. This is the reason due to which the displacement is considerbly less in magnetostriction model II compared to magentostriction model I. It is also observed that the time required for the response to reach from the point of excitation to steady state point is constant as the input increases and equal to 171 ms from Fig. 4.1 and 4.2.
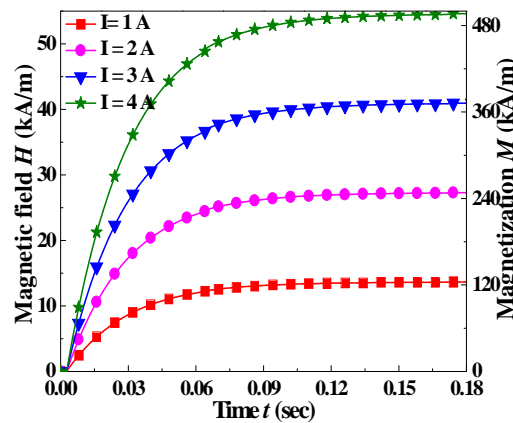
Fig. 4.1. Magnetic field and magnetization of a Terfenol-D material as a function of time at zero preload.

It is observed that the magnetic field strength produced by the coils is increasing as the input current is increased. According to Ampere's law, the Terfenol-D rod surrounded by coaxial coils is theoretically modeled as a conductor wound around with coil of finite number of turns carrying current. The magnetic fields produced by the separate turns of wire pass through the center of coils and superpose to produce a strong magnetic field. This is the reason due to which the magnetic field strength produced by the coils increases as the input current is increased.
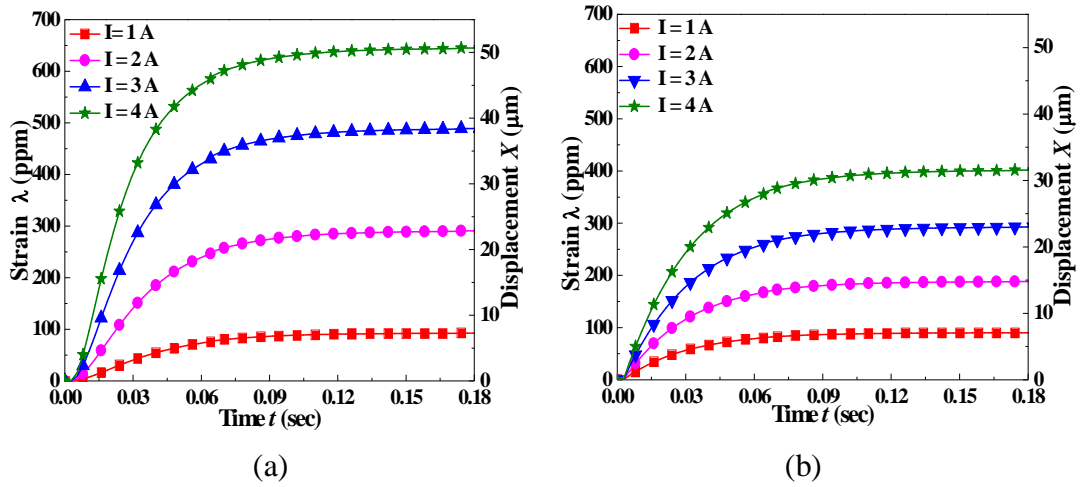
Fig. 4.2. Strain and displacement of a Terfenol-D material from magnetostriction
(a) model-I and (b) model-II as a function of time at zero preload.

Also, it is observed that the magnetization of Terfenol-D material increases as the applied magnetic field is increased. The magnetic moments prefer to align along <111> easy axis in a demagnetized Terfenol-D and at room temperature. Terfenol-D material starts from a demagnetized state at which bulk magnetization is zero due to a random distribution of magnetic domain orientations. The magnetization at low applied fields can be attributed to reversible domain wall motion. The magnetic domains are aligned in a direction along or closer to the direction of applied magnetic field as the magnetic field is increased. As the input field is increased, due to change of reversible domain wall motion to irreversible motion and rotation a large change in magnetization is observed (Thoelke, 1993).

Fig. 4.3 shows the magnetization behaviour of a Terfenol-D material against the applied magnetic field. Magnetization of a material increases as the applied magnetic field is increased. The reason is due to an irreversible motion and rotation of magnetic domains along the direction of applied magnetic field as the input field is increased. It is also observed that the behaviour of Terfenol-D material is linear for an applied magnetic till 18 kA/m. It indicates that the behaviour of magnetization is independent of magnetic domain movements in a Terfenol-D material at which the Young's modulus is constant. The material behaves non-linearly for an applied magnetic field beyond 18 kA/m. It indicates that the magnetization is dependent on movement of

99

magnetic domains at which the Young's modulus of material is intrinsic (Thoelke, 1993).
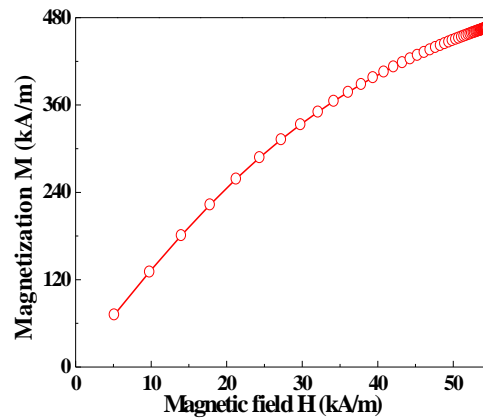
Fig. 4.3. Magnetization of a Terfenol-D actuator as a function of applied magnetic field under zero preload.

(a)	(b)
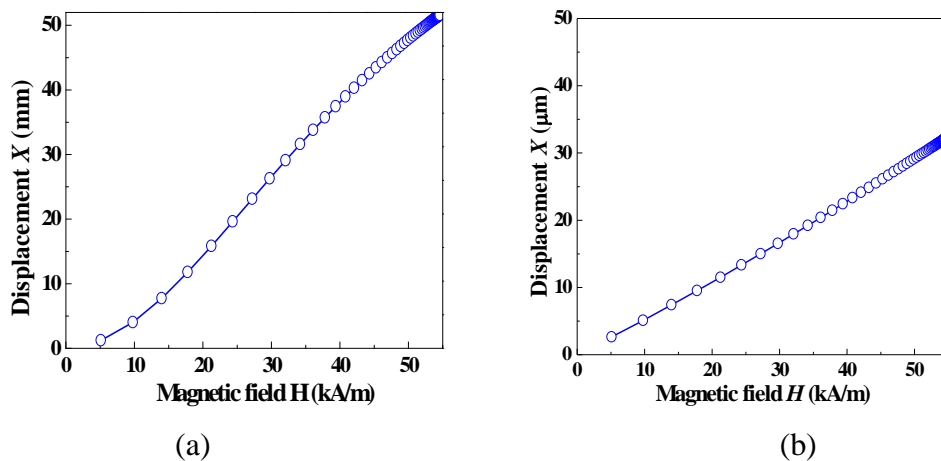
Fig. 4.4. Displacement of a Terfenol-D actuator as a function of applied magnetic field from magnetostrictive (a) model-I and (b) model-II under zero preload.

Fig. 4.4 (a) and (b) shows the displacement achieved from the magnetostrictive model I and II for an applied magnetic field. Magnetic processes that are accountable for huge change in magnetization are not always the same processes responsible for changes in magnetostriction (Thoelke, 1993). The displacement from model I and II increases as the input magnetic field is increased. The displacement obtained from Terfenol-D material is non-linear till 18 kA/m and is proportional to the applied magnetic field beyond 18 kA/m up to 50 kA/m from model I. The non-linear behaviour may be due to variation in elastic modulus of a Terfenol-D material as it depends on movement of magnetic domains till the applied magnetic field of 18

kA/m. The displacement is linear between 18 kA/m to 50 kA/m. The reason is that the elastic modulus is constant between this range of applied magnetic field implies the independent of movement of magnetic domains. The displacement of a Terfenol-D obtained with magnetostrictive model II is linear.

4.7 COMPARISON OF DISPLACEMENT FROM TERFENOL-D ACTUATOR FOR VARYING PRELOADS

Theoretically the displacement obtained from magnetostrictive models I and II are compared for an applied DC input of 4 A under zero, 500 and 1000 N preload conditions as shown in Fig. 4.5. The displacement from the Terfenol-D rod increases sharply until 0.06 sec irrespective of applied preload. Beyond 0.06 sec, the output displacement from Terfenol-D rod increases very slowly and reaches steady value at about 0.171 sec. The displacement from the Terfenol-D material is markedly transient between excitation point to till 0.06 sec.

| (a) | (b) |
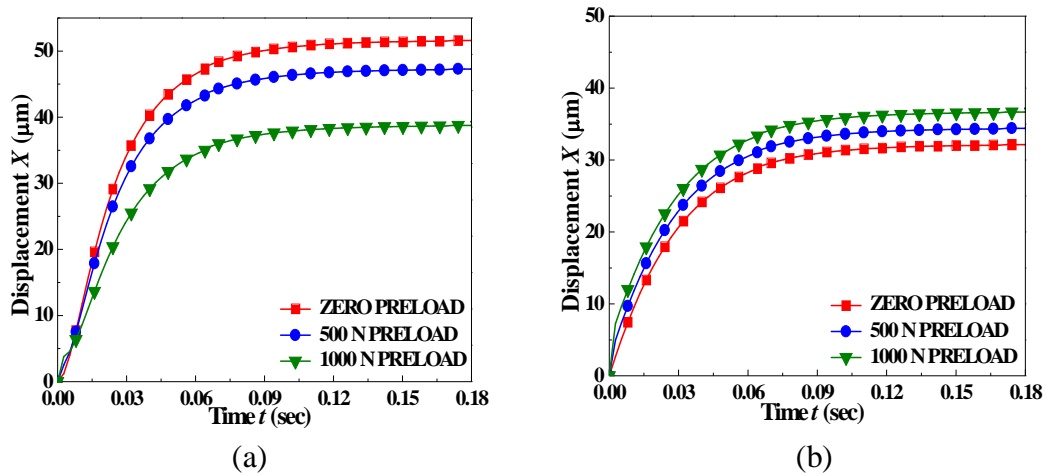
Fig. 4.5. Response characteristics from magnetostrictive (a) model I and (b) model II for different preloads.

The displacement attains steady at 0.171 sec. The magnetic field strength due to applied preload is weighted with quality factor in a magnetostrictive model I, due to which the displacement increases for an applied magnetic field compared to magnetostriction model II. It is quite different in the proposed magnetostriction model II, where in magnetization of Terfenol-D is directly weighted with quality factor. Due to this fact, the displacement achieved from model II is less than that from model I for an applied magnetic field. Also it is observed that the displacement obtained from the

Terfenol-D is decreasing as the applied preload is increased using magnetostriction model I. The reason may be due to decreased net magnetic moment rotation when the Terfenol-D material moments rotate into alignment with the applied magnetic field. On the other hand, the displacement achieved from the Terfenol-D is increasing as the preload is increased in case of magnetostrictive model II. The applied preload causes rotation of the Terfenol-D rod's magnetic moment so as align initially perpendicular to the applied preload. This yields larger displacement due to increased net moment rotation whenever the Terfenol-D rod moments rotate into alignment with the applied magnetic field (Kellogg, 2000). The maximum displacements obtained are 51.6, 47.3 and 38.8 μm with magnetostrictive model I and 32, 34.4, and 36.7 μm with magnetostrictive model II respectively for a preload of 0, 500 and 1000 N at an applied 4 A of direct current input.

4.8 A COMPARISON OF VARIOUS MAGNETOSTRICTIVE MODELS

The magnetostriction of a Terfenol-D material is evaluated using Eq. (4.24) and Eq. (4.26) for magnetostrictive model I and II. The displacement of a Terfenol-D is evaluated from the magnetostriction for both models. Further, the displacements are compared with quadratic model, Eq. (4.19), and analytical constitutive model given by Eq. (4.20) at zero and 1000 N preload conditions.

Fig. 4.6 (a) and (b) shows the comparison of displacement obtained with all magnetostrictive models for a step input of 4 A to coil 1 and coil 2 under zero and 1000N preload against the time. The output displacement obtained with quadratic model is more compared to other magnetostriction models and equal to 77 μm for applied zero preloads. Quadratic model directly represents the relationship between applied input current to coil and magnetostriction achieved from the Terfenol-D material irrespective of applied preload. The domain magnetic moments rotation produces a change in bulk magnetostriction for an applied magnetic field. Magnetostriction obtained from a Terfenol-D material does not quantify the effect of domain order, due to which large amount of displacement has been observed (Calkins et al., 2000). Quadratic model and non-constitutive model proposed by Zheng and Liu, 2005 behave similarly at zero preload. Quadratic model is associated with a

factor 1.5 compared to non-constitutive models as given by Eq. 4.19 and 4.20 under zero preload.
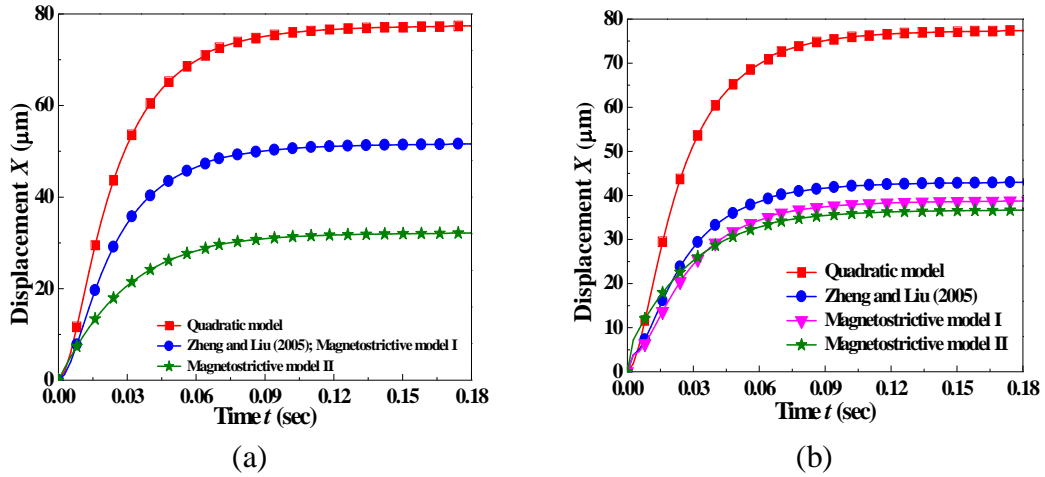
Fig. 4.6. Comparison of theoretical displacement of a Terfenol-D rod from different magnetostrictive models as a function of time for (a) zero and (b) 1000 N preload.

This is the reason due to which the displacement achieved from non-constitutive model is less compared to quadratic model at zero preload. The displacement achieved with the non-constitutive model is 51.6 and 43 μm which is less compared to quadratic model for an applied zero and 1000 N preload. This model takes into account the effect of Young's modulus that changes with applied magnetic field (known as ΔE effect) apart from applied prestress on magnetostriction of a Terfenol-D material. These factors make the Terfenol-D material to behave non-linearly with this magnetostriction model, due to which the displacement may be less compared to quadratic model for all applied preloads. The proposed magnetostriction model I is another form of non-constitutive model that considers the effect of quality factor to predict the magnetostriction of a Terfenol-D. Magnetic field strength and hence magnetization due to preload on Terfenol-D is considered with quality factor. The non-constitutive and magnetostrictive model I do not take the effect of Young's modulus and quality factor respectively for a zero preload. Hence, the displacement achieved from the Terfenol-D material using both models is same and is equal to 51.6 μm at zero preload as shown in Fig. 4.6 (a). However, the displacement due to the effect of quality factor in a proposed magnetostriction model I is equal to 43 μm for an applied preload of 1000 N as shown in Fig. 4.6 (b). The effect of quality factor is

103

considered in another proposed magnetostrictive model II to depict the magnetostriction of a Terfenol-D material. Here, the magnetic field strength on Terfenol-D is a function of magnetization alone in the consideration of quality factor. The effect of quality factor taken into account can be observed in a magnetostrictive model II even at the zero preload apart from each applied preload. The reason is that the magnetic field strength on Terfenol-D is a function of magnetization instead of applied prestress as in magnetostrictive model I. The displacement obtained using magnetostriction model II accounts quality factor for all preloads, whereas the influence of the same accounts on displacement for all preloads other than zero preload. The maximum displacement achieved with the magnetostrictive model II is 32 and 37 μm for an applied input current of 4 A respectively under zero and 1000 N preload. An average reduction in displacement is found to be 33 % and 50 % respectively under zero preload, 59 % and 52 % respectively with magnetostrictive model I and II compared to quadratic model.

Fig. 4.7 (a), (b) and 4.8 (a), (b) shows the comparison of theoretical displacement obtained from various models against the applied magnetic field and magnetization. It is observed that the displacement obtained from all models is increasing as the applied magnetic field increases and shows non-linear behaviour except for proposed magnetostriction model II under zero and 1000 N preload shown in Fig. 4.7 (a) and (b).

(a)   (b)
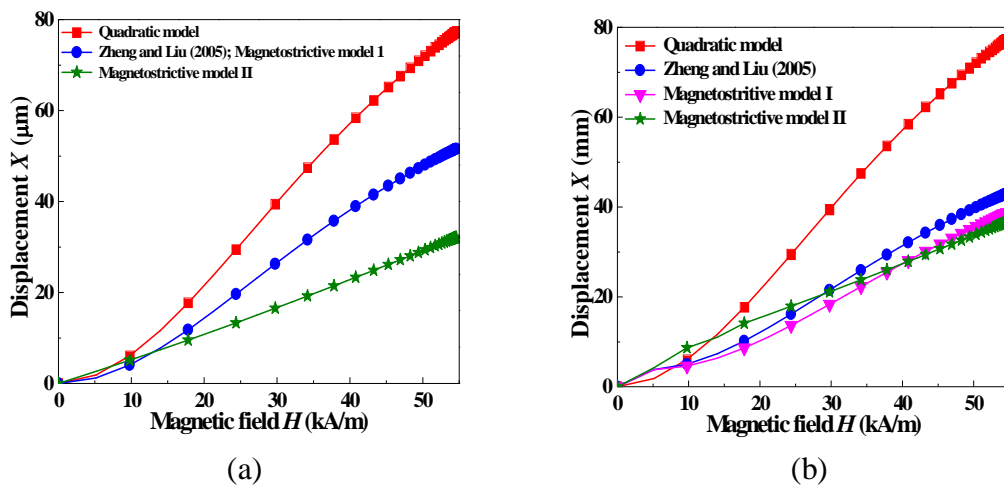
Fig. 4.7. Comparison of theoretical displacement of a Terfenol-D rod from different magnetostrictive models as a function of applied magnetic field for (a) zero and (b) 1000 N preload.

Non-linear behaviour may be due to presence of non-linear term associated with all models except magnetostrictive model II. The other reason may due to the contingent of magnetic moment alignment with the applied magnetic field. The behaviour is linear for a proposed magnetostrictive model II as shown in Fig. 4.7 (a) and (b) under an applied preload of zero and 1000 N. The linear behaviour may be due to independent of magnetic moment alignment with the applied magnetic field. Young's modulus of a Terfenol-D material may be constant due to which the model is behaving linearly for an applied magnetic field under zero and 1000 N preload.
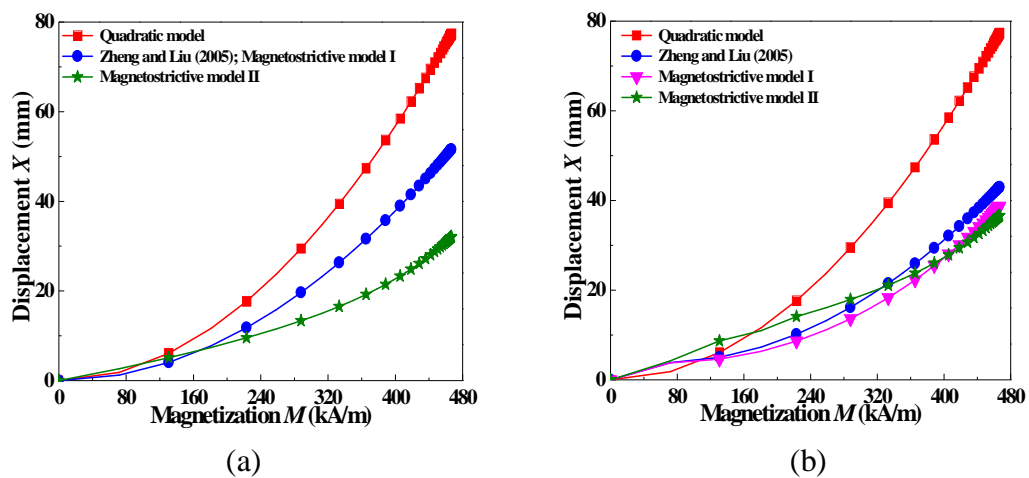
Fig. 4.8. Comparison of theoretical displacement of a Terfenol-D rod from different magnetostrictive models as a function of magnetization for (a) zero and (b) 1000 N preload.

The displacement achieved from various models is increasing as the magnetization of Terfenol-D material increases under zero and 1000 N preload shown in Fig. 4.8 (a) and (b). Another important observation is that the behaviour of all models is non-linear even with a proposed magnetostriction model II as shown in Fig. 4.8 (a) and (b). The reason may be due to inadequate anisotropy energy of magnetic moments among unfavourable magnetic moments. This indicates the dependence of magnetic moment to align with the direction of applied magnetic field to show linear behaviour in addition to predict huge displacement from the Terfenol-D material.

4.9 SUMMARY

Self inductance and mutual inductance was considered in the formulation of magnetic field strength of a Terfenol-D actuator. Two magnetostrictive models considering the

quality factor that influences the magnetostriction of a Terfenol-D were proposed. Magnetostriction model I that consider quality factor on magnetostriction due to the field produced by the applied preload. Magnetostriction model II considers quality factor on magnetostriction due to the magnetization of a Terfenol-D material. The response characteristics of a Terfenol-D actuator under DC driving conditions for different preloads were evaluated. The results obtained from the proposed magnetostrictive models have been compared with the existing magnetostrictive models such as quadratic and non-constitutive magnetostricitve models. Based on the results obtained, the following observations are made,

- The analytical formulation and evaluation of magnetic field strength from driving coils revealed that the factors like self inductance and mutual inductance of coils should be considered apart number of coil turns, length of coil and input current for the effective distribution of magnetic field strength on Terfenol-D.

- Magnetostriction of a Terfenol-D material is evaluated using various magnetostrictive models that includes proposed two analytical magnetostrictive models accounts quality factor for DC input conditions under different preloads. On comparison, it revealed that the quality factor included magnetostrictive model I and II can be used for predicting magnetostriction of a Terfenol-D material.

- Response from the Terfenol-D was initially transient till to reach maximum amplitude and thereafter it is steady for an applied input. Response time is less than 1 sec takes to reach steady state. It is revealed that the response time is 171 ms for an applied input of 4 A for all magnetostrictive models.

- Displacement achieved from the Terfenol-D decreases for an applied magnetic field apart non-linear behaviour due to non-linear parameter of magnetic field strength associated with quality factor in a magnetostrictive model I. Similarly, the displacement obtained from the Terfenol-D increases for an applied magnetic field apart linear behaviour due to linear parameter of magnetic field strength associated with quality factor considered in a magnetostrictive model II.

106

- Displacement of a Terfenol-D actuator is non-linear with magnetostrictive model I and linear with magnetostritive model II for the applied magnetic field. Displacement obtained from the Terfenol-D decreases with magnetostriction model I and increases with magentostriction model II as the preload increases for an applied DC input.

- The output displacement with the proposed magnetostriction model I and II is very less when compared to quadratic and non-constitutive magnetostriction models. The maximum displacements obtained are 51.6, 47.3 and 38.8 µm with magnetostrictive model I and 32, 34.4, and 36.7 µm with magnetostrictive model II respectively for a preload of 0, 500 and 1000 N at an applied DC input of 4 A. An average reduction of 33 % and 50 % under zero preload, 59 % and 52 % with magnetostrictive model I and II compared to quadratic model.

CHAPTER 5

EXPERIMENTAL SETUP AND RESPONSE CHARACTERISTICS OF A TERFENOL-D ACTUATOR UNDER DC DRIVING CONDITIONS

5.1. INTRODUCTION

In this chapter a detailed description of the experimental set up, its components and the details of the experimental data recorded during this study are presented. Effective use of Terfenol-D actuator requires the knowledge of displacement and force output under a given current input. The experimental data was recorded for different operating conditions of zero prestress and definite prestress. Response characteristics of Terfenol-D actuator like displacement and subsequently blocked force is estimated.

Pre-stress is one of the major factors which influence the performance of the Terfenol-D actuator. Terfenol-D material produces more strain under application of pre-stress. Belleville springs are being designed and used for preloading the Terfenol-D rod. When pre-stress is applied, the domain in the Terfenol-D material will align perpendicular to the applied load and produce negative strain. After supplying the input to the actuator, it will generate total strain equal to strain produced under zero pre-stress plus strain produced by the application of pre-stress. Therefore total strain will be more than the strain under zero pre-stress. Experimentally measured displacement and blocked force values will be compared with theoretical results to analyze the performance of the Terfenol-D actuator.

Tests were conducted to understand the response at regular time intervals as well as for continuous operation of actuator at desired input due to hysteretic behaviour of Terfenol-D material. Response time of a Terfenol-D actuator is evaluated for the applied input. Force exerted by a Terfenol-D actuator under different preload

conditions is being evaluated by considering the number of turns of coaxial coils and stiffness of the active material.

5.2. EXPERIMENTAL SET UP FOR MEASURING DISPLACEMENT OF A TERFENOL-D ACTUATOR

The schematic diagram of the experimental set up for measuring the displacement of a Terfenol-D actuator is shown in Fig. 5.1. It illustrates the actuator assembly to comprise of Terfenol-D rod surrounded by coaxial coils namely coil 1 and coil 2, together enclosed in a mild steel housing. Opto NCDT 1402 laser displacement sensor held by means of a digital vernier height guage is used to measure the displacement of a Terfenol-D actuator. It provides a resolution of 1 µm for static measurement and frequency response of 1.5 kHz. The output from the displacement sensor is communicated to the computer using RS422 USB serial converter and is processed by the ILD 1402 v2.03 software. The coaxial coils are energized by a regulated dual power supply unit.
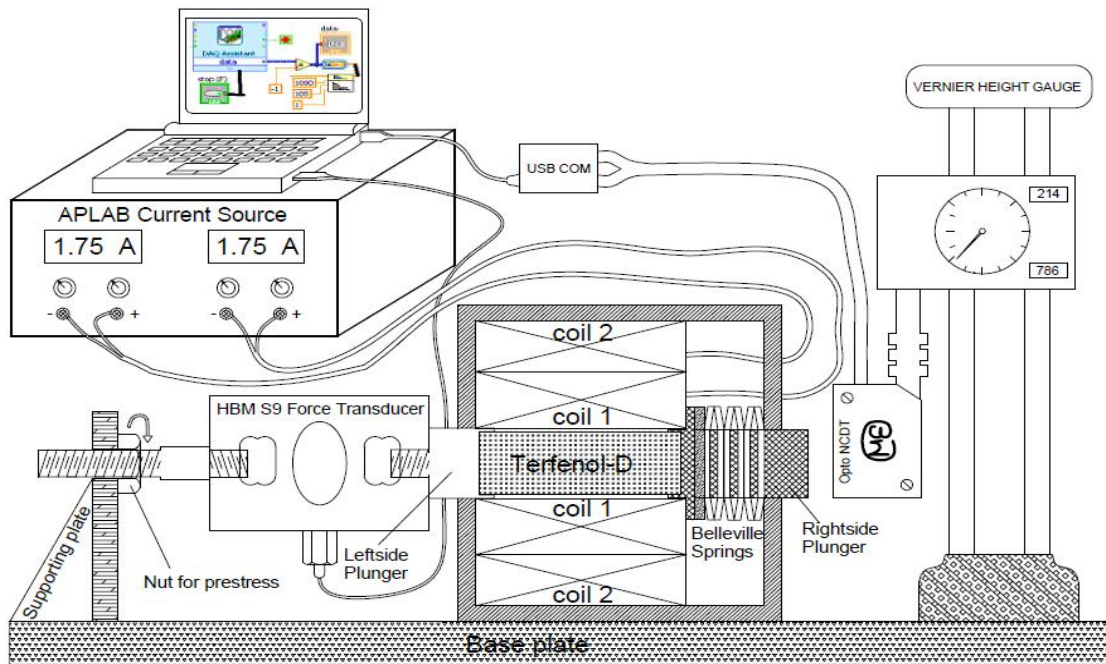
Fig. 5.1. Schematic diagram of experimental set up of a Terfenol-D actuator.

Belleville springs are used to apply prestress on the Terfenol-D rod during the experiment. PT 4000 model of make PT Ltd. force transducer with load range of 0-10 kN was used to monitor the preload being applied on Terfenol-D. It was interfaced to

109

IBM Z60t laptop through Lab VIEW software using NI 9237 module. This module gives output in terms of load with respect to the load applied on the Terfenol-D rod. Force transducer data was collected at a continuous sampling rate of 25000 samples per second with a frequency of 25000 Hz using low pass filter. Low pass filter known as inverse Chebyshev filter was used to capture the output from the transducer without signal noises at a desired frequency. An inverse Chebyshev low pass filter was used with the following specifications: Order 2, lower cutoff frequency 1 Hz, higher cutoff frequency 100 Hz and sampling frequency of 1000 Hz. The specifications of instruments and other accessories used in the setup are illustrated in section II.1 of APPENDIX II. A photograph of the experimental setup is shown in Fig. 5 and the photograph of the individual components in the experimental setup is shown in the Fig. II.1 to Fig. II.12 in APPENDIX II.
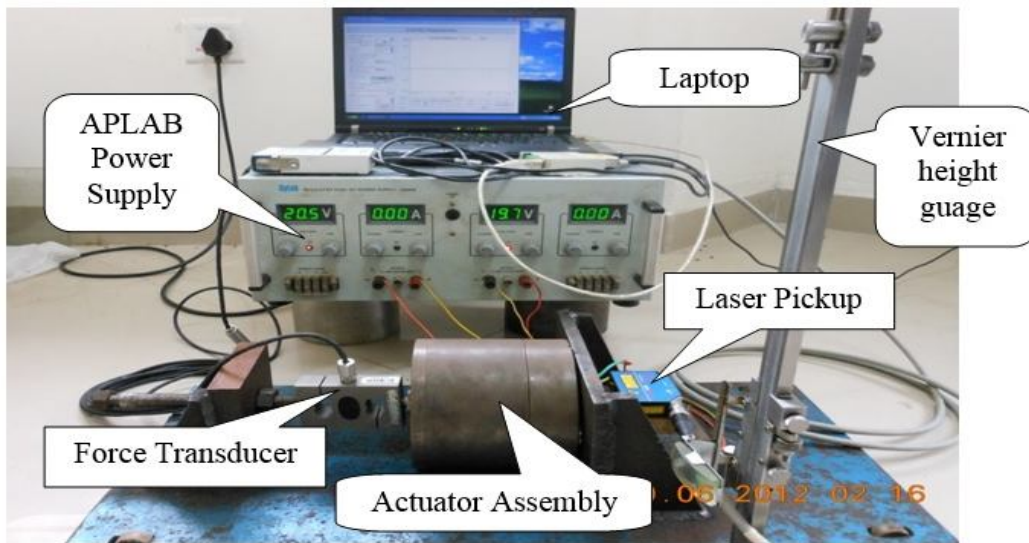
Fig. 5.2. Experimental set up to study performance of Terfenol-D actuator.

5.3. EXPERIMENTAL RESPONSE CURVES OF A TERFENOL-D ACTUATOR

Experiments were conducted on Terfenol-D actuator for different DC input and different pre-stress. The DC input was selected in the range of 1 to 4 A. Input is increased from 1 A to 4 A and decreased from 4 A to 1 A in steps of 0.25 A. The different input operating conditions were (i) applying equal current to both coil 1 and coil 2, (ii) constant biasing to coil 1 and varying DC input to coil 2, and (iii) varying

110

bias field to coil 1 and constant DC input to coil 2. The preload on Terfenol-D rod was in the range of 0 to 2000 N in steps of 500 N. In addition, the different housing materials such as mild steel, cast iron and aluminium are used for Terfenol-D actuator to understand the behaviour of magnetostriction for the applied input conditions.

5.3.1 Effect of equal DC input to coaxial coils on displacement of a Terfenol-D actuator

Typical response curves obtained by varying equal DC input to both coils using laser pick-up sensor for zero preload are shown in Fig. 5.3 (a), (b), (c) and (d).

(a)

(b)

(c)

(d)
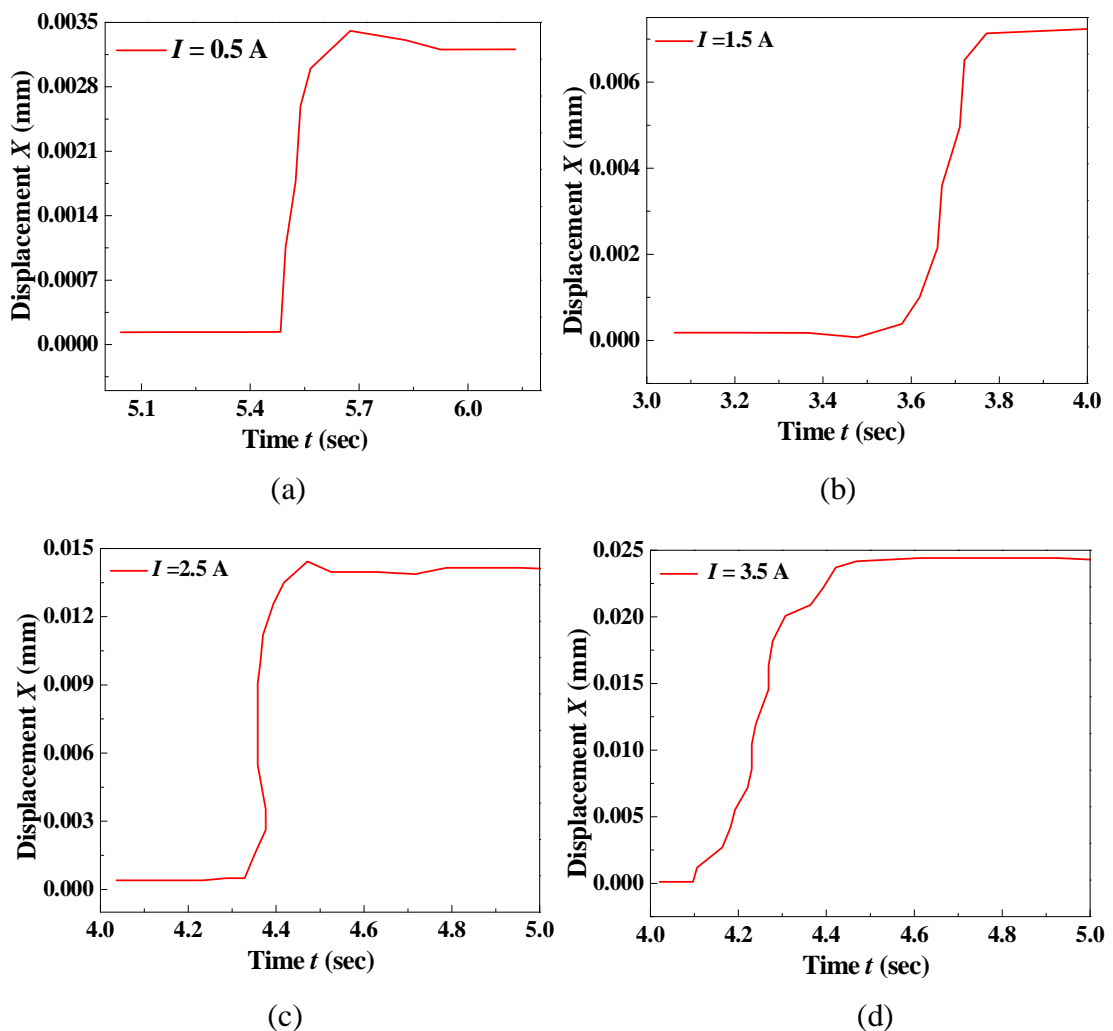
Fig. 5.3. Response of Terfenol-D actuator under zero pre-load for step input of (a) 0.5 A (b) 1.5 A (c) 2.5 A and (d) 3.5 A to coaxial coils.

Screen shots and plots of response, and a response for other preloads such as 500 N, 1000 N, 1500 N and 2000 N are illustrated in section III.1 of Appendix III. An output similar to step response is observed for a given input. It is observed that the output attains a maximum and remains steady. Step input current was supplied to the coaxial coils and brought back to zero for each input excitation. Actuator was completely at demagnetized state before each step input excitation. Response is steady i.e. it follows a straight horizontal line before excitation. However, the ripples were observed in the output after the actuator is excited with step input as shown in Fig. 5.3 (a, b, c and d). The active material is likely to undergoing the longitudinal vibrations during zero preload conditions (Olabi and Grunwald, 2008a) may be the reason for these ripples. The disturbance to the cables that are connecting power supply unit to coaxial coils of an actuator may also be the other reason for ripples. The inherent sensitiveness of the laser pick-up cable may also be the cause. The actuator was tested in an open room due to which the disturbance may be in the form of wind. These ripples were avoided by firmly holding the laser pickup cable with a rigid member. The steady state displacement was found to be 0.0031, 0.0093, 0.0156 and 0.0255 mm (3.1, 9.3, 15.6 and 25.5 μm) for a DC input of 0.5 A 1.5 A, 2.5 A and 3.5 A respectively under zero preload. From the experimental displacement output it was observed that there is finite time to reach the maximum input from zero. The time to reach the maximum output is 333, 568, 273 and 326 ms for step input of 0.5, 1.5, 2.5 and 3.5 A respectively for zero preload. The duration of the actual response is less than 1 second was observed for all preload conditions of 500, 1000, 1500 and 2000 N.

Fig. 5.4 shows hysteresis in the output of Terfenol-D actuator for zero preload. The experiment was conducted for one completer cycle (i.e. increasing and decreasing) and the data was collected at a frequency of 1 kHz. The step input is increased from 1 to 4 A and again decreased to 1 A in steps of 0.25 A equally to coaxial coils of a Terfenol-D actuator. Three trials were taken for each input operating condition and the average obtained during increasing and decreasing case have been plotted (refer Table III-1 of APPENDIX-III). The difference between the measured points for

increasing and decreasing cases is close to 1 µm, which is the resolution of the laser displacement sensor.
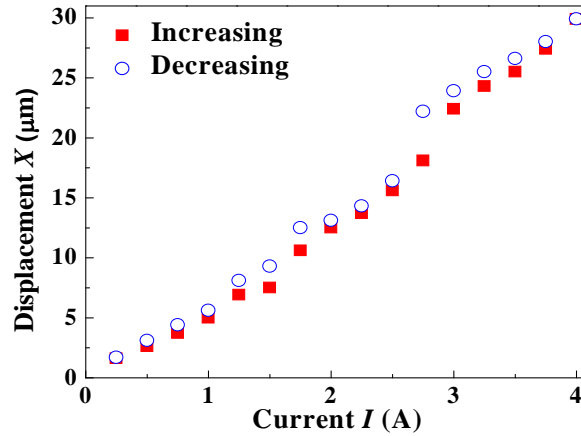
Fig. 5.4. Displacement of a Terfenol-D actuator by varying step input to coil 1 and coil 2 under zero pre-load.

The deviation in experimental displacement between increasing and decreasing input to coaxial coils for zero preload is found to be 9 %. The deviation in displacement may be due to measurement noise. It is also due to inherent property of Terfenol-D material undergoing electron spin, orientation and interaction of spin orbitals and the molecular lattice configuration. Typical response plots by varying step input to coil 1 and coil 2 were plotted for preload of 500 N, 1000 N, 1500 N and 2000 N are illustrated in section III.2 of APPENDIX- III.

5.3.2 Effect of magnetic field from bias coil on displacement of a Terfenol-D actuator

The output of the Terfenol-D rod is being understood depending on the coil used for biasing. One approach is to maintain constant biasing field from coil 1 and varying step input to coil 2. The second approach illustrates that the input to coil 2 is held constant and thus providing bias magnetic field from coil 1 is variable. The maximum displacement of the Terfenol-D rod with mild steel housing is 29.9 µm with constant biasing of coil 1 and varying step input to coil 2 as shown in Fig. 5.5 (a). The deviation between increasing and decreasing is 3 % with constant biasing magnetic field equal to 4 A from coil 1 and varying step input to coil 2 in step of 0.25 A.
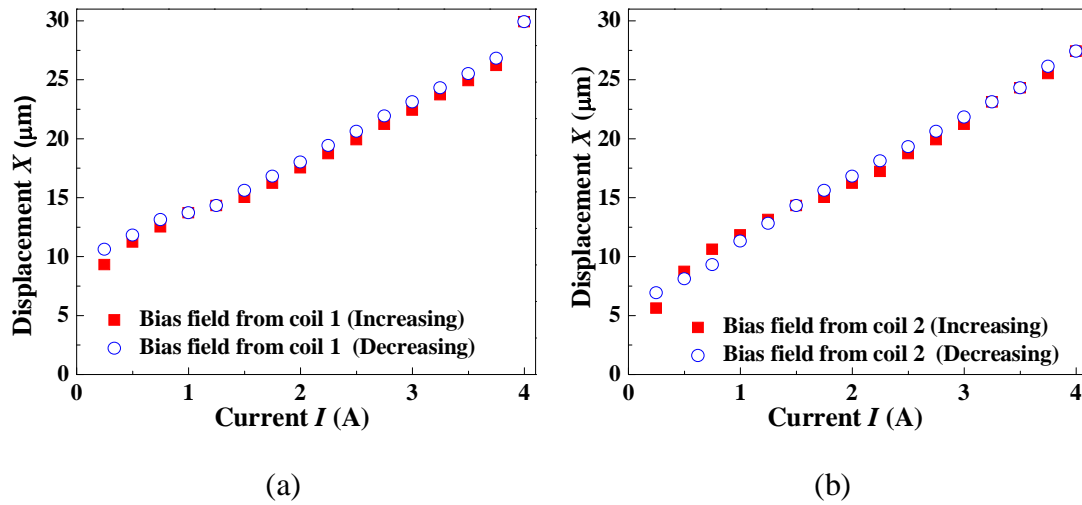
Fig. 5.5. Displacement of a Terfenol-D actuator (a) constant biasing field from coil 1 and varying input to coil 2 (b) constant input to coil 2 and varying biasing field from coil 1 for zero preload conditions.

As seen from Fig. 5.5 (a) and (b), that the displacement obtained with constant and varying biasing field from coil 1 is more than the displacement obtained by varying equal step input to both coils. The reason is that the net available magnetic field produced by the coaxial coils is more at each excitation. On the other hand, referring Fig. 5.5 (b), the displacement achieved is less by varying biasing field to coil 1 when compared to displacement achieved with constant biasing to coil 1. It is because, coil 2 is having less number of turns compared to coil 1 and is far away from Terfenol-D in the actuator assembly. This causes the magneto motive force generated by the coil 2 not reach effectively to the measuring end of Terfenol-D rod to achieve more strain though the net available magnetic field is same in both cases. The deviation between increasing and decreasing is 1 % with constant step input of 4 A to coil 2 and varying step input to coil 1 in step of 0.25 A. Similar studies were undertaken for preload of 500 N, 1000 N, 1500 N and 2000 N and the results are attributed in Fig. III.8 of APPENDIX-III. It can be summarized that when one of the coil is used for biasing, the performance of Terfenol-D actuator improves when compared to varying the equal step input to both coils.

5.3.3 Repeatability of a Terfenol-D actuator

The repeatability and step response of an actuator is examined due to hysteretic behaviour of Terfenol-D material and exploring its potential in braking action. Tests were conducted to study the displacement response at regular time intervals as well as for continuous operation of actuator. Actuator is excited with constant DC input for one hour in a step of 5 min and the response obtained is plotted as shown in Fig. 5.6 (a). It is observed that the output of Terfenol-D actuator is stable and fluctuation is only ±0.6, ±0.6, ±1.5 and ±0.4 µm for 1 A, 2 A, 3 A and 4 A respectively. The reason can be considered as stochastic volatility including environmental factors and measurement errors. On the other hand, referring from Fig, 5.6 (b), the actuator output is recorded over duration of 15 sec when a constant DC input of 1 A, 2 A, 3 A and 4 A was supplied during the test. Each input is supplied continuously for 5 sec and is put off for next 5 seconds. Response of actuator is observed to be in the form of square wave.

(a)   (b)
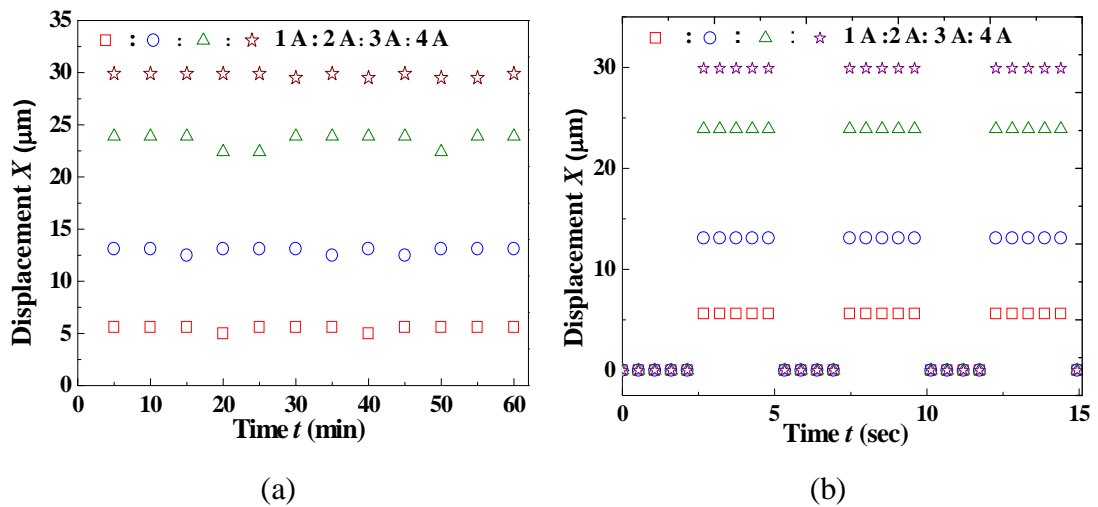
Fig. 5.6. (a) Repeatability and (b) step response of a Terfenol-D actuator by varying equal step input to coaxial coils under zero preload.
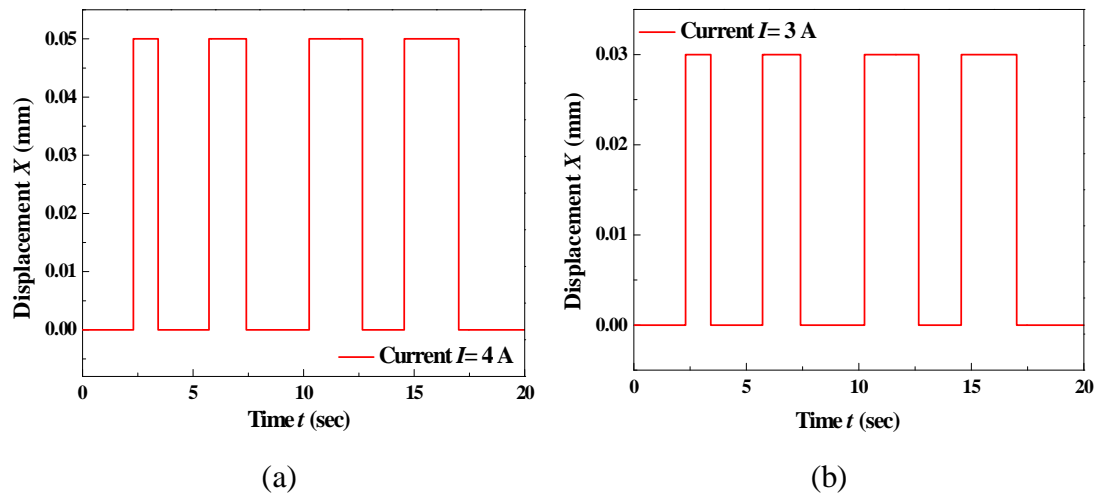
Fig. 5.7. Step response of a Terfenol-D actuator under (a) 1500 N and (b) 2000 N preload by varying equal step input to coil 1 and coil 2.

Fig. 5.7 (a) and (b) shows the response of Terfenol-D actuator obtained by exciting with a constant DC input of 4 and 3 A equally to coil 1 and coil 2 for a preload of 1500 and 2000 N. The Terfenol-D actuator was operated continuously for 20 sec by switching on and off the corresponding DC input equally to coil 1 and coil 2. Maximum displacement of 0.05 and 0.03 mm for 1500 and 2000 N preload was observed and it was constant for every cycle of around 1.5 sec. This test was conducted to quantify the displacement as well as response time due to their significance in the braking action.

The response of Terfenol-D actuator is verified by exciting with a variable DC input i.e. gradually increasing the input from one magnitude to next higher magnitude. Test is conducted for different operating conditions (refer section 5.3) under 1500 N preload. Vertical rise at the beginning of input and vertical fall when the input is put off was observed. Response of the Terfenol-D actuator reached the steady state at an average time of 27 sec. In between extremities, the stepped response has been observed due to the non-uniform operation of regulating knob of a DC power supply. Maximum displacement was 0.023 mm as shown in Fig. 5.8 (a) from the Terfenol-D actuator by varying equal step input to coil 1 and coil 2 from 3 A to 4 A.

116
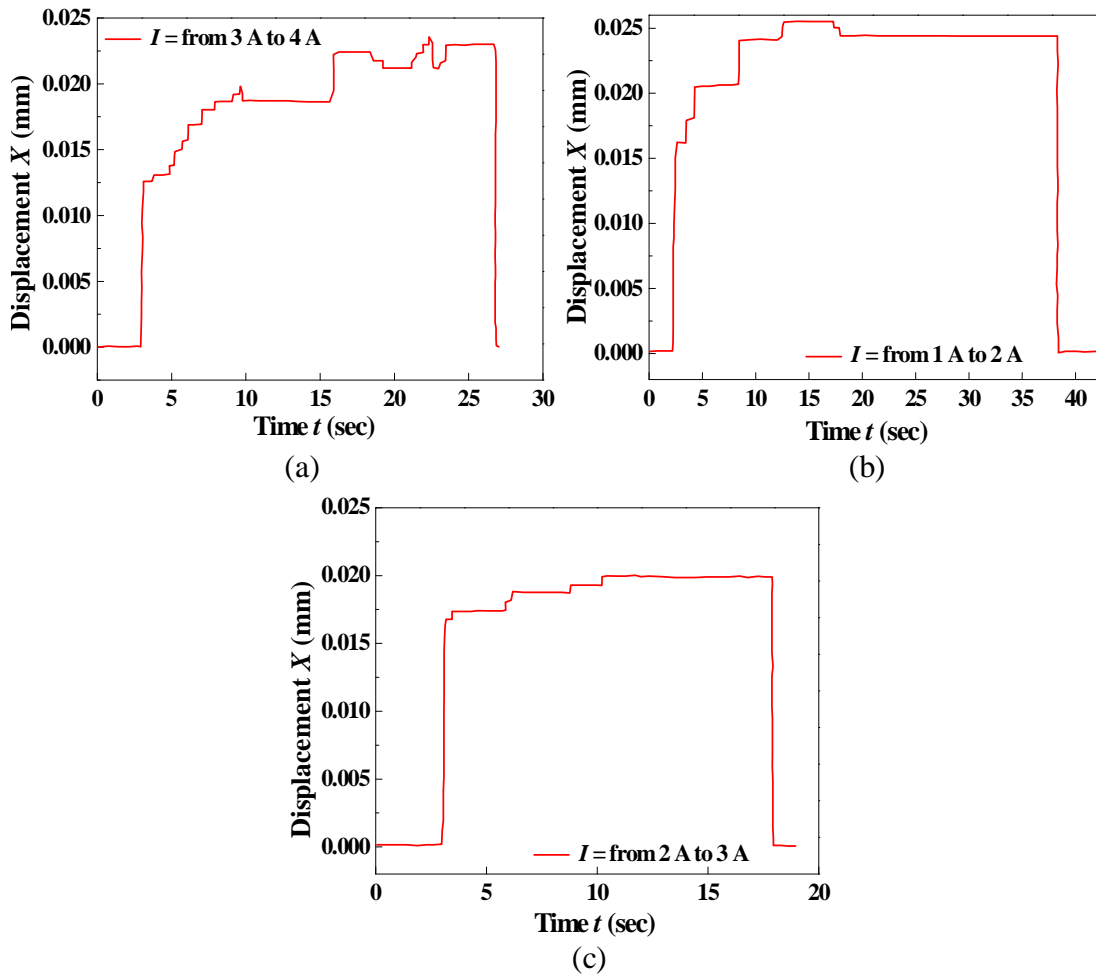
Fig. 5.8. Response of a Terfenol-D actuator (a) by varying equal input to coaxial coils from 3 A to 4 A (b) constant step input of 4 A to coil 1 and varying step input to coil 2 from 1 A to 2 A and (c) constant step input of 4 A to coil 2 and varying step input coil 1 from 2 A to 3 A.

From Fig. 5.8 (b), the maximum displacement of 0.024 mm has been achieved with constant step input of 4 A to coil 1 and gradually varying step input to coil 2 from 1 A to 2 A. For a constant step input of 4 A to coil 2 and gradually varying step input to coil 1 from 2 A to 3 A, the maximum displacement of 0.02 mm was observed from the Terfenol-D actuator as shown in Fig. 5.8 (c). It can be summarized that the maximum displacement from the Terfenol-D actuator can be achieved with constant biasing i.e. constant step input to coil 1 instead of varying step input to coil 1 or providing equal magnitude of input to coaxial coils.

117

5.4. THEORETICAL MAGNETOSTRICTION CURVES OF A TERFENOL-D FOR DIFFERENT PRE-STRESSES

Standard magnetostriction curves (known as butterfly curves) relating the strain to the applied magnetic field are generated using a sinusoidal input with a frequency of 0.2 Hz and field amplitude of 161 kA/m. Butterfly curves are available for Terfenol-D under zero prestress and optimum prestress of 6.9 MPa with a strain approaching 600 and 1800 ppm (refer Fig. III. 11 in APPENDIX-III). The objective is to plot the magnetostriction curves for different prestress in between 0 to 6.9 MPa. Further, the measured output displacement of an actuator can be compared with the theoretical value in between the zero and optimum prestress. Associated data are referred to from Engdahl (2000) and Kellogg and Flatau (2004) to plot magnetostriction curves of a Terfenol-D for different prestresses.

Table 5-1. Various parameters used in the magnetostriction model
(Kellogg and Flatau, 2004).

S. No.	Name of the parameter	Value
1	Pinning constant (k)	3283
2	Anhysteretic parameter (a)	7012
3	Reversibility Coefficient (c)	0.18
4	Saturation magnetostriction (λ_s)	435 ppm
5	Saturation magnetization (M_s)	0.765 MPa
6	Magnetic permeability of a Terfenol-D (μ_T)	3

In the present work, the magnetostriction curves i.e. zero and optimum prestress curves are chosen as two extremities. With these two curves as boundaries, the butterfly curves for the Terfenol-D material under preload of 500 N, 1000 N, 1500 N, 2000 N and 2500 N are generated as shown in Fig. 5.9. Initially, the magnetic field (H) is computed using $H_e(t,x) = H(t,x) + \alpha M(t,x)$ is assumed as $H(t,x) = H_{max} \sin(\omega t)$. Where H_{max} for Terfenol-D used is equal to 161 kA/m, α is mean field parameter representing interdomain coupling and frequency of 0.7 Hz. Eq.

(4.18) is used to evaluated the magnetization of a Terfenol-D (refer chapter 4). Finally the magnetostriction of a magnetostrictive material is computed using the quadratic magnetostriction model (4.19), for different prestresses (refer chapter 4). By referring these curves the required strain at an applied magnetic field for a corresponding preload can be evaluated. It is observed that the applied prestress causes the orientation of magnetic moments of a Terfenol-D rod that yields contraction in length. This in turn gives larger strain due to increased net moment rotation for an applied axial magnetic field.
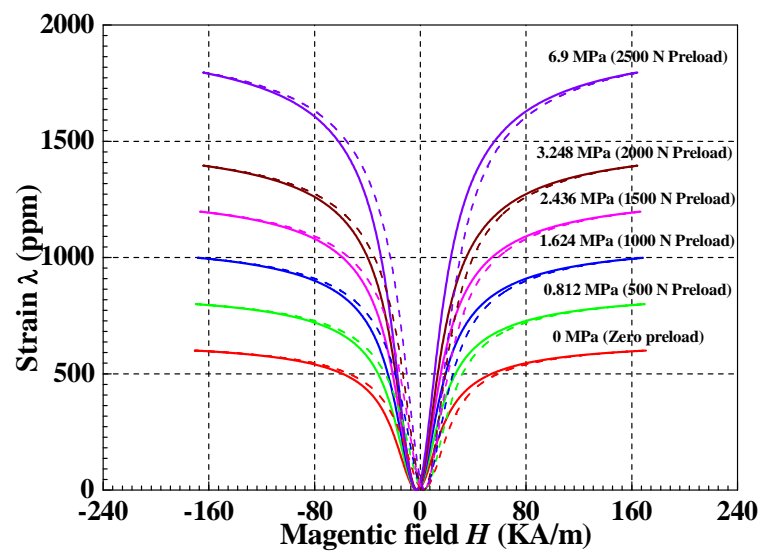
Fig. 5.9. Magnetostriction curves of a Terfenol-D ($Tb_{0.3}Dy_{0.7}Fe_{1.95}$) for different pre-stresses under sinusoidal input.

5.4.1 Young's modulus of a Terfenol-D for different pre-stresses

The elastic modulus of Terfenol-D material is dependent on the material's magnetic state through the magneto-mechanical coupling. It provides an important design parameter, the stiffness of the Terfenol-D material. An extensive research has been carried out to measure changes in modulus of elasticity with magnetization. Fig. 5.10 shows the changes in the Young's modulus at an applied magnetic field for different preload conditions. The Young's modulus for a Terfenol-D for all applied preloads are estimated by interpolation using the Eq. (5.1) and Eq. (5.2) given for zero and 6.9 prestress conditions (Kellogg and Flatau, 2004).

119

Young's modulus $\left(E^H\right)$ of a Terfenol-D under zero and 6.9 MPa pre-stress are given by

$$E^H = \left[20.0\times10^6 \times H + 20.0\times10^9\right] \text{ Pa} \tag{5.1}$$

$$E^H = [18.9\times10^6 \times H + 15.1\times10^9] \text{ Pa} \tag{5.2}$$

Where H is the applied magnetic field in Oestered.

An interesting trend observed from the Fig. 5.10 is that the Young's modulus increases as the applied magnetic field increased. Also, the Young's modulus of Terfenol-D material decreases as the applied prestress increased. This can be reconciled by considering the magnetostrictive processes occurring in a Terfenol-D material. The applied magnetic field favours magnetic moments direct towards the <111> easy axes approximately 19.5^0 to the longitudinal axis of the Terfenol-D material. However, the magnetic moments tend to align with the <111> easy axes virtually perpendicular to the longitudinal axis of Terfenol-D material under an axially applied preload.
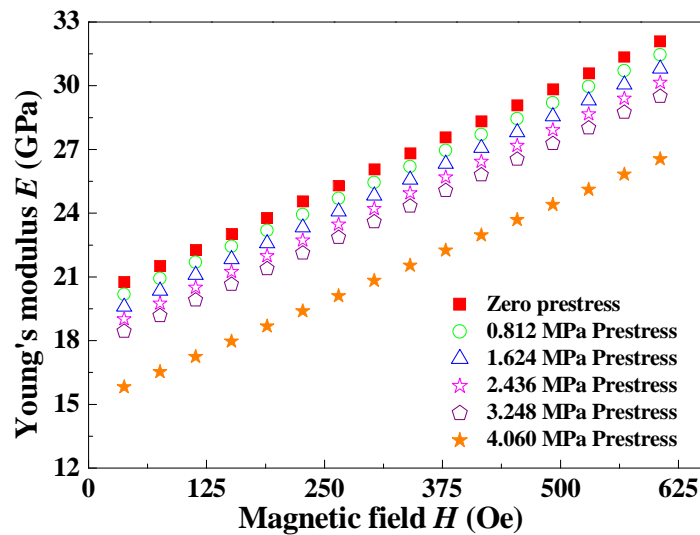
Fig. 5.10. Young's modulus of a Terfenol-D under different prestress conditions.

This makes the Terfenol-D material to give positive strain towards saturation, and magnetic easy axes are lying within the 19.5^0 of the applied magnetic field. This yields increase in the magnetic field of a Terfenol-D. The increase in the magnetic field causes to resist jumping of magnetic moments back to 90^0 easy axes. This makes

the Terfenol-D material appear stiffer to an external load. This is the reason due which an increased magnetic field would produce a higher Young's modulus in elongated Terfenol-D material (Kellogg, 2000). With this discussion, it is concluded that with the increase in magnetic field, the modulus of elasticity of Terfenol-D increases.

5.4.2 Theoretical displacement of a Terfenol-D actuator for different pre-stresses

Firstly the strain is read from the butterfly curves as shown in Fig. 5.9. The linear strain range lies between 75 ppm to 425 ppm for zero pre-stress assuming the actuator to be designed behaves linearly.

According to the Ampere's law, the magnetic flux intensity can be calculated as,

$$H = \frac{N_{coil}I}{l_{coil}} \qquad (5.3)$$

Where N_{coil} =Number of turn of the coil = 1000 turns, I = input current = 0 to 4 A, l_{coil} = length of the coil = 0.083 m

$$H = \frac{1000 \times 0.75}{0.083} = 9.036 \text{ kA/m or 113.5 Oe} \qquad (\because 1 \text{ A/m} = 4\pi \times 10^{-3} \text{ Oe})$$

With this the corresponding strain is read from the plot given by Fig. 5.9 as λ = 112.5 ppm. Theoretical displacement of the Terfenol-D actuator $(\delta l) = \lambda \times l_T$ = 9 µm. The displacement of the Terfenol-D actuator for the input of 0 to 4 A in a step of 0.25 A is calculated and plotted against the applied input to compare with experimental results in the following section.

5.4.3 Comparison of theoretical and experimental displacement of a Terfenol-D actuator

The comparison of theoretical displacement (section 5.4.2) with experimental displacement for zero and 500 N preloads are shown in Fig. 5.11 (a) and (b). The theoretical and experimental displacements are not in agreement with each other for an applied equal step input to coil 1 and coil 2 under zero and 500 N preload. The reason may be fluctuation in applied input, ohmic losses, low resistance of coils and

losses due to air gap presents among the components involved in the actuator assembly. Maximum theoretical displacement was 33 and 49.8 µm, whereas it is 29.7 and 25.5 µm from experiment for zero and 500 N preload. Mean sum of square of error is 39.6 and 42.6 between the theoretical and experimental displacement for an equal input to coaxial coils under 0 and 500 N respectively. The comparison of the same for 1000 and 1500 N is illustrated in Fig. III. 9 of APPENDIX- III.
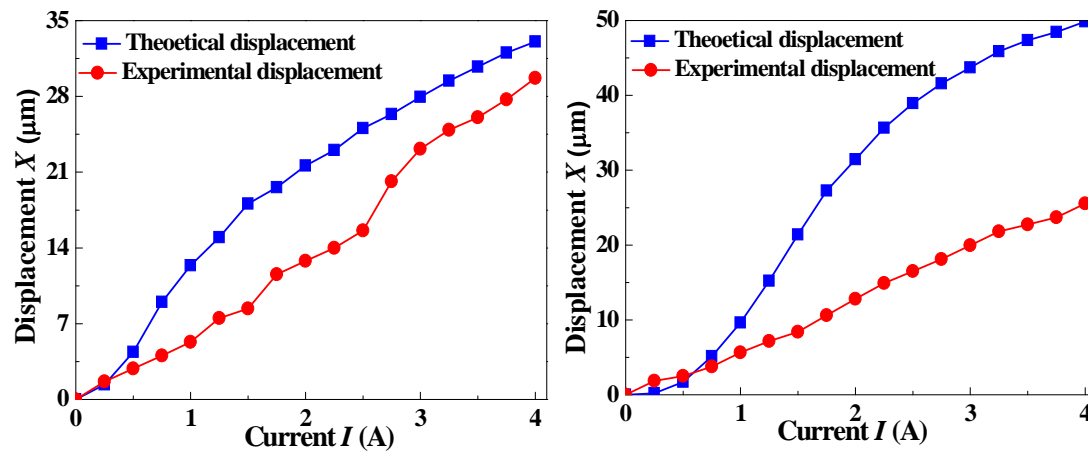
Fig. 5.11. Comparison of theoretical and experimental displacement of a Terfenol-D actuator with mild steel housing for (a) zero and (b) 500 N preloads.
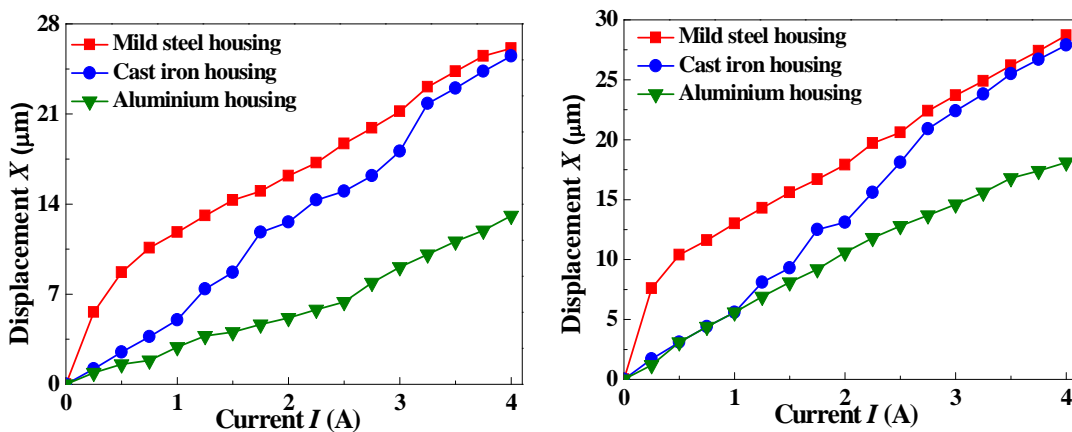
Fig. 5.12. Comparison of experimental displacement of a Terfenol-D actuator contained with different housing materials under (a) zero and (b) 500 N preload for equal step input to coil 1 and coil 2.

The comparison of experimental displacement obtained with different housing materials namely mild steel, cast iron and aluminium for zero and 500 N preload is shown in Fig. 5.12 (a) and (b). The maximum displacement of 26 and 29 µm was achieved by varying DC input simultaneously to coil 1 and coil 2 for an actuator

122

contained with mild steel housing. The displacement obtained for an actuator with mild steel housing is more compared to cast iron and aluminium housing as the permeability of housing materials differ. The maximum displacement obtained with a cast iron housing material is more compared to aluminium housing material. This may be because magneto motive force is not effectively reaching the measuring end of Terfenol-D rod. The maximum displacement achieved are 25.5 and 28 µm with cast iron, 13 and 18 µm with aluminium housing materials respectively under zero and 500 N preload. The percentage decrease in displacement obtained with cast iron and aluminium housing was 29 %, 63 % and 27 %, 45 % compared to that obtained from mild steel housing for zero and 500 N preload.

5.5 BLOCKED FORCE OF TERFENOL-D ACTUATOR

The output force–magnetic field relationship of a Terfenol-D actuator under different operating conditions is being examined to study blocked force characteristics. Blocked force is the force applied on the actuator to oppose the strain completely even after application of magnetic field. Its value will change with corresponding magnetic field. To start with, consider the output characteristics of an ideal actuator (Kellogg and Flatau, 1997 and 2004). Fig. 5.13 represents a DC load line, in which the ability of actuator to generate a DC force is linearly dependent on the displacement of the active material. The maximum displacement is observed at the lower right end of the load line under no load. Maximum force is achieved at the upper left of the load line as the strain produced tends toward zero. The maximum force is termed as the blocked force of an actuator.
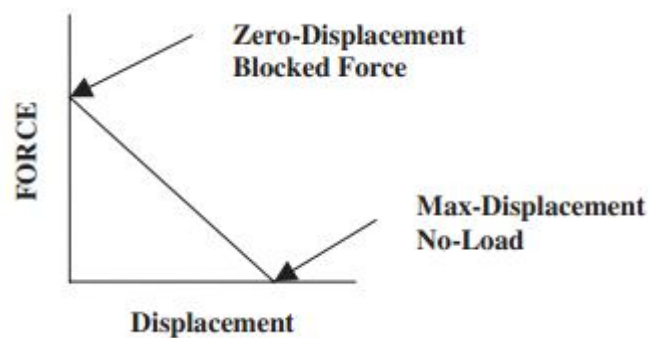
Fig. 5.13. DC load line for an ideal actuator
(Source of figure: Kellogg and Flatau, 2004).

123

Consider a simplified model of a general actuator's quasi-static performance given by the Hookean force-displacement relationship as,

$$F_B = k_T \delta l \tag{5.4}$$

Where F_B is the force produced by the Terfenol-D, k_T and δl are the stiffness and displacement of a Terfenol-D rod respectively.

The displacement is due to magnetostriction generated by an applied magnetic field and stiffness of a Terfenol-D can be computed by:

$$k_T = \frac{A_T E^H}{l_T} \tag{5.5}$$

Where E^H is the Young's modulus of a Terfenol-D rod at constant applied magnetic field, A_T is the cross-sectional are equal to 6.1575×10^{-4} m^2 and l_T is the length equal to 0.08 m of a Terfenol-D rod.

The maximum blocked force that can be developed in an actuator under preload conditions can be evaluated by combining Eq. (5.4) and Eq. (5.5) as reported in Kellogg and Flatau (2004) as follows,

$$F_B = A_T E^H \lambda_{max} \tag{5.6}$$

Where F_B is the blocked force, A_T is the cross-sectional area of a Terfenol-D rod, E^H is the Young's modulus and λ_{max} is the maximum strain potential at constant H can be read from Fig. 5.9.

Fig. 5.14 (a) and (b) shows the comparison of theoretical and observed blocked force of a Terfenol-D actuator under a preload of zero and 500 N. Blocked force of a Terfenol-D actuator was increasing for an applied magnetic field as the preload increased on comparing the theoretical and observed data. A maximum blocked force of 6036 N with theoretical and 3523 N with experimental has been achieved at an applied magnetic field of 48 kA/m for a 500 N preload. The percentage decrease in experimental blocked force was 10 % and 40 %, when compared to theoretical results for 0 N and 500 N respectively. Typical comparison of theoretical and observed blocked force for 1000 N and 1500 N are illustrated in Fig. III.10 of APPENDIX-III.
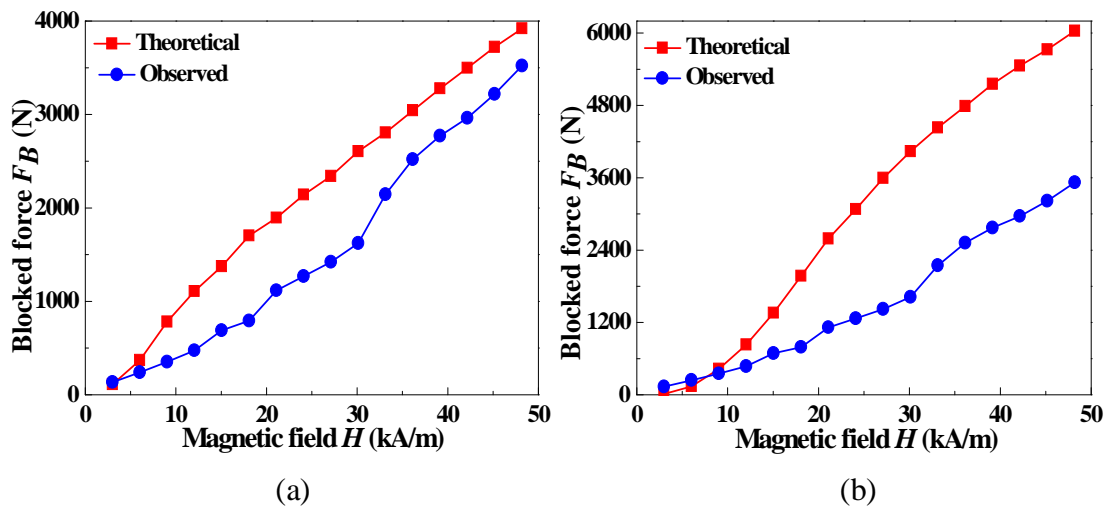
Fig. 5.14. Comparison of calculated and observed blocked force of a Terfenol-D actuator for (a) 0 N and (b) 500 N.

The comparison of experimental blocked force of a Terfenol-D actuator with different housing materials under different prestress conditions are shown in Fig. 5.15 (a), (b), (c) and (d). Blocked force increases as the applied preload is increased. As the magnetic field is varied, the blocked force increases with increased magnetic field for a given preload. As far as the having material of the actuator is concerned, the blocked force from Terfenol-D actuator contained mild steel housing is greater when the preload is large as can be seen from Fig. 5.15 (c) and (d). At low preload, the blocked force from actuator having mild steel and cast iron housing are more or less same magnitude. The actuator having aluminium housing produces low blocked force. Prestress causes the rotation of magnetic moment of Terfenol-D rod to align perpendicular to the applied prestress. This yield larger displacement and in turn exerts huge amount of force due to increase in net moment rotation when the Terfenol-D rod moments rotate into alignment with the magnetic field. The magnetic moments are predominantly perpendicular to the longitudinal axis of Terfenol-D rod at higher prestress. Magnetic moments sustain too much of mechanical load against which work must be done without taking initiation. This causes to produce high magnetostriction in turn larger force (Kellogg, 2000). Other interesting observation is that the blocked force from a Terfenol-D actuator contained with the mild steel housing is very high compared all housing materials, particularly with an aluminium housing. The flux lines produced due to an applied magnetic field penetrates more

125

into the Terfenol-D sample in an actuator contained with mild steel housing material. This causes the amplification of net moment rotation due to the moment rotation of Terfenol-D rod with the applied magnetic field. Thus yields the huge amount of blocked force in an actuator contained with mild steel housing compared to aluminium material of housing. Maximum experimental blocked force of about 3670 N, 6186 N, 6800 N and 6990 N has been achieved with mild steel housing at an applied magnetic field of 48 kA/m for 0 N, 500 N, 1000 N and 1500 N respectively.
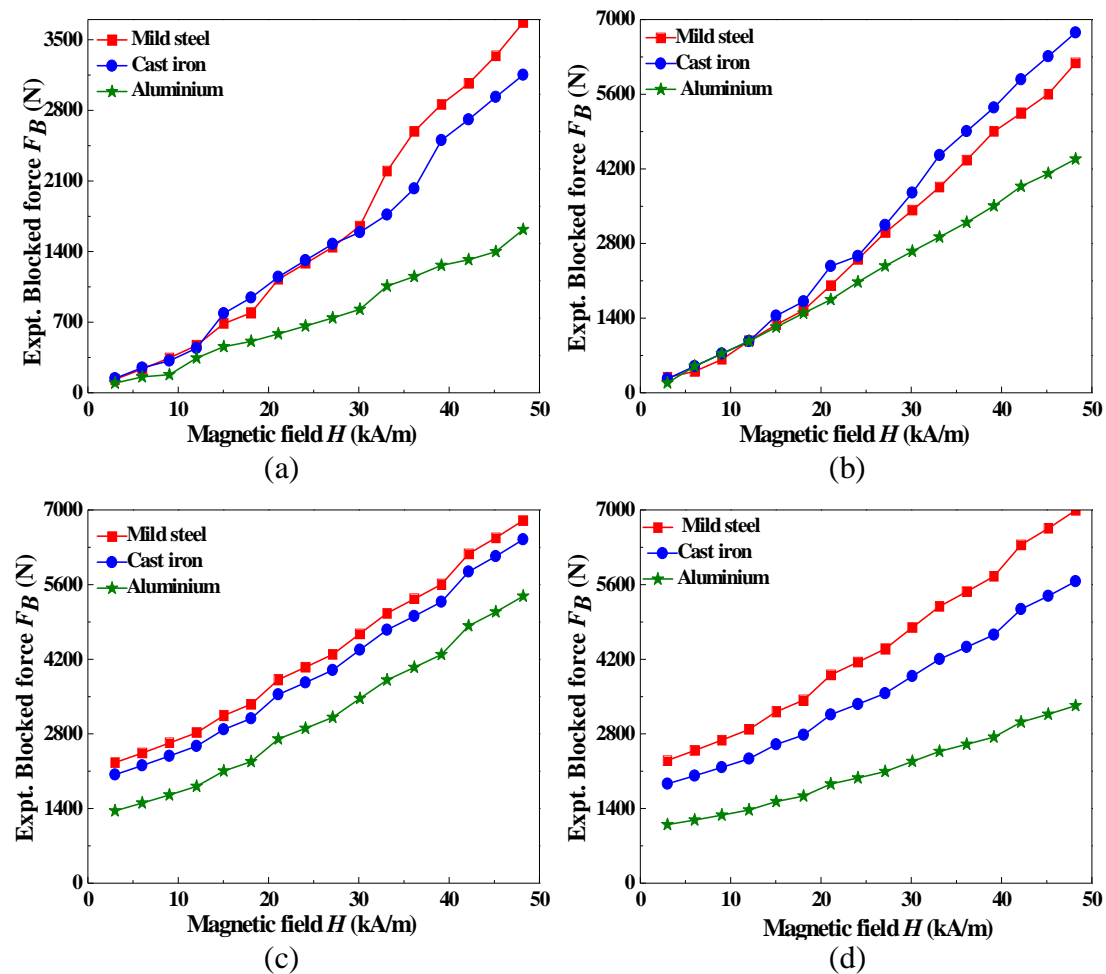
Fig. 5.15. Comparison of experimental blocked force of a Terfenol-D actuator with different housing materials under (a) 0 N (b) 500 N (c) 1000 N and (d) 1500 N preloads.

5.6 THEORETICAL AND EXPERIMENTAL RESPONSE TIME

Response time is one of the key parameters to describe the performance of Terfenol-D actuator in addition to the quantification of output displacement. In this section the comparison of response time calculated experimentally and theoretically has been

analyzed. Fig. 5.16 shows the behaviour of Terfenol-D actuator's response time against the current. It is observed that the theoretical response time of actuator remains unaltered irrespective of input current and variations have been observed with respect to experimental results for a given step input.
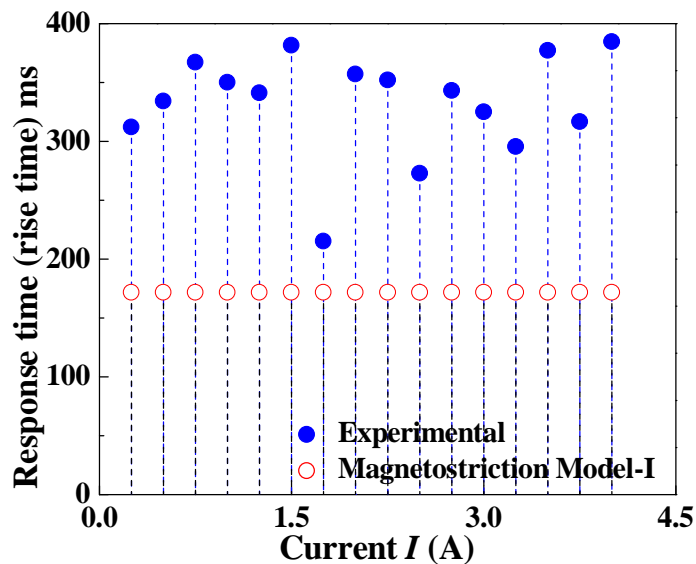
Fig. 5.16. Comparison of theoretical (model I) and experimental response time of a Terfenol-D actuator with zero preload.

The response time obtained from magnetostrictive model I is around 171 ms which is very less compared to the average response time of 300 ms from the experiments. The reason may be due to non-consideration of inertia of Terfenol-D rod, structural damping and internal strain energy in evaluating the response from the magnetostrictive model. Also, the response time of the actuator observed experimentally varies randomly. The existence of frictional forces acting among magnetic domains for an applied step input may be the reason for these variations in the experimental response time. The calculation of theoretical and experimental response time is illustrated in Fig. III.12 of APPENDIX-III.

5.7. EVALUATION OF FORCE EXERTED BY TERFENOL-D ACTUATOR

The complex behaviour of Terfenol-D material can be assumed_linear based on conditions like low working frequencies, reversible processes of magnetostriction, stress and strain uniformity in all the sections of the Terfenol-D rod. With these

assumptions, the coupling between the mechanical strain and the magnetization of a material is represented by the linear magneto-mechanical equations as:

$$S = -s^H T + dH \tag{5.7}$$

$$B = d^* T + \mu^T H \tag{5.8}$$

Where S is the strain, T is the stress, S^H is mechanical compliance at constant applied magnetic field strength H, d and d^* are linear piezomagnetic cross-coupling coefficients, μ^T is magnetic permeability at a constant stress T and B is the magnetic flux density within the material.

If the magnetostriction phenomenon is assumed to be reversible, then

$$d^* = d$$

The force exerted by the Terfenol-D rod is given by:

$$F_T = T_T A_T \tag{5.9}$$

Where the force exerted is F_T, A_T is the cross-sectional area and T_T is the stress induced in a Terfenol-D.

The current flowing in the coil windings and generating the magnetic field (H) can be calculated by the circulation of magnetic field.

$$H = \frac{N_{coil}}{\xi(l_f)} I = \frac{N_{coil}}{\xi(l+x)} I \tag{5.10}$$

Where N_{coil} is the number of the winding turns, l_f is the length of the Terfenol-D rod after elongation, l is the length of the Terfenol-D when $H = H_o$ and $T = T_o$ in which H_o and T_o denotes the magnetic field and stress at initial state of Terfenol-D rod. I is the current flowing in the windings and ξ is a coefficient to take into account the effective length of encircled field lines (≈ 2) and x is the change in the length of the Terfenol-D after an applied magnetic field. With a set of Eq. (5.7) to (5.10), the force exerted by a Terfenol-D rod reported in Braghin et al. (2012) can be written as:

$$F_T = T_T A_T = \left(-\frac{x/l}{s^H} + \frac{N_{coil}d}{s^H}\frac{I}{\xi l} \right) A = -K_s x + \frac{N_{coil}dA_{coil}}{s^H}\frac{I}{\xi l} \tag{5.11}$$

Eq. (5.11) gives the force exerted by Terfenol-D rod in which k_s is known as equivalent mechanical stiffness of the system. The equivalent mechanical system is equal to sum of the reciprocal of stiffness of Terfenol-D rod (k_T) and Belleville springs (k_B) assuming that these two are in series. Stiffness of Terfenol-D is equal to $A_T E^H / l_T$, where E^H the Young's modulus of a Terfenol-D in Pascal is found from Fig. 5.10. Stiffness of spring load (k_B) is equal to 361.925 kN/m.
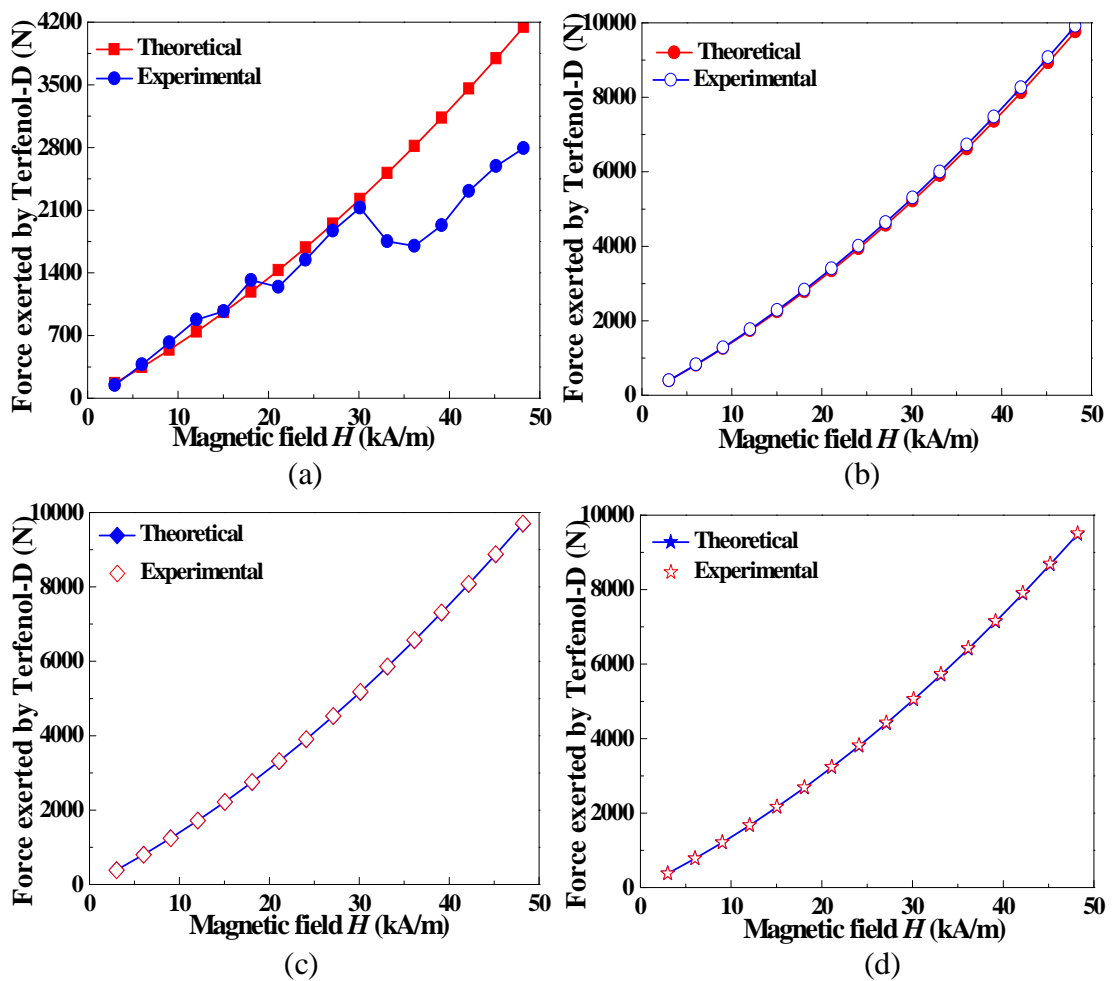
Fig. 5.17. Comparison of theoretical and experimental force exerted by Terfenol-D actuator contained with mild steel housing for (a) zero (b) 500 N (c) 1000 N and (d) 1500 N preload.

The force exerted by a Terfenol-D actuator contained is evaluated using Eq. (5.11) from the theoretical and experimental output displacement of a Terfenol-D actuator. Fig. 5.17 (a), (b), (c) and (d) show the comparison of theoretical and experimental

force exerted by a Terfenol-D actuator under different preloads. It is observed that the force increases as the applied magnetic field increased from the coils of an actuator. The force exerted by Terfenol-D actuator increases as the applied preload increased referring Fig. 5.17 (c) and (d). The theoretical and experimental force from the Terfenol-D actuator is in close agreement with each other for all applied preloads. However, the deviation between the theoretical and experimental force exerted by the Terfenol-D actuator has been observed. This deviation is found beyond an applied magnetic field strength of 30 kA/m under zero preload condition. The reason may be due to non-proper alignment of magnetic domains in a Terfenol-D material. The non-alignment of domains may be due to fluctuations in the applied input current. These fluctuations produce variations in the magnetic field strength produced by the coils. The variations in the magnetic field strength cause drop or decrease in the force that is being exerted by Terfenol-D. The maximum experimental force available from Terfenol-D actuator is around 9760 N for a preload of 1500 N whereas the theoretical force is 9920 N. Maximum deviation of 32 %, 2 %, 0.5 % and 0.3 % has been observed on comparing theoretical results with experimental results.

The comparison of experimental force exerted by a Terfenol-D actuator with different housing materials and preloads are shown in Fig. 5.18 (a), (b), (c) and (d). Force exerted by Terfenol-D is increasing as the applied magnetic field increases irrespective of housing materials. Maximum force of 9700 N is achieved with mild steel housing at an applied field of 48 kA/m for a 1500 N preload. The force exerted by Terfenol-D rod when operated in cast iron and aluminium housing reduces on an average of 10 % and 27 % respectively, compared to the operation of actuator with mild steel housing. The higher permeability of mild steel material may be the reason compared to cast iron and aluminium materials. The flux lines penetrate in to active material as it is surrounded by higher permeability materials. This may be another reason due to which the magnetic domains gain momentum to exert huge amount of force.
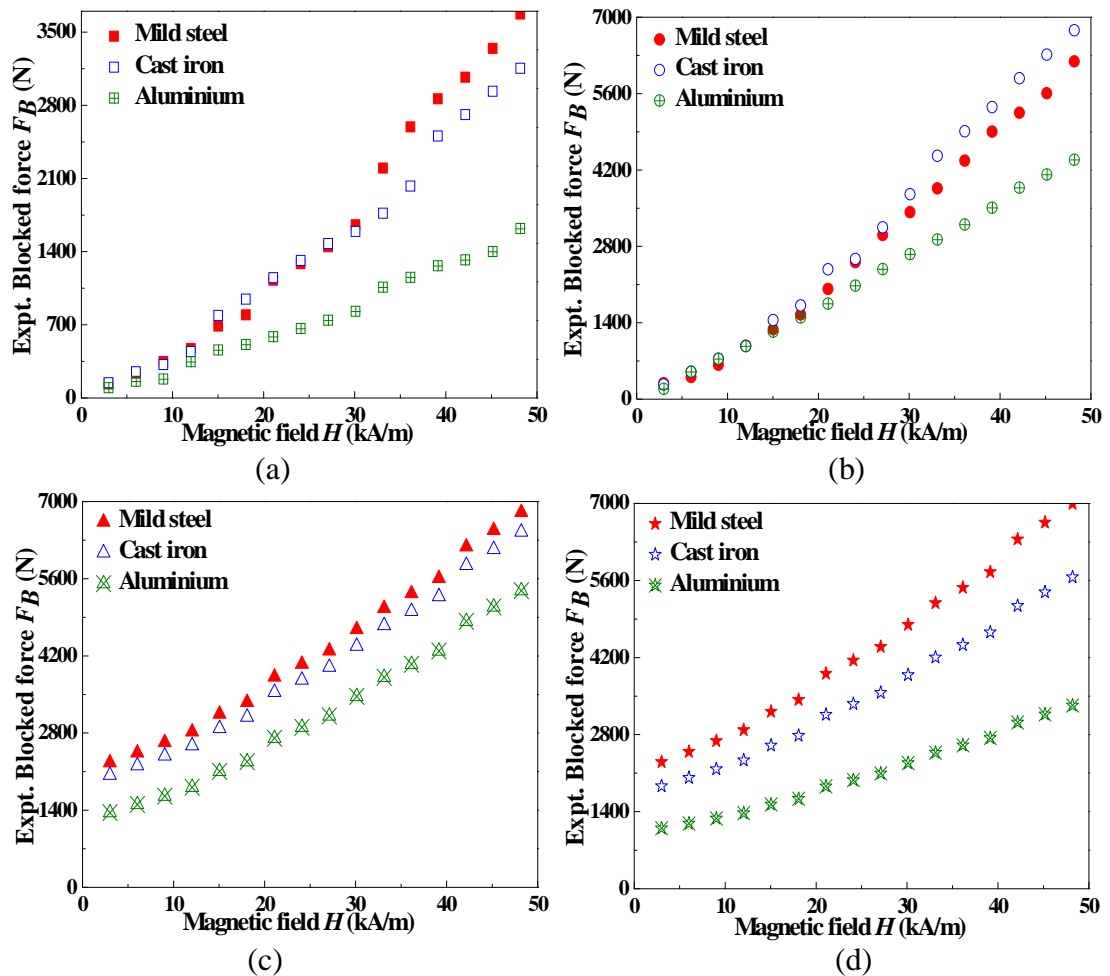
Fig. 5.18. Comparison of experimental force exerted by Terfenol-D actuator with different housing materials for (a) zero (b) 500 N (c) 1000 N and (d) 1500 N preload.

5.8. COMPARISON OF EXPERIMENTAL AND THEORETICAL DISPLACEMENT FROM TERFENOL-D USING DIFFERENT MAGNETOSTRICTION MODEL

The displacement obtained from experimental results are compared with the quadratic and proposed magnetostriction models for a preload of zero, 500 N and 1000 N are shown in Fig. 5.19 (a), (b) and (c). The average displacement obtained is 36 μm for all applied preloads with quadratic model. Average displacement of 24, 15.4 and 14.3 μm, 24.5. 18 and 17 μm, 25.3, 20 and 19 μm are obtained using magnetostrictive model I, magnetostrictive model II and experimental for an applied preload of zero, 500 N and 1000 N preload respectively. Minimum and maximum displacement of 0.87 and 77.4 μm has been achieved with quadratic model for all applied preloads

131

under an input current of 0.25 A and 4 A respectively. Minimum displacement of 0.6, 1.75 and 1.7 µm, 2, 4, 3.9 µm, 4.7, 6.3 and 5.2 µm has been achieved for an input of 0.25 A with magnetostriction model I, magnetostriction model II and experiment under zero, 500 and 1000 N preload. Maximum displacement of 51.6, 32 and 29.9 µm, 51.5, 34.4 and 34.2 µm, 51.5, 37 and 38.6 µm has been achieved for an input of 4 A with magnetostriction model I, magnetostriction model II and experiment under zero, 500 and 1000 N preload. Mean sum of squares of errors are 64, 45, 30 between quadratic model and experiment, 5.8, 1.7, 1.4 between proposed magnetostriction model I and experiment, and 5.9, 1.8, 1.5 between proposed magnetostriction model II and experiment for 0, 500, 1000 N preload conditions.

(a)

(b)

(c)
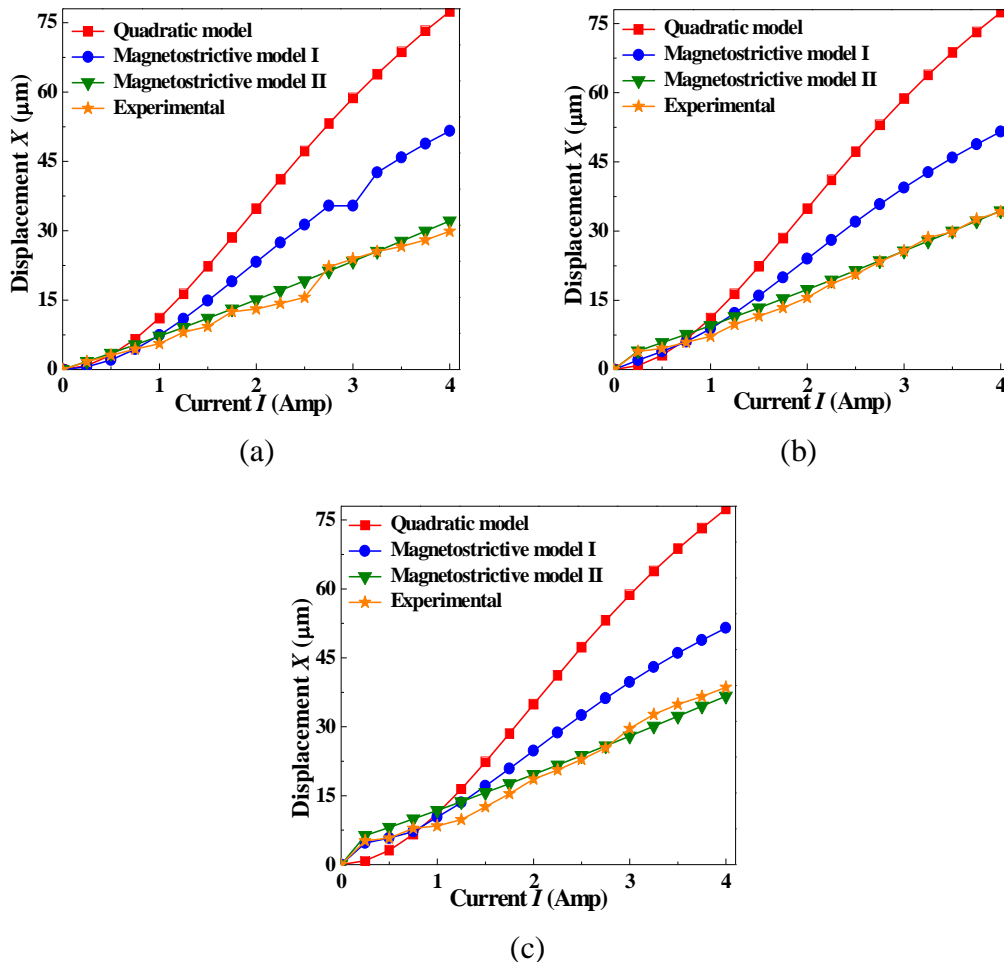
Fig. 5.19. Comparison of theoretical and experimental displacement of a Terfenol-D actuator for (a) zero (b) 500 and (c) 1000 N preload.

It has been observed that the theoretical results of magnetostrictive model I are in close agreement with experimental compared to magnetostrictive model II. It may be concluded that the magnetostriction model with all output parameters that affect the output are to be taken into account due to non-linear hysteretic behaviour of magnetostrictive material. Though the two magnetostriction models take many influencing parameters, the deviation in displacement obtained from experiment has been observed. This may be because of ohmic losses, source instability such as resistance of a coil and air gap present in an actuator among different components due to which there would be flux leakage. It is found with that the Jiles-Atherton model along with improved magnetostriction model I have provided good estimation on the magnetostriction for the designed actuator.
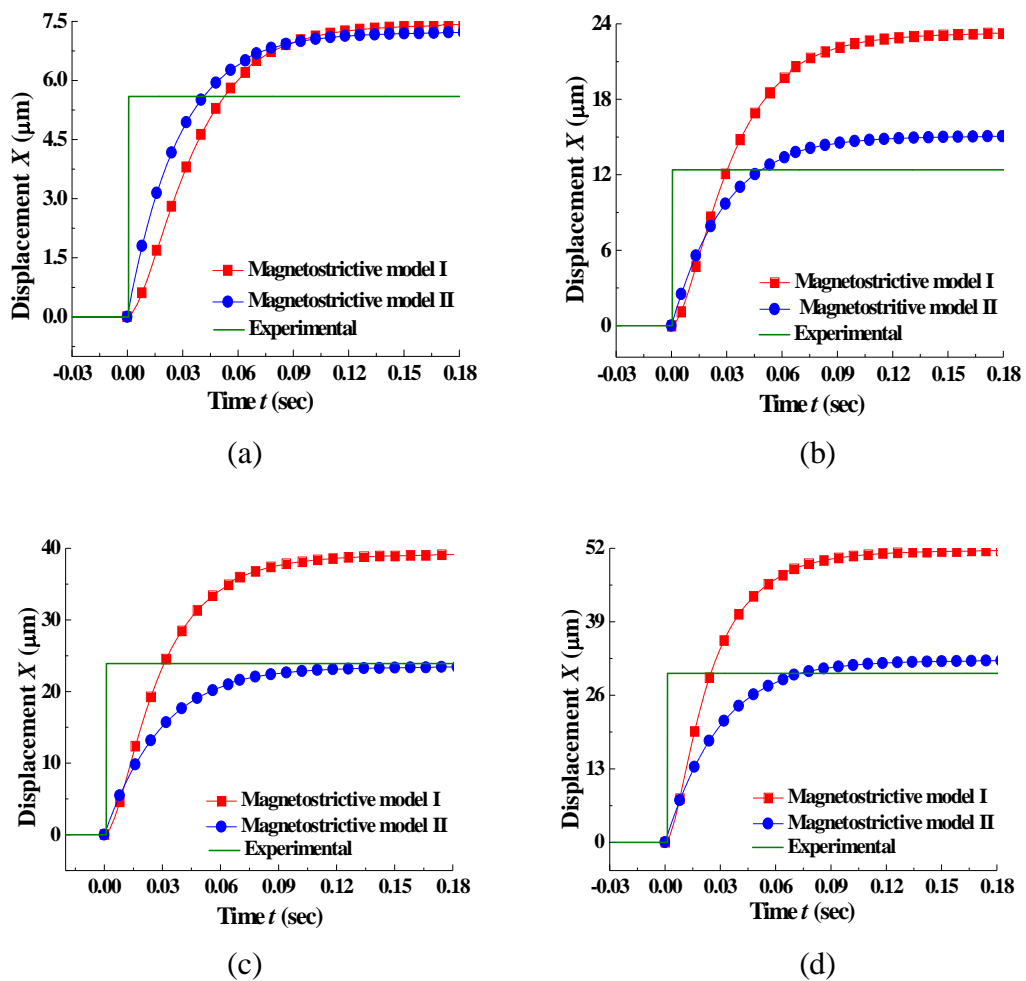
Fig. 5.20. Comparison of theoretical (model I and II) and experimental displacement of a Terfenol-D actuator for (a) 1 A (b) 2 A (c) 3 A and (d) 4 A equal step to coaxial coils.

Figure 5.20 (a), (b), (c) and (d) shows the comparison of displacement obtained from magnetostrictive models I, II and experimental for an applied equal step input of 1 A, 2 A, 3 A and 4 A respectively under zero preload conditions. The displacement achieved from model I and II are in close agreement with each other. The deviation has been observed between the model and experimental displacement. An average percentage reduction of 6 % between model I and experiment, 6 % between the model II and experiment has been observed.

5.9. SUMMARY

This chapter has discussed about the experimental set up and instrumentation with their specifications to conduct experiments on a Terfenol-D actuator under zero prestress and prestress conditions. Belleville springs were used for prestressing the Terfenol-D. The applied load was monitored by using force transducer interfaced to computer through NI Lab view software. The output characteristics such as displacement, repeatability, blocked force and force exerted by Terfenol-D actuator contained with housing materials namely mild steel, cast iron and aluminium has been measured under DC input to coaxial coils in different operating conditions. Magnetostrictive curves for the applied magnetic field were generated under sinusoidal input conditions to evaluate theoretical output displacement of a Terfenol-D actuator. Moreover, theoretically, the other characteristics such as blocked force and force exerted by a Terfenol-D actuator was evaluated and compared with the experimental results. Finally, the output displacement obtained from the magnetostrictive models including quadratic model was compared with the experimental results under different preload conditions. Based on results obtained, the following conclusions are drawn,

- Biasing a magnetic field to one of the coaxial coil on an average has improved the performance of Terfenol-D actuator by 27 % compared to simultaneous step input to coaxial coils in an actuator.
- Displacement achieved by varying magnetic field to one of the coil and with constant field to other coil is more than the displacement obtained by supplying equal step input to coaxial coils. The reason is that the net available

magnetic field produced by the coaxial coils is more at each point of excitation.

- Displacement obtained is less by varying magnetic field to coil 1 with constant field to coil 2 when compared to displacement obtained with constant magnetic field to coil 1 and varying field to coil 2. The magneto motive force produced by coil 2 is not reaching effectively the top end of the Terfenol-D rod to achieve more magnetostriction though the net available magnetic field at each point of excitation is same in both cases. The reason may due to less number of turns in coil 2 as well as it is far away from the Terfenol-D rod compared to coil 1.

- Displacement obtained is more in an actuator contained with all housing materials by varying biasing field to coil 1 when compared to displacement obtained by varying DC input to coil 1 and coil 2.

- Blocked force of a Terfenol-D actuator is increased as the applied magnetic field and preload increased and a deviation of 10 % and 2 % for a 0 N and 500 N respectively was observed when compared to theoretical results.

- Analytical and experimental displacements of a Terfenol-D actuator are in close agreement with each other and achieved a maximum displacement of 51.6, 51.4 and 51.5 µm with the improved model I, 32, 34.4 and 37 µm with improved model II and 29.9, 34.2 and 38.6 µm from experimental at an applied field of 50 kA/m for 0 N, 500 N and 1000 N preloads.

- Different parameters like inertia, structural damping and internal strain energy of a Terfenol-D are not considered, due to which the response time of a Terfenol-D actuator obtained with the magnetostrictive model I is far less than the experimental value. Response time of 171 ms has been obtained from magnetostrictive model I compared to an average experimental response of 300 ms.

- Force exerted by Terfenol-D actuator was discussed and a maximum theoretical force of 9920 N was obtained when compared to 9760 N from experimental with 1500 N preload.

- Experimentally a maximum force of 9700 N is achieved in a Terfenol-D actuator with mild steel housing at an applied field of 48 kA/m for a 1500 N preload. It has been observed the force is increased by 10 % and 27 % compared to contained with cast iron and aluminium housing materials.

- Magnetization using Jiles-Atherton model and magnetostriction using proposed model under DC driving conditions was evaluated. It was observed that the percentage decrease in the displacement was 52 % compared to quadratic magnetostriction model.

CHAPTER 6

ANALYSIS OF PERFORMANCE CHARACTERISTICS OF A MAGNETOSTRICTIVE DISC BRAKE SYSTEM

6.1. INTRODUCTION

Performance parameters of braking action are lower inertia, shorter response time, more stopping distance, heat energy generated and less braking torque (Limpert, 1999). These parameters are to be contented for the efficient and safety working of any automotive brake system. To meet the ever increasing requirements concerning braking performance the challenge is to explore alternative actuation arrangement, and the present chapter focuses on the potentiality of magnetostrictive actuation. In the present chapter, the required amount of axial braking force and torque capacity are estimated based on disc specifications. The hydraulic amplification mechanism is designed for the amplification of displacement obtained from the Terfenol-D actuator. Theoretical amplification concepts are discussed, maximum output energy and displacement capability of a Terfenol-D actuator is evaluated using stiffness match principle. Braking force and torque capacity of each annular pad available after amplification are evaluated from the theoretical and experimental output of a Terfenol-D actuator. Further, these results are verified with the data obtained based on disc specifications. In addition, the stopping distance and stopping time of magnetostrictive disc brake system are evaluated. Finally, the Terfenol-D actuator coupled with hydraulic amplification unit is tested for an applied step input under different preload conditions.

6.2. LAYOUT OF A MAGNETOSTRICTIVE DISC BRAKE SYSTEM

A schematic layout and block diagram of a magnetostrictive disc brake system are shown in Fig. 6.1 and 6.2. It consists of three units namely Terfenol-D actuator, displacement amplifying unit and caliper with rotor or disc unit driven by external DC

motor. Terfenol-D actuator will be excited by energizing the coaxial coils with a DC step input.
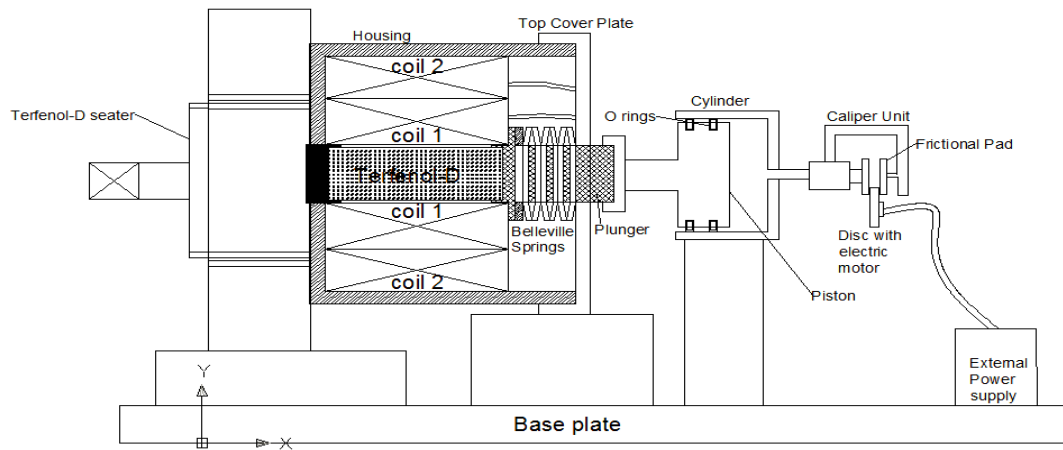
Fig. 6.1. Illustration of layout of a magnetostrictive disc brake.
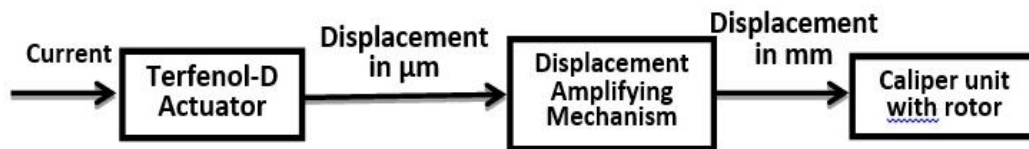
Fig. 6.2. Block diagram of a magnetostrictive disc brake system.

The Terfenol-D rod is kept at the center of coaxial coils and elongates along the axial direction. The output from the actuator will be in microns. The outcome from the Terfenol-D actuator is being amplified using displacement amplification unit to boost the output. The amplification unit consists of a small hydraulic cylinder filled with SAE 20-40 lubricating oil, and a piston is reciprocating inside it (Murata and Yamada, 1998). Due to the motion of piston driven by the Terfenol-D actuator, the pressure of SAE 20-40 lubricating oil inside the cylinder increases and further enters into two integrated small cylinders in a caliper unit. This pressurized fluid thus moves the frictional pads of a caliper unit and the rotor which is being rotated by external source will stop.

138

6.3. COMPUTATION OF AXIAL BRAKING FORCE FOR DISC BRAKE SYSTEM

The actuator is designed based on the required braking force which is one of the key factors in developing the prototype disc brake system. The axial braking force is computed by equating the kinetic energy possessed by the disc to the braking torque required to decelerate the disc. A disc of 160 mm diameter and an average disc speed of 3315 rpm are chosen for illustration in the present work. The disc speed of 3315 rpm corresponds to the vehicle moving at 100 km/hr. Cast iron is the material assumed for disc. Assuming the thickness equal to 3 mm and density of material as 7200 kg/m^3, the kinetic energy possessed by the disc equal to 83.8 Joules at disc speed of 3500 rpm. In disc brake system, the disc or rotor is stopped by applying the force perpendicular to the plane of the disc from either side. The procedure for calculating the axial force required to stop the rotor is discussed in Newcomb and Spurr (1967). The complete procedure and computation of axial braking force and braking torque for disc speed of 10 km/hr is illustrated in section IV.1 and IV.2 of APPENDIX-IV.

Table 6-1. Braking torque and axial braking force for different speeds.

Speed of the disc (km/hr)	Braking torque T (N-m)	Axial braking force (P_1) in (N) based on uniform pressure condition from Eq. (IV.7) in Appendix IV	Axial braking force (P_2) in (N) based on uniform wear condition from Eq. (IV.11) in Appendix IV	Maximum braking force (P_f) (N)
10	0.8	40	40.4	40.4
20	3.4	159.4	161.5	161.5
30	7.5	358.7	363.5	363.5
40	13.4	637.7	646.2	646.2
50	21	996.4	1009.7	1009.7
60	30.2	1435	1454	1454
70	41	1953	1979	1979
80	53.6	2550.8	2585	2585
90	68	3228.5	3271.5	3271.5
100	83.8	3985.7	4093	4093
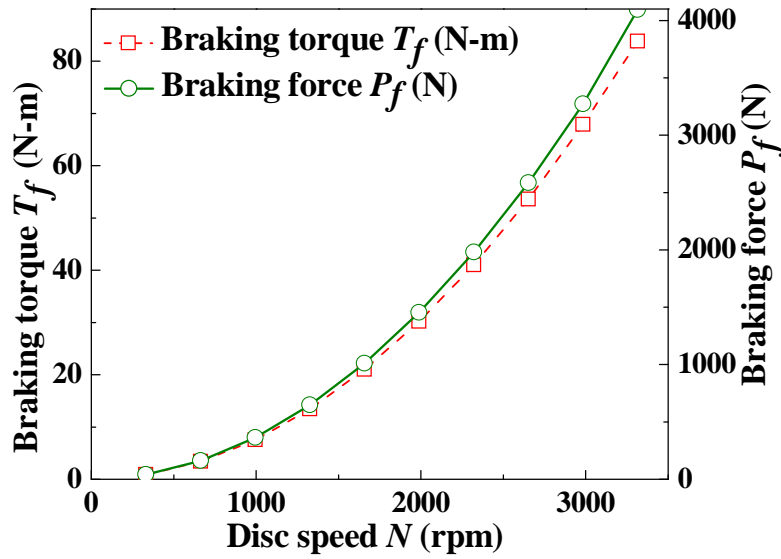
Fig. 6.3. Variation of braking torque and braking force with respect to disc speed.

The variation of braking torque and force for different disc speeds based on disc specifications such as disc diameter and disc speed were computed. The results calculated for the different speeds are listed in Table 6.1. As illustrated in Fig. 6.3, the behaviour of torque and force is quadratic in nature as the disc speed increases. A maximum braking torque and force of 83.8 N-m and 4039 N are required at a disc speed of 100 km/hr.

6.4. EVALUATION OF STOPPING DISTANCE AND STOPPING TIME FOR A DISC BRAKE SYSTEM

Stopping distance is extremely vital for emergency braking. It is based on the deceleration rate. It is also affected by the tyre deflection, air resistance, engine braking effort and the inertia of the drive line. From one of the Equations of motion,

$$v_1^2 - u_1^2 = 2as \tag{6.1}$$

Where v_1 is the final velocity of the disc equal to zero as it is brought to rest, u_1 is the initial velocity of the disc, a is the retardation produced by the braking force and s is the stopping distance.

Substituting $v_1 = 0$ and $a = \mu g$ in Eq. (6.1) yields,

140

$$s = \frac{u_1^2}{2a} = \frac{u_1^2}{2\mu g} \tag{6.2}$$

Eq. (6.2) gives the expression for the stopping distance due to retardation of the disc in meter (Giri, 1994). The stopping distance evaluated for different speeds of the rotating disc is available in Table IV.1, section IV.3 of APPENDIX IV.

From the Equations of motion,

$$v_1 = u_1 + at_s \tag{6.3}$$

$$t_s = \frac{v_1 - u_1}{a} \tag{6.4}$$

Eq. (6.4) gives the expression for the stopping time due to retardation of the disc in seconds. However for a given input, the time required to respond by the Terfenol-D actuator, time required for displacing the fluid from the hydraulic amplification unit as well as from each wheel cylinder of caliper unit to bring the annular pad towards rotating disc, time required to stop the disc together yields the total stopping time of disc brake setup. Firstly, the response time of a Terfenol-D actuator is identified from the response curves plotted as a function of time (refer chapter 4) in the present work. Secondly, the hydraulic amplification unit consists of cylinder and caliper unit integrated with cylinders. The time of response from these two units will be determined based on volume of the fluid displaced from the cylinders. In general, the time required to displace the fluid from a hydraulic cylinder can be evaluated by using the Eq. (6.5).

Time required to displace the fluid from a hydraulic cylinder $= (A \times L)/Q \tag{6.5}$

Where the cross-sectional area of a cylinder is A, L is the stroke length of a cylinder and Q is the discharge of the fluid from the cylinder. The stopping distance evaluated for different speeds of the rotating disc is available in Table IV.2, section IV.3 of APPENDIX IV.

Fig. 6.4 shows the variation of stopping distance and stopping time at different disc speeds. It is observed that the stopping distance is quadratic in nature as the disc speed increases. Minimum and maximum stopping distance of 1.3 m and 131 m has been observed at a disc speed of 331 rpm and 3315 rpm. The behaviour of stopping time is

linear i.e. stopping time is proportional to the disc speed as the speed of disc increases. Minimum and maximum stopping time of 1.2 s and 9.6 s has been observed at a disc speed of 331 and 3315 rpm respectively.
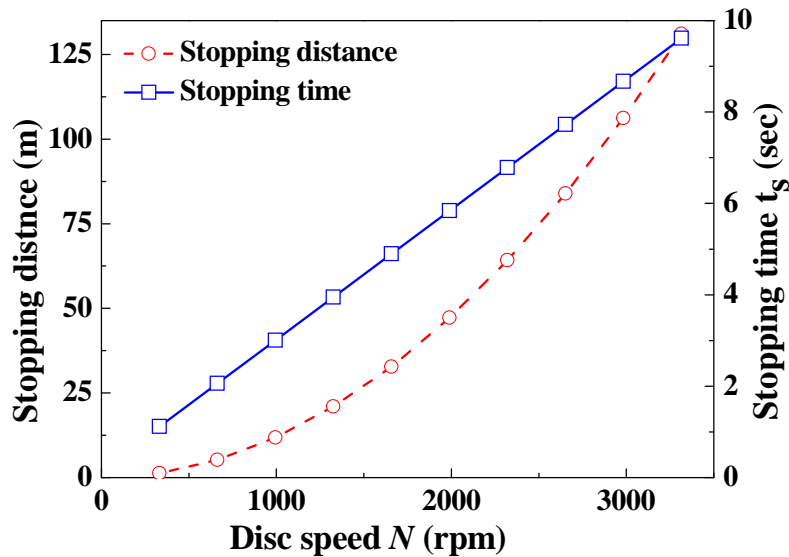
Fig. 6.4. Stopping distance and stopping time of a disc vs. disc speed.

6.5. EVALUATION AND VERIFICATION OF AXIAL BRAKING FORCE AVAILABLE AT ANNULAR FRICTION PADS OF A CALIPER UNIT

The axial braking force and torque available after amplification at the frictional pads of a caliper unit are evaluated from the theoretical and experimental displacement obtained from the Terfenol-D actuator. These results are verified with the braking force and torque obtained based on disc specifications. Terfenol-D material is capable of responding very fast and can produce only 0.1 % strain. To use this material in actual practice for bulk application, displacement amplification is necessary. Therefore, the output obtained from the Terfenol-D actuator for an applied input will be fed to the hydraulic amplifying unit to boost the displacement in the present work.

6.5.1. Design of hydraulic amplification unit

Amplifying mechanism is important in understanding smart-material based actuators. In general, the flexure hinge (Sun et al., 2011) and hydraulic types of amplification mechanisms are used (Sun et al., 2011; Giurgiutiu et al., 1995; Giurgiutiu et al.,

142

1996a). However, the hydraulic amplification is attractive due to variety of advantages (Giurgiutiu et al., 1997; Sun et al., 2011; Giurgiutiu et al., 1995; Giurgiutiu et al., 1996a and b; Chaudhuri et al., 2009), one among is that it can generate large mechanical gain in a compact package. Fig. 6.5 shows the coupling of components contributing to the amplification displacement at the annular friction pads of a caliper unit. Design of hydraulic amplification unit will be primarily based on the displacement required for the friction pads. This imposes additional forces like friction and compressibility of fluid on the magnetostrictive actuator.
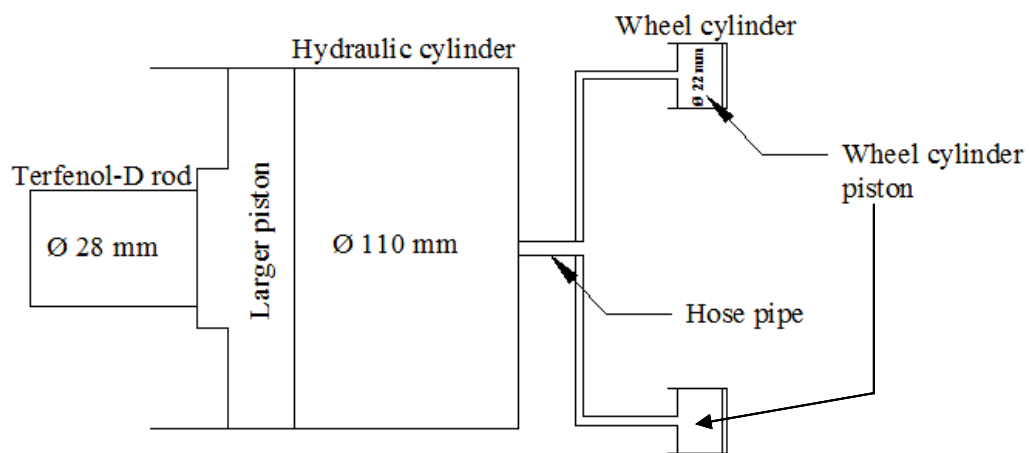
Fig. 6.5. Schematic diagram of a coupling between Terfenol-D, amplifying unit and wheel cylinder of a caliper unit.

In the present work, the mechanism consists of a hydraulic cylinder with a piston driven by a Terfenol-D rod at one end. The larger piston compresses the fluid in the cylinder due to displacement of Terfenol-D rod. The hydraulic cylinder is connected to the wheel cylinder unit using hose pipe. With increased pressure, the fluid from the larger cylinder enters into the wheel cylinders and acts on pistons of a wheel cylinder. The force exerted and displacement from the Terfenol-D actuator are 4146 N and 30 µm respectively for a step input of 4 A under zero preload. Based on these two outcomes and assuming an amplification ratio of 5, the diameter of larger piston is fixed as 110 mm in the hydraulic cylinder. Readily available caliper unit of two wheeler (Pulsar) is brought from the local market in which the diameter of each wheel piston is 22 mm.

The force exerted by a Terfenol-D rod is evaluated as described in section 5.7 (CHAPTER 5) that will be acted on larger piston. Corresponding to the force, the pressure on the fluid in the hydraulic amplification unit can be computed. According to Pascal's law, the force available at each wheel piston of the caliper unit is calculated. After amplification, the braking torque and braking force available at each annular pad are evaluated from the theoretical and experimental output displacement of a Terfenol-D actuator for an applied step input and preload. The detailed evaluation of braking force and torque achievable at the frictional pads of a caliper assembly is discussed in section IV.4 of APPENDIX-IV for zero preload. Braking force and displacement available at each annular friction pad at zero preload is tabulated in Table 6.2.

Table 6-2. Details of force, torque and amplified displacement.

S. No.	Parameter	From theoretical output displacement of a Terfenol-D actuator	From experimental output displacement of a Terfenol-D actuator
1	Pressure exerted by a Terfenol-D on larger piston	0.442 N/mm^2	0.3 N/mm^2
2	Force acting on each wheel piston	168 N	114 N
3	Torque capacity of each frictional annular pad	0.85 N-m	0.58 N-m
4	Amplified displacement at annular pads = 1.2 mm		

6.5.2. Comparison of available force and torque capacity on annular pads for different preloads

The braking force and torque capacity achieved after amplification at the frictional pads of a caliper assembly from the theoretical and experimental output displacement of a Terfenol-D actuator is compared for an applied step input under different preloads. Fig. 6.6 (a) and (b) shows the comparison of axial braking force and braking torque available at the annular pads of caliper unit in prototype magnetostrictive disc brake system for an applied input under zero and 1500 N preload conditions. It is observed that the braking force calculated from the theoretical and experimental output displacement of a Terfenol-D actuator is increasing as the applied step input is increased for an applied preload of zero and 1500 N preload, and its behaviour is non-

144

linear as shown in Fig. 6.6 (a). The braking force available at the annular pads is in close agreement with each other for 1500 N preload. The braking force show large deviation beyond an applied step input of 2.5 A for zero preload conditions. Maximum braking force achieved from the theoretical and experimental output of a Terfenol-D actuator is 168 N and 114 N with zero preload, 380 N and 378 N with 1500 N preload for an applied step input of 4 A respectively. It is concluded that the available amount of braking force is well within the range of force being computed based on disc or rotor design specifications as tabulated in Table 6.1.

(a)   (b)
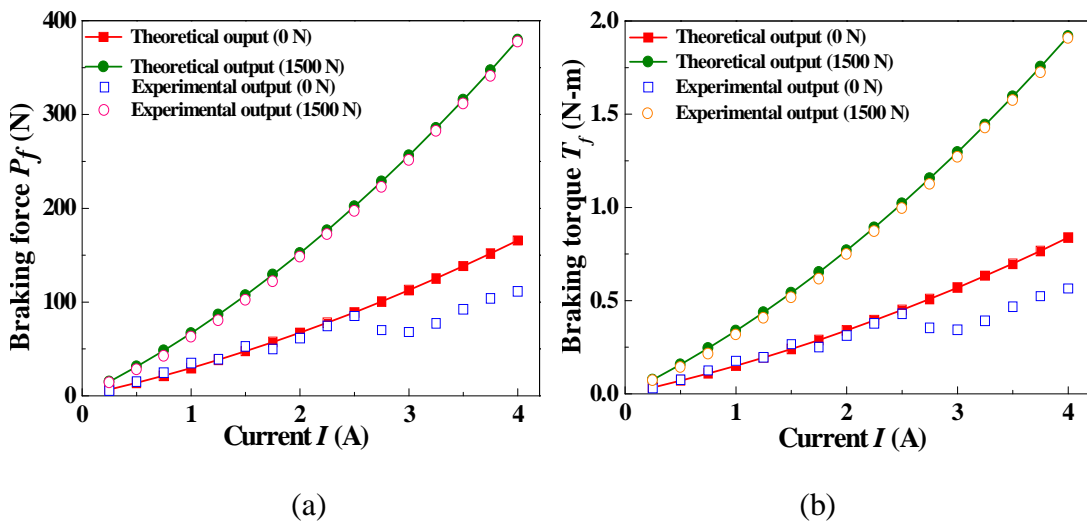
Fig. 6.6. Comparison of (a) braking force (b) torque capacity of frictional pads as a function of applied step input from the theoretical and experimental output of a Terfenol-D actuator for 0 and 1500 N preloads.

The torque capacity on each annular pad evaluated from the theoretical and experimental output of a Terfenol-D is compared for zero and 1500 N preload shown in Fig. 6.6 (b). The brake torque capacity of each annular pad achieved from the theoretical and experimental output of a Terfenol-D actuator is increases as the applied step input is increased for zero and 1500 N preload, and its behaviour is non-linear as similar to braking force. The braking torque available at the annular pads is in close agreement with each other for a 1500 N preload. The results are deviating beyond an applied step input of 2.5 A for zero preload conditions. Maximum braking torque achieved from the theoretical and experimental output of a Terfenol-D actuator is 0.84 N-m and 0.56 N-m with zero preload, 1.92 N-m and 1.9 N-m with 1500 N preload for an applied step input of 4 A respectively. This maximum torque

145

achievable is sufficient to decelerate or stop the disc or rotor till the rated speed of 800 rpm as tabulated in Table 6.1. It is summarized that the required amount of braking force and torque for the remaining speeds of 1000 and 1200 rpm or higher can be achieved by increasing the applied prestress on Terfenol-D actuator. The braking force and torque shows non-linear behaviour due to variation in the modulus of elasticity of a Terfenol-D material as it depends on movement of magnetic domains for an applied input under zero and 1500 N preload. The large variation observed in case of braking force and torque beyond 2.5 A input current due to decrease in the experimental output compared to theoretical output displacement for an applied step input under zero preload. The decrease in experimental output displacement may due to leakage of flux, ripples that are forming in the response at higher applied magnetic fields. These reasons may cause the large variations in the available braking force and braking torque for the applied input beyond 2.5 A.

6.6. DISPLACEMENT AND OUTPUT ENERGY OF A TERFENOL-D ACTUATOR USING STIFFNESS MATCH PRINCIPLE

Actuator using Terfenol-D is supposed to do work in most of the applications. It means that, the Terfenol-D rod should displace external mass. However, the external mass offers reaction force and if this external reaction is large then it will deform Terfenol-D rod to some extent thus reducing the induced strain. The other case can be the effective utilization of induced displacement from Terfenol-D actuator, when the external elements offer negligible resistance. From this view point, it is necessary to examine how the stiffness of Terfenol-D rod will overcome the stiffness of all other external elements (Giurgiutiu et al., 1995 and 1996a).

Overall performance of a Terfenol-D actuator is governed by two parameters namely, the displacement (X) and internal stiffness (K_i). The output displacement is due to magnetostriction effect, which is the basic property of the active material. Fig. 6.7 shows the representation of a Terfenol-D actuator in terms of spring elements possessing internal stiffness and external stiffness. One of the conditions is zero preloading condition at which $F = F(s_e)$. Other is due to external elements with

146

equivalent stiffness equal to K_e. It is assumed that all the external elements are connected in series possessing an equivalent stiffness, which is the resultant of stiffnesses of Belleville springs and plunger.
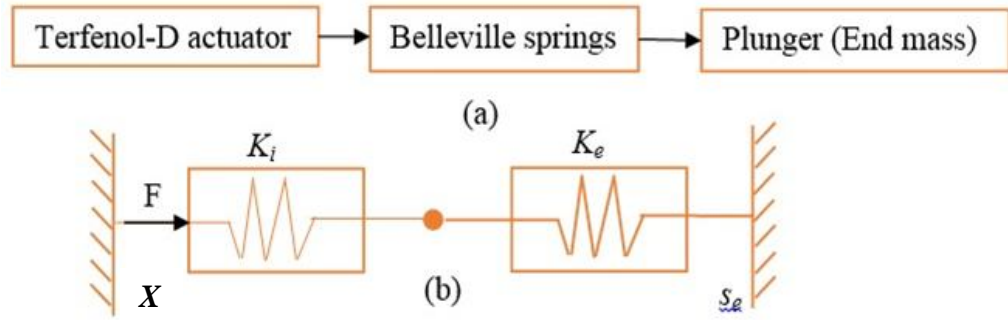
Fig. 6.7. Schematic of a Terfenol-D actuator with external elements (a) and representation of Terfenol-D and other external elements by means of springs (b).

The external load $F(s_e)$ produces a resistive elastic displacement $F(s_e)/K_i$, due to the compressibility of the Terfenol-D actuator.

The actuator output displacement s_e under external load is given by:

$$s_e = X - \frac{F(s_e)}{K_i} \tag{6.6}$$

Assuming that the external reaction load varies linearly with the output displacement, it can be represented by an external spring of equivalent stiffness as shown in Fig. 6.7 (b).

The external load is given by:

$$F(s_e) = K_e s_e \tag{6.7}$$

Substituting Eq. (6.6) in Eq. (6.7) and on simplifying, the output displacement is expressed as:

$$s_e = \frac{1}{1+b} s_{TA} \tag{6.8}$$

Where b is the stiffness ratio equal to K_e / K_i.

Output energy of the Terfenol-D actuator is given by:

$$E_{TA} = \frac{1}{2} K_e s_e^2 \tag{6.9}$$

Substituting Eq. (6.8) into Eq. (6.9) yields the output energy of the Terfenol-D actuator in terms of stiffness ratio.

$$E_{TA} = \frac{b}{(1+b)^2} \left[\frac{1}{2} K_i s_{TA}^2 \right] \tag{6.10}$$

Using Eq. (6.10), the output energy of a Terfenol-D actuator is evaluated as a function of a stiffness ratio. Where internal stiffness of Terfenol-D $A_T E^H / l_T$ equal to 230.9×10^3 kN/m and external stiffness is equal to $1/K_e = 1/K_B + 1/K_p$. Where K_B is the stiffness of Belleville springs equal to 361.9 kN/m and K_p is the stiffness of plunger equal to 45300 kN/m.

The Eq. (6.8) can be expressed as,

$$S = \frac{1}{1+b} \tag{6.11}$$

Where S is known as output displacement coefficient equal to s_e/X.

The output energy of a Terfenol-D actuator given by Eq. (6.10) comprises a variable coefficient that depends on the stiffness ratio and a constant energy coefficient depends only on displacement of a Terfenol-D actuator and internal stiffness of Terfenol-D. These two parameters are reference parameters of the Terfenol-D actuator, therefore the second term of an Eq. (6.10) is known as reference energy of a Terfenol-D actuator.

$$E_{ref} = \left[\frac{1}{2} K_i X^2 \right] \tag{6.11}$$

The ratio of variable term and constant term given by Eq. (6.10) is known as output energy coefficient denoted as E_e' is given by,

$$E_e' = \frac{E_{TA}}{E_{ref}} = \frac{b}{(1+b)^2} \tag{6.12}$$

From Eq. (6.11) and (6.12), it is observed that the governing factor in the design of a Terfenol-D actuator depends on stiffness ratio.

6.7. CONCEPT OF AMPLIFICATION FOR TERFENOL-D ACTUATOR

In present day practice, the displacement amplifiers are used to enhance the output of a Terfenol-D actuator. Simple mechanism like lever with unequal arms to complex systems such as flex-tensional, deformable triangles and hydrostatic can be used to improve the output of a Terfenol-D based actuator. Hydrostatic concept is used to amplify the output displacement of Terfenol-D actuator in the present work.

6.7.1. Output energy and displacement of a displacement amplified Terfenol-D actuator

An actuator comprising Terfenol-D is represented by means of spring with internal stiffness K_i is shown in Fig. 6.8. It is acted upon by external elements such as Belleville springs, end mass (plunger), large piston of a hydraulic amplification unit, two pistons of a wheel cylinders in a caliper unit as shown in Fig. 6.8. The amplification mechanism consists of a hydraulic cylinder with A_l and A_s being the cross-sectional areas of the larger and smaller pistons of cylinder. Assuming all these external elements in series and represented by an external spring with an equivalent stiffness K_e. External stiffness is equal to $1/K_e = 1/K_B + 1/K_P + 1/K_{PR} + 1/K_{WC}$. Where K_B is the stiffness of Belleville springs equal to 361.9 kN/m, K_P is the stiffness of plunger equal to 45300 kN/m, K_{PR} is the stiffness of piston rod of a hydraulic cylinder equal to 454650 kN/m and K_{WC} is the stiffness of pistons of a wheel cylinder equal to 22800 kN/m.
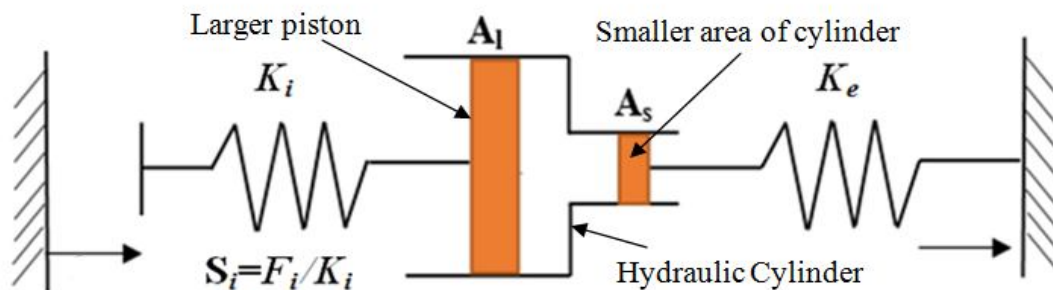
Fig. 6.8. Schematic of a displacement amplified Terfenol-D actuator with rigid support and hydraulic amplification mechanism.

At the input end, larger piston of a cylinder is actuated by Terfenol-D actuator producing the displacement of X .

Displacement of the larger end of a piston$= X - F_i/K_i$ (6.13)

Where F_i is the force exerted by the Terfenol-D actuator.

The displacement of larger end of the piston is expressed in terms of the volume of the fluid displaced V_l to the cross-sectional area of larger piston. Mathematically it is expressed as,

$$V_l/A_l = X - F_i/K_i$$ (6.14)

The external reaction (F_s) for an equivalent external stiffness (K_e) can be expressed as,

$$F_s = K_e s_s$$ (6.15)

Also, the pressure of the fluid in the cylinder from the larger end of piston is transmitted equally well and this pressure acts on the smaller end of piston, hence

$$p_l = p_s \implies F_l/A_l = F_s/A_s \implies F_l = F_s \times A_l/A_s = Z \times F_s$$ (6.16)

Where Z is the hydraulic gain of a cylinder equal to A_l/A_s.

Now expressing the internal force in the Terfenol-D actuator in terms of external reaction as,

$$F_l = ZF_s \text{ and } F_s = F_l/Z$$ (6.17)

Assuming the hydraulic amplifying cylinder is rigid with negligible losses then the displacement by the larger end of the piston is equal to the desired amplified displacement at the smaller end of the piston.

$$V_s = A_s s_s, \ V_s = V_l \text{ and } F_i = F_l,$$

Substituting V_s and F_i in Eq. (6.14) and introducing K_e/K_i as b, s_s/X as S' and on simplifying yields,

$$S' = \frac{s_s}{X} = \frac{Z}{1 + bZ^2}$$ (6.18)

The output energy coefficient for a displacement amplified Terfenol-D actuator (Giurgiutiu et al., 1997) is given by,

$$E_e'' = \frac{E_s}{E_{ref}} = \frac{bZ^2}{\left(1 + bZ^2\right)^2}$$ (6.19)

Where $E_e^{"}$ is the output energy coefficient and it is a function of both the stiffness ratio and hydraulic gain, E_{ref} is the reference energy coefficient and E_s is the output energy of a Terfenol-D actuator depends on stiffness ratio.

The optimal stiffness ratio in terms of hydraulic gain is obtained by differentiating the output energy coefficient of a Terfenol-D actuator given by Eq. (6.19) with respect to stiffness ratio and equating it to zero as follows,

$$\frac{d}{db}\left(E_e^{"}\right) = 0 \tag{6.20}$$

$$\frac{d}{db}\left[\frac{bZ^2}{\left(1+bZ^2\right)^2}\right] = 0 \tag{6.21}$$

On differentiating and simplifying the Eq. (6.21) yields,

$$b_{opt} = \frac{1}{Z^2} \tag{6.22}$$

Where b_{opt} is the optimum stiffness ratio.

For the fixed external and internal stiffness values, the optimum hydraulic gain can be written as,

$$Z_{opt} = \frac{1}{\sqrt{b}} \tag{6.23}$$

The output displacement coefficient of a Terfenol-D actuator corresponding to the optimum hydraulic gain is obtained by substituting the Z_{opt} in Eq. (6.18). It is given by,

$$S_{opt}^{'} = \frac{0.5}{\sqrt{b}} \tag{6.24}$$

From the Eq. (6.24) it is observed that the optimum amplification ratio is half the value of the optimum gain.

Fig. 6.9 (a) shows the variation of output energy coefficient of a Terfenol-D actuator plotted against stiffness ratio using Eq. (6.19). It is observed that the maximum output displacement will be obtained as the stiffness ratio approaches zero. The zero resistance is a situation when the external stiffness is less than internal stiffness and

leads to maximum displacement from the Terfenol-D actuator. This condition is of limited interest in the applications of actuator, since the actuation force is zero and does not deliver energy (Giurgiutiu et al., 1995, 1996 a and b).

(a)   (b).
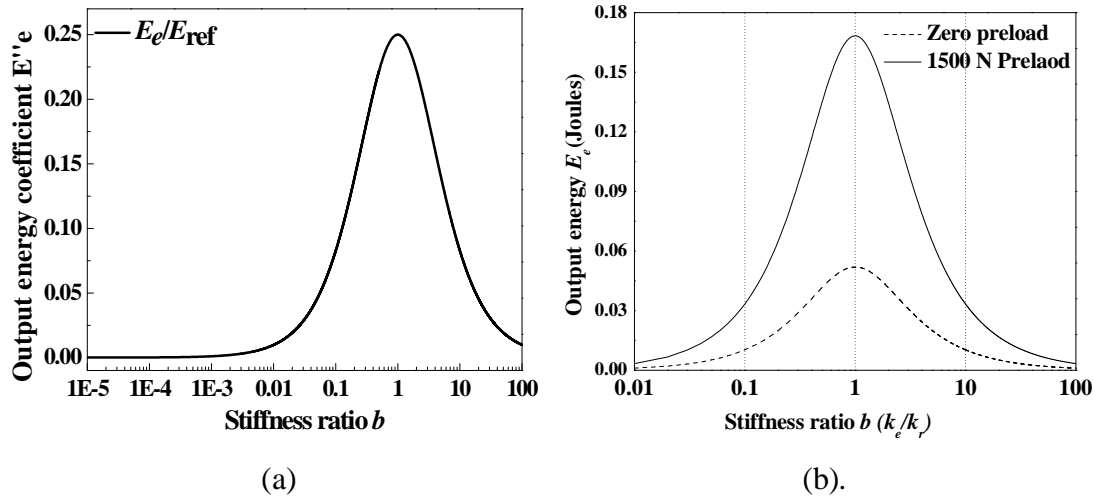
Fig. 6.9. Variation of (a) output energy coefficient and (b) output energy of a Terfenol-D actuator with stiffness ratio.

When the external stiffness is very much greater than the internal stiffness, the output force is maximum but the output displacement is zero and therefore the work done is null. Referring to Fig. 6.9 (a), it may be summarized that for stiffness ratio around 1 is an optimum value and can be determined using Eq. (6.19).

Fig. 6.9 (b) shows the comparison of output energy from a Terfenol-D actuator given by Eq. (6.10) as a function of stiffness ratio for zero and 1500 N preload. It is observed that the output energy is maximum when the internal stiffness of Terfenol-D rod is equal to equivalent stiffness of all the external elements involved in the prototype magnetostrictive disc brake system i.e. at b =1. This point is a stiffness match point and its significance is that it identifies the maximum value of the output energy that can be delivered by the Terfenol-D actuator. In the present work, the stiffness ratio of a Terfenol-D actuator equal to 0.0015. The corresponding output energy from the actuator will be 0.00016 and 0.001 Joules which is far less than expected output of 0.05 and 0.16 Joules at zero and 1500 N preload. The reason for less expected output from the actuator may be due to higher external stiffness compared to internal stiffness of Terfenol-D rod.

152

Fig. 6.10 (a) shows the variation of output displacement coefficient of a Terfenol-D actuator given by Eq. (6.18) plotted against stiffness ratio. It is observed that the maximum output displacement will be obtained as the stiffness ratio (b) approaches zero. The zero resistance exhibits when the external stiffness (K_e) is less than that internal stiffness (K_i) and as a result, the maximum displacement can be achieved from the Terfenol-D actuator. This condition is of limited interest in the actuator application since the actuation force is zero and does not deliver energy. When the external stiffness (K_e) is very much greater than the internal stiffness (K_i), the output force is maximum but the output displacement is zero and therefore again the output energy is zero. It is summarized that the optimal solution is to be extracted from these two extremities using Eq. (6.19) and found at stiffness ratio (b) equal to 1.

(a)   (b)
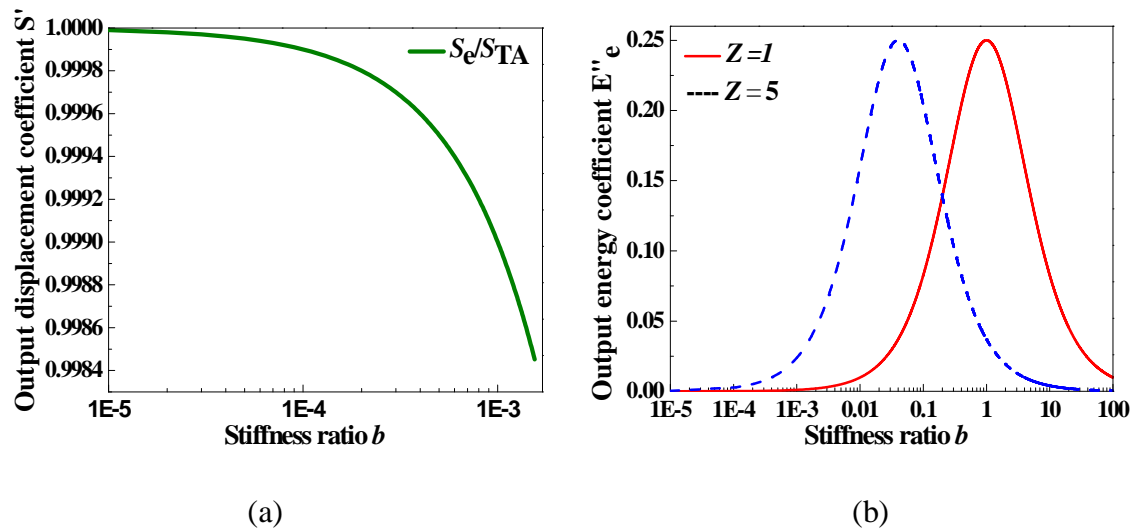
Fig. 6.10. Variation of (a) output displacement coefficient with stiffness ratio and (b) output energy coefficient with stiffness ratio for a hydraulic gain (Z) equal to 1 and 5 of a Terfenol-D actuator.

Fig. 6.10 (b) shows the output energy coefficient of a Terfenol-D actuator given with and without amplification using Eq. (6.19). The hydraulic gain is 1 and 5 for Terfenol-D actuator without and with amplification. It is observed that the Terfenol-D actuator without amplification reaches maximum value of the output energy coefficient for optimum stiffness ratio i.e. when external stiffness is equal to internal stiffness of a Terfenol-D actuator. When the hydraulic gain is 5 i.e. for the amplified

153

Terfenol-D actuator the optimal stiffness ratio changes and reaches output energy coefficient at lower optimal stiffness ratio. The output energy coefficient of a Terfenol-D actuator without amplification is equal to 0.25 Joules at $b = 1$ and at $b = 0.04$ for with amplification.

Fig. 6.11 (a) shows the variation of the optimum hydraulic gain and amplification ratio given by Eq. (6.23) and Eq. (6.22) against the inverse stiffness ratio. It is observed that both optimum hydraulic gain and amplification increases non-linearly as the inverse stiffness ratio increases. Optimum hydraulic gain of 316 and optimum amplification ratio of 158 has been achieved at an inverse stiffness ratio of 100000.

(a)   (b)
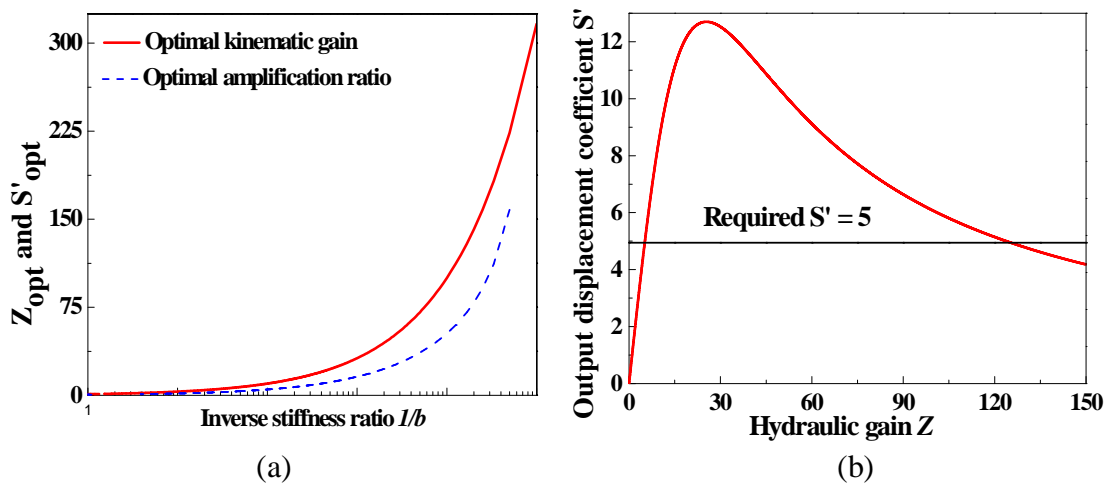
Fig. 6.11. Variation of (a) optimal kinematic gain and amplification ratio against inverse stiffness ratio and (b) output displacement coefficient with kinematic gain for a fixed stiffness ratio of 0.00155.

The hydraulic gain of a stepped cylinder can be chosen by knowing the output displacement coefficient and the stiffness ratio. The output displacement coefficient given by Eq. (6.18) can be solved for a given amplification ratio to determine the required value of hydraulic gain. Fig. 6.11 (b) shows the amplification ratio against the hydraulic gain for a fixed value of stiffness ratio equal to 0.0015. The hydraulic gain that produces a required output displacement coefficient is obtained by intersecting the $S' - Z$ curve with a constant amplification ratio line. From the Fig. 6.11 (b), it is also observed that the two solutions are possible i.e. Z_1 and Z_2. The two possible values of hydraulic gain are 5.21 and 123.8 for stiffness ratio equal to 0.0015.

154

6.8. TESTING OF TERFENOL-D ACTUATOR COUPLED WITH AMPLIFICATION UNIT

The individual units of prototype disc brake system were fabricated according to the design specifications and assembled as shown in Fig. 6.12. It was found that when the cylinder piston assembly of hydraulic amplification unit was filled with oil there was leakage. This indicates that the manufacture tolerances and the type of piston with O-rings used were insufficient for successful operation and test of brake unit. Attempts have been made to experimentally measure output at the end of larger piston of hydraulic amplification unit without brake fluid by coupling a Terfenol-D actuator assembly. Photographs of individual components of the magnetostrictive disc brake setup are illustrated in section IV.5 of APPENDIX IV. The pre-load is applied on Terfenol-D rod using a top cover plate provided with internal threads. By mounting and rotating a top cover plate over the housing, the belleville springs are compressed. This in turn causes load to act on the Terfenol-D. The load being applied on the Terfenol-D rod is extracted from the force-deflection curve. The force-deflection curve is plotted by calibrating Belleville springs using universal testing machine. Two trials were conducted to compress the six Belleville springs till flatten. The applied load from the load guage of universal testing machine and the corresponding deflection from the dial guage were noted. The deflection of individual trials and average deflection against the applied load was plotted. The resultant force-deflection curve is illustrated in section IV.6 of APPENDIX IV.
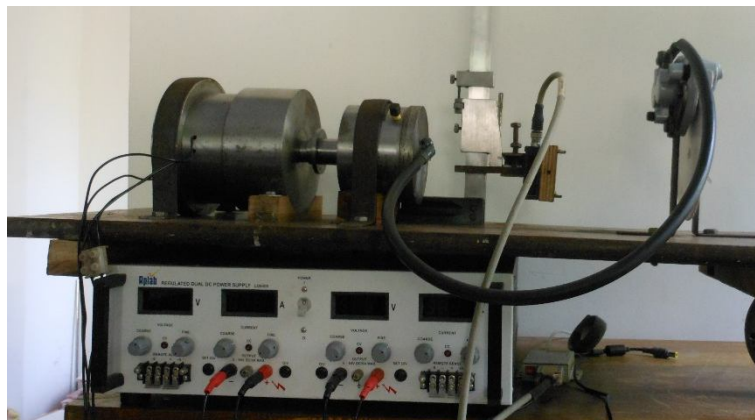
Fig. 6.12. Photograph of an assembled magnetostrictive disc brake system.

6.8.1. Capability of Terfenol-D actuator to displace external load

Fig. 6.13 shows the comparison of the output from the Terfenol-D actuator and the output from the larger piston of the assembly of Terfenol-D actuator with hydraulic amplification unit (also called as external load). A vertical step output obtained from the Terfenol-D rod and from the larger end of the piston for a step input of 4 A and a preload of 500 N is illustrated therein. The output from the larger end of the piston is reduced when compared to the output from the actuator alone. Primarily the piston has to overcome large frictional force. The displacement from the Terfenol-D actuator was 22 µm whereas the displacement available at the larger end of the piston moving inside was 16 µm. There is a deviation of 27 % due to the existence of friction in between the larger piston and cylinder surface.
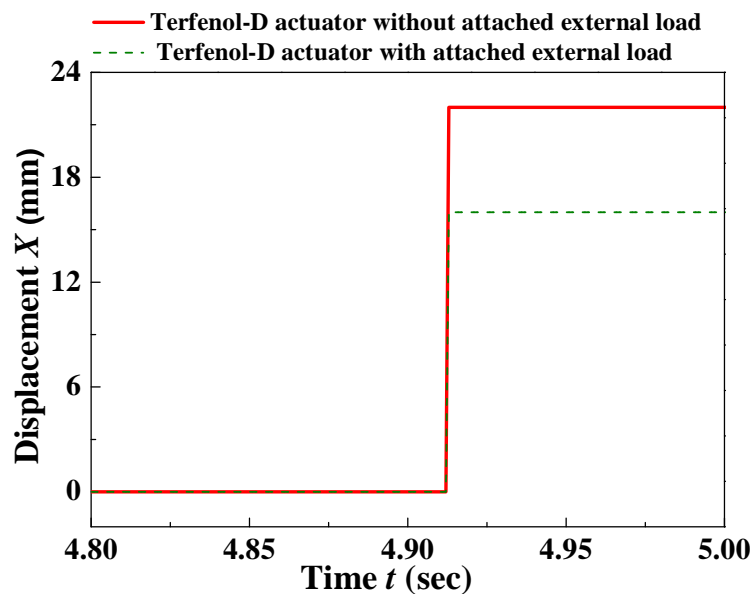
Fig. 6.13. Comparison of displacement of a Terfenol-D actuator with and without external load for 4 A step input.

The displacement at the larger end of the piston for different operating conditions and with preload of 500 N is shown in Fig. 6.14. It has been observed that the displacement at the larger piston when moving inside the cylinder was more with constant biasing to coil 1 and varying step input to coil 2 at each point of excitation compared other two operating conditions. The maximum displacement of 22 µm is achieved for all the input operating conditions for a Terfenol-D actuator only,

156

whereas 16 µm with constant biasing to coil 1 and varying step input to coil 2 is achieved for Terfenol-D actuator attached external load compared to other two operating conditions. Typical response plots for a Terfenol-D actuator with and without external load obtained from ILD software 1402 for an applied step input are illustrated in section IV.7 of APPENDIX-IV.
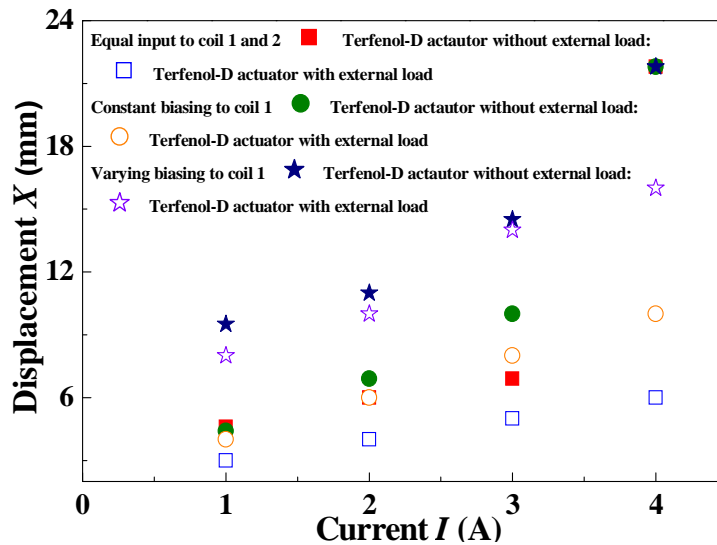
Fig. 6.14. Comparison of displacement of a Terfenol-D actuator without and with external load for different input operating conditions.

6.8.2. Comparison of theoretical and experimental response time of a Terfenol-D actuator without and with external load

Fig. 6.15 shows the comparison of response time obtained from the Terfenol-D actuator and the response when Terfenol-D rod does work to move the larger piston of the hydraulic cylinder for an applied step input under 500 N preload. The response time of the Terfenol-D actuator and with larger piston load from the experimental did not show consistent trend with respect to the applied input current. The existence of frictional forces acting among magnetic domains may be the reason for these variations in the experimental response time for the actuator. The response time of the larger piston in a hydraulic cylinder varies randomly for the applied input current. The reasons attributable are alignment and friction between moving surfaces.
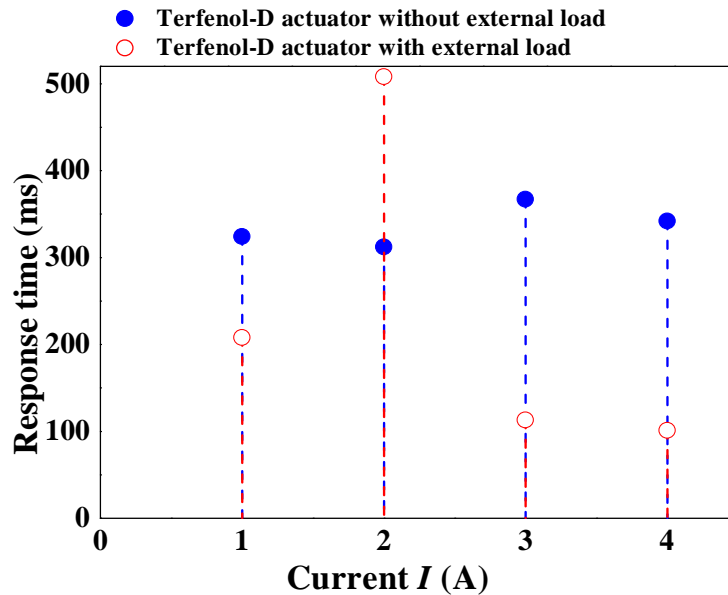
Fig. 6.15. Comparison of experimental response time of a Terfenol-D actuator with and without external load for 500 N preload.

6.9. SUMMARY

The layout of a proposed magnetostrictive disc brake system for the operation of frictional pads has been discussed. Hydraulic amplification mechanism has been designed to amplify 5 times the output displacement of a Terfenol-D actuator. The required amount of axial braking force, braking torque, stopping distance and stopping time have been evaluated based on disc design specifications. The axial braking force and torque capability of a disc evaluated from the theoretical and experimental output displacement of a Terfenol-D actuator. Further, the axial braking force and torque available after amplification at the frictional pads has been compared with the results evaluated based on disc specifications. Displacement and output energy of a Terfenol-D actuator has been analyzed using the stiffness match principle. Further, the output energy and displacement of a rigidly supported displacement amplified Terfenol-D actuator has been analyzed for the maximum output energy, optimum stiffness ratio and optimum amplification ratio. Based on the results obtained, the following conclusions are drawn,

1. Comparison of axial braking force and torque evaluated from the theoretical and experimental output displacement of a Terfenol-D actuator reveals that maximum braking force of 168 N and 114 N with zero preload, 380 N and 378

N with 1500 N preload, maximum braking torque of 0.84 N-m and 0.56 N-m with zero preload, 1.92 N-m and 1.9 N-m with 1500 N preload can be achieved for an applied step input of 4 A respectively. On comparison with the results based on chosen disc specifications, the rotating disc can be decelerated or stopped at a rated speed of 800 rpm. The required amount of braking force and torque for the remaining speeds of 1000 and 1200 rpm or higher can be achieved by increasing the applied prestress on Terfenol-D actuator.

2. The maximum output energy of 0.00016 and 0.001 Joules for a stiffness ratio of 0.00155 under a preload of zero and 1500 N have been achieved from the Terfenol-D actuator using the stiffness match principle. However, the expected maximum output energy is 0.05 and 0.16 Joules at an optimum stiffness ratio of 1.

3. The optimal stiffness ratio changes and reaches output energy coefficient at lower optimal ratio for the displacement amplified Terfenol-D actuator at a hydraulic gain equal to 5.

4. From the $S^{'} - Z$ curve, the possible hydraulic gain equal to 5.21 has been achieved which is very close to value of 5 assumed in the design of hydraulic amplification unit.

5. Response of a Terfenol-D actuator was examined for its capability in moving the larger piston of coupled hydraulic cylinder. A reduction of 27 % has been observed compared to Terfenol-D actuator alone for a step input of 4 A under 500 N preload.

6. Response time of a Terfenol-D actuator without and with attached external load was examined under 500 N preload. It is concluded that the time required for response is randomly fluctuating for an applied step input due to alignment and existence of frictional forces between moving surfaces.

CHAPTER 7

CONCLUSIONS AND SCOPE FOR FUTURE WORK

Prototype magnetostrictive disc brake has been designed, fabricated and an attempt was made to implement magnetostrictive actuation in automotive disc brake system. Terfenol-D actuator using coaxial coils (TCC layout) was designed.

Based on the magnitude of braking force which was sufficient to decelerate or stop the rotating disc, the diameter of Terfenol-D was found to be 13 mm. Readily available Terfenol-D rod of 28 mm was used in the actuator, and length of the rod was 80 mm. Suitable size of hollow cross-sectioned coaxial coils with required number of turns has been designed based on size of Terfenol-D rod. The number of turns for coil 1 and coil 2 were 560 and 440 respectively, which are close to 567 and 446 turns evaluated by reluctance approach. A separate coil used for biasing magnetic field proved effective in the layout of Terfenol-D actuator instead of permanent magnet.

Coaxial coils in free air were verified for axial magnetic field using analytical procedure based on shape factor. The coaxial coils (namely coil 1 and coil 2) were capable of providing a magnetic field of 28 kA/m and 21 kA/m with a flux leakage of 4.4 % and 18 % respectively corresponding to 4 A of input current.

Magnetic field parameters such as flux density, field intensity and flux distribution are analyzed for a coaxial coil alone in free air as well as for a Terfenol-D actuator contained with different housing materials namely mild steel, cast iron and aluminium using Maxwell 2D solver. It reveals that the magnetic flux distribution in a Terfenol-D assembly with mild steel housing becomes stronger by 2 % and 58 % compared to cast iron and aluminium housing materials used for actuator.

The different input operating conditions such as continuous step input, intermittent and gradually varying step input under different prestress conditions were imposed on

a Terfenol-D actuator to quantify displacement and its step response, repeatability and response time. From the experimental investigations, it was proved that when bias field from coil 1 is preferred the performance of Terfenol-D actuator improves by 27 % on an average compared to simultaneous step input equally to coaxial coils. Experimental tests on the Terfenol-D actuator have been illustrated to show its capability for the operation of brakes. Under ideal conditions, it has been shown that the theoretical and experimental displacement output when used for estimating brake force and brake torque were found to be well within the required amount as per the disc speed.

Inductance of driving coaxial coils was considered in arriving at magnetic field strength required for a Terfenol-D actuator. Quality factor was included in the existing magnetostrictive model in the evaluation of magnetostriction from a Terfenol-D rod. An average reduction in displacement was found to be 33 % and 50 % respectively under zero preload, 59 % and 52 % respectively with magnetostrictive model I and II compared to quadratic model. Analytical and experimental displacements obtained from a Terfenol-D actuator are in agreement with each other. An average deviation of 6 % has been obtained on comparing the displacements obtained from magnetostriction models (model I and II) with experimental results. It has been concluded that the Jiles- Atherton model along with the effect of quality factor in magnetostriction model can be used to obtain magnetization for the actuator.

Based on output obtained at zero preload, the displacement amplification unit was built to amplify 5 times the output of a Terfenol-D actuator. Theoretically the amplification concepts and its associated parameters such as output energy, amplification ratio and hydraulic gain were analyzed. The amplification ratio of 5.21 has been achieved based on stiffness ratio which is very close to an assumed value of 5. The output energy capability of a magnetostrictive disc brake set up using stiffness match principle revealed that the Terfenol-D actuator can deliver less than the expected output.

After amplification, the braking force and braking torque achievable at the frictional pads of a caliper unit was evaluated from the theoretical and experimental output

displacement of a Terfenol-D actuator. These results are compared and verified with the data obtained based on disc specifications. It was summarized that the disc can be decelerated or stopped till the rated speed of 800 rpm.

The individual units of a magnetostrictive disc brake system such as Terfenol-D actuator, hydraulic amplification unit and caliper unit with disc are assembled. Testing could not be accomplished due to leakage of brake fluid from the hydraulic amplification unit. However, attempts were made to conduct an experiment by coupling a Terfenol-D actuator to amplification unit without fluid.

The displacement of actuator coupled hydraulic amplification unit was reduced by 27 % compared to that obtained from the Terfenol-D actuator under 500 N preload. It reveals that the frictional forces among moving parts in hydraulic amplification unit must be minimized in order to improve response of the larger piston. The theoretical and experimental comparison of response time for a Terfenol-D actuator discloses that the variations in experimental response time may be due to inertia of Terfenol-D rod, structural damping and internal strain energy. The comparison of response time obtained from the Terfenol-D actuator and actuator with hydraulic amplification unit did not show consistent trend with respect to the applied input current which may be due to mis-alignment and friction between moving surfaces.

SCOPE FOR FUTURE WORK

Terfenol-D actuator being designed can be used to study the response characteristics under alternating current excitation (AC) for different preload conditions.

The present Terfenol-D actuator arrangement containing coaxial coils (TCC layout) can be replaced by a coil with permanent magnet (TCM layout) and the comparative studies on response characteristics can be carried out for step input under different prestress conditions.

The braking action can be accomplished with the existing setup by preventing leakage of fluid from the hydraulic amplification unit either by purchasing hydraulic cylinder with piston nearer to design specifications or fabricating a new unit with a lighter material instead used in the present study.

The hydraulic amplification unit can be fabricated to make provision for suitable sensor such that the response can be measured by coupling it to Terfenol-D actuator. Further, the response characteristics from the Terfenol-D actuator as well as actuator with hydraulic amplification unit can be studied for different input operating conditions under different prestress conditions.

The experimental studies to amplify the output displacement by mechanical means can be carried out. The mechanical means of amplification mechanism comprising rigid simple lever having unequal length on either side of pivot can be used. Further, the theoretical analysis can be carried out using amplification concepts to verify the amplification ratio assumed during experiment on actuator coupled rigid simple lever mechanism.

Numerical studies can be carried out on the response of a hydraulic amplification unit; mainly the behaviour of fluid velocity using LuGre (Lund-Grenoble) friction model. Mathematical model for hydraulic hybrid actuator (Terfenol-D actuator coupled hydraulic amplification unit) can be built to capture the phenomenon affecting system performance. Governing equations can be derived for larger piston of a hydraulic cylinder using force equilibrium considering compressibility of the working fluid.

Terfenol-D actuator being designed can be used as an active vibration control device. Experimental studies can be carried out in the application of active vibration control by mounting the actuator on a simple plate connected to a load cell fixed to the ground. The associated vibration phenomenon parameters such as acceleration of the base, inertial mass and the force transmitted to the ground can be acquired using load cell. Numerical studies can be carried out using simple linear model to implement control strategies.

REFERENCES

Angara, R. (2008). "High frequency high amplitude magnetic driving system for magnetostrictive actuators," Doctoral Thesis, University of Maryland, Baltimore County (UMBC).

Angara, R., Si, L. and Anjanappa, M. (2009). "A high speed magnetostrictive mirror deflector," Smart Material and Structures, 18(9), 1-7.

Aston, M.G., Greenough, R.D., Jenner, A.G.I., Metheringham, W.J. and Prajapati, K. (1997). "Controlled high power actuation utilizing Terfenol-D." Journal of Alloys and Compounds, 258(1-2), 97-100.

Bartlett, P.A., Eaton, S.J., Gore, J., Metheringham, W.J. and Jenner, A.G. (2001). "High-power, low frequency magnetostrictive actuation for anti-vibration applications." Sensors and Actuators A, 91(1-2), 133-136.

Benbouzid, M. E. H., Reyne, G. and Meunier, G (1995). "Finite element modeling of magnetostrictive devices: Investigation for the design of the magnetic circuit." IEEE transaction on Magnetics, 31(3), 1813-1816.

Braghin, F., Cinquemani, S. and Resta, F. (2011). "A model of magnetostrictive actuators for active vibration control." Sensors and Actuators A, 165(2), 342-360.

Brauer, J. R. (2006). "Magnetic actuators and sensors," A John Wiley & Sons Inc., Publication, Hoboken, New Jersey.

BS6722, (1986). "Recommendations for dimensions of ferrous & non-ferrous metallic materials in wire form," British Standards Institution, ISBN: 0 580 15358 4.

Bushko, A.D. and Goldie, J.H. (1991). "High performance magnetostrictive actuators." IEEE Aerospace and Electronic Systems Magazine, 2(11), 21-25.

Calkins, F. T., Dapino, M. J. and Flatau, A. B. (1997). "Effect of prestress on the dynamic performance of a Terfenol-D transducer." International Symposium on Smart Structures and Materials, San Diego, California.

Calkins, F. T., Smith, R. C. and Flatau, A. B. (2000). "Energy based hysteresis model for magnetostrictive transducers," IEEE Transactions on Magnetics, 36(2), 429-439.

Callister, W. D. and Balasubramaniam, Jr. R. (2007). "Material Science and Engineering- An Introduction," John Wiley and Sons, Inc., New York, USA, 680-717.

Carman, G. P. and Mitrovic, M. (1995). "Non-linear constitutive relations for magnetostrictive materials with applications to 1-D problems." Journal of Intelligent Material Systems and Structures, 6, 673-683.

Chakrabarti, S. and Dapino, M. J. (2012). "Coupled axi-symmetric finite element model of a hydraulically amplified magnetostrictive actuator for active power train mounts." Finite Elements in Analysis and Design, 60, 25-34.

Chakrabarti. S. B. S. (2011). "Modeling of 3D magnetostrictive systems with applications to Galfenol and Terfenol-D transducers", Doctoral Thesis, Ohio State University.

Chaudhuri, A., Yoo, J. H. and Wereley, N. M. (2009). "Design, test and model of a hybrid magnetostrictive hydraulic actuator." Smart Materials and Structures, 18(8), 1-21.

Chen, M., Chen, D. and Lu, Q. (2006). "Finite element analysis for magnetic field of giant magnetostrictive actuator" International Conference on Computer-Aided Industrial Design and Conceptual Design, 17th -19th November, Hangzhou, 1-4.

Chilambarasan, C., Gowda, A.S., Senthilkumar, S. and Suresh, C. (2014). "Experimental study to determine the variation over the material while exposed to magnetic field," 3(1), 20-22.

Chuan-li, W., Xia, C. and Ping, A. N. (2010). "Modeling and simulation of a high frequency micro-pump based on giant magnetostrictive material (GMM)," Journal of Coal Science & Engineering, 16(2), 206-209.

Claeyssen, F., Lhermet, N., Letty, R.L. and Bouchilloux, P. (1997). "Actuators, transducers and motors based on giant magnetostrictive materials." Journal of Alloys and Compounds, 258(1-2), 61-73.

Clark, A. E. (1980). "Ferromagnetic materials" Volume 1, Chapter 7, 531-589, Ed. E. P. Wohlfarth , North Holland Publishing Co., Amsterdam.

Clark, A. E. (1989). "Rare earth magnetostrictive materials." The Journal of the Acoustical Society of America, 85(S1), S61-S61.

Clark, A. E. and Belson, H. S. (1972). "Giant room temperature magnetostrictions in TbFe2 and DyFe2." Physical Review. B5, 3642-3644.

Culshaw, B. (1996). "Smart structures and Materials, Volume III, Norwood, MA: Artech House.

Dapino, M.J. (2000). "Non linear and hysteretic magnetomechanical model for magnetostrictive transducers," Doctoral Thesis, Iowa State University, Ames, Iowa.

Dehui, L., Quanguo, L. and Yuyun, Z. (2008). "Magnetic circuit optimization design of Giant magnetostricitve actuator." 9th International Conference Computer-Aided Industrial and Conceptual Design (CAID/CD), 22-25th November, Kunming, 688-692.

Dhilsha, K.R., Markandeyulu, G., Subrahmanyeswara Rao, B.V.P. and Rama Rao, K.V.S. (1997). "Design and fabrication of low frequency giant magnetostrictive transducer." Journal of Alloys and Compounds, 258(1-2), 53-55.

Diftler, M. A. and Hulse, A. (2010). "Magnetostrictive brake." NASA Tech Briefs, MSC-23629-1, Lyndon B. Johnson Space Center, Houston, Texas.

Disc vs Drum manual, http:// www.sime-strogmag.com, SIME-Stromag SAS India Pvt. Ltd., France.

Duenas, T., Sehrbrock, A., Lohndolf, M., Ludwig, A., Wecker, J., Grunberg, P., Quandt, E. (2002). "Micro-sensor coupling magnetostriction and magnetoresistive phenomena." Journal of Magnetism and Magnetic Materials, 242-245(2), 1132-1135.

Edwards, M. (2004). "Detecting foreign bodies in food," CRC Press, Woodhead Publishing Ltd., Cambridge, England.

Ekreem (2009)." An Investigation Of Electro-magnetic Rig-Generated Strong Magnetic Fields". Doctoral thesis, Dublin City University, Dublin, Ireland.

Ekreem, N. B., Olabi, A. G., Prescott, T., Rafferty, A. and Hashmi, M. S. J. (2007). "An overview of magnetostriction, its uses and methods to measure these properties." Journal of Materials Processing Technology, 191(1-3), 96-101.

Engdahl, G. (2000). "Handbook of Giant Magnetostrictive materials," Royal Institute of Technology, Stockholm, Sweden, 1-340.

Engdahl, G. (2002). "Design procedures for optimal use of giant magnetostrictive materials in magnetostrictive actuator applications." 8th International Conference on New Actuators, 10-12 June, Bremen, Germany.

Fargier, E. (1991). "Electrically driven brake," US patent, 5000295.

Ge, Z. and Deng, G. (2009). "Design and modeling of jet dispenser based on giant magnetostrictive material." Proceeding of IEEE, International conference on Electronic Packaging Technology and High Density Packaging, 10-13th August, Changsha Hunan, China, 974-979.

Geng, Z.J. and Haynes, L.S. (1994). "Six degree of freedom active control vibration using Stewart platforms." IEEE Transactions on Control Systems Technology, 2(1), 45-53.

Giri, N.K. (2005). "Automobile Mechanics." Khanna Publishers, Delhi, 39-42.

Giurgiutiu, V. (2000). "Review of smart materials actuation solutions for aeroelastic and vibration control." Journal of Intelligent Material Systems and Structures, 11(7), 525-544.

Giurgiutiu, V., Chaudhry, Z. and Rogers, C. A. (1995). "Engineering feasibility of Induced strain actuators for rotor blade vibration control," Journal of Intelligent Material Systems and Structures, 6(5), 583-597.

Giurgiutiu, V., Rogers, C. A. and Chaudhry, Z. (1997). "Design of displacement amplified induced-strain actuators for maximum energy output," Journal of Mechanical Design, 119(4), 511-517.

Giurgiutiu, V., Rogers, C. A. and Rusovici, R. (1996a). "Solid-state actuation of rotor blade servo-flap for active vibration control," Journal of Intelligent Material Systems and Structures, 7(2), 192-202.

Gray, D. E. (1967). "American institute of Physics Hand book." Chapter 4, Section 4, Page 4, McGraw-Hill Book Company Inc., Newyork, USA.

Grunwald, A and Olabi, A.G. (2008). "Design of a magnetostrictive (MS) actuator." Sensors and Actuators A, 144(1), 161-175.

Han, H., Xin, Q. and Wang, S. (2008). "Finite element analysis on magnetic field in the actuator of giant magnetostrictive linear motor with Ansoft." IEEE International Conference on Industrial Technology, Chengdu, 1-5.

Hoseinnezhad, R. and Bab-Hadiashar, A. (2009). "Recent patents on measurement and estimation in brake-by-wire technology." Recent patents on Electrical Engineering, 2(1), 54-64.

Hristoforou, E. and Ktena, A. (2007). "Magnetostriction and magnetostrictive materials for sensing applications." Journal of Magnetism and Magnetic Materials, 316(2), 372-378.

Hua, W., Hooks, R.J., Wu, W. and Wang, W. (2011). "Development of a novel polymeric fiber-optic magnetostrictive metal detector." Proceeding of Society of Optical Instrumentation Engineering, 1-16.

Imoto, Y., Hattori, Y., Takei. T. and Inagaki, M. (1988). "Piezoelectric actuated brake," US patent, 4765140.

Jiles, D. C. (1992). "A Self Consistent Generalized Model for the Calculation of Minor Loop Excursions in the Theory of Hysteresis." IEEE Transactions on Magnetics, 28(5), 2602-2604.

Jiles, D. C. and Atherton, D. L. (1983). "Ferromagnetic Hysteresis." IEEE Transactions on Magnetics, 19 (5), 2183-2185.

Jiles, D. C. and Atherton, D. L. (1984). "Theory of ferromagnetic hysteresis." Journal of Applied Physics, 55(6), 2115-2120.

Jiles, D. C. and Atherton, D. L. (1986). "Theory of ferromagnetic hysteresis." Journal of Magnetism and Magnetic Materials, 61(1-2), 48-60.

Kanizar, W.L., Liu. D., Moon, K.S. and Sutherland, J.W. (2000) "A magnetostrictive actuator based micro-positioner and its application in turning." SPIE, 2721, 385-393.

Karunanidhi. S. and Singaperumal. M. (2010). "Design, analysis and simulation of magnetostrictive actuator and its application to high dynamic servo valve," Sensors and Actuators A, 157(2), 185-197.

Kellogg, R. (2000). "The Delta-E effect in Terfenol-D and its application in a tunable mechanical resonator." M.Tech thesis, Iowa State University, Ames, Iowa.

Kellogg, R. and Flatau, A.B. (1999). "Blocked force investigation of a Terfenol-D transducer," SPIE's Symposium on Smart Structures and Materials, 3668, 19.

Kellogg, R. and Flatau, A.B. (2004). "Blocked–force characteristics of Terfenol-D transducers." Journal of Intelligent Material Systems and Structures, 15(2), 117-128.

Kikuchi, Y. (1968) "Magnetostrictive materials and applications."IEEE Transactions on Magnetics, 4(2), 107-117.

Lei, W., Jiu-bin, T. and Shan, Z. (2010). "A giant magnetostrictive actuator based on use of permanent magnet." Journal of Advanced Manufacturing Technology, 46(9-12), 893-897.

Lhermet, N. and Claeyssen, F., Wendling, P. and Grosso, G. (1993). "Design of actuators based on biased magnetostrictive rare earth-iron alloys." Journal of Intelligent Material Systems and Structures, 4(3), 337-342.

Li, L., Zhang, C., Kou, B. and Li, X. (2008). "Design of Giant Magnetostrictive Actuator for Fuel Injector." IEEE Vehicle Power and Propulsion Conference, 3-5th September, Harbin China, 1-4.

Li, L., Zhang, C., Yang, B. and Li, X. (2007a). "Finite element analysis of the uniformity magnetic field for on-off giant magnetostrictive actuators." International Conference on Electrical Machines and Systems (ICEMS), 17-20th October, Wuhan, China, 3758-3761.

Limpert, R. (1999). "Brake Design and Safety." Society of Automotive Engineers Inc., Warrendale, Pa. USA.

Liu, H., Jia, Z., Wang, F. and Zong, F. (2012). "Research on the constant output force control system for giant magnetostrictive actuator disturbed by external force." Mechatronics, 22(7), 911-922.

Lu, Q., Jing, C., Min, Z. and Dingfang, C. (2010)."Integrated optimized design of GMA with double water-cooling cavums." International Conference on Mechanic Automation and Control Engineering, 26-28th June, Wuhan, 3562-3565.

McMasters, D. (1991). "Power transducers for sonics and ultrasonics," Springer Berlin Heidelberg Publisher, 125-131.

Meeker, D. C. and Dozor, D. M. (1989). "Thermo-magnetic optimization of solenoidal magnetostrictive actuators," SPIE's Symposium on Smart Structures and Materials, 1st March, Newport Beach, CA, 122-133.

Michler, J. R., Moon, K. S., Sutherland, J. W. and Kashani, A. R. (1993). "Development of a magnetostriction based cutting tool micro positioner." Transactions of a NAMRI/SME, 21, 421-427.

170

Moon, S., Lim, C., Kim, B. and Park, Y. (2007). "Structural vibration control using linear magnetostricitve actuators." Journal of Sound and Vibration, 302(4-5), 875-891.

Murata, Y. and Yamada, H. (1998). "Magnetostrictive Brake." US patent number 5826683.

Nakamura, Y., Nakayama, M., Masuda, K., Yasuda, M., Tsuchiya, M. and Fujita, T. (2000). "Development of active six-degree of freedom micro-vibration control system using giant magnetostrictive actuators." Smart Materials and Structures, 9, 175-185.

Nathi, G., Charyulu, T. N., Gowtham, K. and Reddy, P. S. (2012). "Coupled structural/ thermal analysis of disc brake." IJRET, 1(4), 539-553.

Newcomb, T.P. and Spurr, R.T. (1967). "Braking of road vehicles", Chapman and Hall limited, London, 1-292.

Olabi, A. G. and Grunwald, A. (2008a). "Design and application of magnetostrictive materials," Material and Design, 29(2), 469-483.

Olabi, A. G. and Grunwald, A. (2008b). "Computation of magnetic field in an actuator." Simulation Modeling Practice and Theory, 16, 1728-1736.

Orthwein, W. C. (2004). "Clutches and Brakes." Marcel Dekker Inc., New York, USA, 1-351.

Palit, M. (2012). "An investigation on the effect of structural and micro-structural attributes on magnetostriction of Tb-Dy-Fe and Fe-Ga alloys."Doctoral Thesis, Department of Materials Engineering, Indian Institute of Science, Bangalore.

Park, Y. W. and Kim, D. Y. (2004). "Development of magnetostrictive microactuator." Journal of Magnetism and Magnetic Materials, 272-276, E1765-E1766.

Peng, Z., Cheng-rui, Z., Xin-liang, W., Lei, Q. and You-zhi, Q. (2008). "Novel mechanism for boring non-cylinder piston pin-hole based on giant magnetostrictive materials." J Shanghai University England Edition, 12(4), 363-367.

Phun, F. (1985). "Brake Handbook." HP Books Inc., England, 1-178.

Poole, A. D. and Booker, J. D. (2011). "Design methodology and case studies in actuator selection." Mechanism and Machine Theory, 46(5), 647-661.

Pramod Kumar, K., Kadoli, R. and Anil Kumar, M.V. (2010). "Mechanical and magnetic analysis of magnetostrictive disc brake system." 5th International Conference on Industrial and Information Systems (ICIIS), July 20-Aug 01, NITK, Surathkal, Karnataka, India, 644-659.

Rajput, R. K. (2007). "A text book of automobile engineering." Laxmi Publications, New Delhi, 559-587.

Siddiqui, K. U. (2012). "A text book of automobile engineering." Ist Edition, A new age international publishers, New Delhi, 1-380.

Srinivasan, N. (2003). "Automotive Mechanics." IInd Edition, Tata McGraw-Hill Publishing Corporation, New Delhi, 274-286.

Sun, L. and Zheng, X. (2005). "Numerical simulation on coupling behaviour of Terfenol-D rods." International Journal of Solids and Structures, 43, 1613-1623.

Sun, Z., Zhao, M. and Yin, Z. (2011). "Part design of giant magnetostrictive actuator," Physics Procedia, 22: 80-86.

Thoelke, J.B. (1993). "Magnetization and magnetostriction in highly magnetostrictive materials." MS Thesis, Iowa State University, Ames, Iowa.

Wan, Y., Fang, D. and Hwang, K. (2003). "Non-linear constitutive relations for magnetostrictive materials." International Journal of Non-linear Mechanics, 38, 1053-1065.

Wang, C., Wang, J. and Li, G. (2011b). "Finite element analysis of internal stress and strain on Terfenol-D rod in high frequency driven." International Conference on Artificial Intelligence, Management Science and Electronic Commerce, 5576-5579.

Wang, J., Li, G., Wang, C. and Liu, C. (2011a). "Finite element analysis of internal magnetic field on Terfenol-D rod in high frequency driven." International Conference on Artificial Intelligence, Management Science and Electronic Commerce, 5572-5575.

Wang, L., Ye, H., Liu, Y. T. and Yao, S. M. (2006). "Analysis and optimization for uniformity of magnetic field during the giant magnetostriction." Journal of Physics, 48, 1336-1340.

Wang, M., Zhong, K., Zuo, D. and Wang, M. (2010). "The clamping system based on giant magnetostrictive material and displacement amplifier with area effect." Journal of Key Engineering Materials, 431-432, 49-52.

Yamamoto, Y., Makino, T. and Matsui, H. (2000). "Micro positioning and actuation devices using giant magnetostriction materials." Proceedings of IEEE, International Conference on Robotics and Automation, 24-28th April, San Francisco, CA, 3635-3640.

Yang, B., Yang, D., Xu, P., Cao, Y., Feng, Z. and Meng, G. (2012). "Large stroke and nanometer-resolution giant magnetostrictive assembled actuator for driving segmented mirrors in very large astronomical telescopes." Sensors and Actuators A, 179, 193-203.

Yang, B.T., Bonis, M., Tao, H., Prelle, C. and Lamarque, F. (2006). "A magnetostrictive mini actuator for long-stroke positioning with nanometer resolution." Smart Materials and Structures, 16(7), 1227-1232.

Yensen, T.D. (1928). "What is the magnetic permeability of iron?" Journal of Franklin Institute, 206(4), 503-510.

Yi-jie, Wu (2004) "Giant Magnetostrictive Materials and its application research state, Mechanical and Electrical Engineering Magazine, Institute of Manufacturing Engineering, Zhejiang University, Hangzhou, China.

Yong, Y. and Lin, Li. (2009). "Dynamic model considering the DE effect for giant magnetostrictive actuators," IEEE International Conference on Control and Automation, Christchurch, New Zealand, 667-672.

Yongping, W., Daining, F., Soh, A. K. and Hwang, K. C. (2003). "Experimental and theoretical study of the non-linear response of a giant magnetostrictive rod." Acta Mechanica Sinica, 19(4), 324-329.

Yoo, J and Park, Y. (2010). "Experimental investigation of magnetostrictive DoD inkjet head for droplet formation." Current Applied Physics, 11(1), S353-S359.

Yoshioka, H., Shinno, H. and Sawano, H. (2013). "A newly developed rotary-linear motion platform with a giant magnetostrictive actuator." CIRP Annals-Manufacturing Technology, 62(1), 371-374.

Young, H. D., Freedman, R. A. and Ford, L. (2007). "University physics with modern physics with mastering physics," 12th Edition, Addison-Wesley Publishers.

Zhang, J., Ouyang, G. and Wang, M. (2009a). "Study on the magnetostrictive actuator of dual pressure common rail system." Proceedings of IEEE International Conference on Electronic Measurement and Instruments (ICEMI), Wuhan China, 3,155-159.

Zhang, T., Jiang, C., Zhang, H and Xu, H. (2004). "Giant magnetostrictive actuators for active vibration control." Smart Materials and Structures, 13(3), 473-477.

Zheng, X. J. and Liu, X. E. (2005). "A nonlinear constitutive model for Terfenol-D rods". Journal Applied Physics, 97, 1-8.

Zhifeng, T., Fuzai, L. U. and Yang, L. I. U. (2009). "Magnetic field distribution in cross-section of Terfenol-D rod and its applications." Journal of Rare Earths, 27(3), 525-528.

Zhou, H. M., Zhou, Y. H. and Zheng, X. J. (2007). "Active vibration control of Terfenol-D rod of giant magnetostrictive actuator with non-linear constitutive relations." Journal of Theoretical and Applied Mechanics, 45(4), 953-967.

APPENDIX - I

I.1. Coaxial coils for a Terfenol-D actuator

In general, either the combination of coil with permanent magnet or single coil applying a dc bias field superimposing with an alternating field are most often used layouts in a Terfenol-D actuator. The coaxial coils (two separate coils coaxially placed) are used in an actuator layout in the present study. The coaxial type of coil design used in a Terfenol-D actuator is being justified by analyzing numerically the distribution of magnetic field using Maxwell 2D solver and is as follows:

To explore the possible differences in using a single coil and two separate coils, a numerical analysis is presented using three different configurations in an actuator.

- Exercise 1: Single coil of 1000 turns is analyzed for flux density by providing input current of 4 A and the coil is in free air.
- Exercise 2: Two coils placed coaxially, coil 1 with 560 turns and coil 2 with 440 turns in free air is analyzed for flux density by providing input of 4 A to coil 1 and coil 2.
- Exercise 3: Single coil of 440 turns (produces a magnetic field strength of 22 kA/m) with permanent magnet of magnetic field strength 28 kA/m analyzed for flux density by providing input current of 4 A to both coil and permanent magnet in free air.

Axi-symmetric model of coaxial coils (inner and outer radii of coil 1 are 16.5 mm and 36.5 mm, coil 2 are 37.5 mm and 57.5 mm), single coil of same size (inner and outer radii are 16.5 mm and 57.5 mm respectively) and single coil with permanent magnet were built separately in the Maxwell 2D environment in free air. Suitable materials such as copper and Alnico for coils and permanent magnet are assigned. Coils are energized with a DC input current of 4 A. The current density for coaxial coils i.e. for coil 1 and coil 2 are 1350 and 1030 kA/m^2 and for single coil is 1175 kA/m^2. The input to the permanent magnet is 4 A DC input with material properties like magnetic retentivity and magnetic coercivity of 1.27 Tesla and 56 kA/m respectively (material

database from Maxwell 2D). Magnetic flux density is evaluated by solving these three models in free air alone using Ansoft Maxwell 2D solver.

Fig. I.1 (a) and (b) shows the comparison of magnetic flux density of single and coaxial coils, coaxial coils and single coil along with permanent magnet alone in free air along the axial direction. Maximum flux density of 45 mT is obtainable from both single and coaxial coils in free air. The distribution of flux density was more or less uniform with coaxial coils along the axial direction compared to single coil. The leakage of flux from a single coil during the magnetic transduction may be the reason for the variations in the distribution of magnetic flux density. Maximum flux density of 46 mT is obtainable from single coil along with a permanent magnet compared to coaxial coils in free air. The amplitude of flux density is little higher in a single coil along with permanent magnet compared to a coaxial coil of 45 mT. The distribution of flux density along the axial direction with coaxial coil is uniform and compares well with single coil and permanent magnet configuration.

(a)   (b)
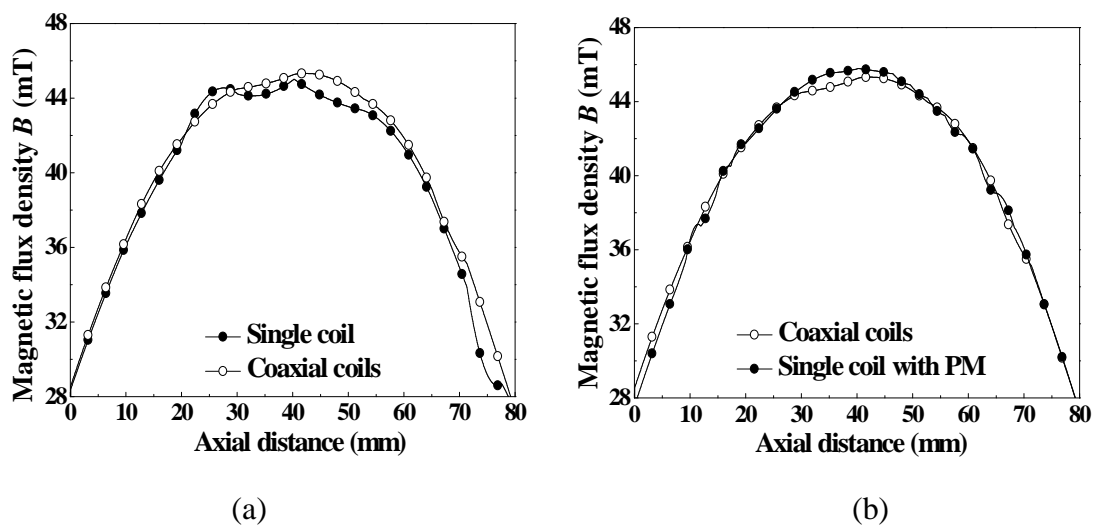
Fig. I.1. Comparison of numerical magnetic flux density of (a) single and coaxial coils (b) coaxial coils and single coil with permanent magnet in free air.

It is summarized that the magnitude of flux density with all the three configurations are approximately same for a given input of 4 A. The distribution of flux density along the axial direction in coaxial coil configuration is symmetrical and compares well to single coil alone and single coil with permanent magnet configuration. With this, it is concluded that the coaxial coils for the actuator can also be good a candidate

176

to generate actuation force with equal density compared to single coil and as well as single coil with permanent magnet. The axi-symmetric model, model discretized with triangular finite elements for each exercise is shown in Fig. I.2 – I.4. The convergence details obtained during finite element analysis for each exercise is shown in Table I-1, I-2 and I-3 respectively.
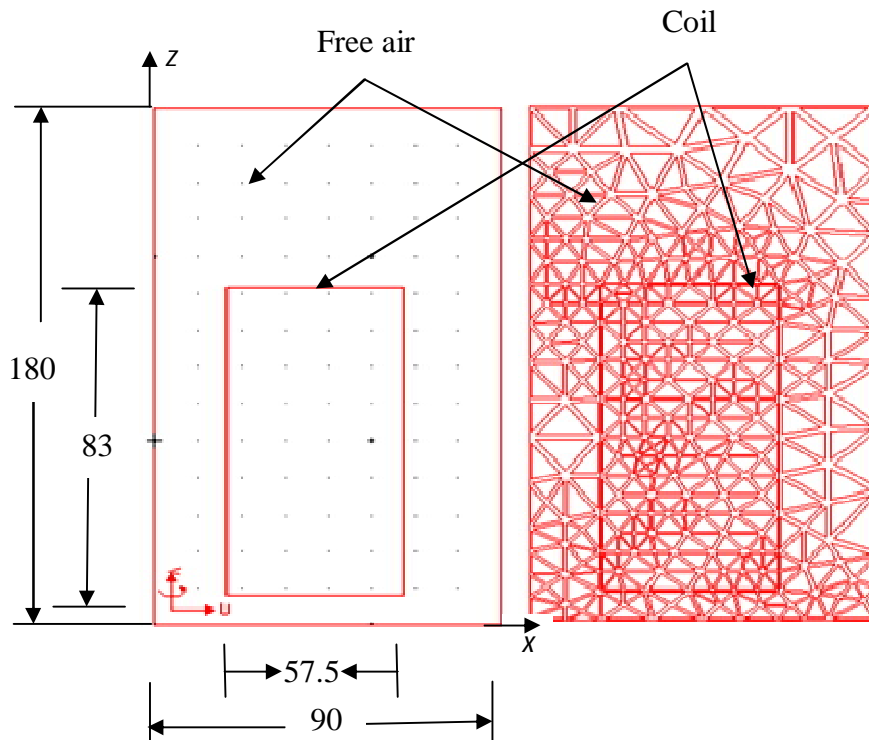
Fig. I.2. (a) Axi-symmetric model and (b) discretized with triangular elements of a single coil in free air.

Table I-1 Convergence data of single coil in free air using finite element Maxwell 2D solver.

Number of passes	Pass	Triangles	Total Energy (J)	Energy Error (%)	Magnetic force (N)
Completed: 11 **Remaining: 0**	1	24	0.268925	202.9396	0.493072
	2	65	0.243383	31.4945	0.316436
	3	83	0.240838	24.6697	0.267149
	4	107	0.239946	22.7787	0.231003
Convergence criteria:	5	135	0.237665	20.6925	0.215624
	6	174	0.236240	17.0261	0.238557
Target Error: 1%	7	222	0.235594	15.8037	0.250390
Energy Error: 14.3 %	8	286	0.235251	15.6643	0.230816
Delta Energy : 0.135 %	9	365	0.235700	14.6039	0.241176
	10	469	0.235144	14.4139	0.244114
	11	607	0.234828	14.2539	0.251242

177
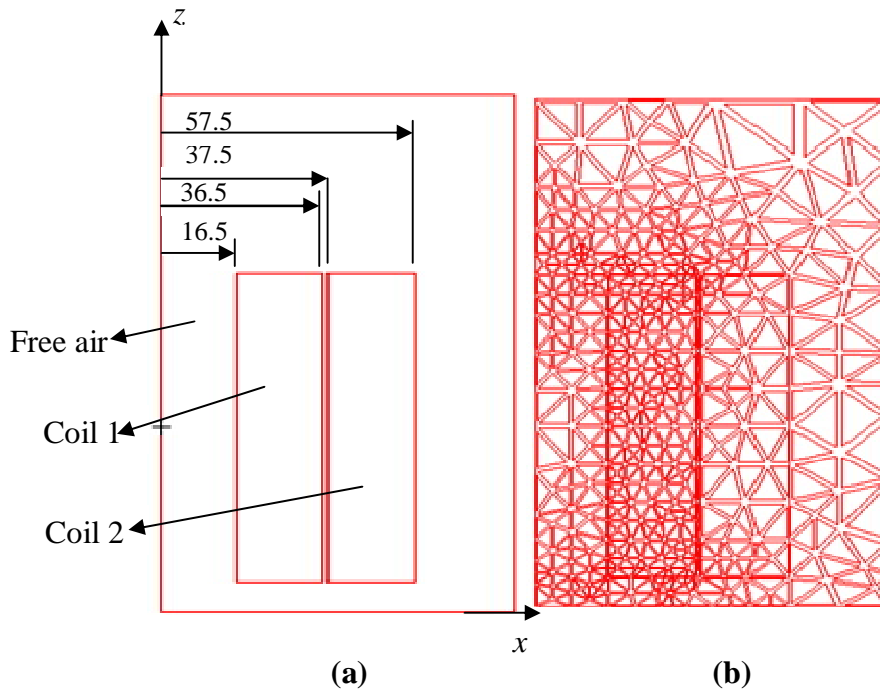
Fig. I.3. (a) Axi-symmetric model and (b) discretized with triangular elements of a coaxial coils in free air.

Table I-2 Convergence data of coaxial coils in free air using finite element Maxwell 2D solver.

Number of passes	Pass	Triangles	Total Energy($\times 10^4$) (J)	Energy Error (%)	Magnetic force ($\times 10^4$) (N)
Completed: 10 **Remaining: 0**	1	34	1.86011	215.8614	3.21013
	2	62	1.79493	37.0925	2.35979
	3	118	1.79665	24.8074	1.95063
	4	152	1.76086	17.0392	1.83872
Convergence criteria:	5	198	1.75794	15.3782	1.77829
	6	248	1.75458	13.0863	1.83091
Target Error: 1% **Energy Error: 9.6 %** **Delta Energy : 0.0938 %**	7	318	1.75633	12.9761	1.86488
	8	408	1.74944	12.4121	1.94266
	9	526	1.74697	10.0461	2.06047
	10	676	1.74533	9.1596	2.09136
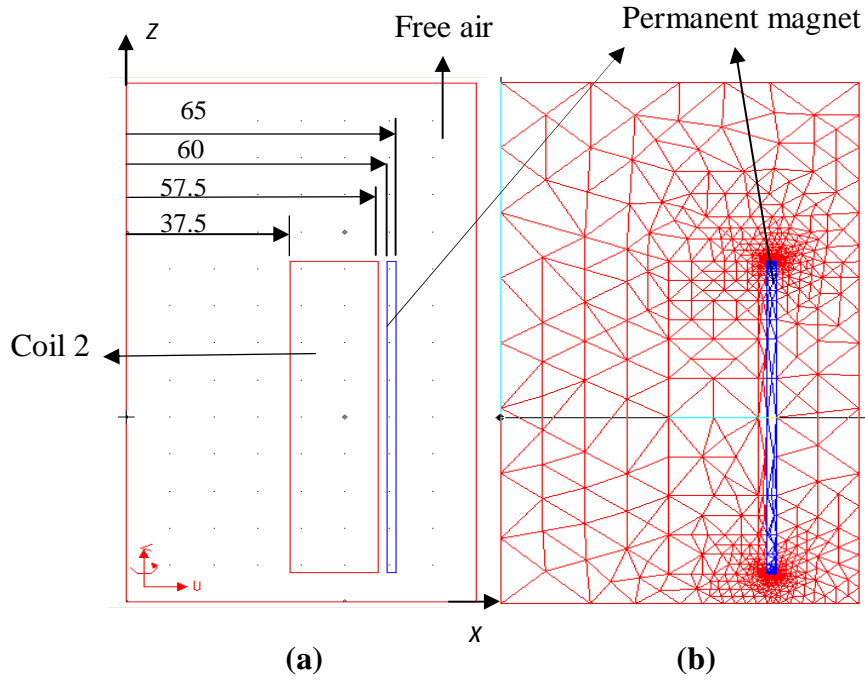
Fig. I.4. (a) Axi-symmetric model (b) discretized with triangular elements and (c) convergence data of a single coil with permanent magnet in free air.

Table I-3 Convergence data of single coil with permanent magnet in free air using finite element Maxwell 2D solver.

Number of passes	Pass	Triangles	Total Energy (J)	Energy Error (%)	Magnetic force (N)
Completed: 13	1	37	0.005012	129.5	0.01543
Remaining: 0	2	100	0.00603	91.6	0.01624
	3	129	0.006614	82.3	0.0445
	4	166	0.007217	66.7	0.02244
	5	213	0.008042	39.2	0.053
Convergence criteria:	6	272	0.00865	18.3	0.05065
	7	350	0.008984	11	0.0552
Target Error: 1%	8	454	0.009254	5	0.02979
Energy Error: 0.922 %	9	587	0.009384	3.43	0.04156
Delta Energy : 0.115 %	10	762	0.009468	2.5	0.02202
	11	988	0.009504	1.7	0.03066
	12	1374	0.009539	1.2	0.02613
	13	1916	0.00955	0.9	0.02291

I.2. Diameter of coaxial coils in a Terfenol-D actuator

The dimensions of coil 1 and coil 2 are calculated using the following set of equations:

Inner diameter Coil 1 = Diameter of Terfenol-D + 5 mm allowance   (I.1)

Number of turns per unit run $\left(P_{coil} \right) = \dfrac{\text{Length of coil}}{\text{Diameter of coil}}$ (I.2)

179

$$\text{Number of runs } (q_{coil}) = \frac{\text{Number of coil turns}}{\text{Number of turns per unit run}} \qquad (I.3)$$

OD of Coil = ID of Coil + 2(q_{coil} × Diameter of Wire) + 11 mm allowance $\qquad$ (I.4)

I.3. Computation of electrical parameters in the design of coaxial coils

In the design of coaxial coils, the detailed computation of the other associated electrical parameters involved is discussed apart the computed number of turns for coaxial coils.

i. Geometry of the coil and flux leakage

Shape factor of each coil is the measure of geometry of the coil. It is calculated by using the following expression,

$$G_{coil} = \frac{1}{5}\left[\frac{2\pi\beta}{\alpha^2 - 1}\right]^{\frac{1}{2}} \ell n\left[\frac{\alpha + \sqrt{\alpha^2 + \beta^2}}{1 + \sqrt{1 + \beta^2}}\right] \qquad (I.5)$$

For coil 1 $\Rightarrow \alpha = \dfrac{a_2}{a_1} = \dfrac{36.5}{16.5} = 2.2121$ and $\beta = \dfrac{l_{coil}}{2a_1} = \dfrac{83}{2 \times 16.5} = 2.5151$

$$G_{coil1} = \frac{1}{5}\left[\frac{2\pi \times 2.5151}{2.2121^2 - 1}\right]^{\frac{1}{2}} \ell n\left[\frac{2.2121 + \sqrt{2.2121^2 + 2.5151^2}}{1 + \sqrt{1 + 2.5151^2}}\right] = 0.1635$$

For coil 2 $\Rightarrow \alpha = \dfrac{115}{75} = 1.5333$ and $\beta = \dfrac{83}{2 \times 37.5} = 1.1067$

$$G_{coil2} = \frac{1}{5}\left[\frac{2\pi \times 1.1067}{1.5333^2 - 1}\right]^{\frac{1}{2}} \ell n\left[\frac{1.5333 + \sqrt{1.5333^2 + 1.1067^2}}{1 + \sqrt{1 + 1.1067^2}}\right] = 0.1154$$

Magnetic field at the center of each coil is given by,

$$H_{coil} = G_{coil} . N_{coil} I_{coil} \sqrt{\frac{\pi}{l_T a_1} \times \frac{(\alpha + 1)}{(\alpha - 1)}} \qquad (I.6)$$

This analytical expression represents the "Best design" as it gives maximum magnetic field at the centre of coaxial coils with respect to dissipate power in coaxial coils.

With G_{coil} (shape factor) and known values of α and β, the maximum magnetic field using Eq. (I.6), at the center of each coil is given by

$$H_{coil1} = 0.1635 \times N_{coil1}I_{coil1} \sqrt{\frac{\pi(2.2121+1)}{0.08 \times 0.0165 \times (2.2121-1)}} = 12.98 N_{coil1}I_{coil1} \qquad (I.7)$$

$$H_{coil2} = 0.1154 \times N_{coil2}I_{coil2} \sqrt{\frac{\pi(1.533+1)}{0.08 \times 0.0375 \times (1.533-1)}} = 8.14 N_{coil2}I_{coil2} \qquad (I.8)$$

The Eq. (I.7) and (I.8) are compared with the ideal magnetic circuit. According to which, the magnetic field from the coil is

$$H_{coil} = \frac{N_{coil}I_{coil}}{l_{coil}} = \frac{N_{coil}I_{coil}}{0.083} = 12.05 N_{coil}I_{coil} \qquad (I.9)$$

On comparing Eq. (I.9) with Eq. (I.7), the flux leakage from the coil 1 can be calculated and is given by,

Flux leakage of coil 1 $= \dfrac{12.98-12.05}{12.98} \times 100 = 4.4\%$

On comparing Eq. (I.9) with Eq. (I.8), the flux leakage from the coil 2 can be calculated and is given by,

Flux leakage of coil 2 $= \dfrac{12.05-8.14}{12.05} \times 100 = 18\%$

ii. Q_{coil} Value of the driving coils

Q_{coil} value of driving coil is the ratio of maximum stored magnetic energy in the Terfenol-D material to the dissipated energy in the coil resistance during one cycle. It is calculated using the shape factor (G_{coil}) of the coil.

The maximum magnetic energy delivered by the coil to the Terfenol-D material can be expressed as:

$$E_{mag,max} = \frac{1}{2} \mu_{r(T)} H_{coil}^2 V_T \qquad (I.10)$$

Where $\mu_{r(T)}$ is the relative magnetic permeability equal to 5 and V_T is the volume of Terfenol-D rod.

The coil losses during one cycle are given by:

$$E_{coil\ losses} = P_{coil\ losses} \times \frac{2\pi}{\omega} = H_{coil}^2 \frac{2\pi\rho a_1}{\chi G_{coil}^2 \omega} \qquad (I.11)$$

According to the definition of Q_{coil}, it is the ratio of Eq. (I.10) to Eq. (I.11),

$$Q_{coil} = \frac{E_{max.mag}}{E_{coillosses}} = \frac{1}{4}\mu_{r(T)}\frac{\chi G_{coil}^2 \omega r_T l_T}{\gamma \rho} \tag{I.12}$$

Where $\gamma = a_1/r_{coil}$, ρ is the resistivity of the copper wire and ω is the frequency of the applied input for one cycle. One cycle means the time between switching on the supply to switching off. It is identified as not more than 1 sec from the numerical and experimental results. Frequency (f) is equal to 1 Hz is assumed in the present work.

Coil 1

$$\gamma = \frac{a_1}{r_T} = \frac{0.0165}{0.014} = 1.1786 \text{ , } \omega = 2\pi f = 2\pi \times 1 = 2\pi \text{ rad/sec and } \rho = 1.68 \times 10^{-8} \text{ }\Omega\text{-m}$$

$$Q_{coil1} = \frac{1}{4} \times 5 \times \frac{\frac{\pi}{4}(0.1635)^2 \times 2\pi \times 0.014 \times 0.08}{1.1786 \times 1.68 \times 10^{-8}} = 3750$$

Coil 2

$$\gamma = \frac{a_1}{r_T} = \frac{0.0375}{0.014} = 2.678 \text{ , } \omega = 2\pi f = 2\pi \times 1 = 2\pi \text{ rad/sec and } \rho = 1.68 \times 10^{-8} \text{ }\Omega\text{-m}$$

$$Q_{coil2} = \frac{1}{4} \times 5 \times \frac{\frac{\pi}{4}(0.1154)^2 \times 2\pi \times 0.014 \times 0.08}{2.678 \times 1.68 \times 10^{-8}} = 1191$$

iii. Magnetic coupling coefficient of driving coils

The magnetic coupling coefficient is the ratio of magnetic energy stored in a Terfenol-D rod to the total magnetic energy stored in an actuator. The coupling coefficient depends entirely on coil on assuming an ideal flux return path.

$$k_c^2 = \frac{1}{1 + \frac{\mu_0}{\mu_r}(\gamma^2 - 1) + \frac{\pi\mu_0}{6\mu_r}\gamma^2(\alpha - 1)(\alpha + 3)} \tag{I.13}$$

$$\text{Coil1} \Rightarrow k_c^2 = \frac{1}{1 + \frac{1}{5}(1.1786^2 - 1) + \frac{\pi \times 1}{6 \times 5} \times 1.1786^2(2.2121 - 1)(2.2121 + 3)} = 0.52$$

$$\text{Coil 2} \Rightarrow k_c^2 = \frac{1}{1 + \frac{1}{5}(2.678^2 - 1) + \frac{\pi \times 1}{6 \times 5} \times 2.678^2(1.5333 - 1)(1.5333 + 3)} = 0.22$$

iv. Inductance of the driving coils

The expression for magnetic energy $E_{mag.coil}$ in the coil winding and between the coil and the magnetostrictive rod for a selected geometry of the coil can be expressed as:

$$E_{mag.coil} = \frac{1}{2}\mu_0 H_{ex}^2 \pi r_T^2 l_T \left(\gamma^2 - 1\right) + \frac{\pi}{12}\mu_0 H_{ex}^2 a_1^2 l_T \left(\alpha - 1\right)\left(\alpha + 3\right) \tag{I.14}$$

Assuming a homogeneous field inside the rod then $H_{ex} = H_{coil}$ which gives

$$H_{ex} = H_{coil} = G_{coil} N_{coil} I \sqrt{\frac{\pi(\alpha+1)}{l_T a_1 (\alpha-1)}} \tag{I.15}$$

Substituting the Eq. (I.15) in Eq. (I.14) and on simplifying yields:

$$L_{coil\ leakage} = \frac{2E_{mag.coil}}{I^2} = G_{coil}^2 N_{coil}^2 \pi^2 \mu_0 \left[r_T \frac{\left(\gamma^2 - 1\right)\left(\alpha+1\right)}{\gamma\left(\alpha-1\right)} + \frac{1}{6}a_1\left(\alpha+1\right)\left(\alpha+3\right) \right] \tag{I.16}$$

The factor $\gamma = a_1/r_{coil}$ is a small value. Taking the square of this term present in the parenthesis gives too small value. Hence, by neglecting first term in the parentheses, then Eq. (I.16) yields:

$$L_{coilleakage} = \mu_o \frac{\pi^2}{6} G_{coil} N_{coil}^2 a_1 \left(\alpha+1\right)\left(\alpha+3\right) \tag{I.17}$$

For known values of α, β and γ with N and a_1, the inductance of the each coil is given by,

Coil1

$$L_{coil\ leakage} = 4\pi \times 10^{-7} \times \frac{\pi^2}{6} \times 0.1635^2 \times 560^2 \times 0.0165(2.2121+1)(2.2121+3) = 3.878 \text{ mH}$$

Coil 2

$$L_{coil\ leakage} = 4\pi \times 10^{-7} \times \frac{\pi^2}{6} \times 0.1154^2 \times 440^2 \times 0.0375(1.5333+1)(1.5333+3) = 2.1824 \text{ mH}$$

I.4. Computation of parameters for the verification of coaxial coils dimensions

Based on shape factor, the dimensions of coaxial coils arrived at are verified using analytical procedure discussed in Dehui et al., 2008. Detailed calculations in the verification procedure for the dimensions of coaxial coils are shown below:

i. Shape factor of coil $\left(G_{coil}\right)$

Shape factor of coil 1 $\left(G_{coil1}\right)$ and coil 2 $\left(G_{coil2}\right)$ is 0.1635 and 0.1154 respectively.

Shape factor of each coil is computed and available in section I.3 of APPENDIX I.

ii. Magnetic field at the centre of coil $\left(H_{coil}\right)$

$$H_{coil1} = G_{coil1}.N_{coil1}I_{coil1}\sqrt{\frac{\pi}{l_T a_1} \times \frac{(\alpha+1)}{(\alpha-1)}}$$

(I.18)

$$H_{coil1} = 0.1635 \times 560 \times 4\sqrt{\frac{\pi}{0.08 \times 0.0165} \times \frac{(2.2121+1)}{(2.2121-1)}} = 28 \text{ kA/m}$$

$$H_{coil2} = 0.1154 \times 440 \times 4\sqrt{\frac{\pi}{0.08 \times 0.0375} \times \frac{(1.5333+1)}{(1.5333-1)}} = 21 \text{ kA/m}$$

iii. Coil compensation coefficient $\left(K_{coil}\right)$

$$N_{coil1}I_{coil1} = K_{coil1}H_{coil1}l_T$$

(I.19)

$$K_{coil1} = \frac{N_{coil1}I_{coil1}}{H_{coil1} \times l_T} = \frac{560 \times 4}{28 \times 10^3 \times 80 \times 10^{-3}} = 0.981$$

$$K_{coil2} = \frac{N_{coil2}I_{coil2}}{H_{coil2} \times l_T} = \frac{440 \times 4}{21 \times 10^3 \times 80 \times 10^{-3}} = 1.233$$

iv. Current density of coil 1 $\left(J_{coil}\right)$

$$J_{coil} = \frac{N_{coil}I_{coil}}{A_{coil}} = \frac{K_{coil}H_{coil}l_T}{A_{coil}}$$

(I.20)

$$J_{coil1} = \frac{N_{coil1}I_{coil1}}{A_{coil1}} = \frac{K_{coil1}H_{coil1}l_T}{A_{coil1}} = \frac{0.981 \times 28 \times 10^3 \times 0.08}{(7.47 \times 10^{-4})} = 1.35 \times 10^6 \text{ A/m}^2$$

Where A_{coil1} = Surface area of Coil 1= $7.47 \times 10^{-4} \text{m}^2$

$$J_{coil2} = \frac{N_{coil2}I_{coil2}}{A_{coil2}} = \frac{K_{coil2}H_{coil2}l_T}{A_{coil2}} = \frac{1.233 \times 21 \times 10^3 \times 0.08}{(5.81 \times 10^{-4})} = 1.06 \times 10^6 \text{ A/m}^2$$

Where A_{coil2} = Surface area of Coil 2 = $5.81 \times 10^{-4} \text{ m}^2$

v. Expression for verification criteria

$$\frac{K_{coil}H_{coil}l_T}{4\times10^6} \le A_{coil} \le \frac{K_{coil}H_{coil}l_T}{2\times10^6}$$

(I.21)

For coil $1 \Rightarrow \dfrac{K_{coil1}H_{coil1}l_T}{4\times10^6} \le A_{coil1} \le \dfrac{K_{coil1}H_{coil1}l_T}{2\times10^6}$

$$\Rightarrow \frac{0.981\times27\times10^3\times0.08}{4\times10^6} \le A_{coil} \le \frac{0.981\times28\times10^3\times0.08}{2\times10^6}$$

$$\Rightarrow 5.8\times10^{-4} \le 7.47\times10^{-4} \le 1.162\times10^{-3}$$

For coil $2 \Rightarrow \dfrac{K_{coil2}H_{coil2}l_T}{4\times10^6} \le A_{coil2} \le \dfrac{K_{coil2}H_{coil2}l_T}{2\times10^6}$

$$\Rightarrow \frac{1.233\times21\times10^3\times0.08}{4\times10^6} \le A_{coil2} \le \frac{1.233\times21\times10^3\times0.08}{2\times10^6}$$

$$\Rightarrow 4.56\times10^{-4} \le 5.81\times10^{-4} \le 9.13\times10^{-4}$$

The surface area of coil 1 and coil 2 meets the constraints of the criteria given by Eq. (I.21) with respect to current density based on long term operation. This implies the high electro-magnetic conversion efficiency from coil 1 and coil 2. The high electro-magnetic conversion efficiency indicates the least power is consumed by the coaxial coils to generate the required amount of magnetic field strength. Another verification criterion is based on shape factor of each coil. The shape factor (G_{coil}) for coil 1 is 0.1635 with $\alpha = 2.2121$, $\beta = 2.5151$ and for coil 2 is 0.1154 with $\alpha = 1.5333$, $\beta = 1.1067$. The shape factor obtained for each coil is well within the range from 0.1 to 0.179 as reported by Engdahl, 2002 for most of the coil geometries. It is concluded that the coaxial coils designed with these arrived dimensions can produce the magnetic field at their center with least dissipated power as they met the constraints of Eq. (3.36) and as well with acceptable shape factor.

I.5. Analytical magnetic flux density along the axis of coil in free air

Magnetic flux density distribution along the axis the coil is evaluated using the analytical expression reported in Wang et al., (2006). According to Biot-Savart law,

$$
\left.
\begin{aligned}
B_\rho &= \frac{\mu_0 J}{2\pi} \int_0^\pi d\theta \int_{a_1}^{a_2} d\rho' \int_{z_1}^{z_2} \frac{-\rho' z' \cos\theta}{r^3} \, dz' \\
B_\theta &= 0 \\
B_z &= \frac{\mu_0 J}{2\pi} \int_0^\pi d\theta \int_{a_1}^{a_2} d\rho' \int_{z_1}^{z_2} \frac{\rho'(\rho' - \rho\cos\theta)}{r^3} \, dz'
\end{aligned}
\right\} \tag{I.22}
$$

Where $r = \left(\rho'^2 + \rho^2 - 2\rho'\rho\cos\theta + z'^2\right)^{\frac{1}{2}}$, $\theta = \phi' - \phi$, z_1 is the coordinate of coil bottom, z_2 is the coordinates of coil top, ρ', ϕ' and z' are cylindrical coordinates and μ_0 is the permeability of free space. Evaluating the integrals given in Eq. (I.22) yields an expression for magnetic flux density is a function of the z-axis.

From the fundamentals of mathematics:

$$
\int \sqrt{a^2 + x^2} \, dx = \frac{x\sqrt{a^2 + x^2}}{2} + \frac{a^2}{2} \log \frac{x + \sqrt{a^2 + x^2}}{a} \tag{I.23}
$$

$$
\int \frac{dy}{\left(y^2 + k^2\right)^n} = \frac{y}{2(n-1)k^2 \left(y^2 + k^2\right)^{n-1}} + \frac{2n-3}{2(n-1)k^2} \int \frac{dy}{\left(y^2 + k^2\right)^{n-1}} \tag{I.24}
$$

$$
\int \frac{1}{\sqrt{a^2 + x^2}} \, dx = \log \frac{x + \sqrt{a^2 + x^2}}{a} \tag{I.25}
$$

Magnetic flux density along the axis of the coil from Eq. (I.22) gives:

$$
B_z = \frac{\mu_0 J}{2\pi} \int_0^\pi d\theta \int_{a_1}^{a_2} d\rho' \int_{z_1}^{z_2} \frac{\rho'(\rho' - \rho\cos\theta)}{r^3} \, dz'
$$

$$
B_z = \frac{\mu_0 J}{2\pi} \int_0^\pi d\theta \int_{a_1}^{a_2} d\rho' \int_{z_1}^{z_2} \frac{\rho'(\rho' - \rho\cos\theta)}{\left(\rho'^2 + \rho^2 - 2\rho'\rho\cos\theta + z'^2\right)^{\frac{3}{2}}} \, dz'
$$

Since B_z is along the axis of the coil, hence substituting $\rho = 0$ yields

$$
B_z = \frac{\mu_0 J}{2\pi} \int_0^\pi d\theta \int_{a_1}^{a_2} d\rho' \int_{z_1}^{z_2} \frac{\rho'^2}{\left(\rho'^2 + z'^2\right)^{\frac{3}{2}}} \, dz'
$$

From Eq. (I.24),

186

$$B_z = \frac{\mu_0 J}{2\pi} \int_0^\pi d\theta \int_{a_1}^{a_2} d\rho' \times \rho'^2 \left[\frac{z'}{2\left(\frac{3}{2}-1\right)\rho'^2 \left(z'^2 + \rho'^2\right)^{\frac{1}{2}}} + 0 \right]_{z_1}^{z_2}$$

$$B_z = \frac{\mu_0 J}{2\pi} \int_0^\pi d\theta \int_{a_1}^{a_2} d\rho' \left[\frac{z'}{\sqrt{z'^2 + \rho'^2}} \right]_{z_1}^{z_2}$$

$$B_z = \frac{\mu_0 J}{2\pi} \int_0^\pi d\theta \int_{a_1}^{a_2} \frac{z_2'}{\sqrt{z'^2_2 + \rho'^2}} - \frac{z_1'}{\sqrt{z'^2_1 + \rho'^2}} \; d\rho'$$

From Eq. (I.25),

$$B_z = \frac{\mu_0 J}{2\pi} \int_0^\pi d\theta \left[z_2' \left\{ \log \frac{\rho' + \sqrt{\rho'^2 + z'^2_2}}{z_2'} \right\} - z_1' \left\{ \log \frac{\rho' + \sqrt{\rho'^2 + z'^2_1}}{z_1'} \right\} \right]_{a_1}^{a_2}$$

$$B_z = \frac{\mu_0 J}{2\pi} \; \theta\Big|_0^\pi \left[z_2' \left\{ \ln \frac{a_2 + \sqrt{a_2^2 + z'^2_2}}{a_1 + \sqrt{a_1^2 + z'^2_1}} \right\} - z_1' \left\{ \ln \frac{a_2 + \sqrt{a_2^2 + z'^2_1}}{a_1 + \sqrt{a_1^2 + z'^2_1}} \right\} - z_2' \ln z_2' + z_1' \ln z_1' \right]$$

The co-ordinates i.e. $z_2' = b+z$ and $z_1' = -(b-z)$

$$B_z = \frac{\mu_0 J}{2} \left[(z+b) \; \ln \frac{a_2 + \sqrt{a_2^2 + (z+b)^2}}{a_1 + \sqrt{a_1^2 + (z+b)^2}} \right.$$
$$\left. + (b-z) \; \ln \frac{a_2 + \sqrt{a_2^2 + (b-z)^2}}{a_1 + \sqrt{a_1^2 + (b-z)^2}} - (b+z)\ln(b+z) - (b-z)\ln(z-b) \right]$$

The constant term in the parenthesis is given by $\left[(b+z)\ln(b+z) - (b-z)\ln(z-b) \right]$ gives too small value. Hence by neglecting the constant in the above equation, it yields,

$$B_z = \frac{\mu_0 J}{2} \left[(z+b) \; \ln \frac{a_2 + \sqrt{a_2^2 + (z+b)^2}}{a_1 + \sqrt{a_1^2 + (z+b)^2}} + (b-z) \; \ln \frac{a_2 + \sqrt{a_2^2 + (b-z)^2}}{a_1 + \sqrt{a_1^2 + (b-z)^2}} \right] \quad \text{(I.26)}$$

Eq. (I.26) gives the distribution of flux density along the axis of coil.

187

I.6. Experimental setup for measuring magnetic flux density

The experimental arrangement for measuring magnetic flux density is shown in Fig. I.5. Magnetic flux density was measured using Lakeshore guassmeter-410 with hall probes HT5891 (Transverse Probe) and HA3863 (Axial Probe).
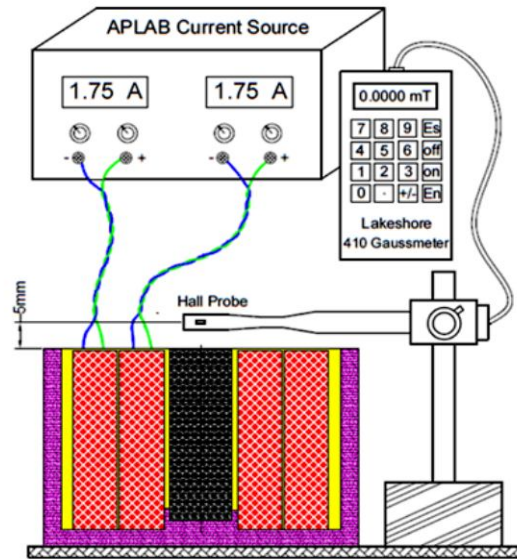

Fig. I.5. Experimental setup for measuring magnetic flux density.

Transverse probe has a hall sensor mounted parallel to the probe axis and measures magnetic fields perpendicular to the probe axis. Axial probe has a hall sensor mounted perpendicular to the probe axis and measures magnetic fields parallel to the probe axis. APLAB-LD6405 power supply is used for varying DC input to coils from 0 A to 4 A in a step of 0.25 A. The distance between the coils and the probe maintained was 5 mm for better measurement. Transverse and axial probes were held by means of a digital vernier height guage to measure axial and radial magnetic flux density. Hall probes were held firmly and moved along the axis of coaxial coils (Hallow cross-section).

I.7. Finite element solution for magnetic field intensity in a coaxial coils containing different sizes of Terfenol-D

Axi-symmetric model of coaxial coils alone and coils carrying Terfenol-D rod of different sizes were built in Maxwell 2D solver. Three sizes of Terfenol-D rod with a diameter of 12.5 mm, 13 mm and 13.5 mm have been opted. The axi-symmetric

models, discretization with triangular elements and converged table for number of passes equal to 10 have been shown below.
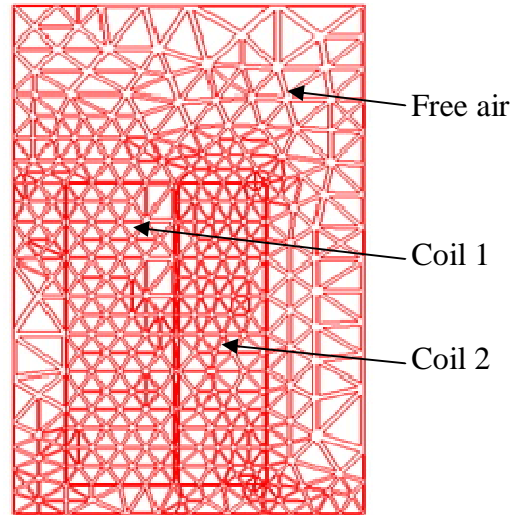

Fig. I.6. Axi-symmetric model of coaxial coils in free air discretized with triangular elements.

Table I-4 Convergence data of coaxial coils in free air using finite element Maxwell 2D solver.

| Number of passes	Pass	Triangles	Total Energy (J)	Energy Error (%)	Magnetic force (N)
Completed: 10 **Remaining: 0**	1	34	0.504632	93.6760	0.876844
	2	93	0.492936	26.3836	0.555088
	3	117	0.487348	22.1570	0.468726
Convergence criteria:	4	148	0.485148	17.4317	0.510868
	5	190	0.483571	15.8243	0.532384
Target Error: 1% **Energy Error: 12 %** **Delta Energy : 0.134 %**	6	245	0.482530	15.0169	0.485124
	7	313	0.480812	14.1698	0.501367
	8	401	0.480362	13.6475	0.493875
	9	516	0.480633	12.9273	0.484858
	10	663	0.479989	12.0496	0.486465

189
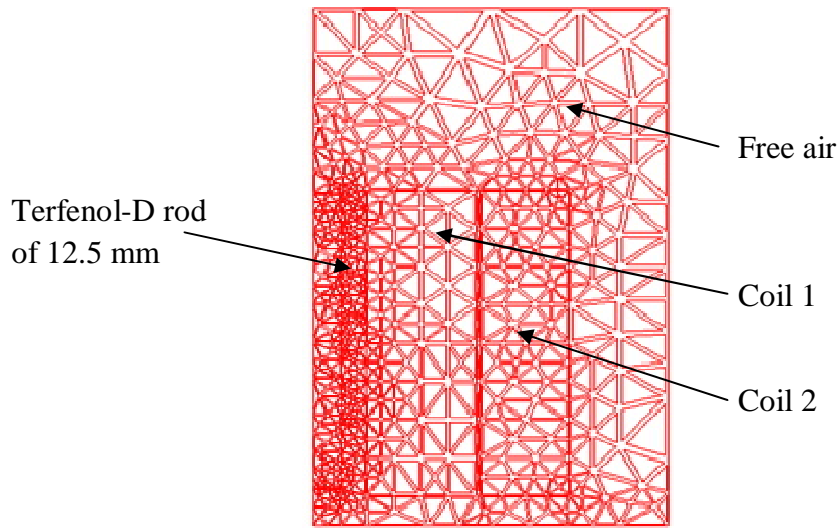
Fig. I.7. Axi-symmetric model of coaxial coils containing Terfenol-D rod of 12.5 mm in free air discretized with triangular elements.

Table I-5 Convergence data of coaxial coils containing Terfenol-D rod of 12.5 mm in free air using finite element Maxwell 2D solver.

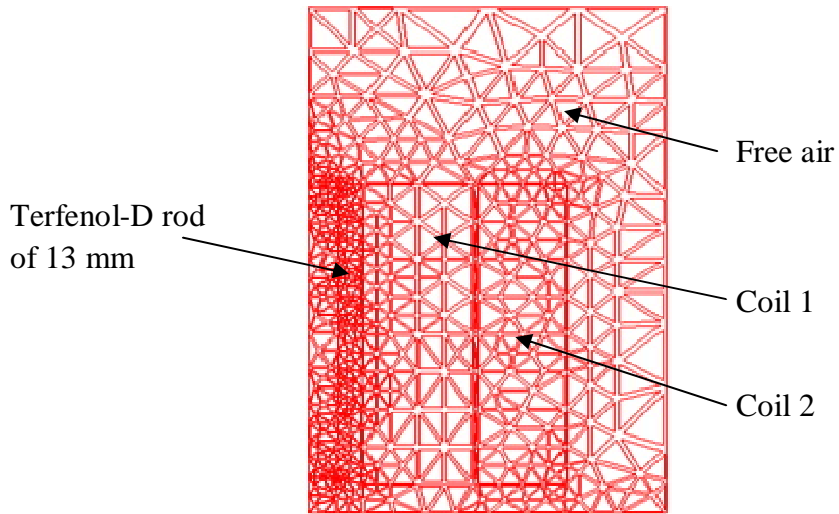| Number of passes	Pass	Triangles	Total Energy (J)	Energy Error (%)	Magnetic force (N)
Completed: 10	1	45	0.563058	116.6271	0.950437
Remaining: 0	2	126	0.554493	39.6466	0.770167
	3	160	0.543856	31.1649	0.706394
Convergence criteria:	4	202	0.541631	23.3676	0.756574
	5	258	0.541223	20.8959	0.720106
Target Error: 1%	6	332	0.540289	18.9158	0.868188
Energy Error: 14 %	7	426	0.540587	18.4593	0.736949
Delta Energy : 0.0406 %	8	546	0.540348	15.5030	0.619814
	9	705	0.540319	14.8908	0.623354
	10	911	0.540099	14.0331	0.627486

Fig. I.8. Axi-symmetric model of coaxial coils containing Terfenol-D rod of 13 mm in free air discretized with triangular elements.

Table I-6 Convergence data of coaxial coils containing Terfenol-D rod of 13 mm in free air using finite element Maxwell 2D solver.

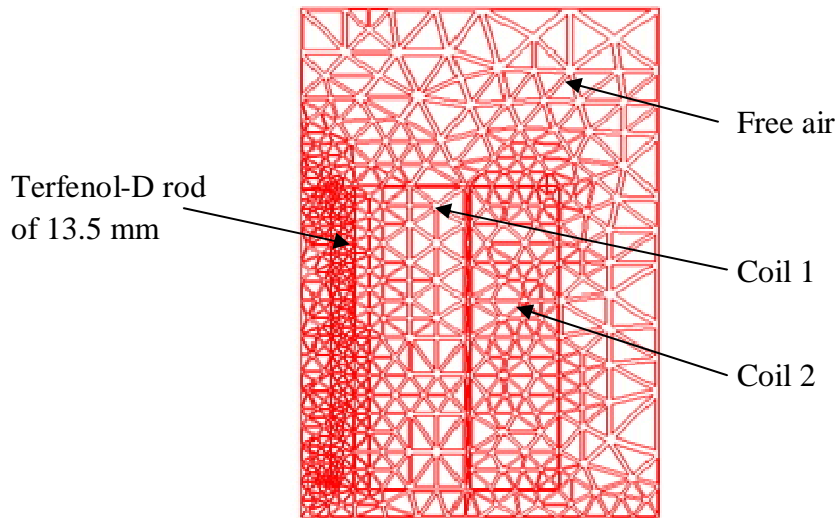| Number of passes	Pass	Triangles	Total Energy (J)	Energy Error (%)	Magnetic force (N)
Completed: 10 **Remaining: 0**	1	45	0.567085	117.5077	0.974681
	2	125	0.558970	39.9736	0.787107
	3	160	0.548133	31.7009	0.683019
	4	204	0.547137	21.7067	0.810427
Convergence criteria:	5	261	0.546652	20.3268	0.756750
	6	335	0.544338	18.8200	0.868643
Target Error: 1% **Energy Error: 13 %**	7	432	0.545060	18.0003	0.627226
Delta Energy : 0.0921 %	8	555	0.544910	16.2120	0.554659
	9	714	0.544728	14.2415	0.608719
	10	926	0.545230	12.9590	0.664940

Fig. I.9. Axi-symmetric model of coaxial coils containing Terfenol-D rod of 13.5 mm in free air discretized with triangular elements.

Table I-7 Convergence data of coaxial coils containing Terfenol-D rod of 13.5 mm in free air using finite element Maxwell 2D solver.

Number of passes	Pass	Triangles	Total Energy (J)	Energy Error (%)	Magnetic force (N)
Completed: 10 **Remaining: 0**	1	45	0.571056	118.4018	0.999439
	2	126	0.563243	40.9733	0.842465
	3	161	0.552717	32.0992	0.676951
Convergence criteria:	4	205	0.552310	22.4979	0.812194
	5	261	0.549787	19.8627	0.765074
	6	335	0.549037	19.2915	0.705171
Target Error: 1% **Energy Error: 13.2 %**	7	431	0.549087	17.5997	0.680278
Delta Energy : 0.0852 %	8	556	0.549276	16.3606	0.627985
	9	717	0.548781	15.5620	0.635724
	10	922	0.549249	13.2018	0.707031

192

APPENDIX – II

II.1 Specifications of instruments

S.No.	Equipment	Specifications
1	APLAB Regulated dual DC power supply LD6405	Power input:- 240V, 50Hz DC voltage output:- 0 to 64 V Maximum current output:- 5 A.
2	Laser pick up opto NCDT 1402	Measuring range:- 10 mm Start of measuring range:- 20mm Mid measuring range:- 25mm End of measuring range:- 30mm Linearity:- 5 to 18 μm Resolution:- 1 μm for static and 2 to 5 μm for dynamic Measuring rate:- 50 to 1.5 kHz Light source:- semiconductor laser 1 mW, 670 nm Spot diameter:- 110 to 1200 μm Weight:- 83 gm Operating temperature:- 0 to 50^0C Measuring value output:- 4 to 20 mA for analog and RSS422 for digital Supply voltage:- 11 to 30 VDC
3	Lakeshore model 410 Gauss meter	Display:- LCD, $3\frac{1}{2}$ digits Resolution:- 0.1 gauss (200 gauss range) DC accuracy:- 2% of reading ±1% of full scale at 25^0C AC accuracy:- ±5% of reading Frequency response: - DC and 20 Hz to 10 kHz. Three ranges:- ±200 G (±20 mT), ±2 kG (±200 mT) and ±20 kG (±2 T) Temperature range:- 0 to 50^0C (operating) Instrument temperature coefficient: - 0.05% of readings per degree C. Weight:- 0.45 kg (1 Pound) Size:- 19.3×9.9×4.32 cm Power:- Battery operated, 4AA (life > 160 hours) Other features: - Max. Hold, Relative reading mode, Alarm, Filter, water resistant enclosure.

4	PT 4000 Model force sensor make PT Ltd.	Nominal force:- 10000 N Nominal sensitivity:- 2 Linearity deviation:- 0.05 Input resistance:- 350....500 Ω Output resistance:- 350....500 Ω Reference excitation voltage:- 5 Operating temperature range:- -30 to +85 Weight:- 0.77 kg
5	Belleville Springs	Number of leaves= 6 Outer diameter of spring = 63.5 mm Inner diameter of spring = 31.75 mm Thickness of spring (t) = 2.014982 mm deflection of spring (h) = 2.841244 mm Overall height of spring (H) = 4.85 mm

II.2 Photographs of components and instruments

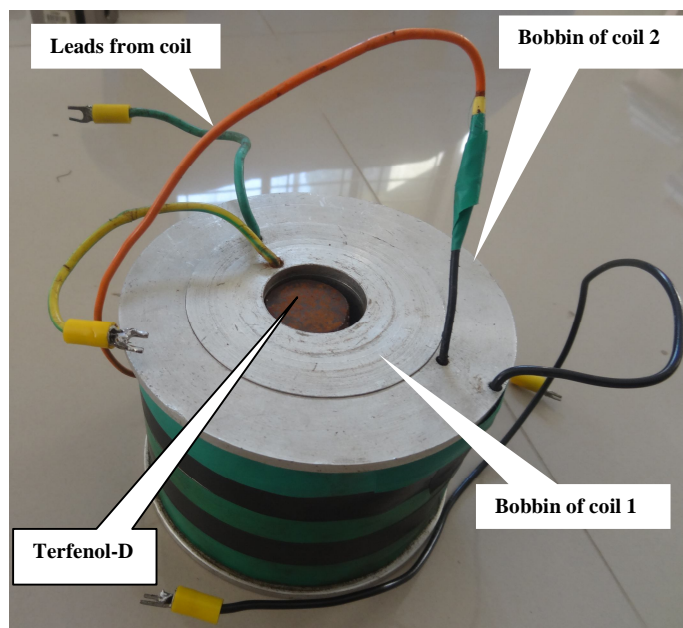Fig. II.1. Magnetostrictive material (Terfenol-D) test specimen (DMRL, Hyderabad).

Fig. II.2. Terfenol-D surrounded by coaxial coils.

194

Fig. II.3. Housing materials (cast iron and aluminium) used to test the performance of a Terfenol-D actuator in the experimental setup.
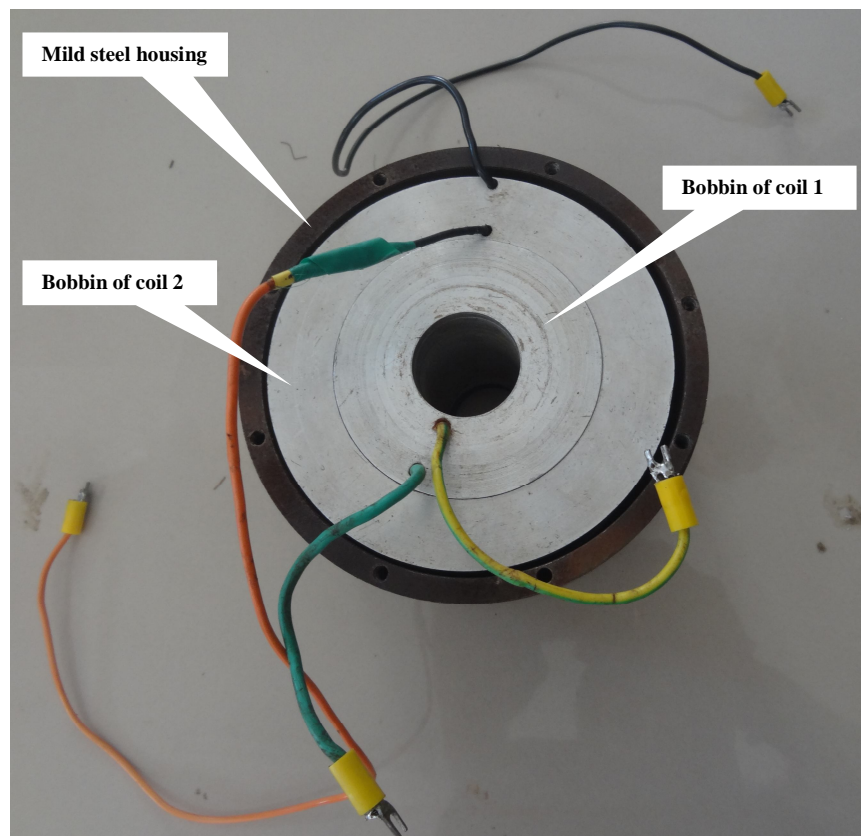
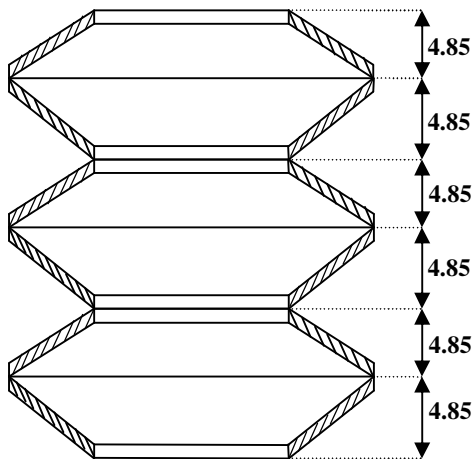

Fig. II.4. Coaxial coils in a mild steel housing.

Fig. II.5. Opto NCDT 1402 laser pick up sensor.

Fig. II.6. RS 422 USB serial converter.

Fig. II.7. Belleville springs (6 numbers of leaves).

(a)   (b)

Fig. II.8. (a) Schematic and (b) photograph of series arrangement of Belleville springs.
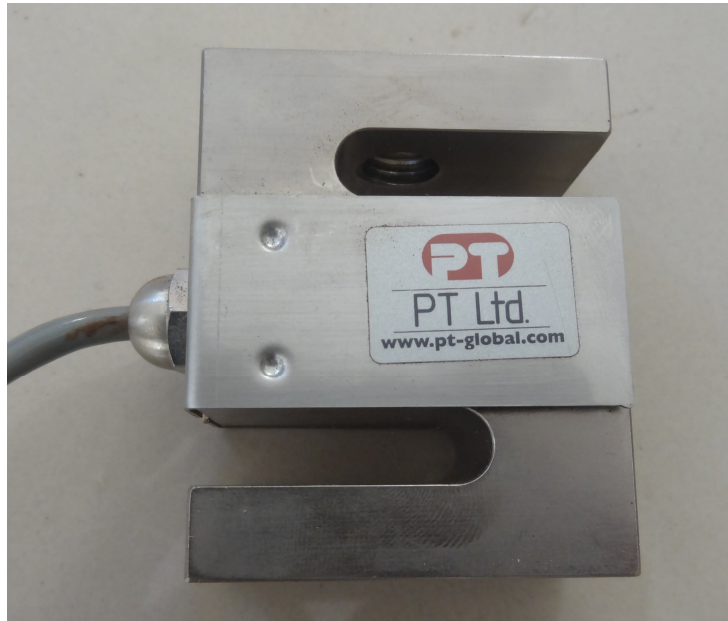
Fig. II.9. PT 4000 Model force transducer (10 KN).

Fig. II.10. 4 Channel 24 Bit half-full bridge analog output NI 9237 module.

Fig. II.11. Lakeshore Guass meter with axial probe.

Fig. II.12. Digital vernier height guage.

APPENDIX III

EXPERIMENTAL RESPONSE CHARACTERISTICS OF A TERFENOL-D ACTUATOR FOR DIFFERENT PRELOADS

In this appendix, the experimental response obtained from the Terfenol-D actuator for different preloads against the individual applied step input to coaxial coils, displacement for one cycle under different input operating conditions, the effect of equal step input to coaxial coils and biasing to one of the coaxial coils on steady state displacement in the form of screen shots from ILD software and origin plots are presented. Finally the comparison of theoretical and experimental displacements, as well the comparison of blocked force achieved from both theoretical and observed for different preload conditions, computation of theoretical and experimental response time are presented.

III.1 Displacement of a Terfenol-D actuator for an applied equal DC input to coaxial coils under different preloads

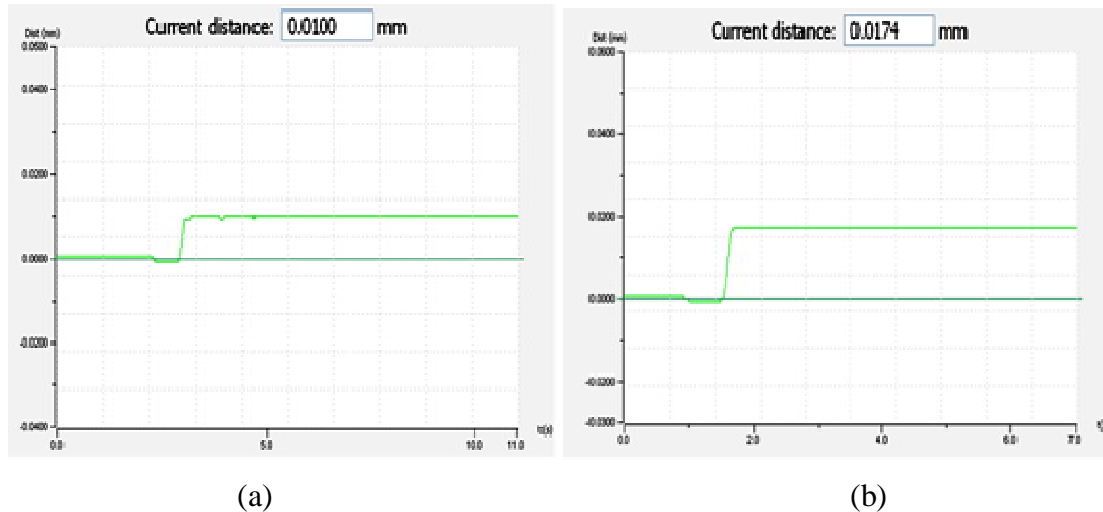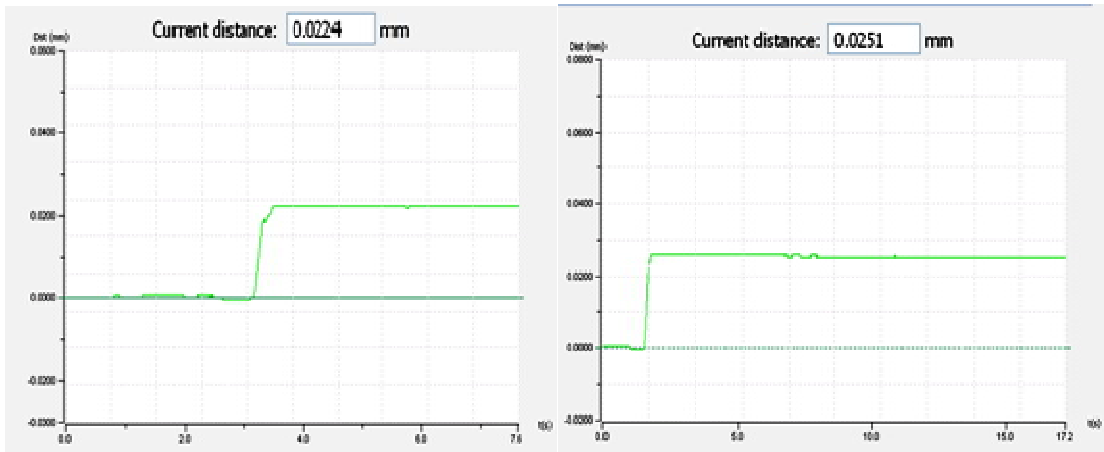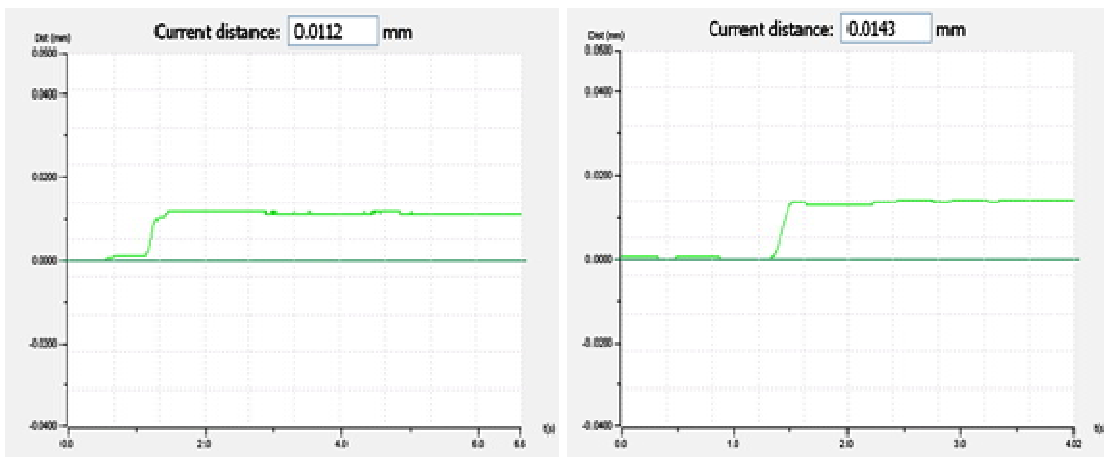(a)   (b)

Fig. III.1. Response of Terfenol-D actuator under 500 N preload for step input of
(a) 1.5 A and (b) 2.5 A to coaxial coils.
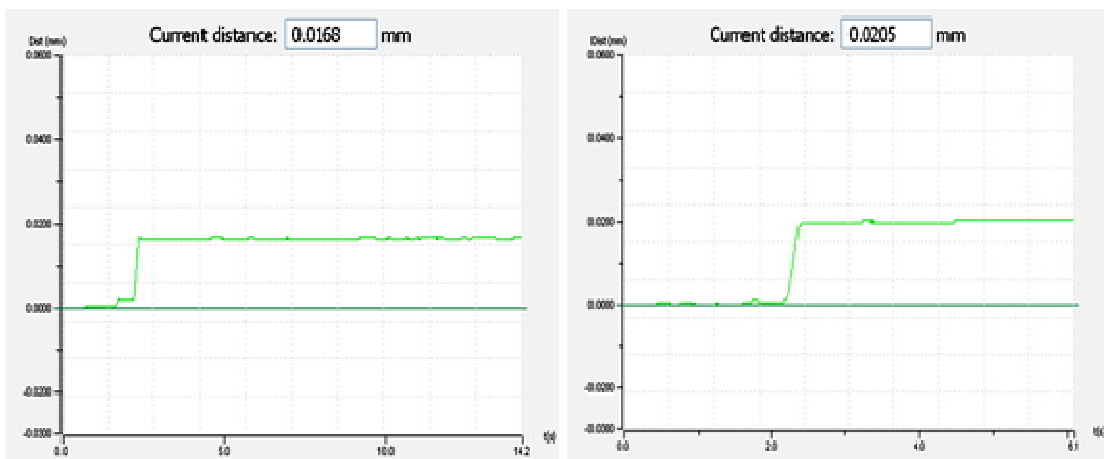
(a)   (b)

Fig. III.2. Response of Terfenol-D actuator under 500 N preload for step input of (a) 3.5 A and (b) 4 A to coaxial coils.

(a)   (b)

(c)   (d)

Fig. III.3. Response of Terfenol-D actuator under 1000 N preload for step input of (a) 0.5 A (b) 1.5 A (c) 2.5 A and (d) 3.5 A to coaxial coils.
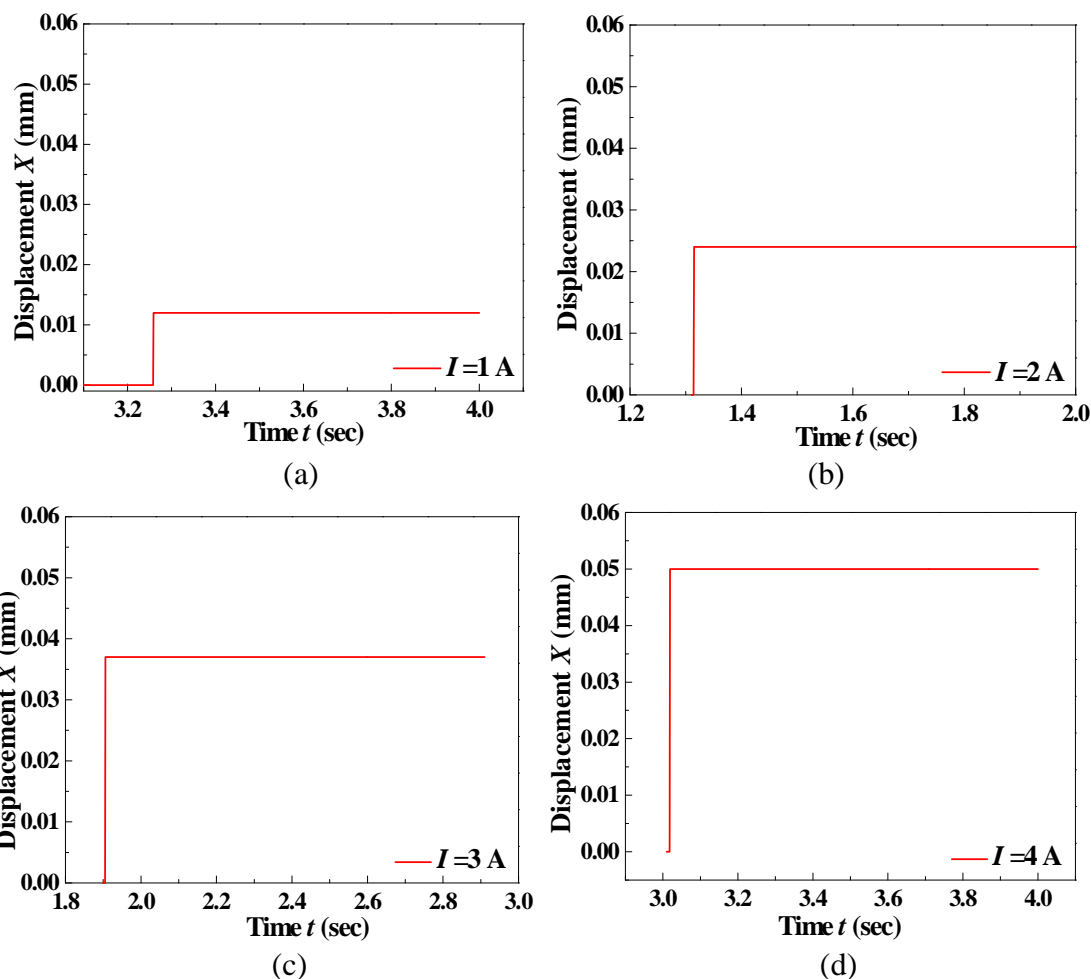
Fig. III.4. Response of Terfenol-D actuator under 1500 N preload for step input of (a) 1 A (b) 2 A (c) 3 A and (d) 4 A to coaxial coils.
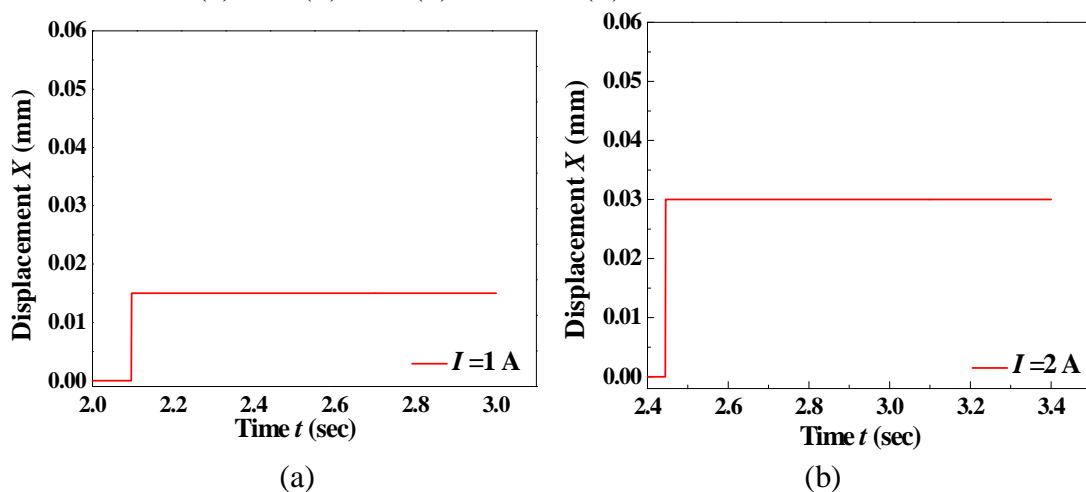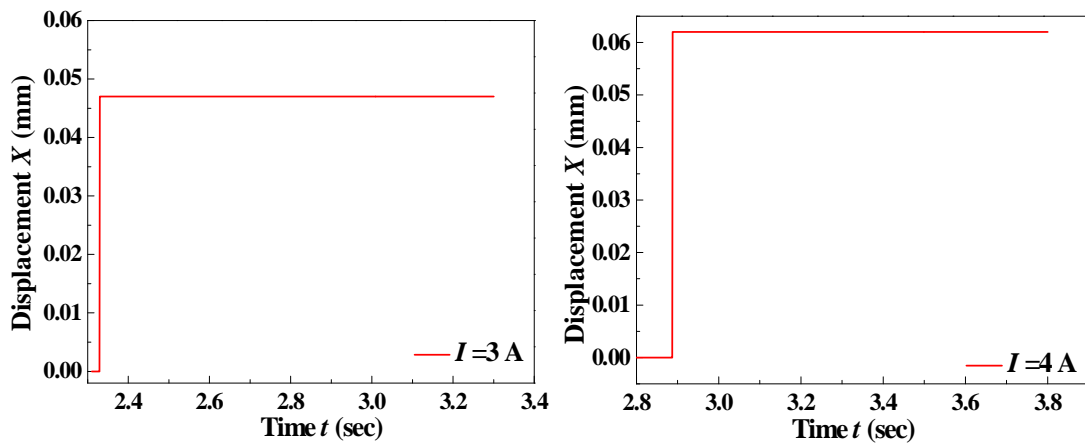

Fig. III.5. Response of Terfenol-D actuator under 2000 N preload for step input of (a) 1 A and (b) 2 A to coaxial coils.

(a)   (b)

Fig. III.6. Response of Terfenol-D actuator under 2000 N preload for step input of (a) 3 A and (b) 4 A to coaxial coils.

Three trials were conducted for each input operating condition to examine the performance of a Terfenol-D actuator. Average displacement of three trials has been considered to plot the response curve. Summary of the displacement obtained from the Terfenol-D actuator for equal input coaxial coils is tabulated in Table III-1.

Table III-1. Displacement of a Terfenol-D actuator for different trials.

Current (I)	Increasing			Decreasing		
	Trail 1	Trail 2	Trail 3	Trail 1	Trail 2	Trail 3
0.25	0.0016	0.0006	0.0026	0.0017	0.0006	0.0026
0.5	0.0026	0.0027	0.0025	0.0037	0.0031	0.0025
0.75	0.0036	0.0036	0.0037	0.0056	0.0036	0.0044
1	0.005	0.0056	0.0044	0.0056	0.005	0.0044
1.25	0.0056	0.0069	0.0081	0.0087	0.0081	0.0075
1.5	0.0069	0.0081	0.0075	0.0112	0.0137	0.0093
1.75	0.0106	0.01	0.0112	0.0125	0.0137	0.0125
2	0.0112	0.0125	0.0137	0.0137	0.0131	0.0125
2.25	0.0143	0.0131	0.0137	0.0148	0.0137	0.0143
2.5	0.0156	0.0181	0.0131	0.0156	0.0181	0.0131
2.75	0.0148	0.0181	0.0213	0.0218	0.0222	0.0224
3	0.0218	0.023	0.0224	0.0243	0.0239	0.0239
3.25	0.0243	0.023	0.0255	0.0255	0.0266	0.0243
3.5	0.0243	0.0255	0.0266	0.0266	0.0266	0.0266
3.75	0.0274	0.0274	0.0274	0.0295	0.0255	0.028
4	0.0295	0.0295	0.0295	0.0299	0.0299	0.0299

III.2 Effect of equal DC input to coaxial coils on displacement of a Terfenol-D actuator
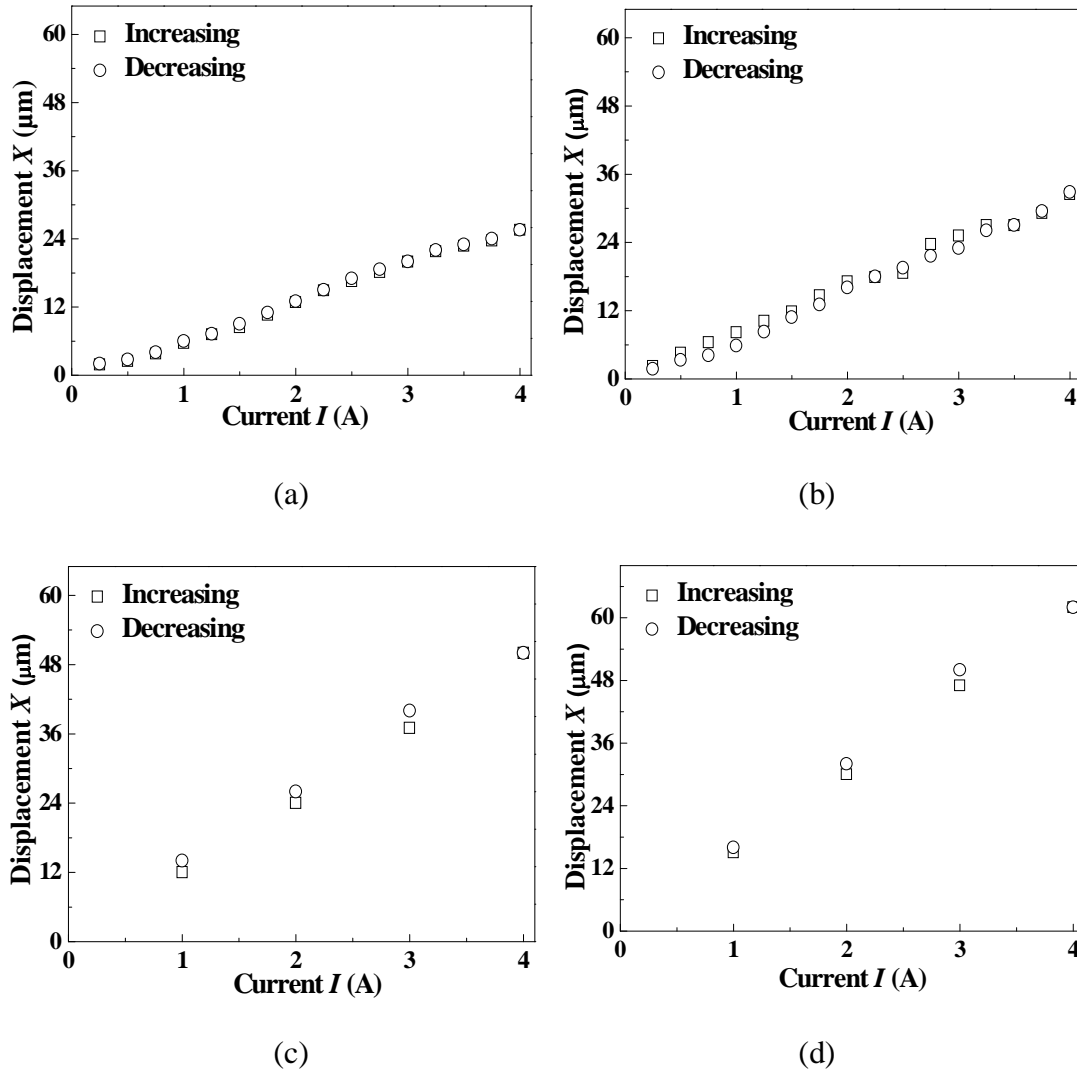

(a)

(b)

(c)

(d)

Fig. III.7. Displacement of a Terfenol-D actuator by varying step input to coil 1 and coil 2 under (a) 500 N (b) 1000 N (c) 1500 N and (d) 2000 N preload.

III. 3 Effect of bias magnetic field from coil 1 or coil 2 on the displacement of a Terfenol-D actuator
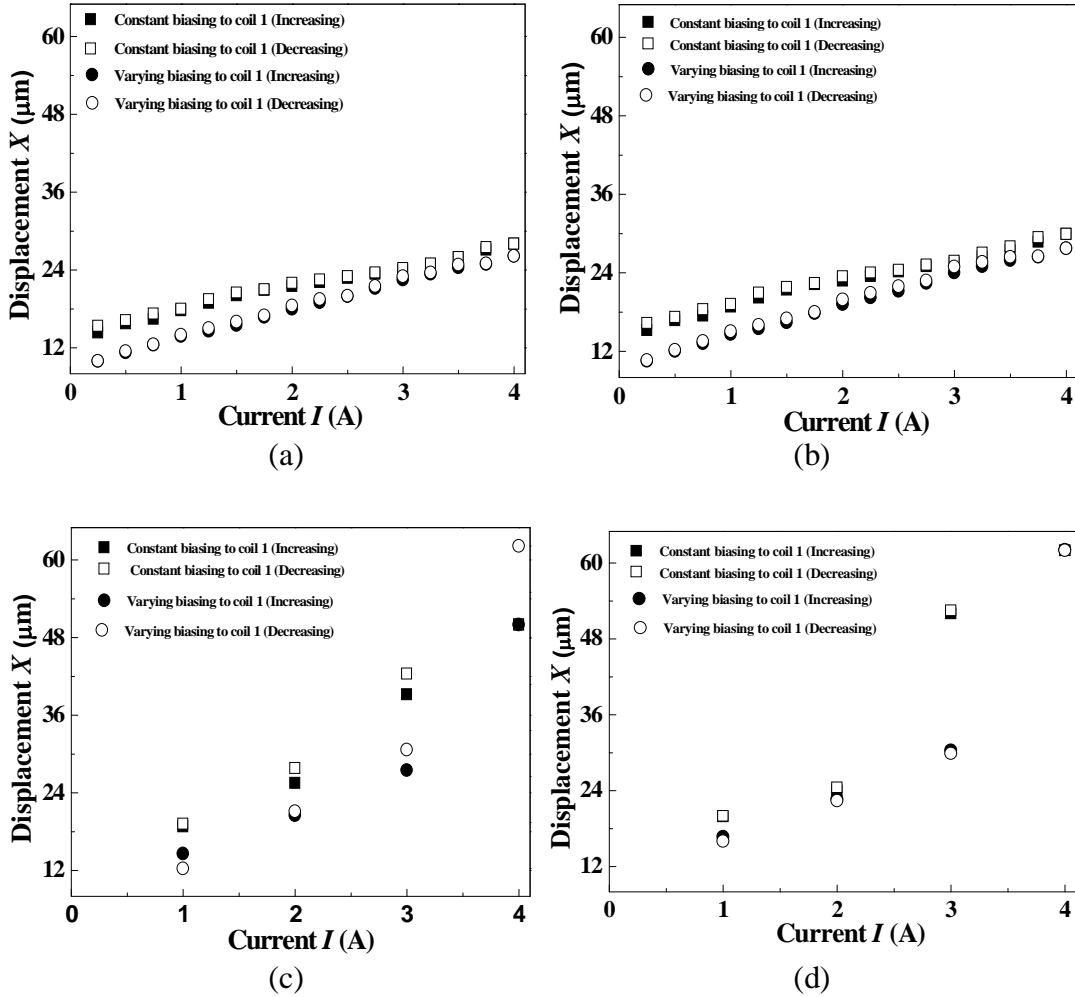

Fig. III.8. Displacement of a Terfenol-D actuator for (a) 500 N (b) 1000 N (c) 1500 N and (d) 2000 N preload under biasing conditions.

III. 4 Displacement and blocked force from the Terfenol-D actuator for different preloads
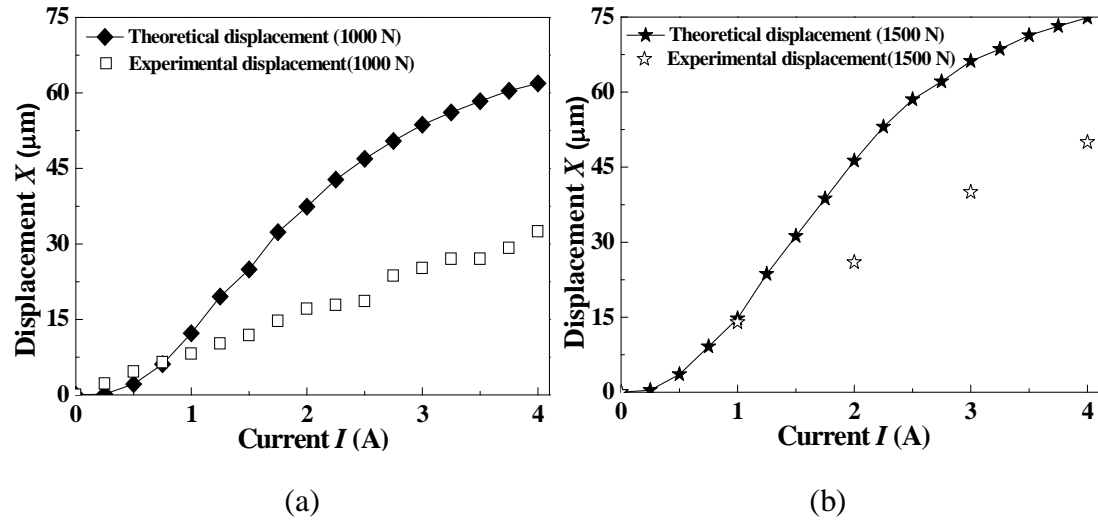

(a)

(b)

Fig. III.9. Comparison of theoretical and experimental displacement of a Terfenol-D actuator for (a) 1000 N and (b) 1500 N preload.
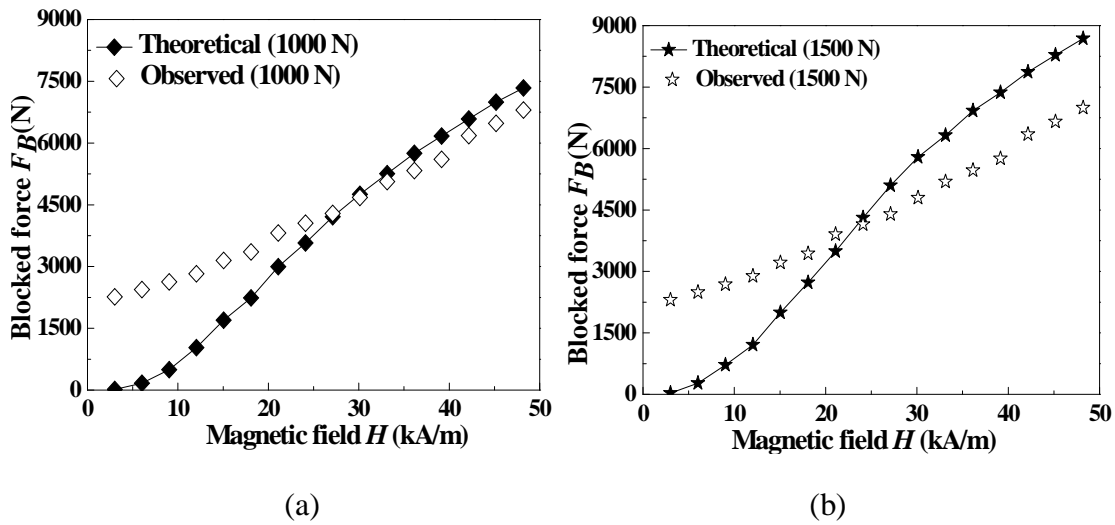

(a)

(b)

Fig. III.10. Comparison of blocked force from Terfenol-D actuator for (a) 1000 N and (b) 1500 N preload.
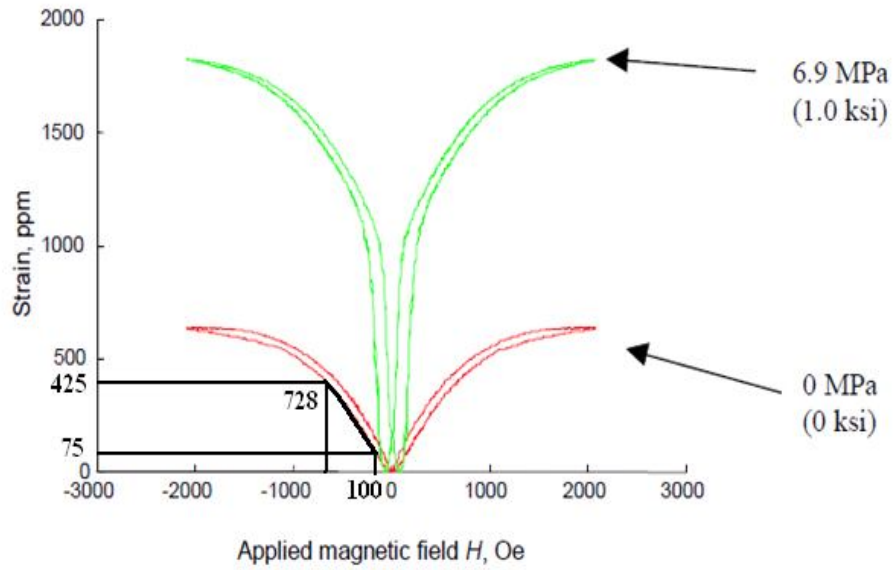
Fig. III.11. Butterfly curves for zero and 6.9 MPa (1.0 ksi) preload condition
(Source of figure: Kellogg and Flatau, 1999).

III. 5 Computation of response time from theoretical and experimental curve

Fig. III.12 (a) and (b) shows the theoretical and experimental response curve of an actuator for the applied step input of 3.5 A. The theoretical and experimental response time is computed and the same is illustrated with the aid of Fig. III.12 (a) and (b). It is between the point, where the step input is applied and the point, where the response becomes steady.
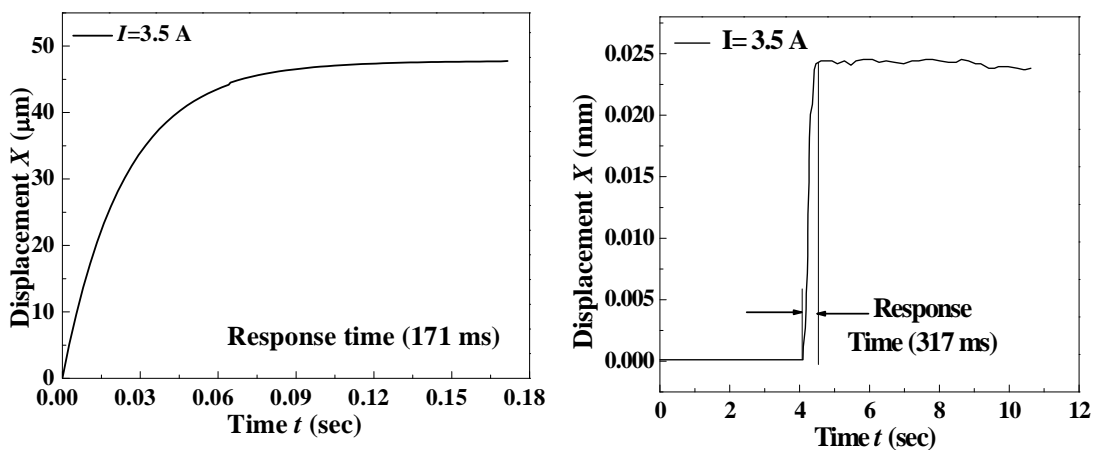

Fig. III.12. Illustration showing the computation of response time with (a) theoretical model and (b) experimental curve.

APPENDIX IV

In this appendix, procedure and computations for the axial braking force, torque capacity of frictional pads based on disc specifications and as well after amplification from the theoretical and experimental output of a Terfenol-D actuator are shown. In addition, photographs of individual components of a magnetostrictive disc brake setup, calibration of Belleville springs to know the load to be applied on Terfenol-D rod, the screen shots of experimental response obtained from ILD 1402 software for a Terfenol-D actuator and actuator with hydraulic amplification unit are provided.

IV.1. Procedure for computation of axial braking force and brake torque for disc brake system

Kinetic energy possessed by the rotor depends on mass moment of inertia and angular velocity.
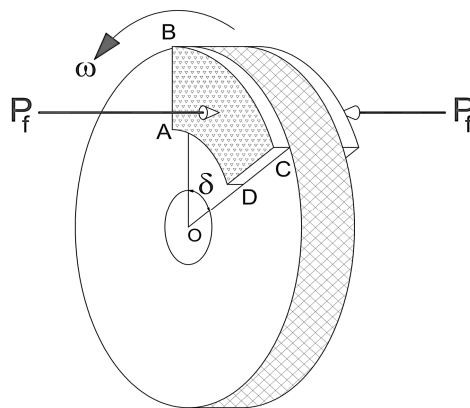
Fig. IV.1. Disc rotor with friction pad ABCD.

Fig. IV.1 shows the schematic of the disc with friction pads ABCD in which P_f is the axial force to stop the rotating disc and δ is the angle subtended by the frictional pads at the center of the disc. In the present work, a disc of 160 mm diameter and an average disc speed of 3315 rpm are chosen for illustration. The disc speed of 3315 rpm corresponds to the vehicle moving at 100 km/hr. The kinetic energy possessed by the disc is given by:

$$K.E = \frac{1}{2}I_{disc}\omega^2 \qquad\qquad\qquad\qquad\qquad\qquad\qquad (IV.1)$$

Where I_{disc} is the mass moment of inertia of the disc equal to mk^2, ω is the angular velocity of the disc equal to $2\pi C/60$ in rad/sec, C is the speed of the disc in rpm, m is the mass of the disc equal to $\rho \times V$ in kg, ρ is density of the cast iron material equal to 7200 kg/m^3, V is the volume of the disc equal to At in m^3, A is the cross-sectional area of the disc equal to $\pi d^2/4$, d is the diameter of the disc in mm, t is the thickness of the disc equal to 3 mm, k is the radius of gyration of the disc equal to $d/\sqrt{8}$. With this, the kinetic energy possessed by the disc equal to 83.8 Joules at disc speed of 3500 rpm.

In disc brake system, the disc or rotor is stopped by applying the force perpendicular to the plane of the disc from either side. The procedure for calculating the axial force required to stop the rotor is explained in Newcomb and Spurr (1967). Fig. IV.2 (a) shows the enlarged view of a friction pad ABCD whose outer and inner radii are r_0 and r_i respectively. Frictional pad is divided into finite elements and each element is located at radius r, included angle be $\delta\psi$ and having area $r\delta\psi\delta r$ located at a distance of l_p from the center. If p is the pressure acting on the unit area of the frictional pad then the frictional force on the elemental area is given by:

$$\delta f = \mu p r \delta r \delta \psi \qquad\qquad\qquad\qquad\qquad\qquad\qquad (IV.2)$$

Torque acting on each pad is given by:

$$T = \int_{r_i}^{r_0} \int_{-\frac{\delta}{2}}^{\frac{\delta}{2}} \mu p r^2 \delta r \delta \psi = \int_{ri}^{r_0} \mu p r^2 \delta dr \qquad\qquad\qquad\qquad (IV.3)$$

The force acting on the elemental area of the pad is resolved into the components perpendicular and parallel to the line of action of force as in Fig. IV.2 (b). The two components are, and on evaluation results in:

$$R_x = \int_{r_0}^{r_i} \int_{-\frac{\delta}{2}}^{\frac{\delta}{2}} \mu p r \sin\psi \delta r \delta \psi = 0 \text{ and } R_y = \int_{r_i}^{r_0} \int_{-\frac{\delta}{2}}^{\frac{\delta}{2}} \mu p r \cos\psi \delta r \delta \psi = 2\int_{r_i}^{r_0} \mu p r \sin\left(\frac{\delta}{2}\right) dr \quad (IV.4)$$
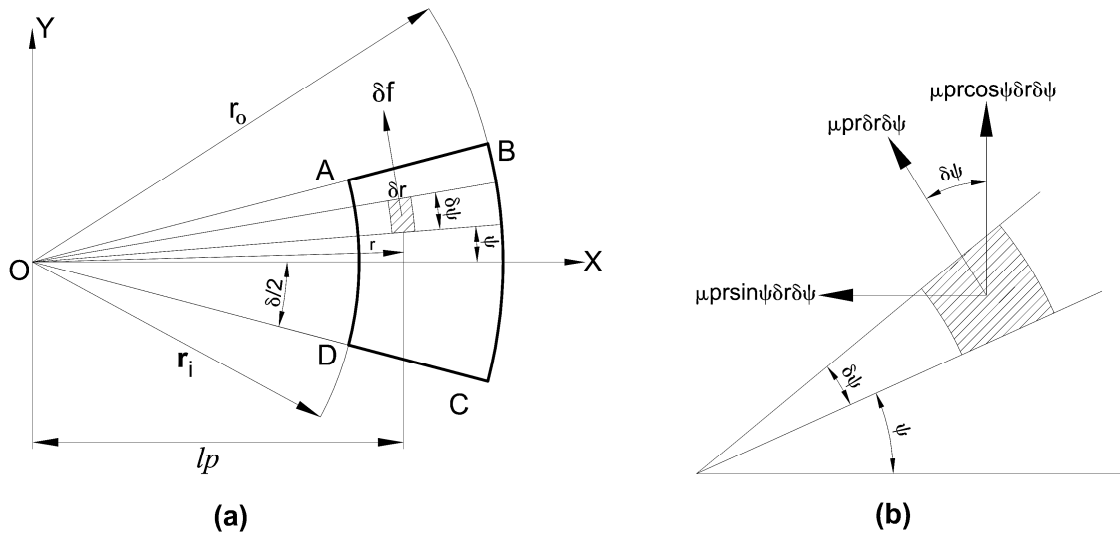
Fig. IV.2. Frictional force on an elemental area of friction pad (a) and its components (b).

Torque acting on each pad is also equal to the moment of the horizontal component (R_y) of the resultant about its center and is expressed as:

$$T = R_y l_p \tag{IV.5}$$

Where l_p is the perpendicular distance from the center to the line of action of horizontal component of force. This perpendicular distance depends on the operating conditions of the disc brake that decides the capacity of a disc brake.

One of the operating conditions is uniform pressure condition applicable to new brakes. According to this condition, when a disc brake is subjected to uniform pressure p_1, every point of the frictional pad experiences a maximum design pressure. Substituting Eq. (IV.3) and (IV.4) into (IV.5) and on integrating and simplifying yields the perpendicular distance (l_1) from the center to the line of action of force as:

$$l_1 = \frac{2\delta}{3\sin\frac{\delta}{2}} \frac{(r_i + r_0)}{2}\left[1 - \frac{r_i r_0}{(r_i + r_0)^2}\right] \tag{IV.6}$$

The torque capacity of the frictional pads based on uniform pressure T_1 is given by

$$T_1 = 2\mu P_1 l_1 = \frac{4\mu P_1 2\delta}{3\sin\dfrac{\delta}{2}}\frac{(r_i + r_0)}{2}\left[1 - \frac{r_i r_0}{(r_i + r_0)^2}\right] = 2\mu P_1 K_1 R_m \tag{IV.7}$$

$$R_m = \frac{(r_i + r_0)}{2} \tag{IV.8}$$

$$K_1 = \frac{2\delta}{3\sin\dfrac{\delta}{2}}\left[1 - \frac{r_i r_0}{(r_i + r_0)^2}\right] \tag{IV.9}$$

Where μ is the coefficient of friction between the frictional pads and disc equal to 0.3, P_1 is the axial braking force acting on each pad in uniform pressure condition, R_m is the mean radius of frictional pads, r_0 and r_i are the outer and inner radii of annular pads equal to 40 and 26.6 mm (from the data sheet of Bajaj Pulsar motor cycle) , K_1 is the constant identified from Eq. (IV.7) is given by Eq. (IV.9) and δ is the included angle of the frictional pads sector. It is assumed as equal to 45^0 in the present work.

The other operating condition is uniform wear. Here the performance of brake is based on the amount of usage of the friction pads i.e. the amount of wear. If the wear is proportional to the work done by the frictional pads, then the product of pressure intensity times the local radius will be constant. When a disc brake is assumed to have undergone uniform wear, the perpendicular distance (l_2) from the center to the line of action of force is given by:

$$l_2 = \frac{\delta}{4\sin\dfrac{\delta}{2}}(r_i + r_0) \tag{IV.10}$$

The torque capacity of the frictional pads based on uniform wear T_2 is given by

$$T_2 = 2\mu P_2 l_2 = \frac{2\mu P_2 \delta}{2\sin\dfrac{\delta}{2}}\frac{(r_i + r_0)}{2} = 2\mu P_2 K_2 R_m \tag{IV.11}$$

Where P_2 is the axial braking force acting on each pad in uniform wear condition and K_2 is the constant being identified in Eq. (IV.11) as,

$$K_2 = \frac{\delta}{2\sin\dfrac{\delta}{2}} \qquad\qquad\qquad\qquad (IV.12)$$

The kinetic energy possessed by the disc rotor obtained from the Eq. (IV.1) is equal to torque capacity of the frictional pads based on (i) uniform pressure and (ii) uniform wear condition. The axial braking forces P_1 and P_2 are calculated using Eq. (IV.7) and (IV.11) based on two operating conditions. The maximum of P_1 and P_2 is the required axial braking force P_f required to stop the disc.

IV.2. Illustration of computation of axial braking force and brake torque for disc brake system

A disc of 160 mm diameter, 3 mm thickness and an average disc speed of 100 km/hr (3500 rpm) are chosen. The kinetic energy possessed by the disc is equated to torque capacity of the disc computed based on uniform pressure and uniform wear conditions. The calculations are as follows for a disc speed of 10 km/hr (331.5 rpm).

a. Kinetic energy of the disc

$$K.E = 1/2 \times I\omega^2 \qquad\qquad\qquad\qquad (IV.13)$$

Angular velocity of the disc $(\omega) = 2\pi C/60 = 34.7$ rad/sec.

Volume of the disc $(V) = A \times t = \pi d^2/4 \times t = 6.03 \times 10^{-5}$ m^3

Density of the disc material $(\rho) = 7200$ kg/m^3.

Radius of the gyration of the disc $(k) = d/\sqrt{8} = 0.05657$

Mass of the disc $(m) = \rho V = 0.434$ kg.

Mass moment of inertia of the disc $(I) = mk^2 = 1.4 \times 10^{-3}$ kg-m^2

Kinetic energy of the disc equal to 0.838 N-m at a speed of 10 km/hr.

b. Axial braking force based on uniform pressure

$$T_1 = 2fP_1K_1R_m \qquad\qquad\qquad\qquad (IV.14)$$

Where constant $(K_1) = 2\delta \left[1 - \dfrac{r_i r_0}{(r_i + r_0)^2}\right] \Big/ 3\sin\dfrac{\delta}{2} = 1.04$

Mean radius of each frictional pad $(R_m) = (r_i + r_0)/2 = 0.0337$ mm

Coefficient of friction (f) between the disc and frictional pad is equal to 0.3 and axial braking torque (T_1) is equal to kinetic energy possessed by the disc equal to 0.838 N-m. With this the axial braking force (P_1) required for the disc is equal to 39.86 N based on uniform pressure at a disc speed of 10 km/hr.

c. Axial braking force based on uniform wear

$$T_2 = 2fP_2K_2R_m \qquad\qquad\qquad\qquad (IV.15)$$

Where constant $(K_2) = \delta \Big/ 2\sin\dfrac{\delta}{2} = 1.026$

Coefficient of friction (f) between the disc and frictional pad is equal to 0.3, mean radius (R_m) of the each frictional pads is 0.0337 mm and axial braking torque (T_2) is equal to kinetic energy possessed by the disc equal to 0.838 N-m. With this the axial braking force (P_2) required for the disc is equal to 40.4 N based on uniform pressure at a disc speed of 10 km/hr.

The maximum from P_1 and P_2 will be the required axial braking force equal to 40.4 N and the corresponding braking torque equal to 0.838 N-m.

IV.3. Computation of stopping distance and stopping time for a disc brake system

Stopping distance and stopping time due to retardation of rotating disc is calculated using one of the fundamental equations of motion (Giri, 1994).

$$s = \dfrac{u_1^{\,2}}{2a} \qquad\qquad\qquad\qquad (IV.16)$$

$$t_s = \dfrac{v_1 - u_1}{a} \qquad\qquad\qquad\qquad (IV.17)$$

Where v_1 is the final velocity of the disc equal to zero as it is brought to rest, u_1 is the initial velocity of the disc, a is the retardation produced by the braking force, s is the stopping distance and t is the stopping time respectively. The stopping distance and stopping time calculated using Eq. (IV.16) and Eq. (IV.17) for a disc rotating at different speeds between 10 to 100 km/hr are listed in Tables IV.1 and IV.2.

Table IV-I. Stopping distance for the different speeds of a rotating disc.

Speed (km/hr)	Speed (m/sec)	Deceleration (m/sec^2)	Stopping distance (m)
10	2.7	2.943	1.3
20	5.5	2.943	5.2
30	8.3	2.943	11.8
40	11	2.943	21
50	13.8	2.943	32.7
60	16.7	2.943	47.2
70	19.4	2.943	64.2
80	22.2	2.943	84
90	25	2.943	106
100	27.7	2.943	131

Table IV-2. Stopping distance for the different speeds of a rotating disc.

Speed (km/hr)	Speed (m/sec)	Stopping time (sec)				Total Stopping time (sec)
		Actuator	Amplification unit	Wheel cylinder	Rotor	
10	2.7	0.171	0.00174	0.00076	0.944	1.2
20	5.5	0.171	0.00174	0.00076	1.88	2
30	8.3	0.171	0.00174	0.00076	2.83	3
40	11	0.171	0.00174	0.00076	3.77	3.94
50	13.8	0.171	0.00174	0.00076	4.72	4.89
60	16.7	0.171	0.00174	0.00076	5.66	5.84
70	19.4	0.171	0.00174	0.00076	6.6	6.8
80	22.2	0.171	0.00174	0.00076	7.55	7.72
90	25	0.171	0.00174	0.00076	8.5	8.67
100	27.7	0.171	0.00174	0.00076	9.44	9.6

IV.4. Estimation of available braking force and torque at frictional pads

The available braking force and torque capacity of frictional pads of caliper unit after amplification from the theoretical and experimental output displacement of a Terfenol-D actuator is evaluated as follows:

a. Available braking force and torque at frictional pads after amplification from the theoretical output displacement of a Terfenol-D actuator

i. Pressure and braking force on each frictional pad

Force exerted by a 28 mm diameter Terfenol-D rod is equal to 4146 N under zero preload conditions. With this, the pressure exerted by a Terfenol-D rod on larger piston is given by:

Pressure exerted by a Terfenol-D rod on larger piston (p_L)

$$= \text{Output force by Terfenol-D/Area of larger piston}$$
$$= 4146/\,9503.32$$
$$= 0.442 \text{ N/mm}^2$$

According to Pascal's law, the pressure exerted by larger piston on wheel cylinder piston (p_W) is equal to the pressure exerted by a Terfenol-D rod on larger piston (p_L).

Therefore, the pressure exerted by a Terfenol-D rod on larger piston (p_L)

$$= \text{Force acting on each wheel cylinder/ Area of each wheel cylinder.}$$

Force acting on each wheel piston $= p_L \times \text{Area of each wheel cylinder}$

$$= p_L \times \pi \left(22^2\right)\!\Big/4 \,=\, 168 \text{ N}$$

Pressure acting on each annular pad (p_A)

$$= \text{Fluid force from wheel cylinder on each pad / Area of each annular friction pad}$$

Where area of each annular pad is equal to,

$$\theta \pi \left(r_o^2 - r_i^2\right)\!\Big/360^o = \theta \pi \left(40^2 - 26.67^2\right)\!\Big/360^o = 349 \text{ mm}^2$$

With this, the pressure and force acting on each annular pad is equal to 0.48 N/mm² and 168 N respectively from actuator output for 4 A DC input under zero prestress conditions.

ii. Torque capacity of each annular pad

Torque capacity of each annular pad $(T) = \mu F r$ (IV.18)

Where μ is coefficient of friction between pads and disc equal to 0.15, F is force acting on each annular pad and r is effective mean radius of annular pads equal to $(r_i + r_0)/2 = 0.0337$ m.

Torque capacity of each frictional annular pads= $0.15 \times 168 \times 0.0337 = 0.85$ N-m.

b. Available braking force and torque at frictional pads after amplification from the experimental output displacement of a Terfenol-D actuator

i. Pressure and braking force on each frictional pad

Force exerted by a 28 mm diameter Terfenol-D rod is equal to 2793 N under zero preload conditions. With this, the pressure exerted by a Terfenol-D rod on larger piston is given by:

Pressure exerted by a Terfenol-D rod on larger piston (p_L)

$$= \text{Output force by Terfenol-D/Area of larger piston}$$
$$= 2793/\ 9503.32$$
$$= 0.3 \text{ N/mm}^2$$

According to Pascal's law, the pressure exerted by larger piston on wheel cylinder piston (p_W) is equal to the pressure exerted by a Terfenol-D rod on larger piston (p_L).

Therefore, the pressure exerted by a Terfenol-D rod on larger piston (p_L)

$$= \text{Force acting on each wheel cylinder/ Area of each wheel cylinder.}$$

Force acting on each wheel piston $= p_L \times$ Area of each wheel cylinder

$$= p_L \times \pi \left(22^2\right)/4 = 114 \text{ N}$$

Pressure acting on each annular pad (p_A)

$$= \text{Fluid force from wheel cylinder on each pad / Area of each annular friction pad}$$

Where area of each annular pad is equal to,

$$\theta \pi \left(r_o^2 - r_i^2\right)/360^o = \theta \pi \left(40^2 - 26.67^2\right)/360^o = 349 \text{ mm}^2$$

With this, the pressure and force acting on each annular pad is equal to 0.32 N/mm^2 and 114 N respectively from actuator output for 4 A DC input under zero prestress conditions.

ii. Torque capacity of each annular pad

Torque capacity of each annular pad $(T) = \mu F r$

Where μ is coefficient of friction between pads and disc equal to 0.15, F is force acting on each annular pad and r is effective mean radius of annular pads equal to $(r_i + r_0)/2 = 0.0337$ m.

Torque capacity of each frictional annular pads= $0.15 \times 114 \times 0.0337 = 0.58$ N-m.

c. Amplified displacement at each annular pad

The amplified displacement available at the annular pads can be computed by equating the volume of fluid displaced by the larger piston of a hydraulic cylinder and wheel cylinder piston of caliper unit.

Volume of lubricating displaced by the larger piston $= \pi d_L^2 \times l_L / 4$

Where d_L and l_L are the diameter and displacement of a larger piston equal to 110 and 0.048 mm respectively.

Volume of water displaced by the wheel cylinder piston $= \pi d_W^2 \times l_W / 4$

Where d_W and l_W are the diameter and displacement of a wheel cylinder piston in a caliper unit. With this, the amplified displacement is equal to 1.2 mm.

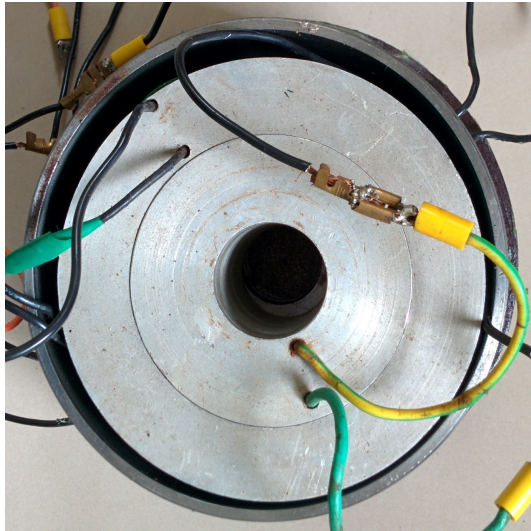**IV.5. Photographs of individual components of a magnetostrictive disc brake system**

Fig. IV.3. Actuator housing with coaxial coils.
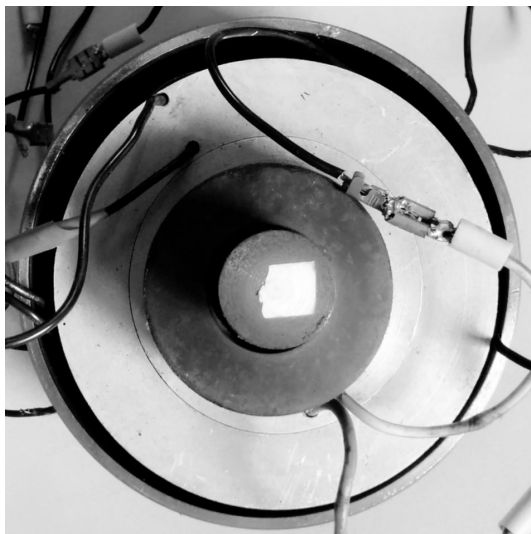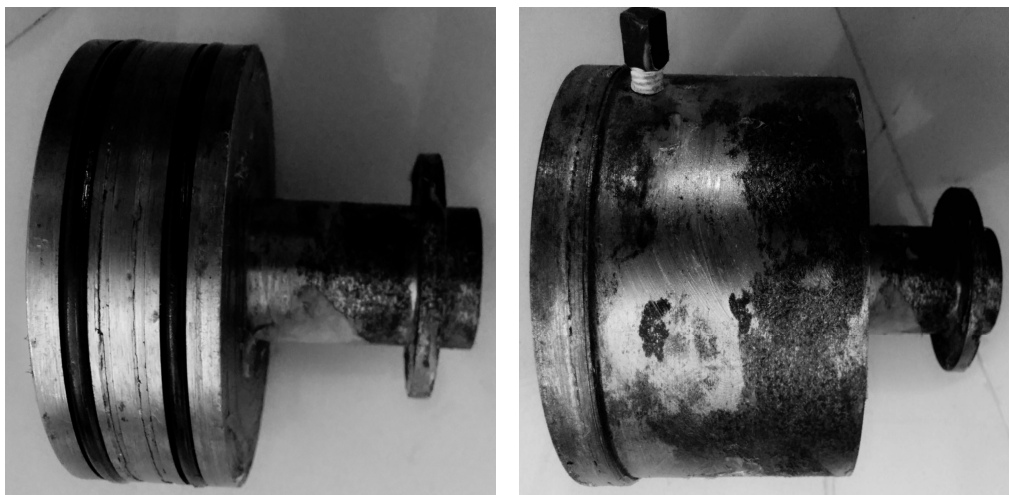

Fig. IV.4. Actuator housing with coaxial coils, end plunger and Belleville springs.

Fig. IV.5. Top cover plate of actuator housing.

(a)

(b)   (c)

Fig. IV.6. Hydraulic amplification unit (a) cylinder (b) piston and (c) cylinder with
and piston.

IV.6. Calibration of Belleville springs using universal testing machine

The calibration of Belleville springs is carried out using universal testing machine. Six number of Belleville springs arranged in series were placed between the jaws of a universal testing machine. This arrangement is made to conduct the compression test. The dial guage is held by means of vertical stand having magnetic base. Two trials were conducted to compress the Belleville springs flatten. The applied load and the corresponding deflection were noted for each trial. The average and individual deflections of Belleville springs plotted against the applied load is shown in Fig. IV.7.
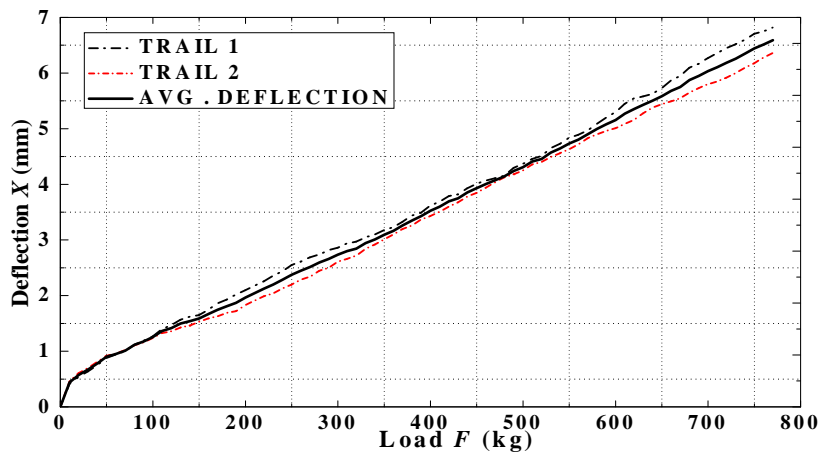
Fig. IV.7. Force-deflection curve for Belleville springs.

IV.7. Screen shots of response curves from ILD software 1402 for a Terfenol-D actuator and actuator with hydraulic amplification unit.

The response curves for a Terfenol-D actuator and actuator with hydraulic amplification unit for constant biasing with coil 1 (4 A) and varying DC input to coil 2 under 500 N preload are shown below:

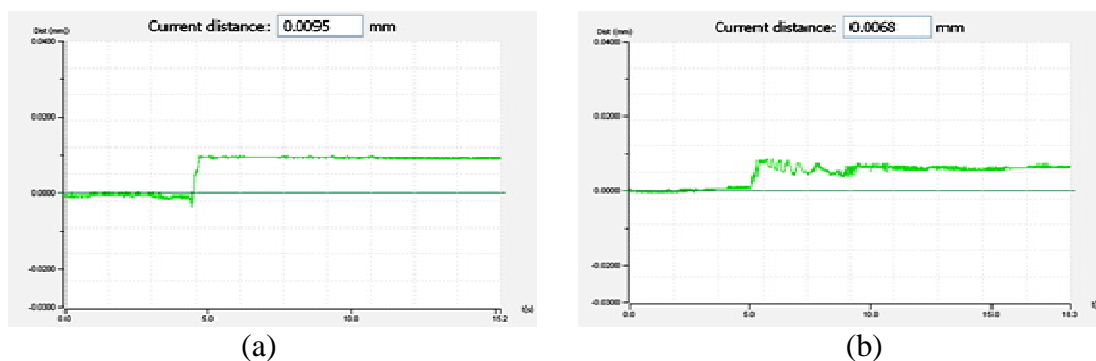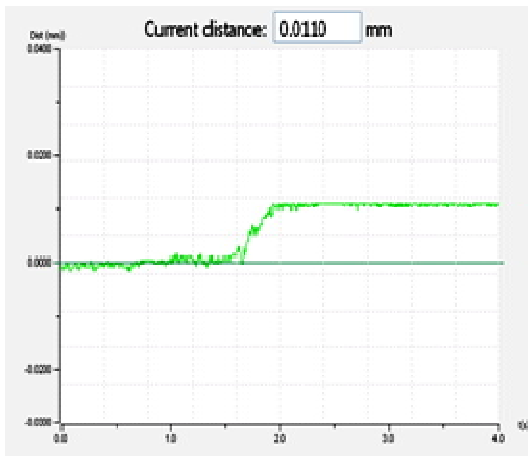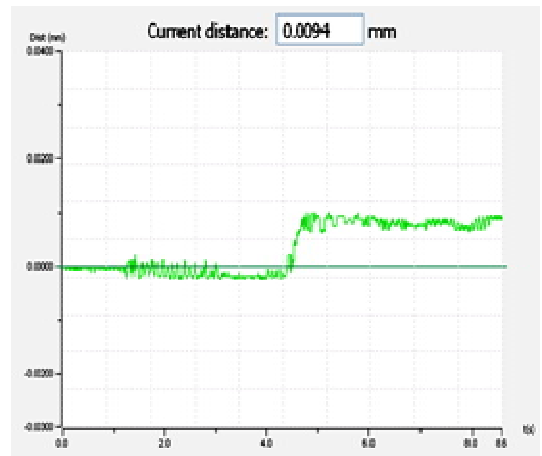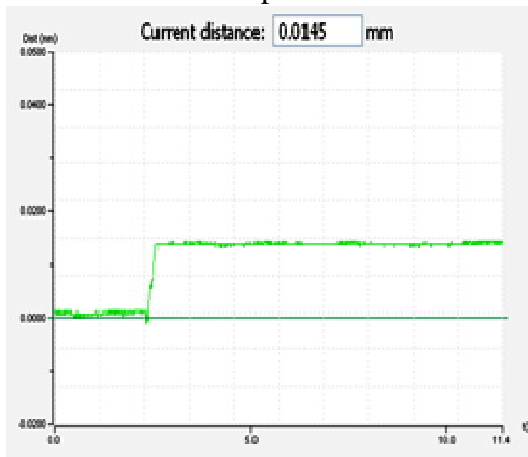(a)   (b)

Fig. IV.8. Response of (a) Terfenol-D actuator (b) Terfenol-D actuator with amplification unit for 4 A to coil 1 and 1 A to coil 2.

220

Fig. IV.9. Response of (a) Terfenol-D actuator (b) Terfenol-D actuator with amplification unit for 4 A to coil 1 and 2 A to coil 2.
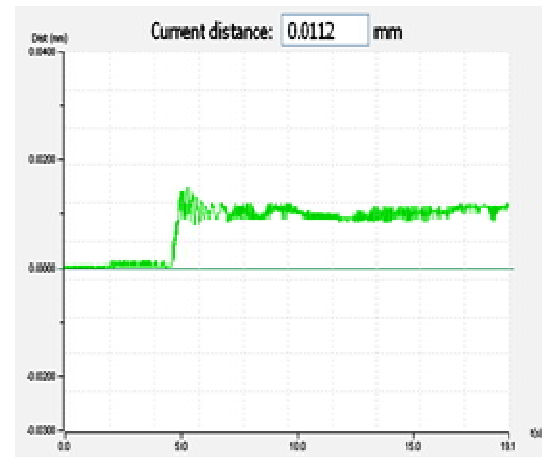

Fig. IV.10. Response of (a) Terfenol-D actuator (b) Terfenol-D actuator with amplification unit for 4 A to coil 1 and 3 A to coil 2.

Fig. IV.11. Response of (a) Terfenol-D actuator (b) Terfenol-D actuator with amplification unit for 4 A to coil 1 and 4 A to coil 2.

221
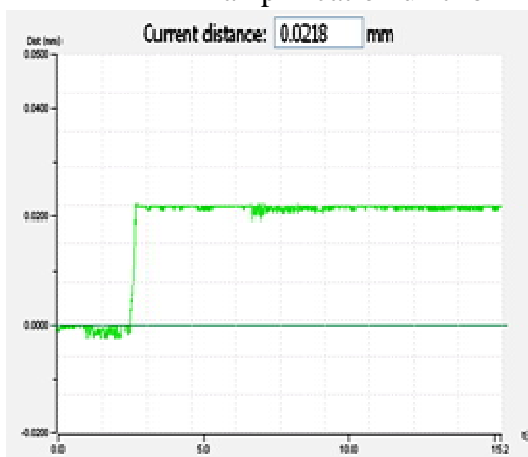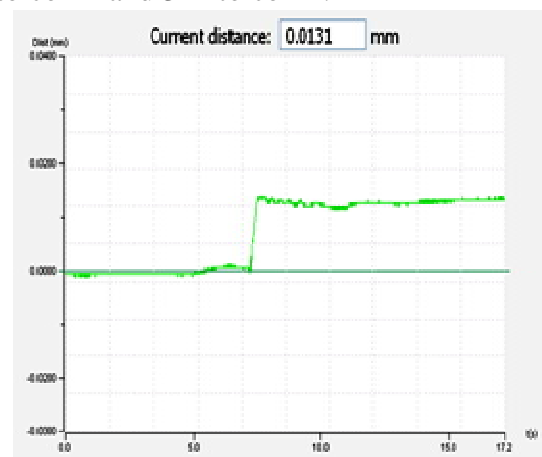
BIO DATA

NAME   : RAGHAVENDRA JOSHI

DATE OF BIRTH   : 06 -11-1971

ADDRESS   : Res: Sri Achyut Nilaya, Sanjay Gandhi Nagar,

                          Bellary, Karnataka, India.

                    : Off: Faculty, Department of Mechanical Engineering

                          Bellary Institute of Technology and Management, Bellary.

QUALIFICATION   : B.E. Mechanical Engineering - Gulbarga University-1994

                    : M. Tech. Machine Design – JNTU – Hyderabad – 1998

PUBLICATIONS FROM PRESENT RESEARCH WORK
JOURNALS

1   <u>Joshi, R.</u>, Subbarao, M and Kadoli, R. (2012). "Design procedure for optimum efficacy of magnetostrictive material ($Tb_{0.3}Dy_{0.7}Fe_{1.95}$) in actuator applications." *International Journal of Engineering and Advanced Technology*, 2(2), 187-190.

2   <u>Joshi, R.</u>, Subbarao, M and Kadoli, R. (2013). "Finite element magnetostatic analysis of Magnetostrictive ($Tb_{0.3}\ Dy_{0.7}\ Fe_{1.95}$) actuator with different housing materials" *Defence Science Journal, DRDO,* 63(4), 423-428.

3   <u>Joshi, R.</u> and Kadoli, R. (2013). "Design and study of magnetization characteristics of a magnetostrictive ($Tb_{0.3}Dy_{0.7}Fe_{1.95}$) actuator under zero pre-stress conditions for direct current input" *Advanced Materials Research*, 705, 281-287.

CONFERENCES

1   <u>Joshi, R.</u>, Subbarao, M and Kadoli, R. "Optimal use of magnetostrictive material ($Tb_{0.3}Dy_{0.7}Fe_{1.95}$) in actuator applications." National conference on Emerging Trends in Materials for Advanced Technology (NETMAT), 20-21st March 2012, KVGCE, Sullia.

2   Joshi, R., Subbarao, M and Kadoli, R. "Finite element magnetostatic analysis of magnetostrictive ($Tb_{0.3}Dy_{0.7}Fe_{1.95}$) actuator, Ist International Conference on functional materials for Defence (ICFMD), 18-20th May 2012, Defence Institute of Advanced Technology, Pune.

3   Joshi, R. and Kadoli, R. "Magnetization and Magnetostriction of a Terfenol-D actuator under ac driving conditions." International Conference on Emerging Trends in Engineering (ICETE), 15-16th May 2013, NMAM Institute of Technology, Nitte.

4   Joshi, R. and Kadoli, R. "Magneto-mechanical coupled magnetostriction model for Terfenol-D actuator under step input." International Conference on Advances in Manufacturing and Materials Engineering (ICAMME), 27-29th March 2014, NITK, Surathkal.